THE MINISTRY OF SCIENCE AND HIGHER EDUCATION OF THE RUSSIAN FEDERATION

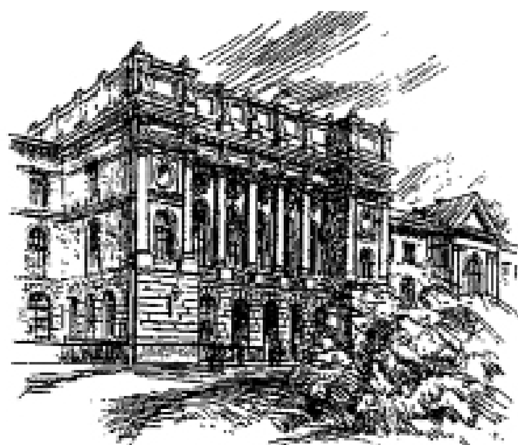

ST. PETERSBURG STATE POLYTECHNICAL UNIVERSITY JOURNAL

Physics and Mathematics

VOLUME 17, No.3, 2024

Peter the Great St. Petersburg
Polytechnic University
2024

ST. PETERSBURG STATE POLYTECHNICAL UNIVERSITY JOURNAL. PHYSICS AND MATHEMATICS

JOURNAL EDITORIAL COUNCIL

A.I. Borovkov – vice-rector for perspective projects;
VA.I. Rudskoy – full member of RAS;
R.A. Suris – full member of RAS;
A.E. Zhukov – corresponding member of RAS

JOURNAL EDITORIAL BOARD

V.K. Ivanov – Dr. Sci. (phys.-math.), prof., SPbPU, St. Petersburg, Russia, – editor-in-chief;
A.E. Fotiadi – Dr. Sci. (phys.-math.), prof., SPbPU, St. Petersburg, Russia, – deputy editor-in-chief;
V.M. Kapralova – Candidate of Phys.-Math. Sci., associate prof., SPbPU, St. Petersburg, Russia, – executive secretary;
V.I. Antonov – Dr. Sci. (phys.-math.), prof., SPbPU, St. Petersburg, Russia;
I.B. Bezprozvanny – Dr. Sci. (biology), prof., The University of Texas Southwestern Medical Center, Dallas, TX, USA;
A.V. Blinov – Dr. Sci. (phys.-math.), prof., SPbPU, St. Petersburg, Russia;
A.S. Cherepanov – Dr. Sci. (phys.-math.), prof., SPbPU, St. Petersburg, Russia;
D.V. Donetski – Dr. Sci. (phys.-math.), prof., State University of New York at Stony Brook, NY, USA;
V.V. Dubov – Dr. Sci. (phys.-math.), prof., SPbPU, St. Petersburg, Russia;
D.A. Firsov – Dr. Sci. (phys.-math.), prof., SPbPU, St. Petersburg, Russia;
P.A. Karaseov – Dr. Sci. (phys.-math.), prof., SPbPU, St. Petersburg, Russia;
A.S. Kheifets – Ph.D., prof., Australian National University, Canberra, Australia;
O.S. Loboda – Candidate of Phys.-Math. Sci., associate prof., SPbPU, St. Petersburg, Russia;
J.B. Malherbe – Dr. Sci. (physics), prof., University of Pretoria, Republic of South Africa;
V.M. Ostryakov – Dr. Sci. (phys.-math.), prof., SPbPU, St. Petersburg, Russia;
V.E. Privalov – Dr. Sci. (phys.-math.), prof., SPbPU, St. Petersburg, Russia;
E.M. Smirnov – Dr. Sci. (phys.-math.), prof., SPbPU, St. Petersburg, Russia;
A.V. Solov'yov – Dr. Sci. (phys.-math.), prof., MBN Research Center, Frankfurt am Main, Germany;
A.K. Tagantsev – Dr. Sci. (phys.-math.), prof., Swiss Federal Institute of Technology, Lausanne, Switzerland;
I.N. Toptygin – Dr. Sci. (phys.-math.), prof., SPbPU, St. Petersburg, Russia.

The journal is included in the List of leading peer-reviewed scientific journals and other editions to publish major findings of theses for the research degrees of Doctor of Sciences and Candidate of Sciences.

The publications are presented in the VINITI RAS Abstract Journal and Ulrich's Periodical Directory International Database.

The journal is published since 2008 as part of the periodical edition 'Nauchno-tekhnicheskie vedomosti SPb-GPU'.

The journal is registered with the Federal Service for Supervision in the Sphere of Telecom, Information Technologies and Mass Communications (ROSKOMNADZOR). Certificate ПИ № ФС77-52144 issued December 11, 2012.

The journal is distributed through the CIS countries catalogue, the «Press of Russia» joint catalogue and the «Press by subscription» Internet catalogue. The subscription index is 71823.

The journal is in the **Web of Science** (Emerging Sources Citation Index), **Scopus,** the **Russian Science Citation Index** (RSCI) and the **Directory of Open Access Journals** (DOAJ) databases.

© Scientific Electronic Library (http://www.elibrary.ru).

No part of this publication may be reproduced without clear reference to the source.

The views of the authors may not represent the views of the Editorial Board.

Address: 195251 Politekhnicheskaya St. 29, St. Petersburg, Russia.

Phone: 8 (812) 552-62-16.

http://ntv.spbstu.ru/physics

© Peter the Great St. Petersburg Polytechnic University, 2024

МИНИСТЕРСТВО НАУКИ И ВЫСШЕГО ОБРАЗОВАНИЯ РОССИЙСКОЙ ФЕДЕРАЦИИ

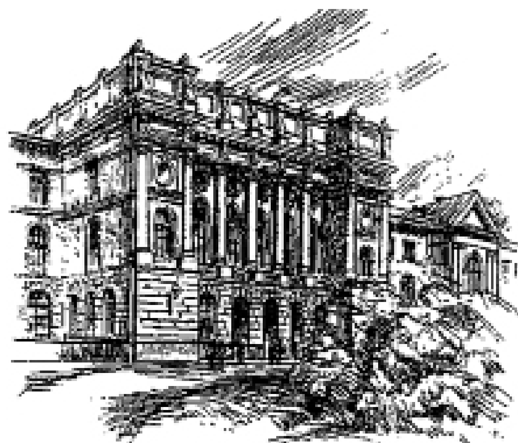

НАУЧНО-ТЕХНИЧЕСКИЕ ВЕДОМОСТИ
САНКТ-ПЕТЕРБУРГСКОГО ГОСУДАРСТВЕННОГО ПОЛИТЕХНИЧЕСКОГО УНИВЕРСИТЕТА

Физико-математические науки

ТОМ 17, №3

2024

Санкт-Петербургский политехнический
университет Петра Великого
2024

НАУЧНО-ТЕХНИЧЕСКИЕ ВЕДОМОСТИ САНКТ-ПЕТЕРБУРГСКОГО ГОСУДАРСТВЕННОГО ПОЛИТЕХНИЧЕСКОГО УНИВЕРСИТЕТА. ФИЗИКО-МАТЕМАТИЧЕСКИЕ НАУКИ

РЕДАКЦИОННЫЙ СОВЕТ ЖУРНАЛА

Боровков А.И., проректор по перспективным проектам;
Жуков А.Е., чл.-кор. РАН;
Рудской А.И., академик РАН;
Сурис Р.А., академик РАН.

РЕДАКЦИОННАЯ КОЛЛЕГИЯ ЖУРНАЛА

Иванов В.К., д-р физ.-мат. наук, профессор, СПбПУ, СПб., Россия, – главный редактор;
Фотиади А.Э., д-р физ.-мат. наук, профессор, СПбПУ, СПб., Россия, – зам. главного редактора;
Капралова В.М., канд. физ.-мат. наук, доцент, СПбПУ, СПб., Россия – ответственный секретарь;
Антонов В.И., д-р физ.-мат. наук, профессор, СПбПУ, СПб., Россия;
Безпрозванный И.Б., д-р биол. наук, профессор, Юго-Западный медицинский центр Техасского университета, Даллас, США;
Блинов А.В., д-р физ.-мат. наук, профессор, СПбПУ, СПб., Россия;
Донецкий Д.В., д-р физ.-мат. наук, профессор, университет штата Нью-Йорк в Стоуни-Брук, США;
Дубов В.В., д-р физ.-мат. наук, профессор, СПбПУ, СПб., Россия;
Карасёв П.А., д-р физ.-мат. наук, профессор, СПбПУ, СПб., Россия;
Лобода О.С., канд. физ.-мат. наук, доцент, СПбПУ, СПб., Россия;
Малерб Й.Б., Dr.Sc. (Physics), профессор, университет Претории, ЮАР;
Остряков В.М., д-р физ.-мат. наук, профессор, СПбПУ, СПб., Россия;
Привалов В.Е., д-р физ.-мат. наук, профессор, СПбПУ, СПб., Россия;
Смирнов Е.М., д-р физ.-мат. наук, профессор, СПбПУ, СПб., Россия;
Соловьёв А.В., д-р физ.-мат. наук, профессор, Научно-исследовательский центр мезобионаносистем (MBN), Франкфурт-на-Майне, Германия;
Таганцев А.К., д-р физ.-мат. наук, профессор, Швейцарский федеральный институт технологий, Лозанна, Швейцария;
Топтыгин И.Н., д-р физ.-мат. наук, профессор, СПбПУ, СПб., Россия;
Фирсов Д.А., д-р физ.-мат. наук, профессор, СПбПУ, СПб., Россия;
Хейфец А.С., Ph.D. (Physics), профессор, Австралийский национальный университет, Канберра, Австралия;
Черепанов А.С., д-р физ.-мат. наук, профессор, СПбПУ, СПб., Россия.

Журнал с 2002 г. входит в Перечень ведущих рецензируемых научных журналов и изданий, в которых должны быть опубликованы основные результаты диссертаций на соискание ученых степеней доктора и кандидата наук.

Сведения о публикациях представлены в Реферативном журнале ВИНИТИ РАН, в международной справочной системе «Ulrich’s Periodical Directory».

С 2008 года выпускается в составе сериального периодического издания «Научно-технические ведомости СПбГПУ».

Журнал зарегистрирован Федеральной службой по надзору в сфере информационных технологий и массовых коммуникаций (Роскомнадзор). Свидетельство о регистрации ПИ № ФС77-52144 от 11 декабря 2012 г.

Распространяется по Каталогу стран СНГ, Объединенному каталогу «Пресса России» и по Интернет-каталогу «Пресса по подписке». Подписной индекс 71823.

Журнал индексируется в базах данных **Web of Science** (Emerging Sources Citation Index), **Scopus**, а также включен в базы данных **«Российский индекс научного цитирования»** (РИНЦ), размещенную на платформе Научной электронной библиотеки на сайте http://www.elibrary.ru, и **“Directory of Open Access Journals”** (DOAJ).

При перепечатке материалов ссылка на журнал обязательна.

Точка зрения редакции может не совпадать с мнением авторов статей.

Адрес редакции и издательства:

Россия, 195251, Санкт-Петербург, ул. Политехническая, д. 29.

Тел. редакции 8 (812) 552-62-16.

http://ntv.spbstu.ru/physics

© Санкт-Петербургский политехнический университет Петра Великого, 2024

Contents

Condensed matter physics

Revin A. A., Konakov A. A., Korolev D. S. *The electronic structure of gallium oxide nanocrystals doped with shallow donors* 7

Baranov A. I., Vtorygin G. E., Uvarov A. V., Maksimova A. A., Vyacheslavova E. A., Gudovskikh A. S. *Admittance spectroscopy of boron phosphide heterostructures grown by plasma enhanced chemical vapor deposition on silicon substrates* 17

Dvoretckaia L. N., Mozharov A. M., Komarov S. D., Vyacheslavova E. A., Moiseev E. I., Fedorov V. V., Mukhin I. S. *Creation of optical isolated GaP(NAs) microcavities on silicon* 25

Castro R. A., Karulina E. A., Galikhanov M. F., Reztsov T. V., Fomicheva E. E. *Relaxation of electric charge in polymer blends based on low-density polyethylene and copolymer of ethylene with vinyl acetate* 36

Simulation of physical processes

Barykin D. A., Shugurov K. Yu., Mozharov A. M., Mukhin I. S. *Numerical simulation of the tunnel effect in the gallium nitride heterostructure on silicon* 46

Zemskov A. V., Vestyak A. V., Tarlakovskii D. V. *A model of unsteady mechanodiffusion vibrations of a rectangular orthotropic Timoshenko plate with mixed edge fixing* 57

Physical materials technology

Nikitina E. A., Kapralova V. M., Sudar N. T., Studzinskii V. M., Gerasimov V. I. *Electrical and optical properties of a nanocomposite based on polyvinyl alcohol and fullerenol* 76

Abduvayitov A. A., Tashmukhamedova D. A., Umirzakov B. E., Khujaniyozov J. B., Bekpulatov I. R., Loboda V. V. *Effect of argon ion bombardment on the composition, electronic structure and physical properties of cadmium fluoride* 87

Donaev S. B., Shirinov G. M. ugli, Umirzakov B. Y., Loboda V. V. *Influence of low-energy electron bombardment on the composition and structure of the gallium phosphide surface* 97

Mechanics

Astapov Y. K., Lukin A. V., Popov I. A. *An analysis of the accuracy of short-wave and long-wave asymptotics for stationary Lamb waves in the isotropic layer* 105

Afanasov E. N., Kadyrov S. G., Sorokin V. N. *Asymptotic methods for solving the Stokes problem for a flat contour* 118

Novokshenov A. D., Abdulin I., Vershinin D. V. *A topology optimization algorithm for electroelasticity coupled problems* 134

Astrophysics

Teófilo-Salvador E. *Individual behavior of gas hydrodynamics from pairs of isolated galaxies in interaction* 148

Содержание

Физика конденсированного состояния

Ревин А. А., Конаков А. А., Королев Д. С. *Электронная структура нанокристаллов оксида галлия, легированных мелкими донорами* 7

Баранов А. И., Вторыгин Г. Э., Уваров А. В., Максимова А. А., Вячеславова Е. А., Гудовских А. С. *Спектроскопия полной проводимости гетероструктур фосфида бора на кремниевых подложках, полученных методом плазмохимического осаждения* 17

Дворецкая Л. Н., Можаров А. М., Комаров С. Д., Вячеславова Е. А., Моисеев Э. И., Федоров В. В., Мухин И. С. *Создание оптических изолированных микрорезонаторов GaP(NAs) на кремнии* 25

Кастро Р. А., Карулина Е. А., Галиханов М. Ф., Резцов Т. В., Фомичева Е. Е. *Релаксация электрического заряда в полимерных смесях на основе полиэтилена высокого давления и сополимера этилена с винилацетатом (статья на английском языке)* 36

Математическое моделирование физических процессов

Барыкин Д. А., Шугуров К. Ю., Можаров А. М., Мухин И. С. *Численное моделирование туннельного эффекта в гетероструктуре нитрида галлия на кремнии* 46

Земсков А. В., Вестяк А. В., Тарлаковский Д. В. *Модель нестационарных механодиффузионных колебаний прямоугольной ортотропной пластины Тимошенко со смешанным закреплением по краям* 57

Физическое материаловедение

Никитина Е. А., Капралова В. М., Сударь Н. Т., Студзинский В. М., Герасимов В. И. *Электрические и оптические свойства нанокомпозитного материала на основе поливинилового спирта и фуллеренола* 76

Абдувайитов А. А., Ташмухамедова Д. А., Умирзаков Б. Е., Хужаниёзов Д. Б., Бекпулатов И. Р., Лобода В. В. *Влияние бомбардировки ионами аргона на состав, электронную структуру и физические свойства фторида кадмия (статья на английском языке)* 87

Донаев С. Б., Ширинов Г. М., Умирзаков Б. Е., Лобода В. В. *Влияние низкоэнергетической электронной бомбардировки на состав и структуру поверхности фосфида галлия* 97

Механика

Астапов Я. К., Лукин А. В., Попов И. А. *Анализ точности коротковолновых и длинноволновых асимптотик для стационарных волн Лэмба в изотропном слое* 105

Афанасов Е. Н., Кадыров С. Г., Сорокин В. Н. *Асимптотические методы решения задачи Стокса для плоского контура* 118

Новокшенов А. Д., Абдулин И., Вершинин Д. В. *Алгоритм топологической оптимизации для связанных задач электроупругости* 134

Астрофизика

Теофило-Сальвадор Э. *Изучение пар изолированных взаимодействующих галактик в аспекте гидродинамического поведения газа (статья на английском языке)* 148

CONDENSED MATTER PHYSICS

Original article
DOI: https://doi.org/10.18721/JPM.17301

THE ELECTRONIC STRUCTURE OF GALLIUM OXIDE NANOCRYSTALS DOPED WITH SHALLOW DONORS

A. A. Revin, A. A. Konakov, D. S. Korolev✉

National Research Lobachevsky State University of Nizhni Novgorod, Nizhni Novgorod, Russia

✉ dmkorolev@phys.unn.ru

Abstract. The results of theoretical calculations of electronic states of the gallium oxide (Ga_2O_3) nanocrystals both doped with donor impurity and undoped have been presented in the paper. In the envelope function approximation, the structure, states and energy levels of size quantization in the nanocrystals were determined. According to our calculations, the electron-hole pair forms a bound state of the exciton type in the nanocrystal. The typical donor impurities in Ga_2O_3, such as silicon and tin, were shown to create bandgap states localized in a spatial domain being several times smaller than the nanocrystal's volume. Forming a compact neutral pair, the electron and donor ions have no noticeable influence on the states of the optically excited electron-hole pairs. The effect of impurity implantation on recombination processes was also discussed.

Keywords: nanocrystal, gallium oxide, electronic structure, donor impurity, quantum size effect

Funding: The reported study was funded by Russian Science Foundation (Grant No. 21-79-10233, https://rscf.ru/project/21-79-10233/).

Citation: Revin A. A., Konakov A. A., Korolev D. S., The electronic structure of gallium oxide nanocrystals doped with shallow donors, St. Petersburg State Polytechnical University Journal. Physics and Mathematics. 17 (3) (2024) 7–16. DOI: https://doi.org/10.18721/JPM.17301

This is an open access article under the CC BY-NC 4.0 license (https://creativecommons.org/licenses/by-nc/4.0/)

Научная статья
УДК 538.915
DOI: https://doi.org/10.18721/JPM.17301

ЭЛЕКТРОННАЯ СТРУКТУРА НАНОКРИСТАЛЛОВ ОКСИДА ГАЛЛИЯ, ЛЕГИРОВАННЫХ МЕЛКИМИ ДОНОРАМИ

А. А. Ревин, А. А. Конаков, Д. С. Королев✉

Нижегородский государственный университет им. Н. И. Лобачевского, г. Нижний Новгород, Россия

✉ dmkorolev@phys.unn.ru

Аннотация. Приведены результаты теоретических расчетов электронных состояний нанокристаллов оксида галлия (Ga_2O_3) как легированных донорной примесью, так и нелегированных. Определены структура, состояния и энергетические уровни размерного квантования в нанокристаллах в приближении огибающей функции. Согласно расчетам, электронно-дырочная пара образует в нанокристалле связанное состояние экситонного типа. Показано, что типичные донорные примеси в Ga_2O_3, такие как кремний и олово, создают в запрещенной зоне состояния, локализованные в пространственной области, в несколько раз меньшей объема нанокристалла. Образуя компактную нейтральную пару,

© Revin A. A., Konakov A. A., Korolev D. S., 2024. Published by Peter the Great St. Petersburg Polytechnic University.

электрон и донорный ион не оказывают какого-либо заметного влияния на состояния оптически возбужденных электронно-дырочных пар. Обсуждается также влияние внедрения примеси на рекомбинационные процессы.

Ключевые слова: нанокристалл, оксид галлия, электронная структура, донорная примесь, квантово-размерный эффект

Финансирование: Исследование выполнено за счет гранта Российского научного фонда № 10233-79-21, https://rscf.ru/project/21-79-10233/.

Ссылка для цитирования: Ревин А. А., Конаков А. А., Королев Д. С. Электронная структура нанокристаллов оксида галлия, легированных мелкими донорами // Научно-технические ведомости СПбГПУ. Физико-математические науки. 2024. Т. 17. № 3. С. 7–16. DOI: https://doi.org/10.18721/JPM.17301

Статья открытого доступа, распространяемая по лицензии CC BY-NC 4.0 (https://creativecommons.org/licenses/by-nc/4.0/)

Introduction

Wide-bandgap semiconductors are one of the most promising materials for use in electronics. Gallium oxide, a semiconductor material serving as parent compound for 4th-generation electronics devices, is becoming increasingly popular. Due to its characteristics, primarily a sufficiently wide band gap of about 4.5–5.2 eV, gallium oxide is one of the best candidates for power electronics devices, UV radiation detectors, gas sensors, etc. [1–3]. Another important advantage is the technology for producing monocrystalline substrates of large diameter.

Much focus has been placed on developing and exploring the methods for obtaining materials based on gallium oxide (single crystal growth, epitaxy and thin film deposition), modifying its properties, and finding potential applications in instrumentation [4–6]. Numerous experimental as well as theoretical works consider the band structure, electronic states and parameters of defect levels in bulk gallium oxide [7–9].

A major direction in technologies for materials based on gallium oxide is the creation of nanostructures. Practical applications primarily include light-emitting and photodetector devices based on these nanostructures [10, 11]. However, widespread use is limited, as main methods for chemical synthesis of nanostructures that are incompatible with microelectronic technology.

This limitation can be overcome by ion beam synthesis of Ga_2O_3 nanocrystals (NC) in dielectric matrices (for example, silicon or aluminum oxides) on silicon substrates [12]. The advantage of ion synthesis, in addition to full compatibility with silicon technology, is the option for doping the material with impurity atoms, allowing to control the property modifications of synthesized samples. Despite vigorous experimental research on this topic, there are virtually no theoretical papers on gallium oxide nanostructures.

Structures with gallium oxide NC exhibit strong UV and blue luminescence, which can be used both to synthesize LED structures and to convert UV radiation into visible light [13, 14]. The photoluminescence spectra of such nanostructures differ from the emission spectra of bulk Ga_2O_3 samples. However, explanations of the observed patterns, in particular, accounting for size quantization in the luminescence of nanoparticles, are exclusively qualitative [15]. The effect of doping by shallow donors on the band structure and electronic states of Ga_2O_3 NC remains completely unexplored.

This paper presents a theoretical study of the electronic structure of gallium oxide NC without doping impurities as well as NC doped with a shallow donor impurity.

Electronic structure of gallium oxide nanocrystals without impurities (in the zero approximation)

Since the impurity potential should be considered as a perturbation to study the effect of shallow donors on the structure of quasiparticle states in NC, let us start by briefly describing the structure of electron and hole states in pure Ga_2O_3 NC.

© Ревин А. А., Конаков А. А., Королев Д. С., 2024. Издатель: Санкт-Петербургский политехнический университет Петра Великого.

The problem of size quantization of electrons and holes in gallium oxide was solved in the envelope approximation. The equation for determining the eigenfunctions and eigenvalues has the form

$$-\frac{\hbar^2}{2}\left(\frac{1}{m_x}\frac{\partial^2}{\partial x^2}+\frac{1}{m_y}\frac{\partial^2}{\partial y^2}+\frac{1}{m_z}\frac{\partial^2}{\partial z^2}\right)F(\mathbf{r})+U(r)F(\mathbf{r})=EF(\mathbf{r}), \tag{1}$$

where m_y, m_z are the components of the anisotropic effective mass of electron or hole; E is the energy; $F(\mathbf{r})$ is the envelope function; the potential $U(\mathbf{r})$ is assumed to be central.

We assume that $U(\mathbf{r})$ is a spherical well of finite depth (Fig. 1). The magnitude of conduction band discontinuity is about 3 eV, and that of valence band discontinuity is about 1 eV [4]. We also neglect the anisotropy of effective masses [16], as taking it into account for electrons produces corrections beyond the accuracy of calculations, while the magnitude of corrections for holes is slightly larger but still remains small.

Then the solution of Eq. (1) is obtained as follows:

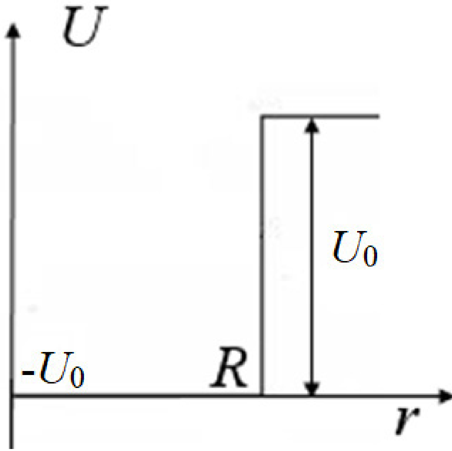

Fig. 1. Potential $U(r)$ of spherical well (R is its radius) with finite depth U_0

$$\psi_{klm}=A\frac{j_l(kr)}{r}Y_{lm}(\theta,\varphi),\ r<R,$$
$$\psi_{klm}=B\frac{h_l(i\kappa r)}{r}Y_{lm}(\theta,\varphi),\ r>R, \tag{2}$$

is the radius of the nanocrystal; $k^2=\frac{2m\left(V_0-|E|\right)}{\hbar^2}$; $\kappa^2=\frac{2m|E|}{\hbar^2}$; $j_l(kr)$ are the spherical Bessel functions; $h_l(ikr)$ are the Hankel functions of an imaginary argument.

The undefined constants are found from the condition for normalization and continuity of the wave function. The energy spectrum of Ga_2O_3 NC is found from the condition for continuity of the logarithmic derivative.

Fig. 2 shows the ground-state (1*s*) energy dependences of the conduction electron and hole, measured from the bottom of the conduction band (up) and the top of the valence band (down), respectively.

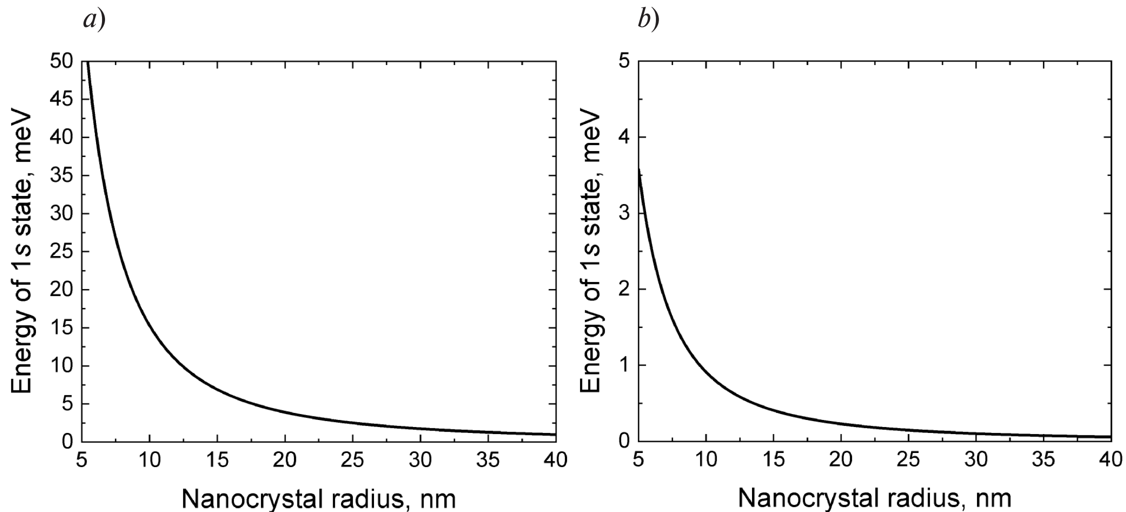

Fig. 2. Energy dependences of 1*s*-state of electron (*a*) and hole (*b*) on radius of β-Ga_2O_3 NC

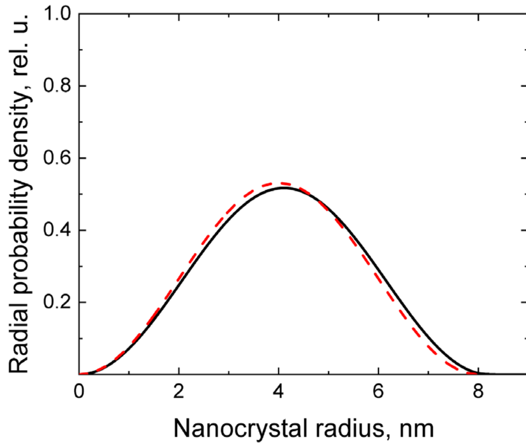

Fig. 3. Comparison of radial probability densities $r^2|\psi|^2$ for spherical wells of finite (solid line) and infinite (dashed line) depths
Density is expressed in 'natural' units for a finite well (rel. u.): $k_0 = \sqrt{2mU_0/\hbar^2}$

Analyzing the graphs, we can conclude that the obtained energies of the ground-state levels of size quantization differ slightly from the energy levels of an infinite spherical well, so wave functions of an infinite spherical well can be used in the calculations below as wave functions of the ground and low-lying excited states. Notably, proximity of wave functions is much more important than that of energies for such an approximation.

Fig. 3 shows the radial densities given by the ground-state wave functions for finite and infinite wells. Evidently, the wave functions are close everywhere, it is justified to use infinite well functions.

Dividing the system of equations for holes and electrons into two independent equations of type (1) is not always justified (see, for example, [17]); in general, a hole and an electron affect each other's states and it is necessary to solve a system of equations that are not divided into independent equations for an electron and a hole.

Let us estimate the interaction energy of particles in states (2) in accordance with the perturbation theory. This estimate can allow to determine whether their states can be considered independent. Apparently, this energy is a diagonal matrix element of the Coulomb interaction:

$$E = \left\langle 1s_e 1s_h \middle| \hat{V} \middle| 1s_e 1s_h \right\rangle, \tag{3}$$

where $\left|1s_e 1s_h\right\rangle$ is the ground-state vector of the electron–hole system.

The wave function corresponding to this vector is equal to the product of the ground-state wave functions of the electron–hole system.

The Coulomb interaction operator $\hat{V}$ in coordinate representation has the form

$$\hat{V} = -\frac{e^2}{\varepsilon_s \left|\mathbf{r}_e - \mathbf{r}_h\right|}, \tag{4}$$

where $\mathbf{r}_e$, $\mathbf{r}_h$ are the radius vectors of the electron and the hole, respectively; ε_s is the static dielectric constant.

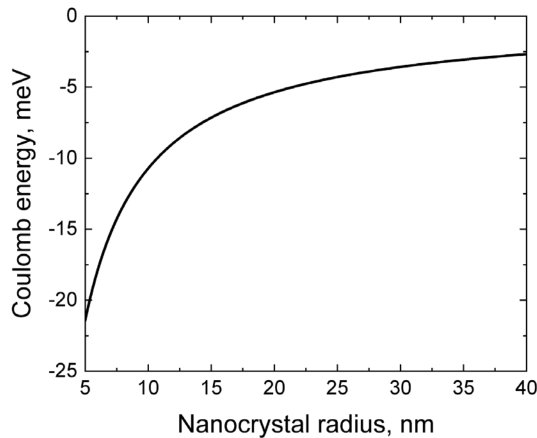

Fig. 4. Dependence of electron–hole Coulomb interaction energy on nanocrystal radius

The dependence of the Coulomb interaction energy on the radius of the nanocrystal is shown in Fig. 4. As seen from the graph, the magnitude of the direct electron–hole Coulomb interaction is comparable to the size quantization energies obtained from independently considered equations of type (1). This suggests that the separation of electrons and holes into independent particles apparently does not occur, with an exciton produced in Ga_2O_3 NC, while an exciton polaron can appear against the background of strong interaction between charge carriers and polar optical phonons.

Importantly, the approximation used for the hole spectra is highly qualitative, allowing to confirm that the size quantization in Ga_2O_3 NC does not affect the width of the optical band gap, but using hole wave functions in form (2) can yield inaccuracies. The reason for this is that, firstly,

the multi-valley structure of the valence band was not taken into account in the construction of the *kp* procedure, and, secondly, there are several closely lying valence bands, such that the distance between them is comparable to the magnitude of the valence band discontinuity used in the study. The latter apparently suggests that a multi-band model should be used to study hole states. However, these issues require separate consideration and are beyond the scope of this paper.

Electronic structure of impurity atoms in gallium oxide nanoinclusions

Bulk materials are characterized by clear separation of defects into shallow and deep ones. This separation primarily depends on the degree of localization of the potential producing this defect. The potential of deep centers is highly localized and acts within a single unit cell. Although shallow defects may include a part of the potential limited by the unit cell (the so-called potential of the central cell [18]), they also always include a long-range Coulomb part of the potential, so they are often called Coulomb centers. It follows then that deep defects virtually do not change the structure of the states they produce in nanoscale systems, since they cannot 'sense' the boundaries of NC. On the other hand, the states of shallow defects can vary greatly. The radii of discrete localized electronic states that they induce in a bulk material can be of the same order or even larger than the sizes of nanoinclusions, i.e., the NC boundaries that generate the confinement potential should inevitably be included in the problem. In view of this, it is much more important to find the states for shallow donors in NC than those for deep centers.

Let us consider how the addition of impurity atoms affects the electron and hole spectra of gallium oxide NC. The Hamiltonian in Eq. (1) takes the following form in the approximation of the envelope function in the presence of a shallow donor:

$$\hat{H} = \frac{\hat{p}^2}{2m} + U(\mathbf{r}) + V(\mathbf{r},\mathbf{h}), \tag{5}$$

where m is the effective mass of electron or hole in the isotropic approximation, $U(\mathbf{r})$ is the potential of the spherical well, $V(\mathbf{r},\mathbf{h})$ is the potential of the donor, depending on the position of the donor at a point with a radius vector $\mathbf{h}$.

The impurity potential contains two terms:

$$V = V_C + W(\mathbf{r}), \tag{6}$$

where $W(\mathbf{r})$ is the short-range potential of the central cell, depending on the nearest neighbors of the donor; V_C is the Coulomb term of the potential, $V_C = \frac{e_0^2}{\varepsilon_s r}$.

The short-range potential can be calculated using the dielectric function, or taken into account phenomenologically, if the positions of impurity levels in bulk material are known. The data available on the levels of different donor impurities is somewhat contradictory. It can be assumed for silicon [19] that the level only slightly differs from the hydrogen-like one (whose value is about 27 MeV) in most cases. The position of the level for tin can vary from 16 MeV [20] to 60 MeV [21] according to different sources, and the concentrations of donors are almost equal ($9{\cdot}10^{17}$ and $10{\cdot}7^{17}$ cm^{-3}, respectively). A decrease in the energy of the donor level compared to the hydrogen-like one is associated with electron delocalization, due to changes in the dielectric constant or the influence of neighboring impurities; an increase in the energy level is generally associated with a strong potential of the central cell. Theoretical analysis is complex because these scenarios happen at almost equal concentrations. Therefore, we neglect the potential of the central cell in the first approximation to calculate the structure of the hydrogen-like donor.

Let us calculate the correction for the ground-state energy of the electron–hole system in accordance with the perturbation theory, where the perturbation potential has the following form:

$$V_C = \pm \frac{e_0^2}{\varepsilon_s |\mathbf{r} - \mathbf{h}|}, \tag{7}$$

where $\mathbf{h}$ is the radius vector of the impurity atom.

The plus sign is assigned to holes, since the donor is positively charged and the hole repels, the minus sign is assigned to electrons.

The following parameters were chosen for the calculations: the radius of the nanocrystal was R = 10 nm, the functions of an infinite well were used as wave functions due to the above-described reasons, the unperturbed energies amounted to $E_{1se} \approx 13$ MeV and $E_{1sh} \approx 1$ MeV. Graphs for the dependence of first-order energy corrections for electrons and holes are shown in Fig. 5.

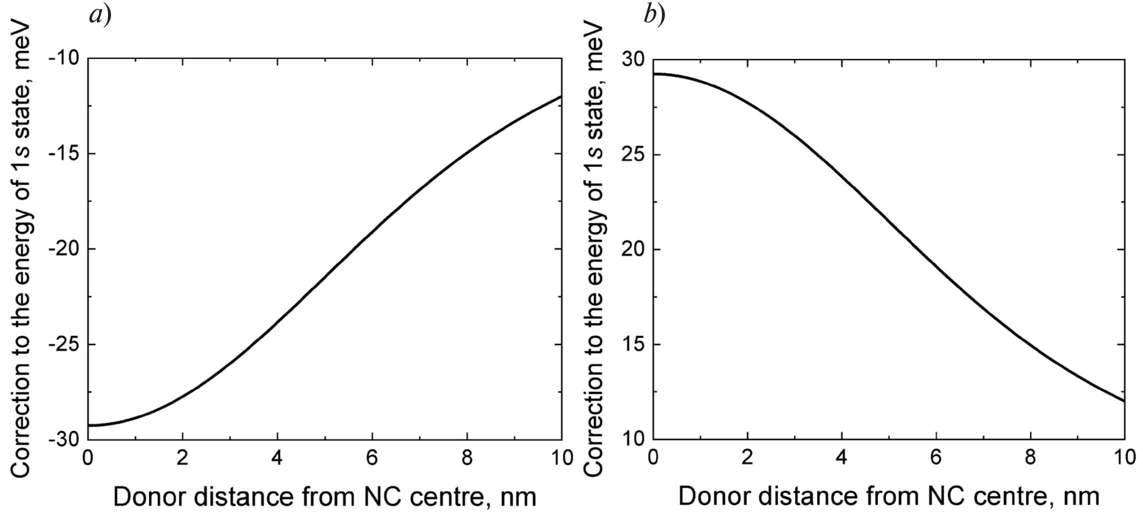

Fig. 5. Dependences of corrections to ground-state energy of electrons (*a*) and holes (*b*) on position of donor in nanocrystal (first-order perturbation theory)

It can be seen from the graphs that the first-order correction to the ground state is not small compared to the ground-state energy, regardless of the position of the donor in the nanocrystal. It follows then that the potential of the donor cannot be considered small, which must be taken into account by the finite series sum of perturbation theory. Therefore, a different method should be used for calculating the spectrum.

A suitable technique for calculating the energy levels of electrons and holes is the Rayleigh–Ritz variational method [22]. Notably, other quantities for which the wave function is used may be far from reality, although the energy levels are calculated rather accurately in this approximation.

Let us first consider the case of a donor in the center of a nanocrystal. Judging from the data in Fig. 5, the electronic structure is influenced by the donor to the greatest extent. It is natural to select a trial function for the electronic ground state that is similar to both the function of a spherical well and the function of the hydrogen atom. Therefore, the trial wave function is taken in the following form:

$$\psi_e = A \frac{\sin \frac{\pi \cdot r}{R}}{r} \exp(-\alpha r), \tag{8}$$

where α, A are constants; α is the variational parameter, A is the normalization constant.

Fig. 6 shows the radial distribution of the electronic ground-state energy level in a nanocrystal with a Coulomb impurity donor.

The graph shows that the donor levels of the doped nanocrystal are only slightly different from those of the bulk material in the case of the hydrogen-like potential; the radius of the wave function is $\alpha^{-1} \sim 1$ nm, i.e., the donor, as in the bulk material, forms a neutral system of a rather small radius, which has virtually no effect on the optically excited electron–hole pair. The evidence for this is that the electron–hole densities are concentrated in states (2) in a spherical layer whose radius is approximately equal to half the radius of the nanocrystal (see Fig. 3), and the system, including a donor electron and an ion, has an effective range of $\alpha \sim 1$ nm. This result suggests that an optically excited electron–hole pair in a doped gallium oxide nanocrystal behaves

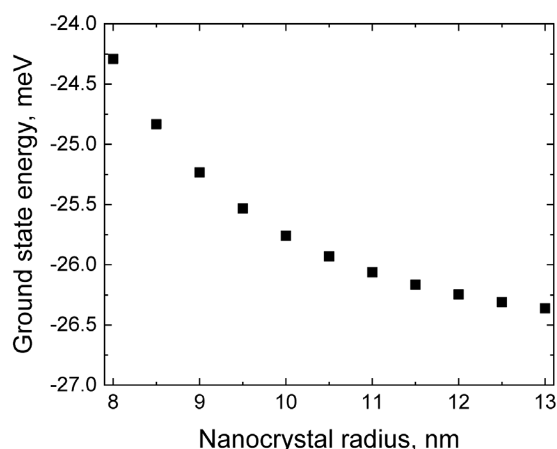

Fig. 6. Radial dependence of electronic ground-state energy in nanocrystal with Coulomb impurity center (donor)

the same as in a nanocrystal without a doping impurity, and the width of the optical band gap practically does not depend on the doping level of the nanocrystal.

An important difference between a doped nanocrystal and an undoped one is the presence of an extra electron, which has a high (on the order of the band gap width) energy of the bulk material in the ground state, i.e., an additional recombination channel associated with the Auger process appears after optical excitation of the electron–hole pair. Auger recombination can play an important practical role for developing ultraviolet detectors based on structures with gallium oxide nanocrystals. This follows from the fact that the electron is always in a localized state in an undoped nanocrystal. Since the electronic wave function differs slightly from the function of an infinite well, the probability of an electron hopping between nanocrystals tends to zero, i.e., photocurrent flow is unlikely in NC arrays that do not contain impurities.

In contrast, an electron can fall into the region of continuous spectrum between the vacuum level and the bottom of the conduction band of the dielectric matrix during Auger recombination. The electronic wave function is delocalized in this energy range, so the electron can successfully move through the entire NC array, generating a photocurrent.

Conclusion

The paper reports on the electronic structure of a β-Ga_2O_3 nanocrystal doped with a shallow donor. It was established that the Coulomb potential cannot be considered as a small perturbation, since it strongly affects the electronic state of the entire system, creating a state close to the impurity state for a bulk semiconductor.

The approach used in the study serves as an excellent approximation for electrons, since the conduction band has a single minimum, well separated from the other bands in terms of energies. On the other hand, this approximation is qualitative in nature for holes and is applicable only for estimating the width of the optical band gap.

Further research should be carried out, accounting for the multi-valley structure in the multiband model and the strong interaction of the hole with optical polar phonons, which can be considerably stronger in low-dimensional systems.

The results obtained can be used to develop light-emitting and photodetector devices based on gallium oxide nanocrystals.

REFERENCES

1. **Wang C., Zhang J., Xu S., et al.,** Progress in state-of-the-art technologies of Ga_2O_3 devices, J. Phys. D: Appl. Phys. 54 (24) (2021) 243001.

2. **Zhang J., Dong P., Dang K., et al.,** Ultra-wide bandgap semiconductor Ga_2O_3 power diodes, Nat. Commun. 13 (July 6) (2022) 3900.

3. **Zhai H., Wu Z., Fang Z.,** Recent progress of Ga_2O_3-based gas sensors, Ceram. Int. 48 (17) (2022) 24213–24233.

4. **Pearton S. J., Yang J., Cary P. H., et al.,** A review of Ga_2O_3 materials, processing, and devices, Appl. Phys. Rev. 5 (1) (2018) 011301.

5. **Nikolskaya A., Okulich E., Korolev D., et al.,** Ion implantation in β-Ga_2O_3: Physics and technology, J. Vac. Sci. Technol. A. 39 (3) (2021) 030802.

6. **Higashiwaki M.,** β-Ga_2O_3 material properties, growth technologies, and devices: A review, AAPPS Bul. 32 (1) (2022) 3.

7. **Zhang J., Shi J., Qi D., et al.,** Recent progress on the electronic structure, defect, and doping properties of Ga_2O_3, APL Mater. 8 (2) (2020) 020906.
8. **Frodason Y. K., Krzyzaniak P. P., Vines L., et al.,** Diffusion of Sn donors in β-Ga_2O_3, APL Mater. 11 (4) (2023) 041121.
9. **Wang M., Mu S., Van de Walle C. G.,** Incorporation of Si and Sn donors in β-Ga_2O_3 through surface reconstructions. J. Appl. Phys. 130 (18) (2021) 185703.
10. **Jamwal N. S., Kiani A.,** Gallium oxide nanostructures: A review of synthesis, properties and applications, Nanomater. 12 (12) (2022) 2061.
11. **Rajamani S., Arora K., Belov A., et al.,** Enhanced solar-blind photodetection performance of encapsulated Ga_2O_3 nanocrystals in Al_2O_3 matrix, IEEE Sens. J. 18 (10) (2018) 4046–4052.
12. **Korolev D. S., Matyunina K. S., Nikolskaya A. A., et al.,** Ion-beam synthesis of gallium oxide nanocrystals in a SiO_2/Si dielectric matrix, Nanomater. 12 (11) (2022) 1840.
13. **Zhou J., Chen H., Fu K., Zhao Y.,** Gallium oxidebased optical nonlinear effects and photonics devices, J. Mater. Res. 36 (23) (2021) 4832–4845.
14. **Sigaev V. N., Golubev N. V., Ignat'eva E. S., et al.,** Light-emitting Ga-oxide nanocrystals in glass: A new paradigm for low-cost and robust UV – to visible solar-blind converters and UV emitters, Nanoscale. 6 (3) (2014) 1763–1774.
15. **Nguyen K., Radovanovic P. V.,** Defects and impurities in colloidal Ga_2O_3 nanocrystals: New opportunities for photonics and lighting, Can. J. Chem. 100 (1) (2022) 2022 1–8.
16. **Yamaguchi K.,** First principles study on electronic structure of β-Ga_2O_3, Solid State Commun. 131 (12) (2004) 739–744.
17. **Rebentrost P., Stopa M., Aspuru-Guzik A.,** Fцrster coupling in nanoparticle excitonic circuits, Nano Lett. 10 (8) (2010) 2849–2856.
18. **Pantelides S. T., Sah C. T.,** Theory of localized states in semiconductors. I. New results using an old method, Phys. Rev. B. 10 (2) (1974) 621–637.
19. **Neal A. T., Mou S., Rafique S., et al.,** Donors and deep acceptors in β- Ga_2O_3, Appl. Phys. Lett. 113 (6) (2018) 062101.
20. **Oishi T., Harada K., Koga Y., Kasu M.,** Conduction mechanism in highly doped β-Ga_2O_3 $(\bar{2}01)$ single crystals grown by edge-defined film-fed growth method and their Schottky barrier diodes, Jap. J. Appl. Phys. 55 (3) (2016) 030305.
21. **Higashiwaki M., Sasaki K., Kamimura T., et al.,** Depletion-mode Ga_2O_3 metal-oxide-semiconductor field-effect transistors on β-Ga_2O_3 (010) substrates and temperature dependence of their device characteristics, Appl. Phys. Lett. 103 (12) (2013) 123511.
22. **Kohn W., Luttinger J. M.,** Theory of donor states in silicon, Phys. Rev. 98 (4) (1955) 915–922.

СПИСОК ЛИТЕРАТУРЫ

1. **Wang C., Zhang J., Xu S., Zhang C., Feng Q., Zhang Y., Ning J., Zhao S., Zhou H., Hao Y.** Progress in state-of-the-art technologies of Ga_2O_3 devices // Journal of Physics D: Applied Physics. 2021. Vol. 54. No. 24. P. 243001.
2. **Zhang J., Dong P., Dang K., et al.** Ultra-wide bandgap semiconductor Ga_2O_3 power diodes // Nature Communications. 2022. Vol. 13. July 6. P. 3900.
3. **Zhai H., Wu Z., Fang Z.** Recent progress of Ga_2O_3-based gas sensors // Ceramics International. 2022. Vol. 48. No. 17. Pp. 24213–24233.
4. **Pearton S. J., Yang J., Cary P. H., Ren F., Kim J., Tadjer M. J., Mastro M. A.** A review of Ga_2O_3 materials, processing, and devices // Applied Physics Reviews. 2018. Vol. 5. No. 1. P. 011301.
5. **Nikolskaya A., Okulich E., Korolev D., et al.** Ion implantation in β- Ga_2O_3: Physics and technology // Journal of Vacuum Science & Technology A. 2021. Vol. 39. No. 3. P. 030802.
6. **Higashiwaki M.** β-Ga_2O_3 material properties, growth technologies, and devices: A review // AAPPS (The Association of Asia Pacific Physical Societies) Bulletin. 2022. Vol. 32. No. 1. P. 3.
7. **Zhang J., Shi J., Qi D., Chen L., Zhang K. H. L.** Recent progress on the electronic structure, defect, and doping properties of Ga_2O_3 // APL Materials. 2020. Vol. 8. No. 2. P. 020906.
8. **Frodason Y. K., Krzyzaniak P. P., Vines L., Varley J. B., Van de Walle C. J., Johansen K. M. H.** Diffusion of Sn donors in β-Ga_2O_3 // APL Materials. 2023. Vol. 11. No. 4. P. 041121.
9. **Wang M., Mu S., Van de Walle C. G.** Incorporation of Si and Sn donors in β-Ga_2O_3 through surface reconstructions // Journal of Applied Physics. 2021. Vol. 130. No. 18. P. 185703.

10. **Jamwal N. S., Kiani A.** Gallium oxide nanostructures: A review of synthesis, properties and applications // Nanomaterials. 2022. Vol. 12. No. 12. P. 2061.

11. **Rajamani S., Arora K., Belov A., et al.** Enhanced solar-blind photodetection performance of encapsulated Ga_2O_3 nanocrystals in Al_2O_3 matrix // IEEE Sensors Journal. 2018. Vol. 18. No. 10. Pp. 4046–4052.

12. **Korolev D. S., Matyunina K. S., Nikolskaya A. A., et al.** Ion-beam synthesis of gallium oxide nanocrystals in a SiO_2/Si dielectric matrix // Nanomaterials. 2022. Vol. 12. No. 11. P. 1840.

13. **Zhou J., Chen H., Fu K., Zhao Y.** Gallium oxide-based optical nonlinear effects and photonics devices // Journal of Materials Research. 2021. Vol. 36. No. 23. Pp. 4832–4845.

14. **Sigaev V. N., Golubev N. V., Ignat'eva E. S., Paleari A., Lorenzi R.** Light-emitting Ga-oxide nanocrystals in glass: A new paradigm for low-cost and robust UV-to visible solar-blind converters and UV emitters // Nanoscale. 2014. Vol. 6. No. 3. Pp. 1763–1774.

15. **Nguyen K., Radovanovic P. V.** Defects and impurities in colloidal Ga_2O_3 nanocrystals: New opportunities for photonics and lighting // Canadian Journal of Chemistry. 2022. Vol. 100. No. 1. Pp. 1–8.

16. **Yamaguchi K.** First principles study on electronic structure of β-Ga_2O_3 // Solid State Communications. 2004. Vol. 131. No. 12. Pp. 739–744.

17. **Rebentrost P., Stopa M., Aspuru-Guzik A.** Fцrster coupling in nanoparticle excitonic circuits // Nano Letters. 2010. Vol. 10. No. 8. Pp. 2849– 2856.

18. **Pantelides S. T., Sah C. T.** Theory of localized states in semiconductors. I. New results using an old method // Physical Review B. 1974. Vol. 10. No. 2. Pp. 621–637.

19. **Neal A. T., Mou S., Rafique S., et al.** Donors and deep acceptors in β- Ga_2O_3 // Applied Physics Letters. 2018. Vol. 113. No. 6. P. 062101.

20. **Oishi T., Harada K., Koga Y., Kasu M.** Conduction mechanism in highly doped β-Ga_2O_3 ($\bar{2}01$) single crystals grown by edge-defined film-fed growth method and their Schottky barrier diodes // Japanese Journal of Applied Physics. 2016. Vol. 55. No. 3. P. 030305.

21. **Higashiwaki M., Sasaki K., Kamimura T., Wong M. H., Krishnamurthy D., Kuramata A., Masui T., Yamakoshi** S. Depletion-mode Ga_2O_3 metal-oxide-semiconductor field-effect transistors on β-Ga_2O_3 (010) substrates and temperature dependence of their device characteristics // Applied Physics Letters. 2013. Vol. 103. No. 12. P. 123511.

22. **Kohn W., Luttinger J. M.** Theory of donor states in silicon // Physical Review. 1955. Vol. 98. No. 4. Pp. 915–922.

THE AUTHORS

REVIN Alexandr A.
National Research Lobachevsky State University of Nizhni Novgorod
23 Gagarin Ave., Nizhni Novgorod, 603950, Russia
revinalexandre@yandex.ru
ORCID: 0000-0001-5701-1171

KONAKOV Anton A.
National Research Lobachevsky State University of Nizhni Novgorod
23 Gagarin Ave., Nizhni Novgorod, 603950, Russia
konakov_anton@mail.ru
ORCID: 0000-0001-8850-2651

KOROLEV Dmitry S.
National Research Lobachevsky State University of Nizhni Novgorod
23 Gagarin Ave., Nizhni Novgorod, 603950, Russia
dmkorolev@phys.unn.ru
ORCID: 0000-0003-1440-2994

СВЕДЕНИЯ ОБ АВТОРАХ

РЕВИН Александр Александрович – *младший научный сотрудник лаборатории физики и технологии тонких пленок Нижегородского государственного университета имени Н. И. Лобачевского.*
603950, Россия, г. Нижний Новгород, пр. Гагарина, 23
revinalexandre@yandex.ru
ORCID: 0000-0001-5701-1171

КОНАКОВ Антон Алексеевич – *кандидат физико-математических наук, доцент кафедры квантовых и нейроморфных технологий Нижегородского государственного университета имени Н. И. Лобачевского.*
603950, Россия, г. Нижний Новгород, пр. Гагарина, 23
konakov_anton@mail.ru
ORCID: 0000-0001-8850-2651

КОРОЛЕВ Дмитрий Сергеевич – *кандидат физико-математических наук, доцент кафедры физики полупроводников, электроники и наноэлектроники Нижегородского государственного университета имени Н. И. Лобачевского.*
603950, Россия, г. Нижний Новгород, пр. Гагарина, 23
dmkorolev@phys.unn.ru
ORCID: 0000-0003-1440-2994

Received 15.04.2024. Approved after reviewing 06.05.2024. Accepted 06.05.2024.
Статья поступила в редакцию 15.04.2024. Одобрена после рецензирования 06.05.2024. Принята 06.05.2024.

© Peter the Great St. Petersburg Polytechnic University, 2024

Original article
DOI: https://doi.org/10.18721/JPM.17302

ADMITTANCE SPECTROSCOPY OF BORON PHOSPHIDE HETEROSTRUCTURES GROWN BY PLASMA ENHANCED CHEMICAL VAPOR DEPOSITION ON SILICON SUBSTRATES

A. I. Baranov[1]✉, *G. E. Vtorygin*[1], *A. V. Uvarov*[1], *A. A. Maksimova*[2,1], *E. A. Vyacheslavova*[1,2], *A. S. Gudovskikh*[1,2]

[1] Alferov University, St. Petersburg, Russia;

[2] Saint Petersburg Electrotechnical University "LETI", St. Petersburg, Russia

✉ itiomchik@yandex.ru

Abstract. The study of BP layers and BP/*n*-Si heterojunctions formed by plasma enhanced chemical deposition on *n*-Si substrates has been carried out at a temperature of 350 °C using diborane and phosphine. The additional enhancement of hydrogen plasma power was established to make it possible to avoid pinning of the Fermi level at the BP/*n*-Si interface. Moreover, additional dilution with a hydrogen flow led to an increase in the BP layer conductivity, and the behavior of the current-voltage characteristic of the Au/BP/*n*-Si structure (golden electrode) became rectifying. Surface states of electrons at the BP/*n*-Si heterojunctions in all the samples and deep electronic levels with energy 0.58–0.65 eV in BP layers grown without the additional hydrogen flow were detected by admittance spectroscopy.

Keywords: boron phosphide, plasma enhanced chemical vapor deposition, admittance spectroscopy, interface states

Funding: The reported study was funded by Russian Science Foundation (Grant No. 21-79-10413, https://rscf.ru/project/21-79-10413/).

Citation: Baranov A. I., Vtorygin G. E., Uvarov A. V., Maksimova A. A., Vyacheslavova E. A., Gudovskikh A. S., Admittance spectroscopy of boron phosphide heterostructures grown by plasma enhanced chemical vapor deposition on silicon substrates, St. Petersburg State Polytechnical University Journal. Physics and Mathematics. 17 (3) (2024) 17–24. DOI: https://doi.org/10.18721/JPM.17302

This is an open access article under the CC BY-NC 4.0 license (https://creativecommons.org/licenses/by-nc/4.0/)

© Baranov A. I., Vtorygin G. E., Uvarov A. V., Maksimova A. A., Vyacheslavova E. A., Gudovskikh A. S., 2024. Published by Peter the Great St. Petersburg Polytechnic University.

Научная статья
УДК 621.383.51
DOI: https://doi.org/10.18721/JPM.17302

СПЕКТРОСКОПИЯ ПОЛНОЙ ПРОВОДИМОСТИ ГЕТЕРОСТРУКТУР ФОСФИДА БОРА НА КРЕМНИЕВЫХ ПОДЛОЖКАХ, ПОЛУЧЕННЫХ МЕТОДОМ ПЛАЗМОХИМИЧЕСКОГО ОСАЖДЕНИЯ

А. И. Баранов[1]✉, Г. Э. Вторыгин[1], А. В. Уваров[1], А. А. Максимова[2,1], Е. А. Вячеславова[1], А. С. Гудовских[1,2]

[1] Академический университет им. Ж. И. Алфёрова РАН, Санкт-Петербург, Россия;

[2] Санкт-Петербургский государственный электротехнический университет «ЛЭТИ» имени В. И. Ульянова (Ленина), Санкт-Петербург, Россия

✉ itiomchik@yandex.ru

Аннотация. Проведены исследования слоев фосфида бора BP и гетеропереходов BP/*n*-Si, сформированных методом плазмохимического осаждения при температуре 350 °C на подложках *n*-Si с использованием диборана и фосфина. Установлено, что увеличение мощности водородной плазмы позволяет избежать пиннинга уровня Ферми на границе BP/*n*-Si. Дополнительное разбавление потоком водорода приводило к увеличению проводимости слоя BP, а поведение вольтамперной характеристики структуры Au/BP/*n*-Si (золотой электрод) становилось выпрямляющим. Методом спектроскопии полной проводимости были обнаружены поверхностные состояния электронов на границах BP/*n*-Si во всех образцах и глубокие электронные уровни с энергией 0,65 – 0,58 эВ в слоях BP, выращенных без дополнительного потока водорода.

Ключевые слова: фосфид бора, плазмохимическое осаждение, спектроскопия полной проводимости, поверхностные состояния

Финансирование: Исследование выполнено за счет гранта Российского научного фонда № 10413-79-21, https://rscf.ru/project/21-79-10413/.

Ссылка для цитирования: Баранов А. И., Вторыгин Г. Э., Уваров А. В., Максимова А. А., Вячеславова Е. А., Гудовских А. С. Спектроскопия полной проводимости гетероструктур фосфида бора на кремнии, полученных методом плазмохимического осаждения // Научно-технические ведомости СПбГПУ. Физико-математические науки. 2024. Т. 17. № 3. С. 17–24. DOI: https://doi.org/10.18721/JPM.17302

Статья открытого доступа, распространяемая по лицензии CC BY-NC 4.0 (https://creativecommons.org/licenses/by-nc/4.0/)

Introduction

Extensive research is underway to find novel semiconductor materials to replace amorphous silicon serving as emitters in solar cells on single-crystal silicon substrates. It was theoretically confirmed in [1] that boron phosphide (BP) is one of the most promising binary compounds for *p*-type emitters on *n*-Si substrates, since it has an indirect band gap, and also a large difference between the energies of indirect (2 eV) and direct (4 eV) transitions, producing a large discontinuity in the conduction band at the *p*-BP/*n*-Si heterojunction, allowing to form hole-selective contacts. Very few papers were published on BP growth by plasma-enhanced chemical vapor deposition (PECVD) and epitaxy [2–4], only considering the structural properties of the layers.

Our previous work [5] studied the electrophysical properties of BP layers grown by PECVD in the temperature range of 250–350 °C; significant embedding of carbon atoms was found for them with trimethylboron used as a boron source. Fermi level pinning was observed at the BP/*n*-Si

© Баранов А. И., Вторыгин Г. Э., Уваров А. В., Максимова А. А., Вячеславова Е. А., Гудовских А. С., 2024. Издатель: Санкт-Петербургский политехнический университет Петра Великого.

interface for structures based on these layers. For this reason, diborane was used as a boron source in subsequent experiments [6], making it possible to increase the optical band gap of BP to 1.9 eV. No peaks corresponding to carbon were detected in the Raman spectra of the sample, pointing to its amorphization [7].

This paper analyzes the electrophysical properties of boron phosphide layers and BP/*n*-Si heterojunctions based on them, grown using diborane and phosphine.

Experimental

Growth of structures. Deposition of BP layers was carried out in an Oxford PlasmaLab 100 PECVD system (13.56 MHz) equipped with phosphine (PH_3) and diborane (B_2H_6) lines serving as sources of phosphorus and boron atoms, respectively. 100% PH_3 gas and 2% B_2H_6/H_2 mixture were used. BP layers were deposited on three-inch polished substrates of single-crystal silicon with a thickness of 380 μm.

These substrates were fabricated by the Czochralski method, doped with phosphorus and had an electrical resistivity of 5–10 Ω·cm. The silicon substrates were treated in a 10% aqueous solution of hydrofluoric acid (HF/H_2O) to remove the natural oxide immediately before they were loaded into the process chamber. Boron phosphide layers were deposited at a fixed temperature of 350 °C and identical pressure of 1000 mTorr at a ratio of gas mixture and gas flows $B_2H_6/H_2 : PH_3 = 2 : 1$ for 20 minutes with different plasma power (20 and 200 W) and additional dilution with hydrogen (100 cm^3/min) (see Table). The obtained thicknesses of the grown layers are also given in Table.

Table

Growth conditions and thicknesses of grown boron phosphide layers

Process	Dilution with H_2 gas	Plasma power, W	Thickness, nm
I	Not used	20	285
II		200	276
III	100 cm^3/min	200	360

Note. The layers were grown at a temperature of 350 °C, the pressure was 1000 mTorr.

An ohmic contact was formed on the back side of the silicon substrate by deposition of a thin (5 nm) highly doped layer of gallium phosphide (*n*-GaP) followed by thermal sputtering of silver (Ag) in the BOC Edwards Auto500 deposition system. Gold was thermally deposited on the front side of boron phosphide samples through a mask with holes 1 mm in diameter to form a Schottky barrier.

Measurements. The current–voltage characteristics of the samples were recorded at room temperature using a Keithley 2400 Source Measure Unit.

Admittance spectroscopy measurements were carried out with the Keysight E4980A-001 Precision RLC Meter at frequencies from 20 Hz to 2 MHz with a test signal amplitude of 50 mV in a Janis CCS-400H/204 closed-cycle helium cryostat in the temperature range from 40 to 400 K.

Results and discussion

The obtained dark current–voltage characteristics are shown in Fig. 1. Analyzing these dependencies, we can conclude that the layers grown without hydrogen dilution exhibit symmetrical curves for forward and reverse bias voltages, and the conductivity of the boron phosphide layer increases with increasing plasma power from 20 to 200 watts. Adding hydrogen flow at a rate of 100 cm^3/min to the gas mixture produces a straightening effect on the current–voltage characteristic: when a positive potential is applied, an exponential increase in current through the sample occurs, and when a negative potential is applied, a weak current occurs, suggesting the existence of a space charge region at the interface between the gold electrode and boron phosphide (Au/BP), due to the presence of a potential barrier.

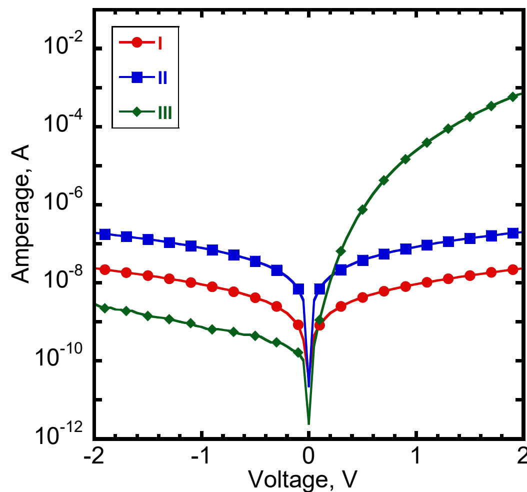

Fig. 1. Current–voltage characteristics of Au/BP/*n*-Si structure samples grown under different conditions (see Table)

It was previously found [8] that the obtained layers have a donor-type conductivity. This result made it possible to measure the capacitance–voltage characteristics at different temperatures. According to the data obtained, the capacitance of a sample grown in low-power plasma weakly depends on the applied voltage in the range from -20 to +20 V at various temperatures. This happens because the width of the space charge region in silicon does not change with varying voltage to Fermi level pinning; pinning appears due to the high defect concentration of defects at the heterointerface. A similar phenomenon was observed earlier for thin layers of BP grown with a trimethylboron precursor at different plasma parameters [5]. However, profiling of the Au/BP/*n*-Si structure could be carried out for the structure grown using diborane, due to an increase in plasma power to 200 W and dilution of gas flows with hydrogen. It was found that at low temperatures (below 100 K), the space charge region extends to the silicon substrate if reverse bias ($V \leq 0$ B) is applied. As the temperature increases, the magnitude of the reverse voltage at which silicon profiling begins increases, and much higher negative voltages (below -4 V) should be applied at room temperature than at a temperature of 100 K. This behavior of the dependence may be related to the presence of defects in boron phosphide layers and at the BP/*n*-Si interface. The data obtained confirm the validity of admittance spectroscopy measurements, allowing to detect defects of this type.

Fig. 2 shows the detected capacitance–frequency spectra for all samples at zero DC bias. The observed capacitance stages mean an additional contribution to the sample capacitance. This contribution may be due to the response from the point defect level or the exchange of carriers on the surface states formed at the BP/Si heterointerfaces.

A similar series of stages in the range of 100 – 180 K is observed in samples grown at 200 W, corresponding to a response with an activation energy of 0.19 and 0.17 eV for samples grown with hydrogen dilution (see Fig. 2,*c*), and without dilution (see Fig. 2,*b*), respectively. In addition, it was found that the capacitance stage shifts towards higher frequencies at the same temperature with an increase in the amplitude of the applied reverse bias (from -1 to -4 V). This leads to an increase in the calculated activation energy of this response at a displacement value of -4 V: up to 0.82 and 0.46 eV for samples grown with hydrogen dilution and without dilution, respectively (the data are not shown in Fig. 2).

The dependence of the activation energy on voltage indicates a response from surface states at the BP/Si heterointerface. According to the results of computer simulation performed in the AFORS-HET software, the response in this case is associated with the transition of electrons from surface states to the conduction band of silicon: when a reverse bias voltage is applied, the quasi-Fermi level shifts towards the mid-gap, which leads to an increase in the transition energy. The obtained result explains the previously observed temperature dependences of the voltage–capacitance characteristics [8]. At low temperatures, the isotype Au/BP/*n*-Si heterojunction is characterized by classical behavior, where the BP layer is completely depleted due to weak doping. At $V_{DC} = 0$ V, the space charge region extends to silicon, and at the reverse bias voltage, profiling of charge carrier concentration in the silicon substrate occurs. The calculated band diagram of the Au/BP/*n*-Si structure at 100 K is shown in Fig. 3,*a*. However, with an increase in temperature, the surface states induce an additional charge at the BP/*n*-Si heterointerface, leading to a change in the shape of band bending. This change, in turn, requires the application of a larger reverse bias amplitude to deplete the silicon region at the interface with boron phosphide at a certain test frequency (the band diagram at 300 K is shown in Fig. 3,*b*).

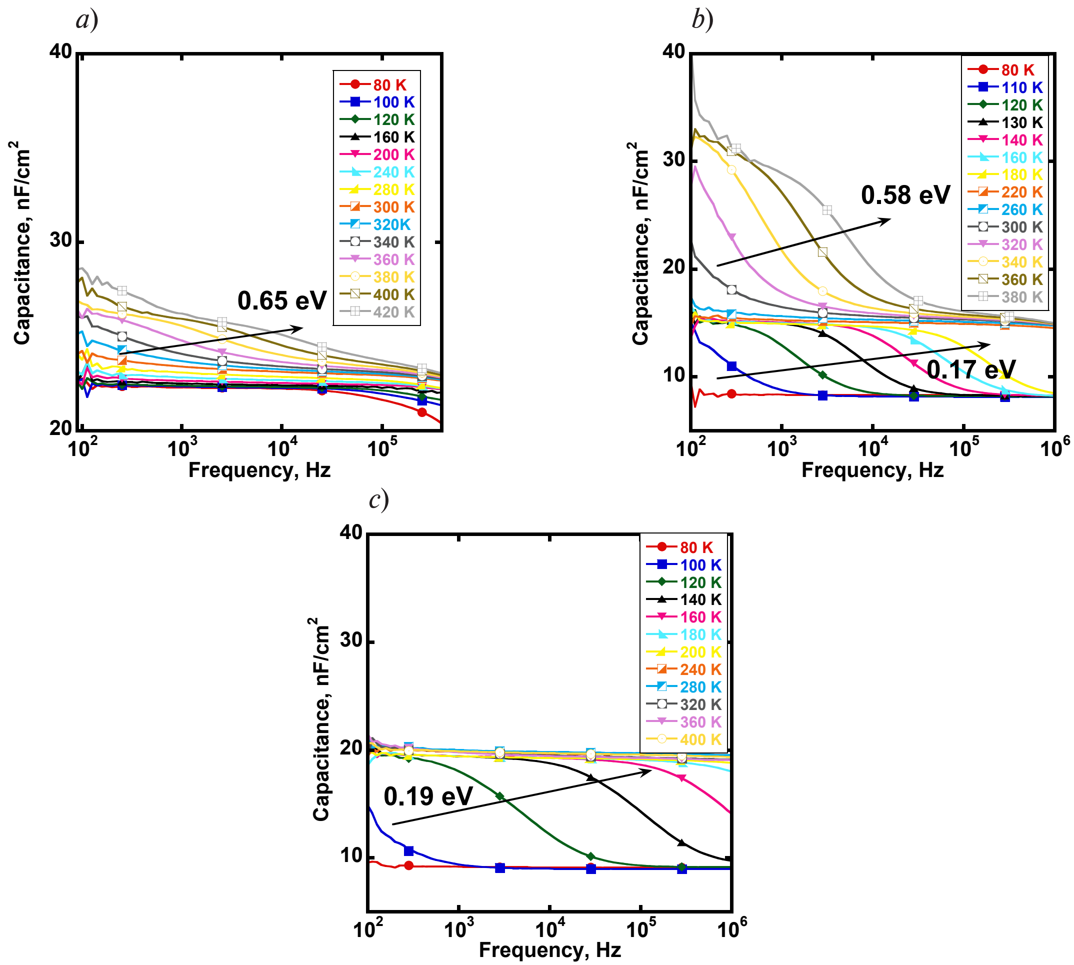

Fig. 2. Capacitance–frequency dependences of samples I (*a*), II (*b*), III (*c*) of Au/BP/*n*-Si structure (see Table) for different temperatures, with zero DC bias
Activation energies of the responses and the deep level energies are shown: E_a = 0.17–0.19 eV and E_a = 0.58 – 0.65 eV

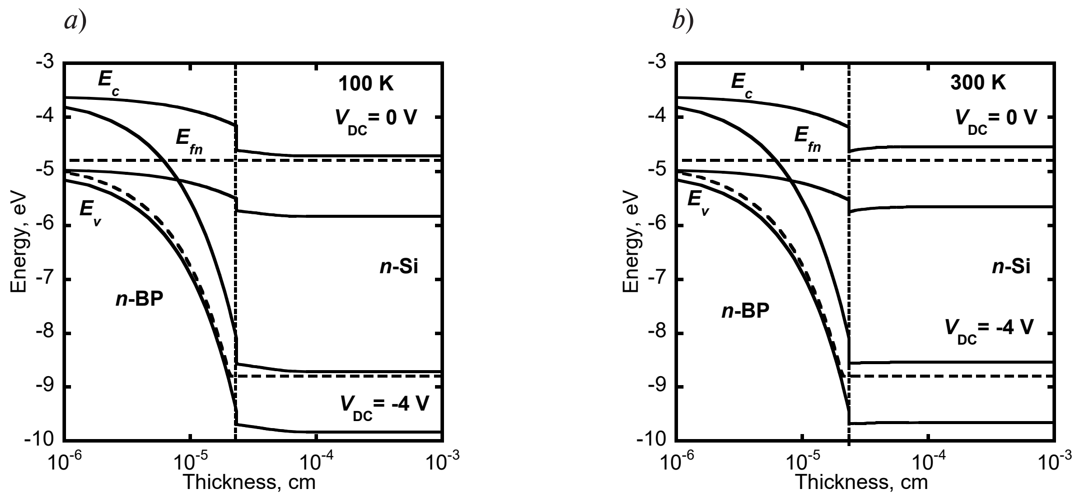

Fig. 3. Band diagrams of the Au/BP/*n*-Si heterointerface at 100 K (*a*) and 300 K (*b*) at different biases V_{DC} (in the presence of surface states at the BP/*n*-Si interface)
Energy positions of the bottom of the conduction band E_c, the quasi-Fermi level for electrons E_{fn} and the top of the valence band E_v are shown

A high-temperature defect with activation energies of 0.65 and 0.58 eV was detected in both samples grown without additional hydrogen flow for processes with plasma power of 20 and 200 W, respectively. In this case, the values do not depend on the DC bias voltage applied, unlike the responses described above; therefore, the detected defect is associated with a defect level in the boron phosphide layer. Since the study of defects in BP layers by capacitive techniques was carried out for the first time, their nature is presently unknown, however, it is reasonable to assume that it is a deep level associated with the structural properties of the layer, which we intend to explore in future experiments.

Conclusion

BP/*n*-Si heterojunctions obtained by plasma deposition of boron phosphide layers with diborane and phosphine flows were analyzed for the first time by capacitive techniques. Using diborane instead of trimethylboron as a boron source allowed to eliminate Fermi level pinning at the BP/*n*-Si heterointerface with an increase in plasma power from 20 to 200 W. Pinning was eliminated due to the absence of parasiting diffusion of carbon into the structure and improvement of the stoichiometric composition of BP, while introducing an additional hydrogen flow to dilute the gas mixture increased the conductivity of the *n*-BP layer. Nevertheless, surface states appear at the BP/*n*-Si interface (detected by admittance spectroscopy); their presence generates an additional charge at the interface at room temperature, therefore, much higher reverse voltages must be applied to spread the depleted region onto the silicon substrate. Furthermore, deep levels with energies E_a = 0.58 – 0.65 eV were found in boron phosphide layers grown without additional hydrogen flow.

Thus, the optimal approach is growing boron phosphide layers with a diborane flow at high plasma power (200 W), additionally diluting the hydrogen flow (at a flow rate of 100 cm^3/min), since this helps minimize defect production in boron phosphide layers and at the BP/*n*-Si interface.

REFERENCES

1. **Varley J. B., Miglio A., Ha V.-A., et al.,** High-throughput design of non-oxide *p*-type transparent conducting materials: Data mining, search strategy, and identification of boron phosphide, Chem. Mater. 29 (6) (2017) 2568–2573.
2. **Ogwu A. A., Hellwig T., Haddow D.,** Fracture and yield behaviour of wear and erosion resistant boron phosphide coatings for aerospace and automotive applications, Arch. Mater. Sci. Eng. 75 (1) (2015) 30–34.
3. **Nishimura S., Hanamoto H., Terashima K., Matsumoto S.,** Growth of GaN on Si(100) substrates using BP as a buffer layer – selective epitaxial growth, Mater. Sci. Eng. B. 93 (1–3) (2002) 135–138.
4. **Padavala B., Frye C. D., Wang X., et al.,** CVD growth and properties of boron phosphide on 3C-SiC, J. Cryst. Growth. 449 (1 Sept) (2016) 15–21.
5. **Maksimova A. A., Uvarov A. V., Baranov A. I., et al.,** Investigation of plasma deposited boron phosphide and its contact to silicon, ACS Appl. Energy Mater. 5 (5) (2022) 5367–5373.
6. **Maksimova A. A., Uvarov A. V., Pozdeev V. A., et al.,** Boron phosphide grown by PECVD and its optical properties, St. Petersburg Polytechnic University Journal. Physics and Mathematics. 16 (3.2) (2023) 273–277.
7. **Maksimova A. A., Uvarov A. V., Vyacheslavova E. A., et al.,** Development of technology for plasma-enhanced chemical vapor deposition of boron phosphide at low temperatures, Phys. Solid State. 16 (12) (2023) 2107–2109.
8. **Vtorygin G. E., Baranov A. I., Uvarov A. V., et al.,** Capacitance-voltage characterization of BP layers grown by PECVD mode, St. Petersburg Polytechnic University Journal. Physics and Mathematics. 16 (3.1) (2023) 473–478.

СПИСОК ЛИТЕРАТУРЫ

1. **Varley J. B., Miglio A., Ha V.-A., van Setten M. J., Rignanese G.-M., Hautier G.** High-throughput design of non-oxide *p*-type transparent conducting materials: Data mining, search strategy, and identification of boron phosphide // Chemistry of Materials. 2017. Vol. 29. No. 6. Pp. 2568–2573.
2. **Ogwu A. A., Hellwig T., Haddow D.** Fracture and yield behaviour of wear and erosion resistant boron phosphide coatings for aerospace and automotive applications // Archives of Materials Science and Engineering. 2015. Vol. 75. No. 1. Pp. 30–34.

3. **Nishimura S., Hanamoto H., Terashima K., Matsumoto S.** Growth of GaN on Si(100) substrates using BP as a buffer layer – selective epitaxial growth // Materials Science and Engineering B. 2002. Vol. 93. No. 1–3. Pp. 135–138.

4. **Padavala B., Frye C. D., Wang X., Raghothamachar B., Edgar J. H.** CVD growth and properties of boron phosphide on 3C-SiC // Journal of Crystal Growth. 2016. Vol. 449. 1 September. Pp. 15–21.

5. **Maksimova A. A., Uvarov A. V., Baranov A. I., et al.** Investigation of plasma deposited boron phosphide and its contact to silicon // ACS Applied Energy Materials. 2022. Vol. 5. No. 5. Pp. 5367–5373.

6. **Maksimova A. A., Uvarov A. V., Pozdeev V. A., Kirilenko D. A., Baranov A. I., Vyacheslavova E. A., Gudovskikh A. S.** Boron phosphide grown by PECVD and its optical properties // St. Petersburg Polytechnic University Journal. Physics and Mathematics. 2023. Vol. 16. No. 3.2. Pp. 273–277.

7. **Максимова А. А., Уваров А. В., Вячеславова Е. А., Баранов А. И., Гудовских А. С.** Разработка технологии плазмохимического осаждения фосфида бора при низкой температуре // Физика твердого тела. 2023. Т. 16. № 12. С. 2198–2200.

8. **Vtorygin G. E., Baranov A. I., Uvarov A. V., Maksimova A. A., Vyacheslavova E. A.** Capacitance-voltage characterization of BP layers grown by PECVD mode // St. Petersburg Polytechnic University Journal. Physics and Mathematics. 2023. Vol. 16. No. 3.1. Pp. 473–478.

THE AUTHORS

BARANOV Artem I.
Alferov University
8/3 Khlopin St., St. Petersburg, 194021, Russia
itiomchik@yandex.ru
ORCID: 0000-0002-4894-6503

VTORYGIN Georgii E.
Alferov University
8/3 Khlopin St., St. Petersburg, 194021, Russia
piespogany@gmail.com
ORCID: 0009-0008-5149-0157

UVAROV Alexander V.
Alferov University
8/3 Khlopin St., St. Petersburg, 194021, Russia
lumenlight@mail.ru
ORCID: 0000-0002-0061-6687

MAKSIMOVA Alina A.
St. Petersburg Electrotechnical University "LETI",
Alferov University;
5 Professor Popov St., St. Petersburg, 197376, Russia
deer.blackgreen@yandex.ru
ORCID: 0000-0002-3503-7458

VYACHESLAVOVA Ekaterina A.
Alferov University
8/3 Khlopin St., St. Petersburg, 194021, Russia
cate.viacheslavova@yandex.ru
ORCID: 0000-0001-6869-1213

GUDOVSKIKH Alexander S.
Alferov University,
St. Petersburg Electrotechnical University "LETI"
8/3 Khlopin St., St. Petersburg, 194021, Russia
gudovskikh@spbau.ru
ORCID: 0000-0002-7632-3194

СВЕДЕНИЯ ОБ АВТОРАХ

БАРАНОВ Артем Игоревич – *PhD, младший научный сотрудник лаборатории возобновляемых источников энергии Академического университета им. Ж. И. Алфёрова, РАН.*
194021, Россия, Санкт-Петербург, ул. Хлопина, 8, к. 3
itiomchik@yandex.ru
ORCID: 0000-0002-4894-6503

ВТОРЫГИН Георгий Эдуардович – *студент Академического университета им. Ж. И. Алфёрова РАН.*
194021, Россия, Санкт-Петербург, ул. Хлопина, 8, к. 3
piespogany@gmail.com
ORCID: 0009-0008-5149-0157

УВАРОВ Александр Вячеславович – *младший научный сотрудник лаборатории возобновляемых источников энергии Академического университета им. Ж. И. Алфёрова РАН.*
194021, Россия, Санкт-Петербург, ул. Хлопина, 8, к. 3
lumenlight@mail.ru
ORCID: 0000-0002-0061-6687

МАКСИМОВА Алина Андреевна – *аспирантка, ассистент кафедры фотоники Санкт-Петербургского государственного электротехнического университета «ЛЭТИ» имени В. И. Ульянова (Ленина); младший научный сотрудник лаборатории возобновляемых источников энергии Академического университета им. Ж. И. Алфёрова РАН.*
197376, Россия, г. Санкт Петербург, ул. Профессора Попова, 5
deer.blackgreen@yandex.ru
ORCID: 0000-0002-3503-7458

ВЯЧЕСЛАВОВА Екатерина Александровна – *аспирантка, младший научный сотрудник лаборатории возобновляемых источников энергии Академического университета им. Ж. И. Алфёрова, РАН.*
194021, Россия, Санкт-Петербург, ул. Хлопина, 8, к. 3
cate.viacheslavova@yandex.ru
ORCID: 0000-0001-6869-1213

ГУДОВСКИХ Александр Сергеевич – *доктор технических наук, ведущий научный сотрудник лаборатории возобновляемых источников энергии Академического университета им. Ж. И. Алфёрова, профессор кафедры фотоники Санкт-Петербургского государственного электротехнического университета «ЛЭТИ» имени В. И. Ульянова (Ленина), РАН.*
194021, Россия, г. Санкт-Петербург, ул. Хлопина, 8, к. 3
gudovskikh@spbau.ru
ORCID: 0000-0002-7632-3194

Received 03.05.2024. Approved after reviewing 21.05.2024. Accepted 21.05.2024.
Статья поступила в редакцию 03.05.2024. Одобрена после рецензирования 21.05.2024. Принята 21.05.2024.

© Peter the Great St. Petersburg Polytechnic University, 2024

Original article
DOI: https://doi.org/10.18721/JPM.17303

CREATION OF OPTICAL ISOLATED GaP(NAs) MICROCAVITIES ON SILICON

L. N. Dvoretckaia[1]✉, *A. M. Mozharov*[1], *S. D. Komarov*[3], *E. A. Vyacheslavova*[1], *E. I. Moiseev*[3], *V. V. Fedorov*[2,1], *I. S. Mukhin*[2]

[1] Alferov University, St. Petersburg, Russia;

[2] Peter the Great St. Petersburg Polytechnic University, St. Petersburg, Russia;

[3] National Research University Higher School of Economics, St. Petersburg branch, St. Petersburg, Russia;

✉Liliyabutler@gmail.com

Abstract. This article presents the technology for the formation of optical microcavities based on the GaP(NAs) semiconductor material system on silicon. For the first time, a plasma etching mode which ensures the achievement of an aspect ratio of 5:1 and low roughness of the side walls has been proposed in etching layers of III–V groups. A technological approach was also put forward to ensure optical separation of the microcavity with the Si substrate, that being important for efficient localization of light in the photonic structure. The optical studies and numerical calculation showed the presence of modulations in the micro-photoluminescence spectra of microstructures caused by the appearance of Fabry – Perot resonances. This research is an important step in the development of the technology of creation and application of combined structures with silicon-based optical waveguides.

Keywords: optical GaP(NAs) microcavity on Si, plasma etching, micro-photoluminescence spectrum

Funding: The author of this article, L. N. Dvoretckaia, is grateful for financial support from the Russian Science Foundation (Grant No. 23-72-01133) in fabrication of microstructures; the author I. S. Mukhin is grateful for financial support from the St. Petersburg Science Foundation (Grant No. 23-РБ-02-08) in performing simulation; the author E. I. Moiseev is grateful for financial support from Higher School of Economics (St. Petersburg branch, The Higher School of Economics Fundamental Research Program) in performing optical measurements.

Citation: Dvoretckaia L. N., Mozharov A. M., Komarov S. D., Vyacheslavova E. A., Moiseev E. I., Fedorov V. V., Mukhin I. S., Creation of optical isolated GaP(NAs) microcavities on silicon, St. Petersburg State Polytechnical University Journal. Physics and Mathematics. 17 (3) (2024) 25–35. DOI: https://doi.org/10.18721/JPM.17303

This is an open access article under the CC BY-NC 4.0 license (https://creativecommons.org/licenses/by-nc/4.0/)

© Dvoretckaia L. N., Mozharov A. M., Komarov S. D., Vyacheslavova E. A., Moiseev E. I., Fedorov V. V., Mukhin I. S., 2024. Published by Peter the Great St. Petersburg Polytechnic University.

Научная статья
УДК 535.015
DOI: https://doi.org/10.18721/JPM.17303

СОЗДАНИЕ ОПТИЧЕСКИХ ИЗОЛИРОВАННЫХ МИКРОРЕЗОНАТОРОВ GaP(NAs) НА КРЕМНИИ

Л. Н. Дворецкая[1]✉, *А. М. Можаров*[1], *С. Д. Комаров*[3], *Е. А. Вячеславова*[1], *Э. И. Моисеев*[3], *В. В. Федоров*[2,1], *И. С. Мухин*[2]

[1] Академический университет им. Ж. И. Алфёрова РАН, Санкт-Петербург, Россия;

[2] Санкт-Петербургский политехнический университет Петра Великого, Санкт-Петербург, Россия;

[3] НИУ «Высшая школа экономики» (Санкт-Петербургский филиал), Санкт-Петербург, Россия;

✉ Liliyabutler@gmail.com

Аннотация. В статье представлена технология формирования оптических микрорезонаторов, основанных на системе полупроводниковых материалов GaP(NAs) на кремниевой подложке. Впервые разработан режим плазмохимического травления, при котором достигается аспектное соотношение 5:1 при травлении слоев, состоящих из элементов III – V групп, и низкая шероховатость боковых стенок. Предложен технологический подход, обеспечивающий оптическое разделение микрорезонатора с кремниевой подложкой, что важно для эффективной локализации света в фотонной структуре. Проведенные оптические исследования и численный расчет показали наличие модуляций в спектрах микрофотолюминесценции микроструктур; модуляции обусловлены возникновением резонансов Фабри – Перо. Выполненное исследование является важным шагом в развитии технологии создания и применения комбинированных структур с оптическими волноводами на кремниевой основе.

Ключевые слова: оптический микрорезонатор GaP(NAs) на кремнии, плазмохимическое травление, спектр микрофотолюминесценции

Финансирование. Автор статьи Л. Н. Дворецкая благодарна за финансовую поддержку Российского научного фонда (грант № 01133-72-23) при фабрикации микроструктур; автор И. С. Мухин благодарен за финансовую поддержку Санкт-Петербургского научного фонда (грант № -23РБ08-02-) при выполнении моделирования; автор Э. И. Моисеев благодарен за финансовую поддержку НИУ «Высшая школа экономики» (Санкт-Петербургский филиал, Программа фундаментальных исследований вуза) при выполнении оптических измерений.

Ссылка для цитирования: Дворецкая Л. Н., Можаров А. М., Комаров С. Д., Вячеславова Е. А., Моисеев Э. И., Федоров В. В., Мухин И. С. Создание оптических изолированных микрорезонаторов GaP(NAs) на кремнии // Научно-технические ведомости СПбГПУ. Физико-математические науки. 2024. Т. 17. № 3. С. 25–35. DOI: https://doi.org/10.18721/JPM.17303

Статья открытого доступа, распространяемая по лицензии CC BY-NC 4.0 (https://creativecommons.org/licenses/by-nc/4.0/).

Introduction

Consistent progress in computing systems is slowed down by the limited bandwidth of traditional information transmission systems via metal conductors. For this reason, systems providing an alternative means for data transmission, for example, as optical signal, are of particular interest in microelectronics. The integration of photonics and microelectronics has been discussed for the past 30 years; technologies have been successfully combined to develop complementary MOSFETs (CMOS) and high-speed light sources, increasing the speed of on-chip processing and transmission of data as well as improving the durability and compactness of the devices [1].

© Дворецкая Л. Н., Можаров А. М., Комаров С. Д., Вячеславова Е. А., Моисеев Э. И., Федоров В. В., Мухин И. С., 2024. Издатель: Санкт-Петербургский политехнический университет Петра Великого.

Group IV compounds (silicon and germanium) are used in light-emitting structures and photodiodes on Si, mainly due to their compatibility with the CMOS platform [2]. On the other hand, light emission from such materials is limited, so effective light-emitting devices are yet to be constructed [3, 4]. In turn, most group III–V elements have a direct-bandgap semiconductor structure, allowing to fabricate thin-film LEDs, effective microscopic solar cells, laser structures, etc.

The disadvantage of devices based on group III–V elements is the high cost of the substrate material based on gallium arsenide (GaAs) and indium phosphide (InP), while large amounts of it are lost during the manufacturing process. Furthermore, the diameters of GaAs and InP substrates produced do not exceed 150 and 100 mm, respectively; in contrast, the standard diameter of silicon or silicon-on-insulator substrates is 450 mm.

In turn, to reduce the cost of fabricated transistors, photonic or optoelectronic circuits, it is necessary to increase the diameter of the substrates used, which is still technologically impossible for wafers made of materials based on group III–V elements.

One of the approaches to fabricating silicon-based optoelectronic devices is directly growing group III–V semiconductor structures on silicon substrates. This low-cost technology generally provides a reliable way to integrate silicon-based optoelectronic circuits [5]. This, however, brings a new challenge, as dislocations appear in the epitaxial layer, induced by the mismatch between the crystal lattices of the grown structure and the silicon substrate, which can cause the entire structure to malfunction.

Technologies circumventing this limitation are based on different types of buffer layers [6, 7] or texturing silicon substrates [8–11] for effective relaxation of elastic stresses, allowing for synthesis of high-quality epitaxial layers. For example, the dislocation density in the GaAs layer was decreased to the level of $2.4 \cdot 10^7$ cm^{-2} in [12] by using a combination of sequential synthesis of buffer layers and thermal annealing. An efficient LED structure operating in the red spectral region was created by this technique. A GaN microdisk cavity grown on silicon was considered in [13], exhibiting ultraviolet lasing under pulsed excitation of a semiconductor structure.

An important particular case of directly growing layers of III–V group structures on silicon is the GaP/GaP(NAs) system, allowing to completely solve the problem of lattice mismatch between the synthesized layers and silicon. Even though GaP is an indirect-bandgap semiconductor, adding only 0.5 mol.% nitrogen makes this material direct-bandgap [14], while the 2% composition is lattice-matched with the silicon crystal lattice and has a bandgap of about 2 eV.

Simultaneously adding nitrogen and arsenic atoms makes it possible to modulate the decrease in the bandgap of the semiconductor material up to about 1.5 eV, while maintaining lattice match with silicon.

To date, researchers have managed to significantly improve the quality of epitaxially grown GaP(NAs) on Si substrate, allowing to create LEDs and photosensors based on it [15, 16], even achieving laser generation in structures with quantum wells [17, 18]. One of the significant advantages of the GaP/GaP(NAs) system is the possibility of using an indirect-bandgap GaP semiconductor to manufacture waveguides or cavity structures based on it [19].

A common problem in fabricating photonic circuits on silicon is low localization of light in the cavity and absorption of the optical mode by the substrate. A possible solution to this problem is the formation of voids between the cavity and the GaP/GaP(NAs) photonic structures, which can be created, for example, by removing the substrate under the sections of the photonic circuit (by etching).

This paper presents the results on the manufacturing technology for microdisk cavities based on the GaP(NAs) system grown on Si substrate, along with analysis of the optical properties of the obtained structures.

Experimental

The GaP/GaP(NAs) heterostructure under study with layer thicknesses of 500/900/200 nm was synthesized on a silicon substrate using the molecular beam epitaxy method in the Veeco GEN III system.

Solid solution composition
in active region of heterostucture, %
P..82.0
As 14.5
N .... 2.6 ± 3.0

The selected composition corresponds to a bandgap of 1.83 eV. A detailed description of the process of synthesis and characterization of epitaxial layers is presented in [20].

Fabrication of optical structures. The fabrication process consisted of several stages.

At the first stage, a micropattern was produced by contact optical lithography from an AZ1518 photoresist using the SUSS MJB4 mask aligner. The diameter of the microstructures varied in the range of 6–40 μm.

At the second stage, plasma cryogenic etching of the layers of the synthesized heterostructure was carried out using the Plasmalab 100 ICP etching system (Oxford Instruments), allowing to independently control the concentration of reactive ions by generating inductively coupled plasma and their directional transport. To achieve optimal etching conditions, the process parameters were varied. The etching parameters are given in Table.

The modification of GaP/GaP(NAs)/GaP heterostructures was monitored at all stages of the fabrication process using a scanning electron microscope (SEM) from Zeiss Supra.

Table

Etching modes of GaP/GaP(NAs)/GaP heterostructure

Technological parameter	Parameter value for structure			
	I	II	III	IV
Temperature, °C	–20		–70	–20
ICP power, W	1000			
RF power, W	30	100		
Pressure, mTorr	5			
BCl_3/Cl_2 flow ratio	40 : 5			
Process time, min	6			

Optical characterization of formed structures. The study was carried out using the micro-photoluminescence (μ-PL) method. The measuring circuit included a lens used both to focus the pumping laser radiation and to collect visual and spectral data. The μ-PL spectra in different regions of the sample were imaged using a lens mounted on an XYZ stage with at least 300 nm travel. The sample was fixed on a copper heat sink and placed in a cryostat to maintain a constant temperature. A 457 nm continuous-wave solid-state laser from CNI Optics was used to perform optical pumping of the semiconductor structure.

All μ-PL measurements were carried out at room temperature (300 K).

Results and discussion

Fig. 1 shows SEM images for the microdisk structures after etching. Analyzing the SEM images, we concluded that the operating conditions allow for etching of the layers of the heterostructure with a high level of selectivity to the silicon substrate. Notably, etching with the selected basic parameters (see Table, Structure I) exhibits significant erosion of the sidewalls of the semiconductor material and photoresist (see Fig. 1,*a*), which may be due to the insufficient directionality of the etching process. An increase in the RF power (Structure II) led to a decrease in erosion of the sidewalls of the resist and an improvement in the quality of the sidewalls of the structure, preserving their verticality (see Fig. 1,*b*). A significant roughness of the sidewall surface of the semiconductor structure was still observed after etching, as well as a decrease in the residual thickness of the photoresist compared to Structure I, which indicated insufficient stability of the

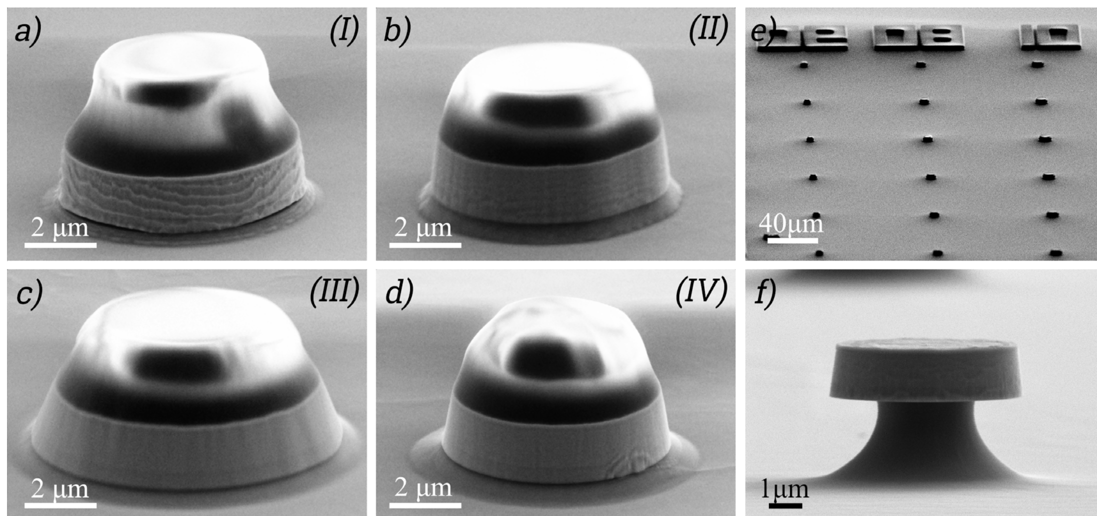

Fig. 1. SEM images of microdisk structures I–IV (*a*, *b*, *c*, *d*, respectively) after photoresist etching on upper surface; after etching of silicon substrate (*e*, *f*)
Panoramic view (*e*) and formed microdisk 6 μm in diameter (*f*) are shown

photoresist. To optimize the etching modes, the structure was additionally cooled to -70 °C while maintaining the remaining parameters (Structure III). As seen from Fig. 1,*c*, this step provided a decrease in both vertical and lateral erosion of the photoresist, as well as an improvement in the quality of the sidewalls of the structure. In turn, a deterioration in the verticality of the sidewalls was observed for the selected etching mode, which is one of the drawbacks in the manufacturing of disk cavities.

Another approach to increasing the strength of the photoresist is baking, in which chemical bonds in the photoresist are cross-linked and polymerized. To ensure crosslinking, the photoresist was heat-treated at 150 °C for 2 minutes, after which the etching of the structure was performed with the same conditions as that of Structure II. A SEM image of the structure after etching is shown in Fig. 1,*d*. Comparing the result obtained with that for Structure II, we observe an increase in the quality of the sidewall surface of the semiconductor structure, with high verticality of the walls maintained. Importantly, a decrease in the lateral dimensions of the structure is observed, which is associated with a change in the shape of the photoresist mask after the annealing procedure.

Since size correction can be performed at the lithography stage, and high quality of the structure's sidewall surface can be achieved, Sample IV was used for further manipulations.

For optical isolation of microcavity structures from silicon, plasma etching of the silicon substrate was carried out at the next technological stage from the front side in a SF_6/O_2 gas mixture with flows of 36 and 4 cm^3/min, respectively, with an ICP power of 2500 W and an RF power of 150 W. The selected mode ensured full selectivity of silicon etching, did not affect the formed microstructure layers based on group III–V elements. Figs. 1, *e*, *f* show the SEM images of microstructures in sample IV after etching of the silicon substrate. The etching depth of silicon was 2.5 μm with lateral etching under the structure at a distance of 1.5 μm, which is sufficient to maintain optical modes at the periphery of microcavities.

Fig. 2 shows the μ-PL measurement results at 300 K with continuous-wave pumping using a high-aperture 100x lens focusing the laser beam into a spot with a diameter of about 0.5 μm. Fig. 2,*a* shows an optical image of the microdisk structure with a diameter of 40 μm and integral PL intensity spectra obtained by raster scanning. Evidently, the μ-PL signal is present over the entire disk; it is amplified by 1.4–1.5 times at the periphery of the disk, compared with the central part, which indicates a more efficient optical pumping of the semiconductor structure. A μ-PL peak is detected in the emission spectrum (see Fig. 2,*b*), with a maximum at a wavelength of 670–680 nm. Unlike traditional direct-bandgap materials based on group III–V elements, the detected μ-PL signal is characterized by a wide asymmetric emission band stretched into the long-wavelength region of the spectrum. This spectrum is typical for semiconductor solid

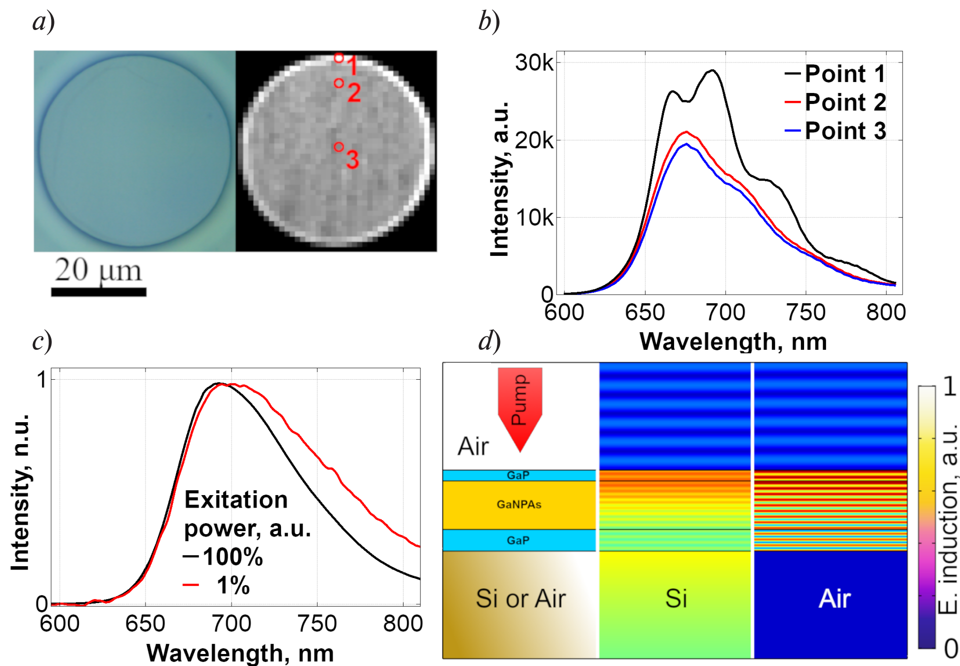

Fig. 2. Optical studies of GaP(NAs) structure:
optical (left) and integral spectral (right) images of the microdisk (a); μ-PL spectra at three points of the disk (*b*, see Fig. 2,*a*); μ-PL spectra at two pumping values (*c*); calculated distribution of the electric field amplitude in layers of the structure with and without Si substrate (*d*)

solutions of dilute nitrides. The shape of the obtained spectrum suggests inhomogeneous composition of the semiconductor material, associated with the peculiarities of nitrogen embedding during epitaxial synthesis, in particular, the formation of dimerized nitrogen as well as nitrogen emitting levels in the bandgap. Therefore, a significant part of the μ-PL signal is due to emission through nitrogen impurity centers, with transition energy below the effective bandgap. This effect is most evident if dynamic μ-PL measurements are carried out with a significant decrease in the overall pumping level (see Fig. 2,*c*). The dependence of the μ-PL signal intensity on the wavelength observed through imaging shows an increase in the overall signal intensity at the periphery of the disk, as well as the appearance of pronounced signal modulation due to standing optical waves (Fabry–Perot modes) along the growth axis of the structure, in the region of silicon etching under the microdisks. Notably, the resonances associated with whispering gallery modes were not observed in the experiment.

As mentioned above, an increase in the integral μ-PL intensity near the edge of the microdisk may be due to both an increase in the absorption of laser radiation and an improvement in the output of the μ-PL signal. To separate the contributions from these phenomena, a numerical calculation of the propagation of electromagnetic radiation incident on the microdisk was carried out (the Comsol Multiphysics program was used). Experimental data on the spectral dependences of the refractive and absorption coefficients of gallium phosphide and silicon substrate were used in the calculations [21]. Similar parameters for the GaP(NAs) compound were taken for a solid solution with a similar composition synthesized on a gallium phosphide substrate [16]. The calculations performed showed that all radiation that was not reflected from the boundary of the upper GaP layer during optical pumping of the semiconductor structure was absorbed in the GaP(NAs) layer, i.e., the presence of silicon under the microdisk practically does not affect the pumping level of the semiconductor structure.

The μ-PL process is characterized by emission with the quantum energy near the band edge of a semiconductor material. Because of this circumstance, the GaP(NAs) absorption coefficient at μ-PL wavelengths is significantly reduced. By analogy with the data in [16], we found that the absorption coefficient α takes values of no more than 1.5 μm^{-1}, inducing resonant optical effects in the geometry under consideration.

The numerical calculation confirmed the occurrence of Fabry—Perot resonances associated with the appearance of standing waves along the growth axis of the structure in the absence of silicon under the layers of the resonant structure (see Fig. 2,*d*). The amplitude of the signal at the resonant wavelengths increased by 1.6 times (the maximum value), which is in good agreement with experimental data.

In turn, the average light propagation distance α^{-1} in the semiconductor structure remains significantly less than the perimeter of the microdisk cavities under consideration, which makes it impossible for resonant peaks associated with whispering gallery modes to appear without reducing the absorption coefficient.

It is known that a decrease in the absorption coefficient in a semiconductor structure can be achieved by injecting charge carriers and increasing the optical bandgap of the material [22].

Conclusion

The paper considered the formation of microdisk cavities based on a system of GaP/GaP(NAs)/GaP semiconductor materials synthesized on a silicon substrate using optical lithography and dry etching methods.

The etching mode was selected to ensure a low level of sidewall roughness while maintaining the verticality of this wall. The combination of etching modes for the GaP/GaP(NAs) and Si systems, which are highly selective to the given group of materials, made it possible to create microdisk cavities with a suspended region near the periphery of the structures.

Micro-photoluminescence spectroscopy revealed the formation of optical Fabry—Perot modes along the growth axis of the semiconductor structure at the periphery of the microcavities.

The technology proposed in the paper can be used to manufacture not only cavities, but also other optical structures, such as waveguides, filters, lasers, etc.

REFERENCES

1. **Cornet C., Léger Y., Robert C.,** Integrated lasers on silicon, ISTE Press —Elsevier, Amsterdam, 2016.

2. **Zinovyev V. A., Smagina Zh. V., Zinovyeva A. F., et al.,** Emission enhancement of Ge/Si quantum dots in hybrid structures with subwavelength lattice of Al nanodisks, Nanomater. 13 (17) (2023) 2422.

3. **Iyer S. S., Xie Y.-H.,** Light emission from silicon, Science. 260 (5104) (1993) 40—46.

4. **Pavesi L., Gaponenko S., Negro L.** (Eds.), Towards the first silicon laser (NATO Sci. Ser. II: Mathematics, Physics and Chemistry, Vol. 93), Springer Science + Business Media, Dordrecht, 2003.

5. **Lee A., Liu H., Seeds A.,** Semiconductor III—V lasers monolithically grown on Si substrates, Semicond. Sci. Technol. 28 (1) (2012) 015027.

6. **Bolkhovityanov Y. B., Pchelyakov O. P.,** GaAs epitaxy on Si substrates: modern status of research and engineering, Phys.-Usp. 51 (5) (2008) 437—456.

7. **Mansor M., Norhaniza R., Shuhaimi A., et al.,** Enhancement of gallium nitride on silicon (111) using pulse atomic-layer epitaxy (PALE) AlN with composition-graded AlGaN buffer, Sci. Rep. 13 (31 May) (2023) 8793.

8. **Ballabio A., Bietti S., Scaccabarozzi A., et al.,** GaAs epilayers grown on patterned (001) silicon substrates via suspended Ge layers, Sci. Rep. 9 (26 Nov) (2019) 17529.

9. **Park J.-S., Tang M., Chen S., Liu H.,** Heteroepitaxial growth of III—V semiconductors on silicon, Crystals. 10 (12) (2020) 1163.

10. **Dvoretckaia L., Gridchin V., Mozharov A., et al.,** Light-emitting diodes based on InGaN/GaN nanowires on microsphere-lithography-patterned Si substrates, Nanomater. 12 (12) (2022) 1993.

11. **Dvoretckaia L. N., Mozharov A. M., Berdnikov Y., Mukhin I. S.,** Optimization of microsphere optical lithography for nano-patterning, J. Phys. D: Appl. Phys. 55 (9) (2022) 09LT01.

12. **Tsai Y. L., Yang H.-H., Fang J.-H., et al.,** GaAs-based optoelectronics grown on GaAs/Si virtual substrates with multiple spaced thermal-cycle annealing, Thin Solid Films. 733 (1 Sept) (2021) 138817.

13. **Zhu G., Li J., Zhang N., et al.,** Whispering-gallery mode lasing in a floating GaN microdisk with a vertical slit, Sci. Rep. 10 (14 Jan) (2020) 253.

14. **Henini M., Razeghi M.** Optoelectronic devices: III nitrides. Elsevier, Amsterdam, 2004.

15. **Dvoretckaia L. N., Bolshakov A. D., Mozharov A. M., et al.,** GaNP-based photovoltaic device integrated on Si substrate, Sol. Energy Mater. 206 (March) (2020) 110282.

16. **Geisz J. F., Friedman D. J., Kurtz S.,** GaNPAs solar cells lattice-matched to GaP, Proc. 29-th IEEE Photovoltaic Specialists Conf., 2002. New Orleans, USA. IEEE (2002) 864–867.

17. **Hossain N., Sweeney S. J., Rogowsky S., et al.,** Reduced threshold current dilute nitride Ga(NAsP)/GaP quantum well lasers grown by MOVPE, Electron. Lett. 47 (16) (2011) 931–933.

18. **Liebich S., Zimprich M., Beyer A., et al.,** Laser operation of Ga (NAsP) lattice-matched to (001) silicon substrate, Appl. Phys. Lett. 99 (7) (2011) 071109.

19. **Mitchell M., Hryciw A. C., Barclay P. E.,** Cavity optomechanics in gallium phosphide microdisks, Appl. Phys. Lett. 104 (14) (2014) 141104.

20. **Fedorov V. V., Dvoretckaia L. N., Mozharov A. M., et al.,** Dual-functional light-emitting and photo-detecting GaAsPN heterostructures on silicon, Mater. Sci. Semicond. Proc. 168 (Dec) (2023) 107867.

21. **Aspnes D. E., Studna A. A.,** Dielectric functions and optical parameters of Si, Ge, GaP, GaAs, GaSb, InP, InAs, and InSb from 1.5 to 6.0 eV, Phys. Rev. B. 27 (2) (1983) 985.

22. **Anselm A.,** Introduction to semiconductor theory, English translation, Mir Publishers, Moscow, 1981.

СПИСОК ЛИТЕРАТУРЫ

1. **Cornet C., Léger Y., Robert C.** Integrated lasers on silicon. Amsterdam: ISTE Press –Elsevier, 2016. 166 p.

2. **Zinovyev V. A., Smagina Zh. V., Zinovyeva A. F., Bloshkin A. A., Dvurechenskii A. V., Rodyakina E. E., Stepikhova M. V., Peretokin A. V., Novikov A. V.** Emission enhancement of Ge/Si quantum dots in hybrid structures with subwavelength lattice of Al nanodisks // Nanomaterials. 2023. Vol. 13. No. 17. P. 2422.

3. **Iyer S. S., Xie Y.-H.** Light emission from silicon // Science. 1993. Vol. 260. No. 5104. Pp. 40–46.

4. **Pavesi L., Gaponenko S., Negro L.** (Eds.). Towards the first silicon laser (NATO Science Series II: Mathematics, Physics and Chemistry, Vol. 93). Dordrecht, the Netherlands: Springer Science + Business Media, 2003. 482 p.

5. **Lee A., Liu H., Seeds A.** Semiconductor III–V lasers monolithically grown on Si substrates // Semiconductor Science and Technology. 2012. Vol. 28. No. 1. P. 015027.

6. **Болховитянов Ю. Б., Пчелков О. П.,** Эпитаксия GaAs на кремниевых подложках: современное состояние исследований и разработок // Успехи физических наук. 2008. Т. 178. № 5. С. 459–480.

7. **Mansor M., Norhaniza R., Shuhaimi A., Hisyam M. I., Omar Al-Z., Williams A., Hussin M. R. M.** Enhancement of gallium nitride on silicon (111) using pulse atomic-layer epitaxy (PALE) AlN with composition-graded AlGaN buffer // Scientific Reports. 2023. Vol. 13. 31 May. P. 8793.

8. **Ballabio A., Bietti S., Scaccabarozzi A., et al.** GaAs epilayers grown on patterned (001) silicon substrates via suspended Ge layers // Scientific Reports. 2019. Vol. 9. 26 November. P. 17529.

9. **Park J.-S., Tang M., Chen S., Liu H.** Heteroepitaxial growth of III–V semiconductors on silicon // Crystals. 2020. Vol. 10. No. 12. Pp. 1163.

10. **Dvoretckaia L., Gridchin V., Mozharov A., Maksimova A., Dragunova A., Melnichenko I., Mitin D., Vinogradov A., Mukhin I., Cirlin G.** Light-emitting diodes based on InGaN/GaN nanowires on microsphere-lithography-patterned Si substrates // Nanomaterials. 2022. Vol. 12. No. 12. P. 1993.

11. **Dvoretckaia L. N., Mozharov A. M., Berdnikov Y., Mukhin I. S.** Optimization of microsphere optical lithography for nano-patterning // Journal of Physics D: Applied Physics. 2022. Vol. 55. No. 9. P. 09LT01.

12. **Tsai Y. L., Yang H.-H., Fang J.-H., Chang C.-L., Chen M.-H., Wu C.-H., Hong H.-F.** GaAs-based optoelectronics grown on GaAs/Si virtual substrates with multiple spaced thermal-cycle annealing // Thin Solid Films. 2021. Vol. 733. 1 September. P. 138817.

13. **Zhu G., Li J., Zhang N., Li X., Dai J., Cui Q., Song Q., Xu Ch., Wang Y.** Whispering-gallery mode lasing in a floating GaN microdisk with a vertical slit // Scientific Reports. 2020. Vol. 10. 14 January. P. 253.

14. **Henini M., Razeghi M.** Optoelectronic devices: III nitrides. Amsterdam: Elsevier, 2004. 575 p.

15. **Dvoretckaia L. N., Bolshakov A. D., Mozharov A. M., et al.** GaNP-based photovoltaic device integrated on Si substrate // Solar Energy Materials and Solar Cells. 2020. Vol. 206. March. P. 110282.

16. **Geisz J. F., Friedman D. J., Kurtz S.** GaNPAs solar cells lattice-matched to GaP // Proceedings of the 29-th IEEE Photovoltaic Specialists Conference, 2002. New Orleans, USA. IEEE, 2002. Pp. 864–867.

17. **Hossain N., Sweeney S. J., Rogowsky S., Ostendorf R., Wagner J., Liebich S., Zimprich M., Volz K., Kunert B., Stolz W.** Reduced threshold current dilute nitride Ga(NAsP)/GaP quantum well lasers grown by MOVPE // Electronics Letters. 2011. Vol. 47. No. 16. Pp. 931–933.

18. **Liebich S., Zimprich M., Beyer A., et al.** Laser operation of Ga (NAsP) lattice-matched to (001) silicon substrate // Applied Physics Letters. 2011. Vol. 99. No. 7. P. 071109.

19. **Mitchell M., Hryciw A. C., Barclay P. E.** Cavity optomechanics in gallium phosphide micro-disks // Applied Physics Letters. 2014. Vol. 104. No. 14. P. 141104.

20. **Fedorov V. V., Dvoretckaia L. N., Mozharov A. M., Fedina S. V., Kirilenko D. A., Berezovskaya T. N., Faleev N. N., Yunin P. A., Drozdov M. N., Mukhin I. S.** Dual-functional light-emitting and photo-detecting GaAsPN heterostructures on silicon // Materials Science in Semiconductor Processing. 2023. Vol. 168. December. P. 107867.

21. **Aspnes D. E., Studna A. A.** Dielectric functions and optical parameters of Si, Ge, GaP, GaAs, GaSb, InP, InAs, and InSb from 1.5 to 6.0 eV // Physical Review B. 1983. Vol. 27. No. 2. P. 985.

22. **Ансельм А. И.** Введение в теорию полупроводников. М.: Наука. Гл. редакция физ.-мат. лит-ры, 1978. 619 с.

THE AUTHORS

DVORETCKAIA Liliia N.
Alferov University
8-3 Khlopin St., St. Petersburg, 194021, Russia
Liliyabutler@gmail.com
ORCID: 0000-0002-4172-940X

MOZHAROV Alexey M.
Alferov University
8-3 Khlopin St., St. Petersburg, 194021, Russia
mozharov@spbau.ru
ORCID: 0000-0002-8661-4083

KOMAROV Sergey D.
National Research University "Higher School of Economics" (St. Petersburg branch)
16 Soyuz Pechatnikov St., St. Petersburg, 190121, Russia
serega.komarow@mail.ru
ORCID: 0000-0002-7025-3527

VYACHESLAVOVA Ekaterina A.
Alferov University;
8-3 Khlopin St., St. Petersburg, 194021, Russia
cate.viacheslavova@yandex.ru
ORCID: 0000-0001-6869-1213

MOISEEV Eduard I.
National Research University "Higher School of Economics" (St. Petersburg branch)
16 Soyuz Pechatnikov St., St. Petersburg, 190121, Russia
emoiseev@hse.ru
ORCID: 0000-0003-3686-935X

FEDOROV Vladimir V.
Peter the Great St. Petersburg Polytechnic University;
Alferov University
29 Politechnicheskaya St., St. Petersburg, 195251, Russia
fedorov_vv@spbstu.ru
ORCID: 0000-0001-5547-9387

MUKHIN Ivan S.
Peter the Great St. Petersburg Polytechnic University
29 Politechnicheskaya St., St. Petersburg, 195251, Russia
muhin_is@spbstu.ru
ORCID: 0000-0001-9792-045X

СВЕДЕНИЯ ОБ АВТОРАХ

ДВОРЕЦКАЯ Лилия Николаевна – *кандидат физико-математических наук, научный сотрудник лаборатории возобновляемых источников энергии Академического университета им. Ж. И. Алфёрова РАН.*
194021, Россия, г. Санкт-Петербург, ул. Хлопина, 8, к. 3
Liliyabutler@gmail.com
ORCID: 0000-0002-4172-940X

МОЖАРОВ Алексей Михайлович – *кандидат физико-математических наук, старший научный сотрудник лаборатории возобновляемых источников энергии Академического университета им. Ж. И. Алфёрова РАН.*
194021, Россия, г. Санкт-Петербург, ул. Хлопина, 8, к. 3
mozharov@spbau.ru
ORCID: 0000-0002-8661-4083

КОМАРОВ Сергей Дмитриевич – *аспирант Санкт-Петербургской школы физико-математических и компьютерных наук, а также стажер-исследователь международной лаборатории квантовой оптоэлектроники Национального исследовательского университета «Высшая школа экономики» (Санкт-Петербургский филиал).*
190008, Россия, г. Санкт-Петербург, ул. Союза Печатников, 16
serega.komarow@mail.ru
ORCID: 0000-0002-7025-3527

ВЯЧЕСЛАВОВА Екатерина Александровна – *аспирантка лаборатории возобновляемых источников энергии Академического университета им. Ж. И. Алфёрова РАН.*
194021, Россия, г. Санкт-Петербург, ул. Хлопина, 8, к. 3
cate.viacheslavova@yandex.ru
ORCID: 0000-0001-6869-1213

МОИСЕЕВ Эдуард Ильмирович – *научный сотрудник международной лаборатории квантовой оптоэлектроники и старший преподаватель Санкт-Петербургской школы физико-математических и компьютерных наук Национального исследовательского университета «Высшая школа экономики» (Санкт-Петербургский филиал).*
190008, Россия, г. Санкт-Петербург, ул. Союза Печатников, 16
emoiseev@hse.ru
ORCID: 0000-0003-3686-935X

ФЕДОРОВ Владимир Викторович – *кандидат физико-математических наук, старший научный сотрудник Высшей инженерно-физической школы Санкт-Петербургского политехнического университета Петра Великого, старший научный сотрудник лаборатории возобновляемых источников энергии Академического университета им. Ж. И. Алфёрова РАН.*
195251, Россия, г. Санкт-Петербург, Политехническая ул., 29
fedorov_vv@spbstu.ru
ORCID: 0000-0001-5547-9387

МУХИН Иван Сергеевич – *доктор физико-математических наук, профессор, директор Высшей инженерно-физической школы Санкт-Петербургского политехнического университета Петра Великого.*
195251, Россия, г. Санкт-Петербург, Политехническая ул., 29
muhin_is@spbstu.ru
ORCID: 0000-0001-9792-045X

Received 23.04.2024. Approved after reviewing 21.05.2024. Accepted 21.05.2024.
Статья поступила в редакцию 23.04.2024. Одобрена после рецензирования 21.05.2024. Принята 21.05.2024.

© Peter the Great St. Petersburg Polytechnic University, 2024

Original article
UDC 538.9, 539.23
DOI: https://doi.org/10.18721/JPM.17304

RELAXATION OF ELECTRIC CHARGE IN POLYMER BLENDS BASED ON LOW-DENSITY POLYETHYLENE AND COPOLYMER OF ETHYLENE WITH VINYL ACETATE

R. A. Castro [1], E. A. Karulina [1] ✉, M. F. Galikhanov [2,3], T. V. Reztsov [1], E. E. Fomicheva [4]

[1] Herzen State Pedagogical University of Russia, St. Petersburg, Russia;

[2] Institute of Applied Research, Tatarstan Academy of Sciences, Republic of Tatarstan, Kazan, Russia;

[3] Kazan National Research Technological University, Republic of Tatarstan, Kazan, Russia;

[4] Military Space Academy named after A. F. Mozhaysky, St. Petersburg, Russia

✉ karulina@mail.ru

Abstract. This paper presents the results of a study of polymer films based on a blend of low-density (high-pressure) polyethylene (LDPE, HPP) with a copolymer of ethylene and vinyl acetate (EVA, sevilen). The use of thermal activation, infrared and dielectric spectroscopy methods made it possible to describe the electric charge relaxation processes in the polymer blends investigated. The data obtained suggested the presence of an α-relaxation process in the samples in the temperature range 250–280 K. An increased value of the activation energy of this process was also found in the LDPE/EVA samples compared to that in the LDPE one. This effect has been interpreted as the appearance of deeper traps of charge carriers in the blends. The dependences obtained by dielectric spectroscopy indicated the presence of hopping conductivity in the subjects of research.

Keywords: polyethylene, copolymer of ethylene with vinyl acetate, thermostimulated depolarization, thermo-activation spectroscopy

Funding: This study was supported by the Ministry of Education of the Russian Federation as a part of the Government Assignment (Project No. VRFY-2023-0005).

For citation: Castro R. A., Karulina E. A., Galikhanov M. F., Reztsov T. V., Fomicheva E. E., Relaxation of electric charge in polymer blends based on low-density polyethylene and copolymer of ethylene with vinyl acetate, St. Petersburg State Polytechnical University Journal. Physics and Mathematics. 17 (3) (2024) 36–45. DOI: https://doi.org/10.18721/JPM.17304

This is an open access article under the CC BY-NC 4.0 license (https://creativecommons.org/licenses/by-nc/4.0/)

Научная статья
УДК 538.9, 539.23
DOI: https://doi.org/10.18721/JPM.17304

РЕЛАКСАЦИЯ ЭЛЕКТРИЧЕСКОГО ЗАРЯДА В ПОЛИМЕРНЫХ СМЕСЯХ НА ОСНОВЕ ПОЛИЭТИЛЕНА ВЫСОКОГО ДАВЛЕНИЯ И СОПОЛИМЕРА ЭТИЛЕНА С ВИНИЛАЦЕТАТОМ

Р. А. К стро [1], Е. А. К рулин [1] ✉, М. Ф. Г лих нов [2,3], Т. В. Резцов [1], Е. Е. Фомичев [4]

[1] Российский государственный педагогический университет им. А. И. Герцена, Санкт-Петербург, Россия;

© Castro R. A., Karulina E. A., Galikhanov M. F., Reztsov T. V., Fomicheva E. E., 2024. Published by Peter the Great St. Petersburg Polytechnic University.

[2] Институт прикладных исследований Академии наук Республики Татарстан,
Республика Татарстан, г. Казань, Россия;
[3] Казанский национальный исследовательский технологический университет,
Республика Татарстан, г. Казань, Россия;
[4] Военно-космическая академия имени А. Ф. Можайского, Санкт-Петербург, Россия
✉ karulina@mail.ru

Аннотация. В статье представлены результаты исследования полимерных пленок на основе смеси полиэтилена высокого давления (низкой плотности) (ПЭВД) с сополимером этилена и винилацетата (СЭВА, сэвилен). Использование методов термоактивационной, инфракрасной и диэлектрической спектроскопии позволило описать процессы релаксации электрического заряда в исследуемых полимерных смесях. Исходя из полученных данных, было сделано предположение о существовании в образцах процесса альфа-релаксации в области 250 – 280 К. Обнаружено повышенное значение энергии активации, соответствующей релаксационному процессу, в образцах ПЭВД/СЭВА, по сравнению с образцом ПЭВД. Этот эффект трактуется как появление в смесях более глубоких ловушек носителей заряда. Зависимости, полученные методом диэлектрической спектроскопии, свидетельствуют о наличии в объектах исследования прыжкового механизма проводимости.

Ключевые слова: полиэтилен, сополимер этилена с винилацетатом, термостимулированная деполяризация, термоактивационная спектроскопия, дипольно-сегментальная релаксация

Финансирование: Работа выполнена в рамках государственного задания при финансовой поддержке Министерства просвещения Российской Федерации (проект № VRFY-2023-0005).

Для цитирования: Кастро Р. А., Карулина Е. А., Галиханов М. Ф., Резцов Т. В., Фомичева Е. Е. Релаксация электрического заряда в полимерных смесях на основе полиэтилена высокого давления и сополимера этилена с винилацетатом // Научно-технические ведомости СПбГПУ. Физико-математические науки. 2024. Т. 17. № 3. С. 36–45. DOI: https://doi.org/10.18721/ JPM.17304

Статья открытого доступа, распространяемая по лицензии CC BY-NC 4.0 (https://creativecommons.org/licenses/by-nc/4.0/)

Introduction

The electret effect is observed in dielectrics and consists in the ability of a material to maintain a polarized state for a long time in the absence of an external electric field [1]. Today, electrets are successfully used in various fields of science and technology. The most popular fields of application are electronics (microphones, electromechanical transducers, sensors), high-tech industry (electret filters), medicine (applicators, implants), etc. [1 – 3].

Low-density polyethylene (LDPE) is used to produce electrets because it has good dielectric properties and is inexpensive to produce. However, the disadvantage of polyethylene is the relatively short relaxation time of the electret state [1]. One of the most successful ways to improve the electret properties of polymers is the creation of composite materials by introducing chemical additives, foaming, mixing with solid dispersed fillers or with other polymers [4 – 7]. The method of combining one or several layers of polymer films is also promising [9]. These techniques make it possible to improve a set of properties of polymers, including electrical, mechanical and deformation characteristics.

Currently, the attention of researchers is attracted to a material called EVA, which is a copolymer of ethylene and vinyl acetate (EVA, SEVA, sevilen). The properties of EVA are determined by the vinyl acetate content. It is known that elasticity and adhesive properties of material are improved if it contains vinyl acetate. Improving elasticity has practical implications for electret material when it is used for active packaging, electret patches, and also as a component for stretchable bioelectronics [10, 11].

© Кастро Р. А., Карулина Е. А., Галиханов М. Ф., Резцов Т. В., Фомичева Е. Е., 2024. Издатель: Санкт-Петербургский политехнический университет Петра Великого.

Earlier studies of the electret properties of EVA and its compositions with polyethylene [8, 9] did not provide a clear answer to the question of how the vinyl acetate content affects the dielectric properties and stability of the electret state. Nevertheless, it can be assumed that the EVA content has a positive effect on the electret properties of the composites.

In this connection, the purpose of our work was to identify the features of polarization processes in mixtures of LDPE and EVA using dielectric and thermal activation spectroscopy.

Research methods and materials

Blends of LDPE with EVA copolymer, differing in the ratio of components, were selected as samples for research. The film samples had a thickness of about 300 μm.

The blending of polymers was carried out on laboratory microrollers at a temperature of 130 ± 5 °C for 3 min. The films were prepared by pressing method at a temperature of 170 ± 5 °C for 5 min. Samples of blends of LDPE and EVA were provided by the Kazan National Research Technological University (Republic of Tatarstan, Russia).

The electrical properties were studied using thermal activation, infrared and dielectric spectroscopy methods.

Temperature dependences of thermostimulated depolarization (TSD) currents were recorded in the heating mode at a constant speed on a TSC-II installation (Setaram). Attenuated total internal reflection (ATR) spectra of the samples under study were recorded using an FSM 1202 Fourier spectrometer (an infrared range). Dielectric spectroscopy measurements were carried out using a Concept 41 installation (Novocontrol Technologies GmbH&Co).

Experimental results and discussion

The study of the frequency dependence of the imaginary part of the complex permittivity ε'' (the loss factor) revealed the existence of a dispersion maximum of this value in a wide temperature range (253 – 283 K). The shift of the ε'' maximum to the region of higher frequencies with increasing temperature was detected (Fig. 1). This shift of the maximum is typical of dipole-segmental losses (α-relaxation). It is observed in the mentioned graphs for nonpolar polymers and is bound up with orientational rotations of the polar units of the macromolecule [12]. Polyethylene contains a small number of polar groups (carbonyl and hydroxyl ones >C=O, –O–H, etc.). It also contains methyl groups $-CH_3$ and >C=C< bonds, which have small dipole moments. A rise in the maximum on the frequency dependence curves obtained for a mixture of polymers was also observed with increasing temperature (Fig. 1, *b*). The maximum value of ε'' for the mixture is several times higher than that for the original polymer.

The relaxation process was also observed in the TSD spectra over the temperature range 273 – 283 K (Fig. 2). The course of the process does not depend on the percentage of blend components, and the maximum height escalates with increasing proportion of EVA. This behavior of the TSD peak can be explained by an increase in the number of relaxers in the polymer. It is also known from Ref. [13] that the height of the maximum related to α-relaxation on the frequency dependence of the loss factor ε'' is determined by the number of dipoles and their moments.

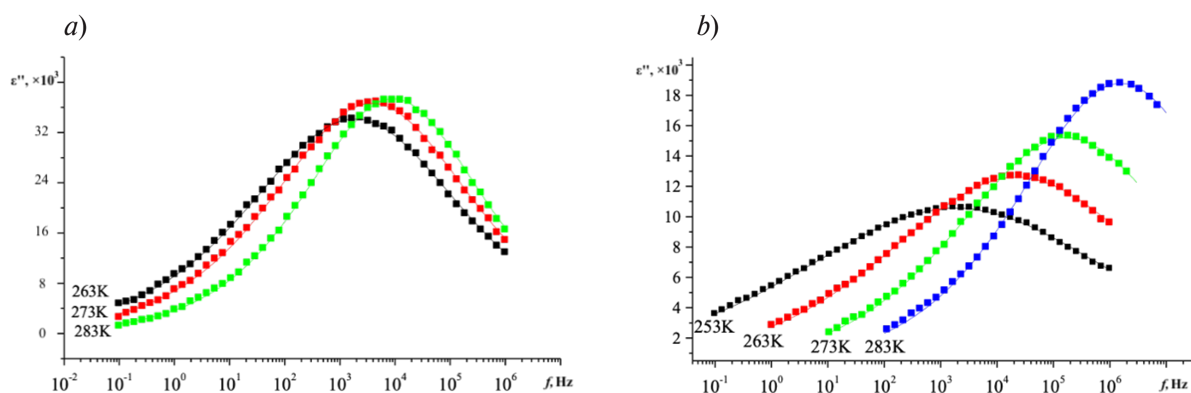

Fig. 1. Frequency dependences of the loss factor for LDPE (*a*) and LDPE+EVA (*b*) samples at different temperatures

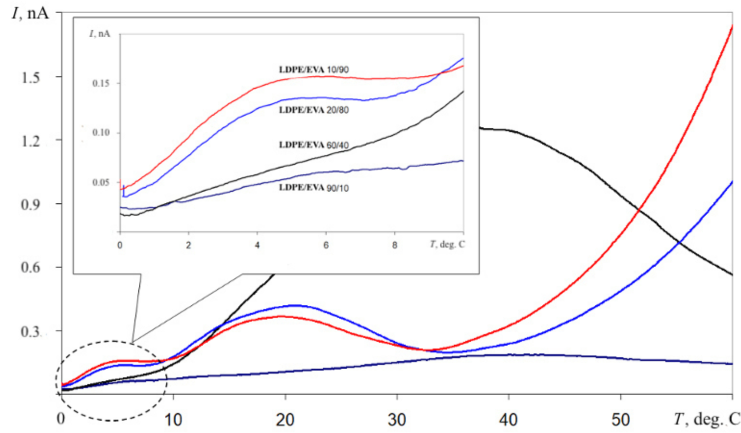

Fig. 2. Temperature dependences of TSD currents for various ratios of LDPE and EVA

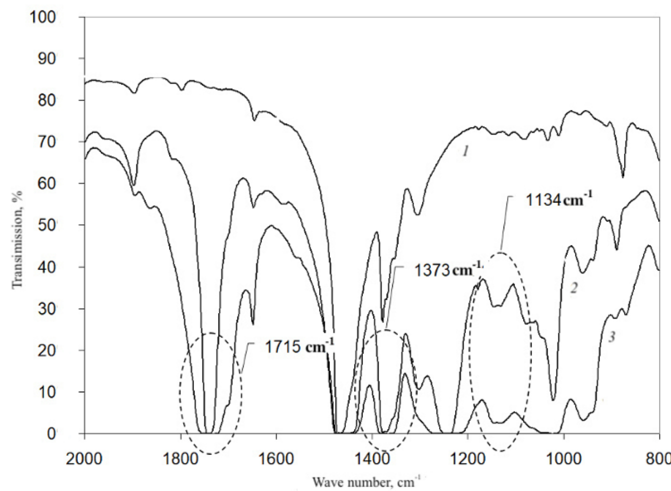

Fig. 3. Infrared transmission spectra for the samples of LDPE (*1*), LDPE/EVA 90/10 mixtures (*2*), and EVA (*3*)

Mixing the LDPE and EVA polymer materials led to the appearance of side polar groups –O–(C=O)–CH_3 in the polymer chain. There are a lot of transmission bands in the IR spectra for EVA samples and LDPE/EVA mixtures (Fig. 3). For example, one can observe stretching vibrations of the >C=O groups of polyvinyl acetate (1715 cm^{-1}), bending vibrations of the –CH_3 bonds of the acetyl group (1373 cm^{-1}), stretching vibrations of the ~C–O–C~ ether groups in the composition of polyvinyl acetate (1134 cm^{-1}). Thus, the number of dipoles that contributed to dipole-segmental relaxation increased with increasing the proportion of EVA in the blend.

Complex dispersion dependences of dielectric parameters and features of the disordered structure of a polymer system suggest that the detected relaxation processes should be bound up with the existence of not only one relaxation time, but with a whole set of them.

The Havriliak – Negami (HN) model was used to study the features of the spectrum of relaxers. The Havriliak – Negami function is an empirical modification of the Debye relaxation model. Nevertheless, unlike the Debye model, the HN model explains the asymmetry and width of the dielectric dispersion curve. It also establishes a relation between the dispersion of permittivity in the polymer systems and relaxation parameters [14 –16]:

$$\varepsilon^*(\omega) = \varepsilon_\infty + \frac{\Delta\varepsilon}{\left[1+(i\omega\tau)^{\alpha_{HN}}\right]^{\beta_{HN}}}, \quad (1)$$

where ε_∞ is the high-frequency limit of the real part of the dielectric constant; $\Delta\varepsilon$ is the dielectric increment (the difference between the low-frequency limit and high-frequency one); $\omega = 2\pi f$; α_{HN}, β_{HN} are the shape parameters describing, respectively, the asymmetric and symmetric expansions of the relaxation time distribution function (RTDF); in this case $\alpha = 1.00$ is the Cole – Davidson distribution, and $\beta = 1.00$ is the Cole – Cole one.

The HN parameters for the studied relaxation processes were determined according to Eq. (1) using Winfit 3.3 software (Novocontrol Technologies GmbH). The obtained values of relaxation parameters are presented in Table. Taking into account the approximation error, we can conclude that a non-Debye oscillatory process (with a set of relaxation time values) obeying the Cole – Cole model over the studied ranges of frequency and temperature is observed in LDPE samples and LDPE/EVA blends.

Table

Temperature dependences of relaxation parameters for the polymer systems under study

Polymer system	Average temperature, K	α_{max}, μs	β_{HN}
LDPE	263	0.8561	0.33200
	273	0.4185	0.35310
	283	0.1748	0.39110
	293	0.8419	0.35620
LDPE/EVA	253	0.8522	0.22790
	263	0.7116	0.27470
	273	0.9217	0.32050
	283	0.1016	0.34650

Footnote. Parameter β_{HN} = 0.10000 at all specified temperatures for the both systems.

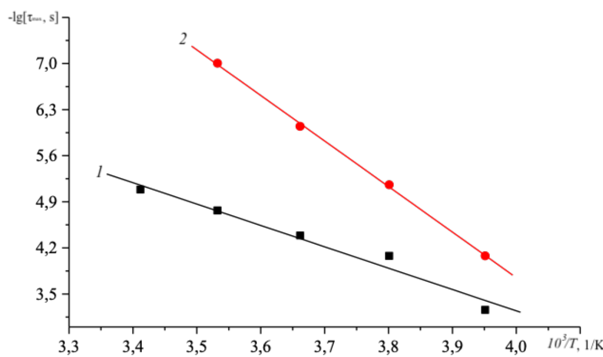

Fig. 4. Temperature dependences of the most probable relaxation time τ_{max} for the samples of LDPE (*1*) and LDPE/EVA (*2*); the found values of activation energies E_a are 0.69 eV (*1*) and 1.37 eV (*2*)

The activation energy E_a was determined from the temperature dependence of the most probable relaxation time τ_{max} (Fig. 4) for the samples of the both systems. It turned out to be equal to 0.69 eV and 1.37 eV for the LDPE and LDPE/EVA samples, respectively. An approximately twofold increase in the E_a value for the blend samples may be bound up with the appearance of deeper traps in the energy spectrum. The appearance of these traps may be caused by two reasons. The first one is the rotation of the polar groups of the EVA molecules. The second one is the charge accumulation at the polymer boundary in the blends of LDPE and EVA.

The frequency dependence of the specific conductivity σ' for LDPE sample and the blend of two polymers is characterized by a growth in σ' with an increasing field frequency (Fig. 5). This corresponds to the power-law dependence in the form $\sigma'(\omega) \sim \omega^s$. In this case, the s value increases with increasing temperature (Fig. 6).

When s value becomes greater than 1, the movement of charge carriers is considered localized [17, 18]. These results can be explained within the theory of nonstationary hopping electrical conductivity in disordered systems [19].

In the system in question, there is a hopping mechanism of charge transfer at the indicated values of frequency and temperature. The signs of such a mechanism are the power law of conductivity dispersion and the characteristic change in exponent with temperature [20]. This mechanism involves charge carriers jumping through a disordered structure and overcoming energy barriers. It should be noted that the fundamental parameter in this process is the energy required to complete the jump. It is also necessary to take into account the distributions of the energy barriers magnitudes.

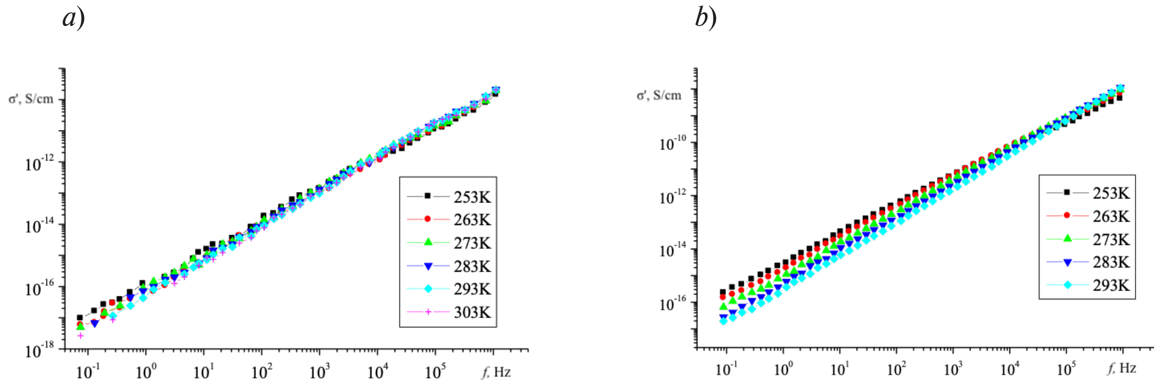

Fig. 5. Frequency dependences of specific conductivity for the samples of LDPE (*a*) and LDPE/EVA (*b*) at different temperatures

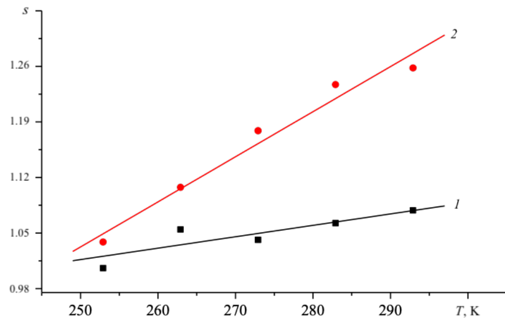

Fig. 6. Temperature dependences of the exponent for the samples of LDPE (*1*) and LDPE/EVA (*2*)

In the samples under study, such charge carriers can be negatively and positively charged hydrogen vacancies in the polymer chains [21, 22]. Such vacancies are created during the interaction between water molecules and its ions (H_3O^+, OH^-) with hydrogen atoms, which are contained in the structural groups of $–CH_2–$, >CH–, $–CH_3$ chains. The EVA chains contain side polar groups $–O–(–C=O)–CH_3$ and polyethylene molecules contain >CH– groups.

Notice that the specific conductivity of LDPE/EVA blends is more than that of pure polyethylene. This can be explained by the fact that EVA has greater electrical conductivity than LDPE.

To explain the resulting linear frequency dependence of conductivity it is convenient to use the model proposed by the authors of Ref. [20]. According to this model, the frequency versus temperature characteristic of the AC conductivity σ_{ac} (ω, T) forms as a result of tunneling the center-to-center bipolaron transitions. This also assumes that there is no correlation between the potential barrier height and the jump distance.

For the case of the strong spatial correlations, when the pair correlation function

$$f(r) = Ae^{-\beta r} > 1,$$

the expression for the AC conductivity can be written as

$$\sigma_{ac}(\omega) = \frac{A}{48} \frac{e^4 \omega (\omega \nu_{ph})^{\beta/2\alpha}}{\cos(\beta/2\alpha)\alpha^4 \varepsilon\varepsilon_0} \left[\ln\left(\frac{\nu_{ph}}{\omega} \frac{2\alpha-\beta}{2\alpha+\beta} \right) \right]^3 N^2(E), \tag{2}$$

where ω is the cyclic frequency; ν_{ph} is the phonon frequency (similar to that in a crystal); ε is the static dielectric constant; α^{-1} is the localization radius; r is the center-to-center jump distance; $N(E)$ is the concentration of centers in unit interval energies.

Eq. (2) explains the linear frequency dependence in the region of medium and high frequencies, taking into account that

$$s = 1 + \beta/2\alpha,\ \beta = 1{,}6\cdot 10^{-7}\ \text{cm}^{-1}.$$

It can be concluded that the main contribution to dynamic conductivity is made by spatially correlated pairs of defects, for example, dangling bonds, etc.

Summary

Based on the results of the studies, it can be argued that the process of α-relaxation has been observed in blends of LDPE and EVA in the temperature range 250 – 280 K. The activation energies corresponding to this process in LDPE films and in the films of blends are 0.69 and 1.37 eV, respectively. The increased value of activation energy in the LDPE/EVA samples compared to the LDPE one can be explained by the appearance of deeper traps in the blends. These traps are bound up with the rotation of the polar groups in the EVA molecules or with the charge accumulation at the interface of two polymers.

The frequency dependence of the conductivity of the samples indicated the presence of hopping conductivity. Charge carriers involved in the conductivity can be negatively and positively charged hydrogen vacancies in polymer chains.

REFERENCES

1. **Sessler G. M.** (Ed.), Electrets (Book Series “Topics in Applied Physics”), Springer-Verlag, Berlin, Heidelberg, 1987.

2. **Hillenbrand J., Haberzettl S., Sessler G. M.,** Electret microphones with stiff diaphragms, J. Acoust. Soc. Am. 134 (6) (2013) 499–505.

3. **Goel M.,** Electret sensors, filters and MEMS devices: New challenges in materials research, Curr. Sci. 85 (4) (2005) 443–453.

4. **Rychkov D., Altafim R. A. P., Qiu X., Gerhard R.,** Treatment with orthophosphoric acid enhances the thermal stability of the piezoelectricity in low-density polyethylene ferroelectrets, J. Appl. Phys. 111 (12) (2012) 124105.

5. **Ismayilova R. S., Kuliev M. M.,** Features of the charge state of UHMWPE + α-SiO_2 nanocomposites, Surf. Eng. Appl. Elect. 56 (3) (2020) 267–271.

6. **Moody M. J., Marvin C. W., Hutchison G. R.,** Molecularly-doped polyurethane foams with massive piezoelectric response, J. Mater. Chem. C. 4 (20) (2016) 4387–4392.

7. **Galikhanov M.,** Corona electrets based on filler-loaded polymers: Structure, properties and applications, IEEE Trans. Dielectric. Elect. Insul. 29 (3) (2022) 788–793.

8. **Galikhanov M. F., Budarina L. A.,** Koronoelektrety na osnove polietilena i sopolimerov etilena s vinilacetatom [Corona electret based on polyethylene and ethylene/acetate copolymer], Russian Journal “Plasticheskiye massy”. (1) (2002) 40–42 (in Russian).

9. **Galikhanov M. F., Temnov D. E., Kozlov A. A., et al.,** Specific features of the electret effect in two-layer polymeric films, Russ. J. Appl. Chem. 81 (1) (2008) 86–90.

10. **Galikhanov M. F., Deberdeev R. Ya.,** Corona-poled electrets based on vinyl chloride/vinyl acetate copolymer-zinc white composites, Russ. J. Appl. Chem. 78 (3) (2005) 496–499.

11. **Galihanov M. F.,** Izuchenie koronoelektretov na osnove smesey polietilena s sopolimerami etilena s vinilacetatom [Investigation of corona electrets based on cast alloys of polyethylene with copolymers of ethylene and vinyl acetate], Materialovedenie. (12) (2006) 30–34 (in Russian).

12. **Tager A.,** Physical chemistry of polymers, 2-nd edition, Mir Publishers, Moscow, 1978.

13. **Bartenev G. M., Frenkel' S. Ya.,** Fizika polimerov [Physics of polymers], Khimiya Publishing, Leningrad, 1990 (in Russian).

14. **Sazhin B. I., Lobanov A. M., Romanovskaya A. S.,** Elektricheskie svojstva polimerov [Electrical properties of polymers], Khimiya Publishing, Leningrad, 1986 (in Russian).

15. **Kremer F., Schönhals A.,** Broadband dielectric spectroscopy, Springer-Verlag, Berlin, Heidelberg, 2003.

16. **Havriliak S., Negami S.,** A complex plane representation of dielectric and mechanical relaxation processes in some polymers, Polymer. 8 (1967) 161–210.

17. **Kumari S., Ortega N., Kumar A., et al.,** Dielectric anomalies due to grain boundary conduction in chemically substituted ViFeO3, J. Appl. Phys. 117 (11) (2015) 114102.

18. **Jaiswal A., Das R., Maity T., et al.,** Temperature-dependent Raman and dielectric spectroscopy of $ViFeO_3$ nanoparticles: Signatures of spin-phonon and magnetoelectric coupling, J. Phys. Chem. C. 114 (29) (2010) 12432–12439.

19. **Mott N. F., Devis E. A.,** Electronic processes in non-crystalline materials, Clarendon-Press, Oxford, UK, 1971.

20. **Roizin Ya. O., Tsybeskov L. V., Shumeiko V. R.,** Dynamic conductivity of amorphous SiN, Fizika Tverdogo Tela. 32 (1) (1990) 293–296 (in Russian).
21. **Gorohovatskiy Yu., Aniskina L., Viktorovich A., et al.,** Demonstration of spin-orbital interaction of vibration spectra of polyelectrolyte of fiber and films based electrets on the basis of polypropylene and polyethylene, Izvestia: Herzen University Journal of Humanities & Sciences. Physics. (11(79)) (2009) 47–61 (in Russian).
22. **Aniskina L., Viktorovich A., Galikhanov M. F., Temnov D. E.,** Poly-electrolytic model of fiber polymers on the basis of polyethylene and polypropylene, Izvestia: Herzen University Journal of Humanities & Sciences. Physics. (135) (2010) 24–36 (in Russian).

СПИСОК ЛИТЕРАТУРЫ

1. Электреты. Под ред. Сесслера Г. Пер. с англ. М.: Мир, 1983. 487 с.
2. **Hillenbrand J., Haberzettl S., Sessler G. M.** Electret microphones with stiff diaphragms // Journal of the Acoustical Society of America. 2013. Vol. 134. No. 6. Pp. 499–505.
3. **Goel M.** Electret sensors, filters and MEMS devices: New challenges in materials research // Current Science. 2005. Vol. 85. No. 4. Pp. 443–453.
4. **Rychkov D., Altafim R. A. P., Qiu X., Gerhard R.** Treatment with orthophosphoric acid enhances the thermal stability of the piezoelectricity in low-density polyethylene ferroelectrets // Journal of Applied Physics. 2012. Vol. 111. No. 12. P. 124105.
5. **Ismayilova R. S., Kuliev M. M.** Features of the charge state of UHMWPE + α-SiO_2 nanocomposites // Surface Engineering and Applied Electrochemistry. 2020. Vol. 56. No. 3. Pp. 267–271.
6. **Moody M. J., Marvin C. W., Hutchison G. R.** Molecularly-doped polyurethane foams with massive piezoelectric response // Journal of Materials Chemistry C. 2016. Vol. 4. No. 20. Pp. 4387–4392.
7. **Galikhanov M.** Corona electrets based on filler-loaded polymers: Structure, properties and applications // IEEE Transactions on Dielectrics and Electrical Insulation. 2022. Vol. 29. No. 3. Pp. 788–793.
8. **Галиханов М. Ф., Бударина Л. А.** Короноэлектреты на основе полиэтилена и сополимеров этилена с винилацетатом // Пластические массы. 2002. № 1. С. 40–42.
9. **Галиханов М. Ф., Темнов Д. Е., Козлов А. А., Петрова А. А., Гороховатский Ю. А., Дебердеев Р. Я.** Изучение особенностей проявления электретного эффекта в двухслойных полимерных пленках // Журнал прикладной химии. 2008. Т. 81. № 1. С. 90–94.
10. **Галиханов М. Ф., Дебердеев Р. Я.** Короноэлектреты на основе композиций сополимера винилхлорида с винилацетатом и цинковых белил // Журнал прикладной химии. 2005. Т. 78. № 3. С. 502–505.
11. **Галиханов М. Ф.** Изучение короноэлектретов на основе смесей полиэтилена с сополимерами этилена с винилацетатом // Материаловедение. 2006. № 12. С. 30–34.
12. **Тагер А. А.** Физико-химия полимеров. Изд. 4-е, перераб. и доп. М.: Научный мир, 2007. 576 с.
13. **Бартенев Г. М., Френкель С. Я.** Физика полимеров. Ленинград: Химия, 1990. 432 с.
14. **Сажин Б. И., Лобанов А. М., Романовская А. С.** Электрические свойства полимеров. 3-е изд., перераб. Ленинград: Химия, 1986. 224 с.
15. **Kremer F., Schönhals A.** Broadband dielectric spectroscopy. Berlin, Heidelberg: Springer-Verlag, 2003. 729 p.
16. **Havriliak S., Negami S.** A complex plane representation of dielectric and mechanical relaxation processes in some polymers // Polymer. 1967. Vol. 8. Pp. 161–210.
17. **Kumari S., Ortega N., Kumar A., Pavunny S. P., Hubbard J. W., Rinaldi C., Srinivasan G., Scott J. F., Katiyar R. S.** Dielectric anomalies due to grain boundary conduction in chemically substituted $ViFeO_3$ // Journal of Applied Physics. 2015. Vol. 117. No. 11. P. 114102.
18. **Jaiswal A., Das R., Maity T., Vivekanand K., Adyanthaya S., Poddar P.** Temperature-dependent Raman and dielectric spectroscopy of $ViFeO_3$ nanoparticles: Signatures of spin-phonon and magnetoelectric coupling // Journal of Physical Chemistry. C. 2010. Vol. 114. No. 29. Pp. 12432–12439.
19. **Мотт Н., Дэвис Е.** Электронные процессы в некристаллических веществах в 2 тт. Пер. с англ. М.: Мир, 1982. Т. 1 – 368 с. Т. 2 – 664 с.

20. **Ройзин Я. О., Цыбесков Л. В., Шумейко В. Р.** Динамическая проводимость аморфного нитрида кремния // Физика твердого тела. 1990. Т. 32. № 1. С. 293–296.

21. **Гороховатский Ю. А., Анискина Л. В., Викторович А. С., Гороховатский И. Ю., Карулина Е. А., Тазенков Б. А., Темнов Д. Э., Чистякова О. В.** Проявление спин-орбитального взаимодействия в колебательных спектрах полиэлектролитов – волокнистых и пленочных электретов на основе полипропилена и полиэтилена // Известия Российского государственного педагогического университета имени А. И. Герцена. Естественные и точные науки: Физика. 2009. № 11 (79). С. 47–61.

22. **Анискина Л. В., Викторович А. С., Галиханов М. Ф., Темнов Д. Э.** Полиэлектролитная модель волокнитов на основе полиэтилена и полипропилена // Известия Российского государственного педагогического университета имени А. И. Герцена. Естественные и точные науки: Физика. 2010. № 135. С. 24–36.

THE AUTHORS

CASTRO ARATA Rene Alejandro A.
Herzen State Pedagogical University of Russia
48 Moyka Emb., St. Petersburg, 191186, Russia
recastro@mail.ru
ORCID: 0000-0002-1902-5801

KARULINA Elena A.
Herzen State Pedagogical University of Russia
48 Moyka Emb., St. Petersburg, 191186, Russia
karulina@mail.ru
ORCID: 0000-0001-9604-4769

GALIKHANOV Mansur F.
Institute of Applied Research of Tatarstan Academy of Sciences,
Kazan National Research Technological University
20 Bauman St., Kazan, 420111, Russia
mgalikhanov@yandex.ru
ORCID: 0000-0001-5647-1854

REZTSOV Tikhon V.
Herzen State Pedagogical University of Russia
48 Moyka Emb., St. Petersburg, 191186, Russia
sunnyundeadjuvati@icloud.com
ORCID: 0000-0003-2025-0579

FOMICHEVA Elena E.
Military Space Academy Named after A. F. Mozhaysky
13 Zhdanovskaya St., St. Petersburg, 197198, Russia
e.e.fomicheva@gmail.com
ORCID: 0000-0002-9402-5246

СВЕДЕНИЯ ОБ АВТОРАХ

КАСТРО АРАТА Рене Алехандро – *доктор физико-математических наук, ведущий научный сотрудник Института физики Российского государственного педагогического университета им. А. И. Герцена, Санкт-Петербург, Россия.*
191186, Россия, г. Санкт-Петербург, наб. р. Мойки, 48
recastro@mail.ru
ORCID: 0000-0002-1902-5801

КАРУЛИНА Елена Анатольевна – *кандидат физико-математических наук, доцент Института физики Российского государственного педагогического университета им. А. И. Герцена, Санкт-Петербург, Россия.*

191186, Россия, г. Санкт-Петербург, наб. р. Мойки, 48
karulina@mail.ru
ORCID: 0000-0001-9604-4769

ГАЛИХАНОВ Мансур Флоридович – *доктор технических наук, ведущий научный сотрудник Центра новых материалов и перспективных технологий Института прикладных исследований Академии наук Республики Татарстан; профессор кафедры технологии переработки полимеров и композиционных материалов Казанского национального исследовательского технологического университета г. Казань, Республика Татарстан, Россия.*

420111, Россия, Республика Татарстан, г. Казань, ул. Баумана, 20
mgalikhanov@yandex.ru
ORCID: 0000-0001-5647-1854

РЕЗЦОВ Тихон Вадимович – *студент Института детства Российского государственного педагогического университета им. А. И. Герцена, Санкт-Петербург, Россия.*

191186, Россия, г. Санкт-Петербург, наб. р. Мойки, 48
sunnyundeadjuvati@icloud.com
ORCID: 0000-0003-2025-0579

ФОМИЧЕВА Елена Егоровна – *кандидат физико-математических наук, старший преподаватель Военно-космической академии имени А. Ф. Можайского, Санкт-Петербург, Россия.*

197198, Россия, г. Санкт-Петербург, Ждановская ул., 13
e.e.fomicheva@gmail.com
ORCID: 0000-0002-9402-5246

Received 31.03.2024. Approved after reviewing 03.04.2024. Accepted 03.04.2024.

Статья поступила в редакцию 31.03.2024. Одобрена после рецензирования 03.04.2024. Принята 03.04.2024.

© Санкт-Петербургский политехнический университет Петра Великого, 2024

Original article
DOI: https://doi.org/10.18721/JPM.17305

NUMERICAL SIMULATION OF THE TUNNEL EFFECT IN THE GALLIUM NITRIDE HETEROSTRUCTURE ON SILICON

D. A. Barykin[1,2✉], *K. Yu. Shugurov*[1], *A. M. Mozharov*[1], *I. S. Mukhin*[2]

[1] Alferov University, St. Petersburg, Russia;

[2] Peter the Great St. Petersburg Polytechnic University, St. Petersburg, Russia

✉ d.a.barykin02@mail.ru

Abstract. In this study, a numerical simulation of the tunnel effect in the *n*-GaN/*p*-Si heterostructure has been performed. Variations of band diagrams, current-voltage characteristics and cutoff frequencies of the diode heterostructures under study were obtained depending on the doping levels of GaN and Si. The dopant concentration values were found for implementing backward and tunnel diode modes. In the tunnel diode mode, the peak current density and maximal generation frequency were 24.6 kA/cm^2 and 17 GHz, respectively.

Keywords: tunnel effect simulation, gallium nitride, silicon, nanowire, tunnel diode

Funding: The reported study was funded by Russian Science Foundation (Grant No. 23-79-01279, https://rscf.ru/project/23-79-01279/).

Citation: Barykin D. A., Shugurov K. Yu., Mozharov A. M., Mukhin I. S., Numerical simulation of the tunnel effect in the gallium nitride heterostructure on silicon, St. Petersburg State Polytechnical University Journal. Physics and Mathematics. 17 (3) (2024) 46–56. DOI: https://doi.org/10.18721/JPM.17305

This is an open access article under the CC BY-NC 4.0 license (https://creativecommons.org/licenses/by-nc/4.0/)

Научная статья
УДК 537.9
DOI: https://doi.org/10.18721/JPM.17305

ЧИСЛЕННОЕ МОДЕЛИРОВАНИЕ ТУННЕЛЬНОГО ЭФФЕКТА В ГЕТЕРОСТРУКТУРЕ НИТРИДА ГАЛЛИЯ НА КРЕМНИИ

Д. А. Барыкин[1,2✉], *К. Ю. Шугуров*[1], *А. М. Можаров*[1], *И. С. Мухин*[2]

[1] Академический университет им. Ж. И. Алфёрова РАН, Санкт-Петербург, Россия;

[2] Санкт-Петербургский политехнический университет Петра Великого, Санкт-Петербург, Россия

✉ d.a.barykin02@mail.ru

Аннотация. В работе выполнено численное моделирование туннельного эффекта в системе *n*-GaN на кремнии Si *p*-типа проводимости. Получены вариации зонных диаграмм, вольтамперных характеристик и частот отсечки соответствующих диодных гетероструктур в зависимости от уровней легирования GaN и Si. Установлены значения концентраций легирующей примеси для реализации режимов обращенного и туннельного диодов. В режиме туннельного диода наибольшая плотность туннельного тока и предельная частота генерации составили 24,6 кА/см^2 и 17 ГГц, соответственно.

Ключевые слова: моделирование туннельного эффекта, нитрид галлия, кремний, нитевидный нанокристалл, туннельный диод

© Barykin D. A., Shugurov K. Yu., Mozharov A. M., Mukhin I. S., 2024. Published by Peter the Great St. Petersburg Polytechnic University.

Финансирование: Исследование выполнено за счет гранта Российского научного фонда № 01279-79-23 (https://rscf.ru/project/23-79-01279/).

Ссылка для цитирования: Барыкин Д. А., Шугуров К. Ю., Можаров А. М., Мухин И. С. Численное моделирование туннельного эффекта в гетероструктуре нитрида галлия на кремнии // Научно-технические ведомости СПбГПУ. Физико-математические науки. 2024. Т. 17. № 3. С. 46–56. DOI: https://doi.org/10.18721/JPM.17305

Статья открытого доступа, распространяемая по лицензии CC BY-NC 4.0 (https://creativecommons.org/licenses/by-nc/4.0/)

Introduction

Over the past 70 years, various microwave semiconductor devices have been developed, in particular, *p–i–n* diodes, Schottky diodes, Gunn diodes, as well as tunnel and backward diodes, whose operation is based on the tunneling effect. This class of elements occupies an important niche, since it is widely used in circuits for detection, mixing, amplification and generation of high-frequency signals.

Tunnel diodes are commonly manufactured based on gallium arsenide (GaAs) and germanium (Ge), and based on silicon (Si) in very rare cases. Narrow-gap semiconductors (germanium) are primarily used because such materials are characterized by a higher probability of carrier tunneling [1], which increases the efficiency of the device. However, on the other hand, due to the narrow band gap, temperature instability of its characteristics is observed, even though tunnel diodes are less sensitive in this regard than, for example, high-speed *p–i–n* diodes or Schottky diodes. Using silicon is certainly advisable from both the economic and the technological perspectives, interband tunneling current is significantly limited due to the law of momentum conservation, which greatly narrows the applications of components based on these materials [2]. Compared with silicon tunnel diodes, materials fabricated from group III–V elements (for example, GaAs) can provide a much higher ratio of peak-to-valley current due to their direct-bandgap nature, low effective tunneling masses and the possibility of using diverse variations of heterostructures based on them [3]. Gallium arsenide has low thermal conductivity, is prepared by a rather complex procedure with consequently high production cost. In addition, synthesizing *n*-GaAs from impurity concentrations above $2 \cdot 10^{19}$ cm^{-3} is a major technological challenge [4].

These drawbacks stimulate intense research in this field: new systems of materials are considered, in particular those integrated with the silicon platform [5–7].

GaN heterostructures on silicon (GaN/Si) are considered a promising system of materials, combining the advantages of GaN (wide-bandgap material, direct-bandgap structure, high thermal, chemical and radiation resistance) with silicon technology that is well-developed and easily accessible. However, these semiconductors are poorly compatible due to a significant mismatch in the lattice constant and the coefficient of thermal expansion.

An alternative approach involves nanowire crystals (NWs), whose main advantage high crystalline perfection, almost regardless of chosen growth substrate, which significantly expands the possibilities of integrating GaN with other materials. Moreover, research into GaN NWs indicates that such objects are well suited for creating a wide class of components, for example, field-effect transistors in the so-called gate–all-around configuration or core-shell structure [8, 9], Schottky diodes [10], photodiodes [11], piezogenerators [12].

In addition to high crystalline quality, GaN NWs offer a range of major benefits, including in tunnel devices:

the structure has low electrical capacitance because of small transverse dimensions of the NW [10], which generally do not exceed 100–200 nm (relatively high capacitances are characteristic for tunnel junctions, due to small width of the space charge region);

single GaN NWs can switch currents with densities up to 2 MA/cm^2 [13], which is in demand for high-current tunnel devices [14];

© Барыкин Д. А., Шугуров К. Ю., Можаров А. М., Мухин И. С., 2024. Издатель: Санкт-Петербургский политехнический университет Петра Великого.

GaN NWs with a doping level up to 10^{20} cm^{-3} can be synthesized [15], allowing to control the range of operating frequencies and output characteristics of structures;

electronic components can operate in adverse conditions and aggressive environments, due to the material properties of GaN;

large surface-area-to-volume ratio due to high aspect ratio characteristic for NWs, which contributes to efficient heat dissipation [16].

The significant potential of NWs and the development of methods for their synthesis have attracted the attention of many researchers; in particular, InAs/InSb, InAs/GaSb, GaAsSb, InGaAs NWs are increasingly used in tunnel diodes in recent years [7, 17–20]. However, the tunnel effect itself in the GaN NW/Si system still remains unexplored.

This paper is dedicated to theoretical study of the tunneling effect in the GaN NW heterostructure on silicon.

Description of the model

The tunneling effect was simulated for the *n*-GaN/*p*-Si system using the COMSOL Multiphysics package. Since the typical diameter of GaN NWs is 100–200 nm, and the characteristic thickness of the space charge region in tunnel diodes is about 10 nm, it can be argued that the distribution of the electric field is mainly directed across the heterointerface and almost independent of the position in the plane within the NW (Fig. 1). For this reason, a one-dimensional model of the system was chosen for the calculation.

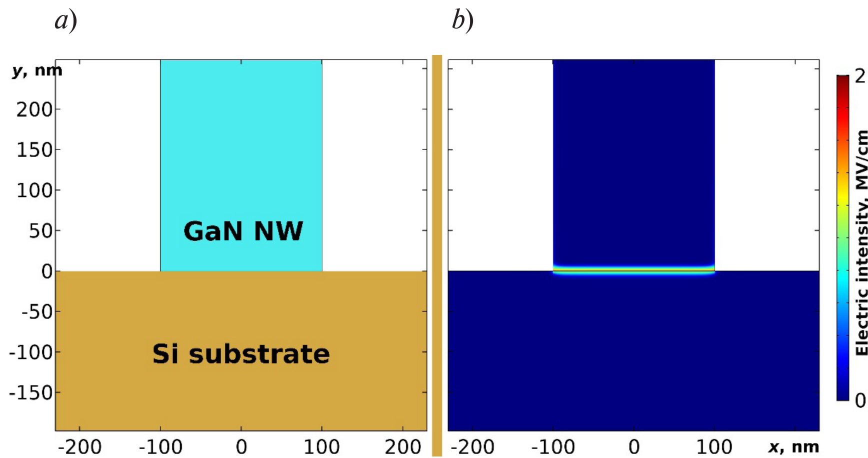

Fig. 1. Schematic model of GaN NW/Si system (*a*) and distribution of electric intensity across *n*-GaN NW/*p*-Si heterointerface at $n = p = 10^{19}$ cm^{-3} (*b*) (COMSOL Multiphysics software package was used)

Numerical simulation was carried out within the framework of the Roosbroeck model [21], taking into account the Fermi–Dirac statistics for charge carriers. The parameters of semiconductor materials were taken from monograph [22]. The process of carrier recombination by the Shockley–Reed–Hall mechanism was taken into account to correctly describe the thermal emission current in silicon. The tunneling current was calculated within the framework of the non-local tunneling model [23] using the following expression:

$$J_t = \frac{eK\sqrt{m_e m_h}}{2\pi^2\hbar^3}\int_{E_C}^{E_V} T(E)\left[F_C(E) - F_V(E)\right]dE, \quad (1)$$

where E is the total charge carrier energy; E_C, E_V are the energies of the bottom of the conduction band in the *n*-layer and the top of the valence band in the *p*-layer, respectively; T is the probability of interband tunneling of carriers; F_C, F_V are the probabilities of finding an electron with the energy E in the conduction band of the *n*-layer and valence band of the *p*-layer, respectively; K is the kinetic energy of the thermal motion of charge carriers; m_e, m_h are the effective masses of electrons and holes, respectively; e is the electron charge; h is Planck's constant ($\hbar = h/2\pi$).

The tunneling probability was calculated using the Wentzel—Kramers—Brillouin approximations with the averaged wave vector **k** for electrons and holes:

$$T \approx \exp\left[-2\int_{x_1}^{x_2} \left|k(x)dx\right|\right], \tag{2}$$

$$k = \frac{k_e k_h}{\sqrt{k_e^{\,2} + k_h^{\,2}}}, \tag{3}$$

$$k_e = \sqrt{\frac{2m_e}{\hbar^2}\left(E_C - E\right)}, \tag{4}$$

$$k_h = \sqrt{\frac{2m_h}{\hbar^2}\left(E - E_V\right)}. \tag{5}$$

The quantities x_1 and x_2 represent the bounds of the energy barrier for electrons with the total energy E and are determined by the condition for equality of $E = E_C$ and $E = E_V$, respectively.

Synthesis of NWs revealed that semiconductor layers in the heterojunction region were stressed due to mismatch with the substrate in terms of the lattice parameter and the coefficient of thermal expansion. However, in the case of GaN on silicon, NWs with fully relaxed layers at the base due to the formation of ultrathin interfacial layers (less than 2 nm) [24—26]. Therefore, this effect was not taken into account in the present calculation.

Results and discussion

The doping levels of Si and GaN were used as variable parameters in the calculation. For silicon, the range of these values was $(1-10)\cdot10^{19}$ cm^{-3}, which corresponds to the impurity concentration in heavily doped commercial substrates. For GaN, this parameter varied over a wider range: $(5-1000)\cdot10^{17}$ cm^{-3}, which is due, on the one hand, to background doping of synthesized NWs, and, on the other hand, to the upper bound of NW doping with silicon, in accordance with the technique described in the literature [15].

Fig. 2 shows the band diagrams without voltage biasing for three structural configurations. In this case, the first (Fig. 2,*a*) and the third (Fig. 2,*c*) configuration correspond to the minimum and maximum limits for the considered dopant concentrations. Evidently, in the case of maximum concentrations, the valence band of Si and the conduction band of GaN overlap (see Fig. 2,*c*).

This picture is typical for tunnel diodes, when a small bias in any direction is accompanied by active carrier tunneling, since electrons in the GaN conduction band have access to levels in the Si valence band (forward bias) with the same energy and vice versa (reverse bias). The minimum width of the barrier is about 3 nm.

For minimum doping levels (see Fig. 2,*a*), GaN turns out to be non-degenerate and there is no band overlap, therefore the tunneling current is absent at near-zero bias. Furthermore, the barrier width in steady state is approximately 40 nm, so active tunneling is only possible in the case of significant reverse bias reducing the barrier width. In general, this picture is typical for a conventional *p—n* diode rectifiers.

Fig. 2,*b* shows some intermediate situation when the top of the Si valence band coincides with the bottom of the GaN conduction band. The forward bias of the structure in such a configuration is accompanied by an increase in the diffusion current, while a small reverse bias leads to the appearance of tunneling current. According to the band diagram, the height of the barrier for electrons moving from GaN to Si along the conduction band is approximately equal to the width of the Si bandgap, which means that the structure becomes well-conducting at voltages of about +1 V. The reverse bias is characterized by two factors: an increase in the overlap zone and a decrease in the barrier width, which in combination cause a sharp increase in the tunneling current. As a result, the conductivity of the structure is significantly higher in the reverse than in the forward direction for a voltage range of the order of ±1 V. This behavior applies to backward diodes, where the current—voltage characteristic is inverted compared with the classical type.

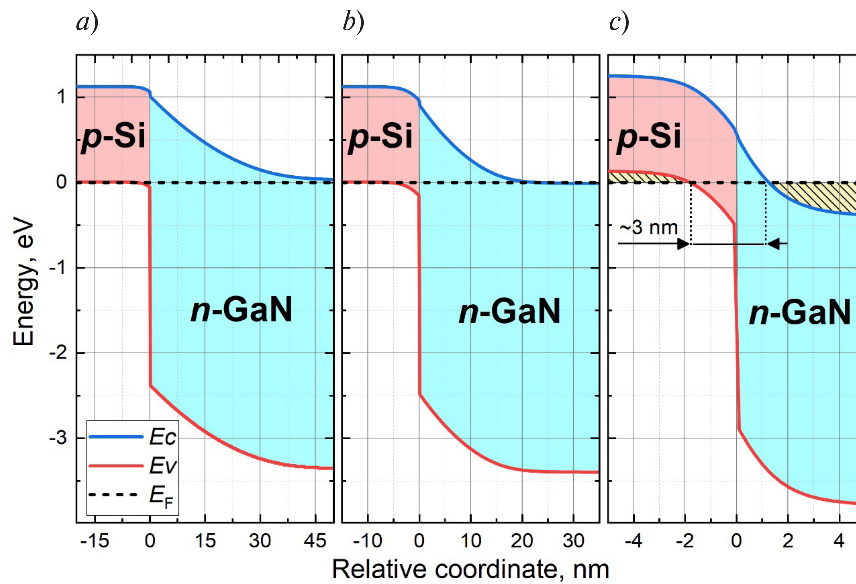

Fig. 2. Energy band diagram of n-GaN/p-Si structures for various doping configurations, cm^{-3}: $n = 5\cdot10^{17}$, $p = 1\cdot10^{19}$ (*a*); $n = 2\cdot10^{18}$, $p = 1\cdot10^{19}$ (*b*); $n = p = 1\cdot10^{20}$ (*c*)
The shaded region in Fig. 2,*c* corresponds to filling with holes in Si and with electrons in GaN
The interfaces of the layers are taken as the origin for the abscissa, and the Fermi level E_F as the origin for the ordinate

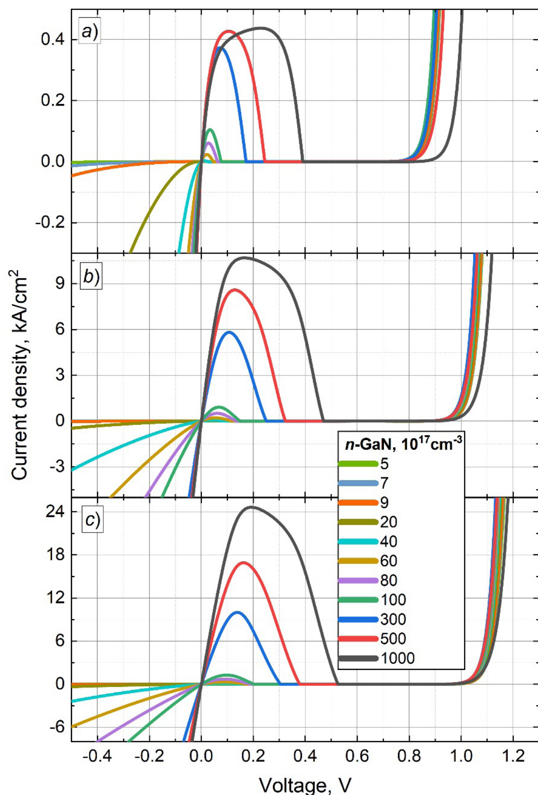

Fig. 3. Calculated current–voltage characteristics for different doping levels doping of n-GaN (see legend) and p-Si, 10^{19} cm^{-3}: 1 (*a*), 5 (*b*), 10 (*c*)

The obtained series of current–voltage characteristics of the structures are shown in Fig. 3. The graphs show characteristic peaks, after which an increase in voltage is accompanied by a decrease in current. This is called the negative differential resistance (NDR) region, a distinctive trait of tunnel diodes. A peak corresponds to the situation when the overlap of the Si valence band above the Fermi level and the GaN conduction band below the Fermi level reaches a maximum value. The highest calculated value of the peak current density was 24.6 kA/cm^2 (see Fig. 3,*c*) at a voltage of 190 mV (for $n = p = 10^{20}$ cm^{-3}).

This result is comparable with the experimental as well as theoretical [27] data for diode structures (including those with NWs) based on GaAs [28–30], Ge/Si [31], Si [32] and GaSb/InAsSb [33], where the peak current density ranges from several up to tens of kA/cm^2.

The positions of both current and voltage peaks are shifted towards zero as the doping level of GaN decreases, as this leads to smaller band overlap. For the same reason, the peak-to-peak voltage (the voltage at which the current through the tunnel diode reaches its maximum for the second time) is shifted towards lower values. Note that the peak-to-peak voltage in our case weakly depends on the dopant concentration in GaN in the range of $(5–500)\cdot10^{17}$ cm^{-3}, however, it is quite sensitive to Si doping.

As the simulation did not take into account defects on the GaN/Si interface, there is a horizontal section with zero current on the current–voltage characteristics after the NDR region. In real diode structures, the valley current does not reach zero, since in the absence of an overlap zone, the corresponding carriers can travel under the barrier along the energy levels of defects. As a result, the valley gains a rounder shape. The defect density at the heterointerface in the GaN NW/Si system can be modified using hydrogen passivation, which we demonstrated earlier [34].

Since this type of device is characterized by operation at high frequencies, we calculated the dependence of the cutoff frequency (the maximum generation frequency for tunnel diodes) of the structures on the doping level of GaN (Fig. 4). Tunnel diodes typically operate in the NDR region of the current–voltage characteristic, therefore, the cutoff frequency is determined from the condition that the real part of the diode's complex resistance be negative [35].

It can be proved that in this case the expression for the cutoff frequency f_{cutoff} is written as follows:

$$f_{cutoff} = \frac{1}{2\pi |R_{\min}| C_j}, \tag{6}$$

where $|R_{\min}|$ is the absolute value of the minimum resistance in the NDR region, C_j is the capacitance of the p–n junction.

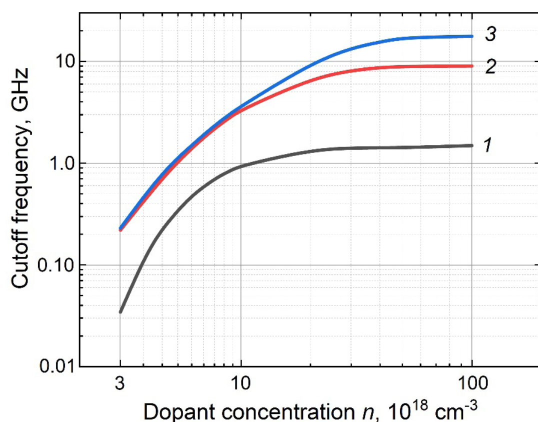

Fig. 4. Calculated dependences of the structure's cutoff frequency on doping level of n-GaN for different doping levels of p-silicon, 10^{19} cm^{-3}: 1 (*1*), 5 (*2*), 10 (*3*)

We should note here that expression (6) in fact includes the differential resistance in the corresponding region, which is not a constant. Using its minimum value $|R_{in}|$ is generally accepted.

Analysis of the data in Fig. 4 shows that an increase in the dopant concentration in both GaN and Si is accompanied by a nonlinear shift of the cutoff to a higher frequency region. The upper bound of the cutoff frequency is in the region of 17 GHz, which corresponds to almost peak doping levels of GaN and Si. Even if it becomes technologically possible to further increase the concentration, it still will not lead to a significant expansion of the operating frequency range.

Importantly, the cutoff frequency increases by several times for dopant concentrations in silicon between $1 \cdot 10^{19}$ and $5 \cdot 10^{19}$ cm^{-3}. The curves for $p = 5 \cdot 10^{19}$ and $1 \cdot 10^{20}$ cm^{-3} differ to a much smaller extent. Considering these data along with the current–voltage characteristics, we can conclude that the doping levels of gallium nitride and silicon should be chosen at least as high as $3 \cdot 10^{19}$ and $5 \cdot 10^{19}$ cm^{-3}, respectively, to implement tunnel diodes combining high peak current density with high performance.

Conclusion

In this paper, numerical simulation of the tunneling effect in the n-GaN NW/p-Si heterostructure is carried out in a wide range of doping levels (in the one-dimensional approximation).

It is established that the backward diode mode is implemented at a dopant concentration of about $2 \cdot 10^{18}$ and $1 \cdot 10^{19}$ cm^{-3} for GaN and Si, respectively, while concentrations of at least $3 \cdot 10^{19}$ cm^{-3} for GaN and $5 \cdot 10^{19}$ cm^{-3} for Si should be chosen for tunnel diodes.

It was observed from the current–voltage characteristics that the calculated peak tunnel current density was 24.6 kA/cm^2, which is in good agreement with the experimental results for structures based on GaAs and Ge as the main industrial materials for tunneling-effect devices. Frequency analysis of the structure generation led to the conclusion that its limiting frequency for tunnel diodes of the GaN/Si system is at the level of 17 GHz.

REFERENCES

1. **Hopkins J. B.,** Microwave backward diodes in InAs, Solid-State Electron. 13 (5) (1970) 697–705.

2. **Tabe M., Tan H.N., Mizuno T., et al.,** Atomistic nature in band-to-band tunneling in two-dimensional silicon pn tunnel diodes, Appl. Phys. Lett. 2016. Vol. 108 (9) (2016) 093502.

3. **Li Q., Han Y., Lu X., Lau K. M.,** GaAs-InGaAs-GaAs fin-array tunnel diodes on (001) Si substrates with room-temperature peak-to-valley current ratio of 5.4, IEEE Electron. Device Lett. 37 (1) (2016) 24–27.

4. **Kalinovskiy V.S., Maleyev N. A., Kontrosh E. V., et al.,** Tunnelnyye diody n^{++}-GaAs:(delta-Si)/p^{++}-$Al_{0.4}Ga_{0.6}$As:(C) dlya soyedinitelnykh elementov mnogoperekhodnykh lazernykh fotopreobrazovateley [n^{++}-GaAs:(delta-Si)/p^{++}-$Al_{0.4}Ga_{0.6}$As:(C) tunnel diodes for connecting the elements of multijunction laser converters], Pisma v Zhurnal Tekhnicheskoy Fiziki. 50 (7) (2024) 39–42 (in Russian)

5. **Jia R., Huang Q., Huang R.,** Vertical SnS_2/Si heterostructure for tunnel diodes, Sci. China Inf. Sci. 63 (2) (2019) 122401.

6. **Zhu Y., Lv H., Zhang Y., et al.,** MoS_2/Si tunnel diodes based on comprehensive transfer technique, Chin. Phys. B. 32 (1) (2023) 018501.

7. **Anandan D., Hsu C.-W., Chang E. Y.,** Growth of III–V antimonide heterostructure nanowires on silicon substrate for Esaki tunnel diode, Mater. Sci. Forum. 1055 (March) (2022) 1–6.

8. **Ajitha D., Lakshmi K.N.V.S., Lakshmi B. K.,** Nanowire transistors: A next step for the low-power digital technology, IETE J. Res. 69 (11) (2021) 1–17.

9. **Im K.-S., Reddy M. S. P., Caulmilone R., et al.,** Low-frequency noise characteristics of GaN nanowire gate-all-around transistors with/without 2-DEG channel, IEEE Trans. Electron Dev. 66 (3) (2019) 1243–1248.

10. **Shugurov K. Yu., Mozharov A. M., Sapunov G. A., et al.,** Microwave Shottky diodes based on single GaN nanowires, Techn. Phys. Lett. 48 (8) (2022) 18–21.

11. **Han S., Noh S., Kim J.-W., et al.,** Stretchable inorganic GaN-nanowire photosensor with high photocurrent and photoresponsivity, ACS Appl. Mater. Interfaces. 13 (19) (2021) 22728–22737.

12. **Jamond N., Chrétien P., Houzé F., et al.,** Piezo-generator integrating a vertical array of GaN nanowires, Nanotechnol. 27(32) (2016) 325403.

13. **Shugurov K., Mozharov A., Sapunov G., et al.,** Single GaN nanowires for extremely high current commutation, Phys. Stat. Solidi (RRL) 15 (4) (2021) 2000590.

14. **Zhang H., Xue J., Sun Z., et al.,** 1039 kA/cm^2 peak tunneling current density in GaN-based resonant tunneling diode with a peak-to-valley current ratio of 1.23 at room temperature on sapphire substrate, Appl. Phys. Lett. 119 (15) (2021) 153506.

15. **Fang Z., Robin E., Rozas-Jiménez E., et al.,** Si donor incorporation in GaN nanowires, Nano Lett. 15 (10) (2015) 6794–6801.

16. **Léonard F.,** Reduced Joule heating in nanowires, Appl. Phys. Lett. 98 (10) (2011) 103101.

17. **Takahashi T., Kawaguchi K., Sato M., Suhara M., Okamoto N.** Highly sensitive p-GaAsSb/n-InAs nanowire backward diodes for low-power microwaves, Proc. 49th Europ. Solid-State Device Res. Conf. (ESSDERC). 23–26 Sept., 2019. Cracow, Poland. (2019) 214–217.

18. **Shao Y., Pala M., Esseni D., del Alamo J. A.,** Scaling of GaSb/InAs vertical nanowire Esaki diodes down to sub-10-nm diameter, IEEE Trans. Electron Dev. 69 (4) (2022) 2188–2195.

19. **Anabestani H., Shazzad R., Fattah M. F. A., et al.,** Review on GaAsSb nanowire potentials for future 1D heterostructures: Properties and applications, Mater. Today Commun. 28 (Sept) (2021) 102542.

20. **Yoshida A., Gamo H., Motohisa J., Tomioka K.,** Creation of unexplored tunnel junction by heterogeneous integration of InGaAs nanowires on germanium, Sci. Rep. 12 (31 Jan) (2022) 1606.

21. **Van Roosbroeck W.,** Theory of the flow of electrons and holes in germanium and other semiconductors, Bell Syst. Tech. J. 29 (4) (1950) 560–607.

22. Adachi S. Properties of Group-IV, III–V and II–VI Semiconductors. John Wiley & Sons, 2005. 408 p.

23. **Liu K.-M., Cheng C.-P.,** Investigation on the effects of gate-source overlap/underlap and source doping gradient of n-type Si cylindrical gate-all-around tunnel field-effect transistors, IEEE Trans. Nanotechnol. 19 (07 May) (2020) 382–389.

24. **Eftychis S., Kruse J. E., Tsagaraki K., et al.,** Effects of ultrathin AlN prelayers on the spontaneous growth of GaN nanowires by plasma assisted molecular beam epitaxy, J. Cryst. Growth. 514 (15 May) (2019) 89–97.

25. **Landré O., Bougerol C., Renevier H., Daudin B.,** Nucleation mechanism of GaN nanowires grown on (111) Si by molecular beam epitaxy, Nanotechnol. 20 (41) (2009) 415602.

26. **Geelhaar L., Chuze C., Jenichen B., et al.,** Properties of GaN nanowires grown by molecular beam epitaxy, IEEE J. Sel. Top. Quantum Electron. 17 (4) (2011) 878–888.

27. **Kumar M. J., Sharma S.,** GaAs tunnel diode with electrostatically doped n-region: Proposal and analysis, IEEE Trans. Electron Dev. 62 (10) (2015) 3445–3448.

28. **Pan J. L., McManis J. E., Grober L., Woodall J. M.,** Gallium-arsenide deep-level tunnel diode with record negative conductance and record peak current density, Solid-State Electron. 48 (10–11) (2004) 2067–2070.

29. **Ahmed S., Melloch M. R., Harmon E. S., et al.,** Use of nonstoichiometry to form GaAs tunnel junctions, Appl. Phys. Lett. 71 (25) (1997) 3667–3669.

30. **Darbandi A., Kavanagh K. L., Watkins S. P.,** Lithography-free fabrication of core–shell GaAs nanowire tunnel diodes, Nano Lett. 15 (8) (2015) 5408–5413.

31. **Chen L., Fung W. Y., Lu W.,** Vertical nanowire heterojunction devices based on a clean Si/Ge interface, Nano Lett. 13 (11) (2013) 5521–5527.

32. **Schmid H., Bessire C., Bjцrk M. T., et al.,** Silicon nanowire Esaki diodes, Nano Lett. 12 (2) (2012) 699–703.

33. **Ganjipour B., Dey A. W., Borg B. M., et al.,** High current density Esaki tunnel diodes based on GaSb-InAsSb heterostructure nanowires, Nano Lett. 11 (10) (2011) 4222–4226.

34. **Shugurov K. Y., Mozharov A. M., Bolshakov A. D., et al.,** Hydrogen passivation of the n-GaN nanowire/p-Si heterointerface, Nanotechnol. 31 (24) (2020) 244003.

35. **Lebedev A. I.,** Fizika poluprovodnikovykh priborov [Physics of semiconductor devices], Fizmatlit Publishing, Moscow, 2008.

СПИСОК ЛИТЕРАТУРЫ

1. **Hopkins J. B.** Microwave backward diodes in InAs // Solid-State Electronics. 1970. Vol. 13. No. 5. Pp. 697–705.

2. **Tabe M., Tan H.N., Mizuno T., Muruganathan M., Anh L.T., Mizuta H., Nuryadi R., Moraru D.** Atomistic nature in band-to-band tunneling in two-dimensional silicon pn tunnel diodes // Applied Physics Letters. 2016. Vol. 108. No. 9. P. 093502.

3. **Li Q., Han Y., Lu X., Lau K. M.** GaAs-InGaAs-GaAs fin-array tunnel diodes on (001) Si substrates with room-temperature peak-to-valley current ratio of 5.4 // IEEE Electron Device Letters. 2016. Vol. 37. No. 1. Pp. 24–27.

4. **Калиновский В. С., Малеев Н. А., Контрош Е. В., Васильев А. П., Прудченко К. К., Толкачев И. А., Малевская А. В., Устинов В. М.** Туннельные диоды n^{++}-GaAs:(delta-Si)/p^{++}-$Al_{0.4}Ga_{0.6}As$:(C) для соединительных элементов многопереходных лазерных фотопреобразователей // Письма в Журнал технической физики. 2024. Т. 50. № 7. С. 39–42.

5. **Jia R., Huang Q., Huang R.** Vertical SnS_2/Si heterostructure for tunnel diodes // Science China Information Sciences. 2019. Vol. 63. No. 2. P. 122401.

6. **Zhu Y., Lv H., Zhang Y., Jia Z., Sun J., Lyu Z., Lu B.** MoS_2/Si tunnel diodes based on comprehensive transfer technique // Chinese Physics B. 2023. Vol. 32. No. 1. P. 018501.

7. **Anandan D., Hsu C.-W., Chang E. Y.** Growth of III–V antimonide heterostructure nanowires on silicon substrate for Esaki tunnel diode // Materials Science Forum. 2022. Vol. 1055. March. Pp. 1–6.

8. **Ajitha D., Lakshmi K.N.V.S., Lakshmi B. K.** Nanowire transistors: A next step for the low-power digital technology // IETE Journal of Research. 2021. Vol. 69. No. 11. Pp. 1–17.

9. **Im K.-S., Reddy M. S. P., Caulmilone R., Theodorou C. G., Ghibaudo G., Cristoloveanu S., Lee J.-H.** Low-frequency noise characteristics of GaN nanowire gate-all-around transistors with/without 2-DEG channel // IEEE Transactions on Electron Devices. 2019. Vol. 66. No. 3. Pp. 1243–1248.

10. **Шугуров К. Ю., Можаров А. М., Сапунов Г. А., Фёдоров В. В., Моисеев Э. И., Блохин С. А., Кузьменков А. Г., Мухин И. С.** Сверхвысокочастотные диоды Шоттки на основе одиночных нитевидных нанокристаллов GaN // Письма в Журнал технической физики. 2022. Т. 48. №. 15. С. 22–25.

11. **Han S., Noh S., Kim J.-W., Lee C.-R., Lee S.-K., Kim J. S.** Stretchable inorganic GaN-nanowire photosensor with high photocurrent and photoresponsivity // ACS Applied Materials & Interfaces. 2021. Vol. 13. No. 19. Pp. 22728–22737.

12. **Jamond N., Chrétien P., Houzé F., et al.** Piezo-generator integrating a vertical array of GaN nanowires // Nanotechnology. 2016. Vol. 27. No. 32. P. 325403.

13. **Shugurov K., Mozharov A., Sapunov G., Fedorov V., Tchernycheva M., Mukhin I.** Single GaN nanowires for extremely high current commutation // Physica Status Solidi (RRL) – Rapid Research Letters. 2021. Vol.15. No. 4. P. 2000590.

14. **Zhang H., Xue J., Sun Z., et al.** 1039 kA/cm^2 peak tunneling current density in GaN-based resonant tunneling diode with a peak-to-valley current ratio of 1.23 at room temperature on sapphire substrate // Applied Physics Letters. 2021. Vol. 119. No. 15. P. 153506.

15. **Fang Z., Robin E., Rozas-Jiménez E., Cros A., Donatini F., Mollard N., Pernot J., Daudin B.** Si donor incorporation in GaN nanowires // Nano Letters. 2015. Vol. 15. No. 10. Pp. 6794–6801.

16. **Léonard F.** Reduced Joule heating in nanowires // Applied Physics Letters. 2011. Vol. 98. No. 10. P. 103101.

17. **Takahashi T., Kawaguchi K., Sato M., Suhara M., Okamoto N.** Highly sensitive *p*-GaAsSb/*n*-InAs nanowire backward diodes for low-power microwaves// Proceedings of the 49th European Solid-State Device Research Conference (ESSDERC). 23–26 September, 2019. Cracow, Poland. 2019. Pp. 214–217.

18. **Shao Y., Pala M., Esseni D., del Alamo J. A.** Scaling of GaSb/InAs vertical nanowire Esaki diodes down to sub-10-nm diameter // IEEE Transactions on Electron Devices. 2022. Vol. 69. No. 4. Pp. 2188–2195.

19. **Anabestani H., Shazzad R., Fattah M. F. A., Therrien J., Ban D.** Review on GaAsSb nanowire potentials for future 1D heterostructures: Properties and applications // Materials Today Communications. 2021. Vol. 28. September. P. 102542.

20. **Yoshida A., Gamo H., Motohisa J., Tomioka K.** Creation of unexplored tunnel junction by heterogeneous integration of InGaAs nanowires on germanium // Scientific Reports. 2022. Vol. 12. 31 January. P. 1606.

21. **Van Roosbroeck W.** Theory of the flow of electrons and holes in germanium and other semiconductors // Bell System Technical Journal. 1950. Vol. 29. No. 4. Pp. 560–607.

22. **Adachi S.** Properties of group-IV, III–V and II –VI semiconductors. Hoboken, New Jersey, USA: John Wiley & Sons, 2005. 408 p.

23. **Liu K.-M., Cheng C.-P.** Investigation on the effects of gate-source overlap/underlap and source doping gradient of *n*-type Si cylindrical gate-all-around tunnel field-effect transistors // IEEE Transactions on Nanotechnology. 2020. Vol. 19. 07 May. Pp. 382–389.

24. **Eftychis S., Kruse J. E., Tsagaraki K., Koukoula T., Kehagias T., Komninou P., Georgakilas A.** Effects of ultrathin AlN prelayers on the spontaneous growth of GaN nanowires by plasma assisted molecular beam epitaxy // Journal of Crystal Growth. 2019. Vol. 514. 15 May. Pp. 89–97.

25. **Landré O., Bougerol C., Renevier H., Daudin B.** Nucleation mechanism of GaN nanowires grown on (111) Si by molecular beam epitaxy // Nanotechnology. 2009. Vol. 20. No. 41. P. 415602.

26. **Geelhaar L., Chиze C., Jenichen B., et al.** Properties of GaN nanowires grown by molecular beam epitaxy // IEEE Journal of Selected Topics in Quantum Electronics. 2011. Vol. 17. No. 4. Pp. 878–888.

27. **Kumar M. J., Sharma S.** GaAs tunnel diode with electrostatically doped *n*-region: Proposal and analysis // IEEE Transactions on Electron Devices. 2015. Vol. 62. No. 10. Pp. 3445–3448.

28. **Pan J. L., McManis J. E., Grober L., Woodall J. M.** Gallium-arsenide deep-level tunnel diode with record negative conductance and record peak current density // Solid-State Electronics. 2004. Vol. 48. No. 10–11. Pp. 2067–2070.

29. **Ahmed S., Melloch M. R., Harmon E. S., McInturff D. T., Woodall J. M.** Use of nonstoichiometry to form GaAs tunnel junctions // Applied Physics Letters. 1997. Vol. 71. No. 25. Pp. 3667–3669.

30. **Darbandi A., Kavanagh K. L., Watkins S. P.** Lithography-free fabrication of core–shell GaAs nanowire tunnel diodes // Nano Letters. 2015. Vol. 15. No. 8. Pp. 5408–5413.

31. **Chen L., Fung W. Y., Lu W.** Vertical nanowire heterojunction devices based on a clean Si/Ge interface // Nano Letters. 2013. Vol. 13. No. 11. Pp. 5521–5527.

32. **Schmid H., Bessire C., Bjцrk M. T., Schenk A., Riel H.** Silicon nanowire Esaki diodes // Nano Letters. 2012. Vol. 12. No. 2. Pp. 699–703.

33. **Ganjipour B., Dey A. W., Borg B. M., Ek M., Pistol M.-E., Dick K. A., Wernersson L.-E., Thelander C.** High current density Esaki tunnel diodes based on GaSb-InAsSb heterostructure nanowires // Nano Letters. 2011. Vol. 11. No. 10. Pp. 4222–4226.

34. **Shugurov K. Y., Mozharov A. M., Bolshakov A. D., et al.** Hydrogen passivation of the n-GaN nanowire/p-Si heterointerface // Nanotechnology. 2020. Vol. 31. No. 24. P. 244003.

35. **Лебедев А. И.** Физика полупроводниковых приборов. М.: Физматлит, 2008. 488 р.

THE AUTHORS

BARYKIN Dmitrii A.
Alferov University;
Peter the Great St. Petersburg Polytechnic University
8-3 Khlopin St., St. Petersburg, 194021, Russia
d.a.barykin02@mail.ru

SHUGUROV Konstantin Yu.
Alferov University
8-3 Khlopin St., St. Petersburg, 194021, Russia
shugurov17@mail.ru
ORCID: 0000-0001-8973-3187

MOZHAROV Alexey M.
Alferov University
8-3 Khlopin St., St. Petersburg, 194021, Russia
mozharov@spbau.ru
ORCID: 0000-0002-8661-4083

MUKHIN Ivan S.
Peter the Great St. Petersburg Polytechnic University
29 Politechnicheskaya St., St. Petersburg, 195251, Russia
muhin_is@spbstu.ru
ORCID: 0000-0001-9792-045X

СВЕДЕНИЯ ОБ АВТОРАХ

БАРЫКИН Дмитрий Артемович – *лаборант центра приоритетных направлений науки и технологий Академического университета им. Ж. И. Алфёрова РАН, студент Института электроники и телекоммуникаций Санкт-Петербургского политехнического университета Петра Великого.*
194021, Россия, Санкт-Петербург, ул. Хлопина, 8, к. 3
d.a.barykin02@mail.ru

ШУГУРОВ Константин Юрьевич – *кандидат физико-математических наук, младший научный сотрудник лаборатории возобновляемых источников энергии Академического университета им. Ж. И. Алфёрова РАН.*
194021, Россия, Санкт-Петербург, ул. Хлопина, 8, к. 3
shugurov17@mail.ru
ORCID: 0000-0001-8973-3187

МОЖАРОВ Алексей Михайлович – *кандидат физико-математических наук, старший научный сотрудник лаборатории возобновляемых источников энергии Академического университета им. Ж. И. Алфёрова РАН.*
194021, Россия, г. Санкт-Петербург, ул. Хлопина, 8, к. 3
mozharov@spbau.ru
ORCID: 0000-0002-8661-4083

МУХИН Иван Сергеевич – *доктор физико-математических наук, профессор, директор Высшей инженерно-физической школы Санкт-Петербургского политехнического университета Петра Великого.*

195251, Россия, г. Санкт-Петербург, Политехническая ул., 29

muhin_is@spbstu.ru

ORCID: 0000-0001-9792-045X

Received 17.04.2024. Approved after reviewing 21.05.2024. Accepted 21.05.2024.

Статья поступила в редакцию 17.04.2024. Одобрена после рецензирования 21.05.2024. Принята 21.05.2024.

© Peter the Great St. Petersburg Polytechnic University, 2024

Original article
DOI: https://doi.org/10.18721/JPM.17306

A MODEL OF UNSTEADY MECHANODIFFUSION VIBRATIONS OF A RECTANGULAR ORTHOTROPIC TIMOSHENKO PLATE WITH MIXED EDGE FIXING

A. V. Zemskov[1,2]✉, *A. V. Vestyak*[1], *D. V. Tarlakovskii*[1,2]

[1] Moscow Aviation Institute (National Research University), Moscow, Russia;

[2] Lomonosov Moscow State University, Moscow, Russia

✉ azemskov1975@mail.ru

Abstract. In the paper, the coupled elastic-diffusion processes arising as a result of unsteady bending vibrations of an orthotropic plate that has a cantilever fastening on one side and hinged support on the sides adjacent to the cantilever have been analyzed. For a mathematical description of physical and mechanical processes, the Timoshenko plate model supplemented with mass transfer equations taking into account the finite speed of propagation of diffusion flows was used. The solution algorithm was based on the use of the equivalent boundary conditions method allowing to express the solution to the problem posed through a known solution to some auxiliary problem of a given class. The nature of the interaction between mechanical and diffusion fields was simulated using the example of a bendable three-component plate.

Keywords: elastic diffusion, cantilever plate, method of equivalent boundary conditions, Timoshenko plate

Funding: The reported study was funded by Russian Science Foundation (Grant No. 20-19-00217, https://rscf.ru/project/20-19-00217/).

Citation: Zemskov A. V., Vestyak A. V., Tarlakovskii D. V., A model of unsteady mechanodiffusion vibrations of a rectangular orthotropic Timoshenko plate with mixed edge fixing, St. Petersburg State Polytechnical University Journal. Physics and Mathematics. 17 (3) (2024) 57–75. DOI: https://doi.org/10.18721/JPM.17306

This is an open access article under the CC BY-NC 4.0 license (https://creativecommons.org/licenses/by-nc/4.0/)

Научная статья
УДК 539.3
DOI: https://doi.org/10.18721/JPM.17306

МОДЕЛЬ НЕСТАЦИОНАРНЫХ МЕХАНОДИФФУЗИОННЫХ КОЛЕБАНИЙ ПРЯМОУГОЛЬНОЙ ОРТОТРОПНОЙ ПЛАСТИНЫ ТИМОШЕНКО СО СМЕШАННЫМ ЗАКРЕПЛЕНИЕМ ПО КРАЯМ

А. В. Земсков[1,2]✉, *А. В. Вестяк*[1], *Д. В. Тарлаковский*[1,2]

[1] Московский авиационный институт (национальный исследовательский университет), Москва, Россия;

[2] Московский государственный университет им. М. В. Ломоносова, Москва, Россия

✉ azemskov1975@mail.ru

Аннотация. В работе анализируются связанные упругие и диффузионные процессы, возникающие в результате нестационарных изгибных колебаний ортотропной пластины, имеющей консольное закрепление с одной стороны и шарнирное опирание по сторонам, примыкающим к консоли. Для математического описания физико-механических

© Zemskov A. V., Vestyak A. V., Tarlakovskii D. V., 2024. Published by Peter the Great St. Petersburg Polytechnic University.

процессов используется модель пластины Тимошенко, дополненная уравнениями массопереноса с учетом конечной скорости распространения диффузионных потоков. Алгоритм решения основан на использовании метода эквивалентных граничных условий, позволяющего выразить решение поставленной задачи через известное решение некоторой вспомогательной задачи данного класса. На примере изгибаемой трехкомпонентной пластины промоделирован характер взаимодействия в ней механического и диффузионного полей.

Ключевые слова: упругая диффузия, консольно-закрепленная пластина, метод эквивалентных граничных условий, пластина Тимошенко

Финансирование: Исследование выполнено при финансовой поддержке Российского научного фонда (грант № 20-19-00217, https://rscf.ru/project/20-19-00217/).

Ссылка для цитирования: Земсков А. В., Вестяк А. В., Тарлаковский Д. В. Модель нестационарных механодиффузионных колебаний прямоугольной ортотропной пластины Тимошенко со смешанным закреплением по краям // Научно-технические ведомости СПбГПУ. Физико-математические науки. 2024. Т. 17. № 3. С. 57–75. DOI: https://doi.org/10.18721/JPM.17306

Статья открытого доступа, распространяемая по лицензии CC BY-NC 4.0 (https://creativecommons.org/licenses/by-nc/4.0/)

Introduction

The paper considers the interaction of mechanical and diffusion fields appearing in calculations of thin-walled structural elements (beams, plates or shells) operating under unsteady external loads, in the presence of aggressive environments and high temperatures (oil and gas pipelines, heating systems, etc.).

It is known that mechano-diffusion processes are especially pronounced in highly elastic polymers. However, the interaction of mechanical and diffusion fields in such materials is essentially nonlinear, and their description requires models based on relations describing mass transfer processes for arbitrary elastic deformations accounting for the geometric and physical nonlinearity of the material properties [1].

Experimental studies on mechano-diffusion have been widely conducted since the mid-1950s. One of the more in-depth papers on the subject [2] analyzes the effect of deformations on mass transfer in a copper-coated polycrystalline nickel plate with a tensile load applied to its edges. The experiments revealed a significant difference (up to 53%) in the average concentrations in plate thickness in the presence and absence of loads.

Despite persistent interest in elasticity problems accounting for diffusion (as well as temperature and other fields) since the 1950s, relatively few studies dealt with mathematical modeling of mechano-diffusion processes in rods, plates and shells.

Several noteworthy studies [3–9] consider the influence of temperature and diffusion factors on the stress–strain state of a shallow transversally isotropic shell. A variational formulation of the thermodiffusion problem for contacting smooth layered shells is given in [6]. A quasi-static approximation of the axisymmetric stressed state of a heated transversally isotropic spherical shell with a circular hole under diffusion saturation is proposed in [7, 8]. Boundary value problems describing thermo-mechano-diffusion phenomena in Bernoulli–Euler beams and Kirchhoff plates are solved in [9–16].

As evident from this brief overview, the main attention focus was on analysis of quasi-static thermo-mechano-diffusion processes. The unsteady models considered in [11, 14] are only intended for solving problems for Kirchhoff plates [11] and Euler–Bernoulli beams [14].

A model of unsteady elastic diffusion vibrations of the plate is proposed in this paper, based on the Timoshenko hypotheses [17–20].

In view of the known difficulties with solving problems for cantilever beams and plates, it is proposed to use the method of equivalent boundary conditions based on replacing the considered

© Земсков А. В., Вестяк А. В., Тарлаковский Д. В., 2024. Издатель: Санкт-Петербургский политехнический университет Петра Великого.

complex problem with some auxiliary one, which differs from the initial statement only by the boundary conditions. These conditions are selected so that it is possible to obtain an analytical solution to the auxiliary problem, which, in this case, is found using Fourier series and the Laplace transform. Next, relations are constructed coupling the right-hand sides of the boundary conditions of both problems. The solution to the initial problem is expressed in terms the solution to the auxiliary one.

The proposed approach was previously used for solving problems of unsteady elastic diffusion vibrations of cantilever Euler–Bernoulli [21, 22] and Timoshenko [23] beams as well as for simulation of mechano-diffusion processes in cylindrical bodies.

Another practical application is that sensors based on microcantilevers shaped as small beams and plates are widely used for physical, chemical and biological measurements [24–26]. Their operating principle is that the vibration modes of these beams change if a certain mass of matter is adsorbed on their surface. Such devices are widely used in medicine, in particular for diagnostics of diseases, detection of point mutations, monitoring blood glucose levels, etc.

Statement of the main problem

The problem of unsteady vibrations in a rectangular orthotropic multi-component Timoshenko cantilever plate. The sides adjacent to the cantilever are hinge-supported. The plate has dimensions $l_1^* \times l_2^*$ and thickness h^*. Loading and fixing conditions for the edges of the plate are shown in Fig. 1.

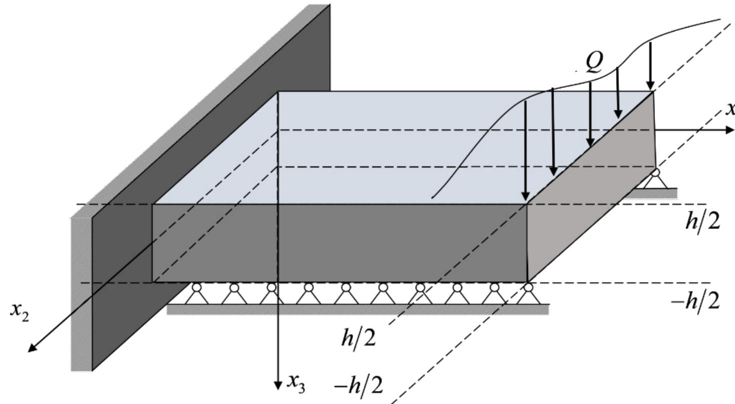

Fig. 1. Statement of main problem:
h is the thickness of the cantilever plate; Q is the transverse force distributed along the free edge

The equation for transverse vibrations of the plate, taking into account diffusion, has the following form [17, 18]:

$$\ddot{\chi}_1 = \frac{\partial^2 \chi_1}{\partial x_1^2} + C_{66}\frac{\partial^2 \chi_1}{\partial x_2^2} + \frac{12C_{55}k_T^2}{h^2}\left(\frac{\partial w}{\partial x_1} - \chi_1\right) + \left(C_{12}+C_{66}\right)\frac{\partial^2 \chi_2}{\partial x_1 \partial x_2} + \sum_{j=1}^{N} \alpha_1^{(j)} \frac{\partial H_j}{\partial x_1},$$

$$\ddot{\chi}_2 = C_{66}\frac{\partial^2 \chi_2}{\partial x_1^2} + C_{22}\frac{\partial^2 \chi_2}{\partial x_2^2} + \frac{12C_{44}k_T^2}{h^2}\left(\frac{\partial w}{\partial x_2} - \chi_2\right) + \left(C_{12}+C_{66}\right)\frac{\partial^2 \chi_1}{\partial x_1 \partial x_2} + \sum_{j=1}^{N} \alpha_2^{(j)} \frac{\partial H_j}{\partial x_2},$$

$$\ddot{w} = C_{55}k_T^2\left(\frac{\partial^2 w}{\partial x_1^2} - \frac{\partial \chi_1}{\partial x_1}\right) + C_{44}k_T^2\left(\frac{\partial^2 w}{\partial x_2^2} - \frac{\partial \chi_2}{\partial x_2}\right),$$

$$\sum_{k=1}^{K} \frac{\tau_q^{k-1}}{(k-1)!}\frac{\partial^k H_q}{\partial \tau^k} = D_1^{(q)}\frac{\partial^2 H_q}{\partial x_1^2} + D_2^{(q)}\frac{\partial^2 H_q}{\partial x_2^2} +$$
$$+\Lambda_{11}^{(q)}\frac{\partial^3 \chi_1}{\partial x_1^3} + \Lambda_{12}^{(q)}\frac{\partial^3 \chi_2}{\partial x_1^2 \partial x_2} + \Lambda_{21}^{(q)}\frac{\partial^3 \chi_1}{\partial x_1 \partial x_2^2} + \Lambda_{22}^{(q)}\frac{\partial^3 \chi_2}{\partial x_2^3}. \quad (1)$$

The dots correspond to the time derivative. All quantities in Eqs. (1) and in Fig. 1 are dimensionless. The following notations are used for them:

$$x_i = \frac{x_i^*}{l},\ w = \frac{w^*}{l},\ \tau = \frac{Ct}{l},\ C_{\alpha\beta} = \frac{C_{\alpha\alpha\beta\beta}}{C_{1111}},\ C_{44} = \frac{C_{2323}}{C_{1111}},\ C_{55} = \frac{C_{1313}}{C_{1111}},\ C_{66} = \frac{C_{1212}}{C_{1111}},$$

$$l_m = \frac{l_m^*}{l},\ m_i = \frac{lm_i^*}{C_{1111}},\ z_q = \frac{lz^{(q)}}{C},\ C^2 = \frac{C_{1111}}{\rho},\ h = \frac{h^*}{l},\ C_{11} = C_{22} = C_{12} + 2C_{66},$$

$$\alpha_i^{(q)} = \frac{\alpha_{ii}^{(q)}}{C_{1111}},\ D_i^{(q)} = \frac{D_{ii}^{(q)}}{Cl},\ \Lambda_{ij}^{(q)} = \frac{m^{(q)} D_{ii}^{(q)} \alpha_{jj}^{(q)} n_0^{(q)}}{\rho R T_0 C l},\ Q = \frac{lQ^*}{C_{1111}},\ \tau_q = \frac{C\tau^{(q)}}{l},$$

where t is the time; x_i^* are the rectangular Cartesian coordinates; w^* is the deflection of the plate; χ_i are the rotation angles of the fiber normal to the mid-surface; l is the characteristic length of the problem; H_q is the concentration increment of the qth material component in the composition of the $(N+1)$-component medium; $n_0^{(q)}$ is the initial concentration of the qth material; C_{ijkl} are the elastic constants; ρ is the density of the plate material; $\alpha_{ij}^{(q)}$ are the coefficients characterizing the relationship between mechanical and diffusion fields; $D_{ij}^{(q)}$ are the diffusion coefficients; R is the universal gas constant; T_0 is the initial temperature of the medium; Q is the transverse force distributed along the free edge $x_1 = l_1$; $\tau^{(q)}$ is the relaxation time of diffusion fluxes [27]; $k_T = \sqrt{5/6}$ is the coefficient taking into account the nonuniform distribution of tangential stresses along the thickness of the plate [19, 28].

Eqs. (1) are supplemented by zero initial conditions and boundary conditions, taking the following form for the case of cantilever support along the edge $x_1 = 0$:

$$w\big|_{x_1=0} = 0,\quad \chi_1\big|_{x_1=0} = 0,\quad H_q\big|_{x_1=0} = 0,\quad \chi_2\big|_{x_1=0} = 0,\quad \chi_2\big|_{x_1=l_1} = 0,$$
$$\left.\left(C_{12}\frac{\partial \chi_1}{\partial x_1} + C_{22}\frac{\partial \chi_2}{\partial x_2} + \sum_{j=1}^{N} \alpha_2^{(j)} H_j\right)\right|_{x_2=0} = 0,\ \left.\left(\frac{\partial \chi_2}{\partial x_1} + \frac{\partial \chi_1}{\partial x_2}\right)\right|_{x_1=l_1} = 0,$$
$$\left.\left(D_1^{(q)}\frac{\partial H_q}{\partial x_1} + \Lambda_{11}^{(q)}\frac{\partial^2 \chi_1}{\partial x_1^2} + \Lambda_{12}^{(q)}\frac{\partial^2 \chi_2}{\partial x_1 \partial x_2}\right)\right|_{x_1=l_1} = 0,\ \left.\left(\frac{\partial w}{\partial x_1} - \chi_1\right)\right|_{x_1=l_1} = \frac{Q}{hC_{55}},$$

$$\left.\left(C_{12}\frac{\partial \chi_1}{\partial x_1} + C_{22}\frac{\partial \chi_2}{\partial x_2} + \sum_{j=1}^{N} \alpha_2^{(j)} H_j\right)\right|_{x_2=l_2} = 0,\ \left.\left(\frac{\partial \chi_1}{\partial x_1} + C_{12}\frac{\partial \chi_2}{\partial x_2} + \sum_{j=1}^{N} \alpha_1^{(j)} H_j\right)\right|_{x_1=l_1} = 0, \tag{2}$$
$$\chi_1\big|_{x_2=0} = 0,\ w\big|_{x_2=0} = 0,\ H_q\big|_{x_2=0} = 0,\ \chi_1\big|_{x_2=l_2} = 0,\ w\big|_{x_2=l_2} = 0,\ H_q\big|_{x_2=l_2} = 0.$$

Formulation and solution of the auxiliary problem

The problem is solved by the method of equivalent boundary conditions [21–23], where instead of problem (1), (2), an auxiliary problem is first considered, described by the same Eqs. (1), but with different boundary conditions (the geometry of the given region is preserved is preserved). These boundary conditions are formulated as follows:

$$w\big|_{x_1=0}=0,\ \chi_1\big|_{x_2=0}=0,\ w\big|_{x_2=0}=0,\ H_q\big|_{x_2=0}=0,\ H_q\big|_{x_1=0}=0,\ \chi_2\big|_{x_1=0}=0,$$

$$\left(C_{12}\frac{\partial\chi_1}{\partial x_1}+C_{22}\frac{\partial\chi_2}{\partial x_2}+\sum_{j=1}^{N}\alpha_2^{(j)}H_j\right)\Bigg|_{x_2=0}=0,\ \left(\frac{\partial\chi_1}{\partial x_1}+C_{12}\frac{\partial\chi_2}{\partial x_2}+\sum_{j=1}^{N}\alpha_1^{(j)}H_j\right)\Bigg|_{x_1=0}=f_2,$$

$$\left(D_1^{(q)}\frac{\partial H_q}{\partial x_1}+\Lambda_{11}^{(q)}\frac{\partial^2\chi_1}{\partial x_1^2}+\Lambda_{12}^{(q)}\frac{\partial^2\chi_2}{\partial x_1\partial x_2}\right)\Bigg|_{x_1=l_1}=0,\ \left(\frac{\partial w}{\partial x_1}-\chi_1\right)\Bigg|_{x_1=l_1}=f_3=\frac{Q}{hC_{55}},\tag{3}$$

$$\left(\frac{\partial\chi_2}{\partial x_1}+\frac{\partial\chi_1}{\partial x_2}\right)\Bigg|_{x_1=l_1}=0,\ \left(C_{12}\frac{\partial\chi_1}{\partial x_1}+C_{22}\frac{\partial\chi_2}{\partial x_2}+\sum_{j=1}^{N}\alpha_2^{(j)}H_j\right)\Bigg|_{x_2=l_2}=0,$$

$$\chi_1\big|_{x_1=l_1}=f_1,\ \chi_1\big|_{x_2=l_2}=0,\ w\big|_{x_2=l_2}=0,\ H_q\big|_{x_2=l_2}=0.$$

Here $f_1(x_2,\tau)$ and $f_2(x_2,\tau)$ are unknown functions to be subsequently determined. The initial conditions remain zero.

The solution of problem (1), (2) is sought in integral form (i = 1,2):

$$\begin{Bmatrix}\chi_i(x_1,x_2,\tau)\\ w(x_1,x_2,\tau)\\ H_q(x_1,x_2,\tau)\end{Bmatrix}=\int_0^{\tau}\int_0^{l_2}\sum_{k=1}^{3}\begin{Bmatrix}G_{ik}(x_1,x_2,\xi,\tau-t)\\ G_{3k}(x_1,x_2,\xi,\tau-t)\\ G_{q+3,k}(x_1,x_2,\xi,\tau-t)\end{Bmatrix}f_k(\xi,t)d\xi dt,\tag{4}$$

where G_{ik} are Green's functions satisfying the initial boundary value problem:

$$\ddot{G}_{1k}=\frac{\partial^2G_{1k}}{\partial x_1^2}+C_{66}\frac{\partial^2G_{1k}}{\partial x_2^2}+\frac{12C_{55}k_T^2}{h^2}\left(\frac{\partial G_{3k}}{\partial x_1}-G_{1k}\right)+$$
$$+\left(C_{12}+C_{66}\right)\frac{\partial^2G_{2k}}{\partial x_1\partial x_2}+\sum_{j=1}^{N}\alpha_1^{(j)}\frac{\partial G_{j+3,k}}{\partial x_1},$$

$$\ddot{G}_{3k}=C_{55}k_T^2\left(\frac{\partial^2G_{3k}}{\partial x_1^2}-\frac{\partial G_{1k}}{\partial x_1}\right)+C_{44}k_T^2\left(\frac{\partial^2G_{3k}}{\partial x_2^2}-\frac{\partial G_{2k}}{\partial x_2}\right),$$

$$\ddot{G}_{2k}=C_{66}\frac{\partial^2G_{2k}}{\partial x_1^2}+C_{22}\frac{\partial^2G_{2k}}{\partial x_2^2}+\frac{12C_{44}k_T^2}{h^2}\left(\frac{\partial G_{3k}}{\partial x_2}-G_{2k}\right)+$$
$$+\left(C_{12}+C_{66}\right)\frac{\partial^2G_{1k}}{\partial x_1\partial x_2}+\sum_{j=1}^{N}\alpha_2^{(j)}\frac{\partial G_{j+3,k}}{\partial x_2},\tag{5}$$

$$\sum_{k=1}^{K}\frac{\tau_q^{k-1}}{(k-1)!}\frac{\partial^kG_{q+3,k}}{\partial\tau^k}=D_1^{(q)}\frac{\partial^2G_{q+3,k}}{\partial x_1^2}+D_2^{(q)}\frac{\partial^2G_{q+3,k}}{\partial x_2^2}+$$
$$+\Lambda_{11}^{(q)}\frac{\partial^3G_{1k}}{\partial x_1^3}+\Lambda_{12}^{(q)}\frac{\partial^3G_{2k}}{\partial x_1^2\partial x_2}+\Lambda_{21}^{(q)}\frac{\partial^3G_{1k}}{\partial x_1\partial x_2^2}+\Lambda_{22}^{(q)}\frac{\partial^3G_{2k}}{\partial x_2^3};$$

$$\left(\frac{\partial G_{1k}}{\partial x_1}+C_{12}\frac{\partial G_{2k}}{\partial x_2}+\sum_{j=1}^{N}\alpha_1^{(j)}G_{j+3,k}\right)\Bigg|_{x_1=0}=\delta_{2k}\delta(\tau)\delta(x_2-\xi),\ G_{3k}\big|_{x_1=0}=0,$$

$$G_{1k}\big|_{x_2=0}=0,\ G_{2k}\big|_{x_1=0}=0,\ G_{q+3,k}\big|_{x_1=0}=0,\ G_{q+3,k}\big|_{x_2=0}=0,\ G_{q+3,k}\big|_{x_2=l_2}=0,$$

$$\left.\left(C_{12}\frac{\partial G_{1k}}{\partial x_1}+C_{22}\frac{\partial G_{2k}}{\partial x_2}+\sum_{j=1}^{N}\alpha_2^{(j)}G_{j+3,k}\right)\right|_{x_2=0}=0,\ G_{3k}\big|_{x_2=0}=0,\ G_{3k}\big|_{x_2=l_2}=0,$$

$$\left.\left(C_{12}\frac{\partial G_{1k}}{\partial x_1}+C_{22}\frac{\partial G_{2k}}{\partial x_2}+\sum_{j=1}^{N}\alpha_2^{(j)}G_{j+3,k}\right)\right|_{x_2=l_2}=0,\ G_{1k}\big|_{x_2=l_2}=0, \tag{6}$$

$$\left.\left(\frac{\partial G_{3k}}{\partial x_1}-G_{1k}\right)\right|_{x_1=l_1}=\delta_{3k}\delta(\tau)\delta(x_2-\xi),\ G_{1k}\big|_{x_1=l_1}=\delta_{1k}\delta(\tau)\delta(x_2-\xi),$$

$$\left.\left(D_1^{(q)}\frac{\partial G_{q+3,k}}{\partial x_1}+\Lambda_{11}^{(q)}\frac{\partial^2 G_{1k}}{\partial x_1^2}+\Lambda_{12}^{(q)}\frac{\partial^2 G_{2k}}{\partial x_1\partial x_2}\right)\right|_{x_1=l_1}=0,\ \left.\left(\frac{\partial G_{1k}}{\partial x_2}+\frac{\partial G_{2k}}{\partial x_1}\right)\right|_{x_1=l_1}=0.$$

Using the Laplace transform and Fourier series expansion, problem (5), (6) is reduced to a system of linear algebraic equations:

$$k_{1nm}(s)G_{1knm}^L(\xi,s)+K_{nm}G_{2knm}^L(\xi,s)-C_{55}k_T^2\lambda_nG_{3knm}^L(\xi,s)-$$
$$-\lambda_n\sum_{q=1}^{N}\alpha_1^{(q)}G_{q+3,knm}^L(\xi,s)=F_{1knm}(\xi),$$
$$K_{nm}G_{1knm}^L(\xi,s)+k_{2nm}(s)G_{2knm}^L(\xi,s)-C_{44}k_T^2\mu_mG_{3knm}^L(\xi,s)-$$
$$-\mu_m\sum_{q=1}^{N}\alpha_2^{(q)}G_{q+3,knm}^L(\xi,s)=F_{2knm}(\xi), \tag{7}$$
$$-C_{55}k_T^2\lambda_nG_{1knm}^L(\xi,s)-C_{44}k_T^2\mu_mG_{2knm}^L(\xi,s)+k_3(s)G_{3knm}^L(\xi,s)=F_{3knm}(\xi),$$
$$k_{q+3,nm}(s)G_{q+3,knm}^L(\xi,s)-M_{1qnm}G_{1knm}^L(\xi,s)-M_{2qnm}G_{2knm}^L(\xi,s)=F_{q+3,knm}(\xi),$$

where the following notations are used:

$$k_{1nm}(s)=s^2+\frac{12}{h^2}C_{55}k_T^2+\lambda_n^2+C_{66}\mu_m^2,\ k_{2nm}(s)=s^2+\frac{12}{h^2}C_{44}k_T^2+C_{66}\lambda_n^2+C_{22}\mu_m^2,$$
$$k_{3nm}(s)=s^2+C_{55}k_T^2\lambda_n^2+C_{44}k_T^2\mu_m^2,\ K_{nm}=(C_{12}+C_{66})\lambda_n\mu_m,$$

$$M_{1qnm}=\lambda_n\left(\Lambda_{11}^{(q)}\lambda_n^2+\Lambda_{21}^{(q)}\mu_m^2\right),M_{2qnm}=\mu_m\left(\Lambda_{12}^{(q)}\lambda_n^2+\Lambda_{22}^{(q)}\mu_m^2\right),$$

$$F_{1knm}(\xi)=\frac{4}{l_1l_2}\left[\lambda_n(-1)^n\delta_{1k}-\delta_{2k}\right]\sin\mu_m\xi,\ k_{q+3,nm}(s)=\sum_{k=0}^{K-1}\frac{\tau_q^k}{k!}s^{k+1}+D_1^{(q)}\lambda_n^2+D_2^{(q)}\mu_m^2,$$
$$F_{2knm}(\xi)=\frac{4}{l_1l_2}C_{12}\mu_m(-1)^n\delta_{1k}\sin\mu_m\xi,\ F_{3knm}(\xi)=\frac{4}{l_1l_2}C_{55}k_T^2(-1)^n\delta_{3k}\sin\mu_m\xi,$$
$$F_{q+3,knm}(\xi)=\frac{4}{l_1l_2}\Lambda_{11}^{(q)}\lambda_n\left[\delta_{2k}-\lambda_n(-1)^n\delta_{1k}\right]\sin\mu_m\xi,\ \lambda_n=\frac{\pi}{l_1}\left(n+\frac{1}{2}\right),\ \mu_m=\frac{\pi m}{l_2};$$

$$\begin{Bmatrix}G_{1k}^L(x_1,x_2,\xi,s)\\G_{2k}^L(x_1,x_2,\xi,s)\\G_{pk}^L(x_1,x_2,\xi,s)\end{Bmatrix}=\sum_{n=0}^{\infty}\sum_{m=1}^{\infty}\begin{Bmatrix}G_{1knm}^L(\xi,s)\cos\lambda_nx_1\sin\mu_mx_2\\G_{2knm}^L(\xi,s)\sin\lambda_nx_1\cos\mu_mx_2\\G_{pknm}^L(\xi,s)\sin\lambda_nx_1\sin\mu_mx_2\end{Bmatrix},\ p\ge 3. \tag{8}$$

Solving system (7), we obtain:

$$G_{iknm}^{L}(\xi,s)=G_{iknm}^{Ls}(s)\sin\mu_m\xi,\ G_{iknm}^{Ls}(s)=\frac{P_{iknm}(s)}{P_{nm}(s)}\quad(i=1,2),$$
$$G_{3knm}^{L}(\xi,s)=\frac{F_{3knm}(\xi)}{k_{3nm}(s)}+G_{3knm}^{Ls}(s)\sin\mu_m\xi,\ G_{3knm}^{Ls}(s)=\frac{P_{3knm}(s)}{Q_{0nm}(s)},\tag{9}$$
$$G_{q+3,knm}^{L}(\xi,s)=\frac{F_{q+3,knm}(\xi)}{k_{q+3,nm}(s)}+G_{q+3,knm}^{Ls}(s)\sin\mu_m\xi,\ G_{q+3,knm}^{Ls}(s)=\frac{P_{q+3,knm}(s)}{Q_{qnm}(s)}.$$

Here $P_{iknm}(s)$, $P_{nm}(s)$, and $Q_{pnm}(s)$ are polynomials with respect to *s*, taking the form

$$\begin{aligned}P_{nm}(s)=&\left[k_{1nm}(s)S_{1nm}(s)+k_{2nm}(s)S_{2nm}(s)-K_{nm}S_{3nm}(s)\right]\Pi_{nm}(s)+\\&+\left[\frac{12}{h^2}K_{nm}C_{44}C_{55}k_T^4\mu_m\lambda_n-k_{1nm}(s)k_{2nm}(s)k_{3nm}(s)\right]\Pi_{nm}(s)-\\&-\mu_mS_{2nm}(s)\sum_{j=1}^{N}\alpha_2^{(j)}M_{2jnm}\Pi_{jnm}(s)-\lambda_nS_{1nm}(s)\sum_{j=1}^{N}\alpha_1^{(j)}M_{1jnm}\Pi_{jnm}(s)+\\&+S_{3nm}(s)\sum_{j=1}^{N}\left(\mu_m\alpha_2^{(j)}M_{1j}+\lambda_n\alpha_1^{(j)}M_{2j}\right)\Pi_{jnm}(s)+\\&+\lambda_n\mu_mk_{3nm}(s)\sum_{j=1}^{N}\sum_{i=1}^{N}M_{1i}M_{2j}\mathrm{A}_{ij}\Pi_{ijnm}(s),\end{aligned}\tag{10}$$

$$\Pi_{nm}(s)=\prod_{q=1}^{n}k_{q+3,nm}(s),\quad\Pi_{inm}(s)=\prod_{q=1,q\neq i}^{n}k_{q+3,nm}(s),$$

$$\Pi_{ijnm}(s)=\prod_{q=1,q\neq i,j}^{n}k_{q+3,nm}(s),\quad\Pi_{ijnm}(s)=\Pi_{jinm}(s),$$

$$Q_{0nm}(s)=k_{3nm}(s)P_{nm}(s),\quad Q_{qnm}(s)=k_{q+3,nm}(s)P_{nm}(s),$$

$$P_{3knm}(\xi,s)=C_{55}k_T^2\lambda_nP_{1knm}(\xi,s)+C_{44}k_T^2\mu_mP_{2knm}(\xi,s),$$
$$P_{q+3,knm}(\xi,s)=M_{1qnm}P_{1knm}(\xi,s)+M_{2qnm}P_{2knm}(\xi,s),$$

$$\begin{aligned}P_{11nm}(s)=&\frac{4}{l_1l_2}\lambda_n(-1)^n\left[S_{1nm}(s)\Pi_{nm}(s)-\mu_mk_{3nm}(s)\sum_{j=1}^{N}\alpha_2^{(j)}M_{2jnm}\Pi_{jnm}(s)\right]-\\&-\frac{4}{l_1l_2}C_{12}\mu_m(-1)^n\left[S_{3nm}(s)\Pi_{nm}(s)-\lambda_nk_{3nm}(s)\sum_{j=1}^{N}\alpha_1^{(j)}M_{2jnm}\Pi_{jnm}(s)\right]-\\&-\frac{4}{l_1l_2}\lambda_n^2(-1)^n\left[\lambda_nS_{1nm}(s)\sum_{j=1}^{N}\alpha_1^{(j)}\Lambda_{11}^{(j)}\Pi_{jnm}(s)-\mu_mS_{3nm}(s)\sum_{j=1}^{N}\alpha_2^{(j)}\Lambda_{11}^{(j)}\Pi_{jnm}(s)\right]+\\&+\frac{4}{l_1l_2}(-1)^n\lambda_n^3\mu_mk_{3nm}(s)\sum_{j=1}^{N}\sum_{i=1}^{N}\mathrm{A}_{ji}\Lambda_{11}^{(j)}M_{2j}\Pi_{jinm}(s),\end{aligned}$$

$$P_{12nm}(\xi,s) = -\frac{4}{l_1 l_2}\left[S_{1nm}(s)\Pi_{nm}(s) - \mu_m k_{3nm}(s)\sum_{j=1}^{N}\alpha_2^{(j)} M_{2jnm}\Pi_{jnm}(s)\right] +$$

$$+\frac{4}{l_1 l_2}\lambda_n\left[\lambda_n S_{1nm}(s)\sum_{j=1}^{N}\alpha_1^{(j)}\Lambda_{11}^{(j)}\Pi_{jnm}(s) - \mu_m S_{3nm}(s)\sum_{j=1}^{N}\alpha_2^{(j)}\Lambda_{11}^{(j)}\Pi_{jnm}(s)\right] +$$

$$+\frac{4}{l_1 l_2}\lambda_n^2\mu_m k_{3nm}(s)\sum_{j=1}^{N}\sum_{i=1}^{N}\mathrm{A}_{ij}\Lambda_{11}^{(j)} M_{2jnm}\Pi_{ijnm}(s),$$

$$P_{13nm}(s) = \frac{4}{l_1 l_2}\frac{12}{h^2}C_{55}k_T^2(-1)^n\left[S_{4nm}(s)\Pi_{nm}(s) - \lambda_n\mu_m\sum_{j=1}^{N}\mathrm{A}_j M_{2jnm}\Pi_{jnm}(s)\right],$$

$$P_{21nm}(s) = -\frac{4}{l_1 l_2}\lambda_n(-1)^n\left[S_{3nm}(s)\Pi_{nm}(s) - \mu_m k_{3nm}(s)\sum_{j=1}^{N}\alpha_2^{(j)} M_{1jnm}\Pi_{jnm}(s)\right] +$$

$$+\frac{4}{l_1 l_2}C_{12}\mu_m(-1)^n\left[S_{2nm}(s)\Pi_{nm}(s) - \lambda_n k_{3nm}(s)\sum_{j=1}^{N}\alpha_1^{(j)} M_{1jnm}\Pi_{jnm}(s)\right] -$$

$$-\frac{4}{l_1 l_2}\lambda_n^2(-1)^n\left[\mu_m S_{2nm}(s)\sum_{j=1}^{N}\alpha_2^{(j)}\Lambda_{11}^{(j)}\Pi_{jnm}(s) - \lambda_n S_{3nm}(s)\sum_{j=1}^{N}\alpha_1^{(j)}\Lambda_{11}^{(j)}\Pi_{jnm}(s)\right] -$$

$$-\frac{4}{l_1 l_2}(-1)^n\lambda_n^3\mu_m k_{3nm}(s)\sum_{j=1}^{N}\sum_{i=1}^{N}\mathrm{A}_{ji}\Lambda_{11}^{(j)} M_{1jnm}\Pi_{jinm}(s),$$

$$P_{23nm}(s) = \frac{4}{l_1 l_2}\frac{12}{h^2}C_{55}k_T^2(-1)^n\left[S_{5nm}(s)\Pi_{nm}(s) + \lambda_n\mu_m\sum_{j=1}^{N}\mathrm{A}_j M_{1j}\Pi_{jnm}(s)\right],$$

$$P_{22nm}(s) = \frac{4}{l_1 l_2}\left[S_{3nm}(s)\Pi_{nm}(s) - \mu_m k_{3nm}(s)\sum_{j=1}^{N}\alpha_2^{(j)} M_{1j}\Pi_{jnm}(s)\right] +$$

$$+\frac{4}{l_1 l_2}\lambda_n\left[\mu_m S_{2nm}(s)\sum_{j=1}^{N}\alpha_2^{(j)}\Lambda_{11}^{(j)}\Pi_{jnm}(s) - \lambda_n S_{3nm}(s)\sum_{j=1}^{N}\alpha_1^{(j)}\Lambda_{11}^{(j)}\Pi_{jnm}(s)\right] +$$

$$+\frac{4}{l_1 l_2}\lambda_n^2\mu_m k_{3nm}(s)\sum_{j=1}^{N}\sum_{i=1}^{N}\mathrm{A}_{ji}\Lambda_{11}^{(j)} M_{1jnm}\Pi_{jinm}(s),$$

$$S_{1nm}(s) = k_{2nm}(s)k_{3nm}(s) - \frac{12}{h^2}C_{44}^2 k_T^4\mu_m^2,\ \ \mathrm{A}_{ji} = \alpha_1^{(j)}\alpha_2^{(i)} - \alpha_2^{(j)}\alpha_1^{(i)},$$

$$S_{2nm}(s) = k_{1nm}(s)k_{3nm}(s) - \frac{12}{h^2}C_{55}^2 k_T^4\lambda_n^2,\ \ \mathrm{A}_j = k_T^2\left(C_{55}\alpha_2^{(j)} - C_{44}\alpha_1^{(j)}\right),$$

$$S_{3nm}(s) = K_{nm}k_{3nm}(s) - \frac{12}{h^2}C_{44}C_{55}k_T^4\mu_m\lambda_n,$$

$$S_{4nm}(s) = k_T^2\left[C_{55}\lambda_n k_{2nm}(s) - K_{nm}C_{44}\mu_m\right],\ S_{5nm}(s) = k_T^2\left[k_{1nm}(s)C_{44}\mu_m - K_{nm}C_{55}\lambda_n\right].$$

The transition to the Laplace space of initial values for rational functions $G_{pknm}^{Ls}(s)$ defined by equalities (9) is carried out by subtractions and tables of operational calculus [29]. Numerical analysis shows that these functions have only prime poles. Therefore, their initial values are written as follows:

$$S_{4nm}(s)=k_T^2\left[C_{55}\lambda_n k_{2nm}(s)-K_{nm}C_{44}\mu_m\right],\ S_{5nm}(s)=k_T^2\left[k_{1nm}(s)C_{44}\mu_m-K_{nm}C_{55}\lambda_n\right].$$

$$G_{iknm}^s(\tau)=\sum_{j=1}^{\Sigma}A_{iknm}^{(j)}e^{s_{jnm}\tau}\quad \left(\Sigma=(K+1)N+K+5,\ i=1,2,\ q=\overline{1,N},\ k=\overline{1,3}\right),$$

$$G_{3knm}^s(\tau)=\sum_{j=1}^{\Sigma+2}A_{3knm}^{(j)}e^{s_{jnm}\tau}+\frac{4C_{55}k_T^2(-1)^n\delta_{3k}}{l_1l_2}\sum_{j=\Sigma+1}^{\Sigma+2}\frac{e^{s_{jnm}\tau}}{k'_{3nm}\left(s_{jnm}\right)},$$

$$G_{q+3,knm}^s(\tau)=\sum_{j=1}^{\Sigma}A_{q+3,knm}^{(j)}e^{s_{jnm}\tau}+\sum_{j=1}^{K+1}A_{q+3,knm}^{(\Sigma+j)}e^{\gamma_{jnm}^{(q)}\tau}+$$

$$+\frac{4\Lambda_{11}^{(q)}\lambda_n\left[\delta_{2k}-\lambda_n(-1)^n\delta_{1k}\right]}{l_1l_2}\sum_{j=1}^{2}\frac{e^{\gamma_{jnm}^{(q)}\tau}}{k'_{j+3,nm}\left(\gamma_{jnm}^{(q)}\right)}, \tag{11}$$

$$A_{iknm}^{(j)}=\frac{P_{iknm}\left(s_{jnm}\right)}{P'_{nm}\left(s_{jnm}\right)},\quad A_{3knm}^{(r)}=\frac{P_{iknm}\left(s_{rnm}\right)}{Q'_{0nm}\left(s_{rnm}\right)}\quad \left(j=\overline{1,\Sigma},\ r=\overline{1,\Sigma+2}\right),$$

$$A_{q+3,kl}^{(j)}=\frac{P_{q+3,knm}\left(s_{jnm}\right)}{Q'_{qnm}\left(s_{jnm}\right)},\quad A_{q+3,knm}^{(\Sigma+i)}=\frac{P_{q+3,knm}\left(\gamma_{jnm}^{(q)}\right)}{Q'_{qnm}\left(\gamma_{jnm}^{(q)}\right)}, \tag{12}$$

where s_{jnm}, $j=\overline{1,\Sigma}$ are the zeros of the polynomial $P_{nm}(s)$; $\gamma_{jnm}^{(q)}$ are the zeros of the polynomial $k_{q+3,nm}(s)$; $s_{\Sigma+i,nm}$ are the zeros of the polynomial $k_{3nm}(s)$, found by the formulas

$$s_{\Sigma+1,nm}=-ik_T\sqrt{C_{55}\lambda_n^2+C_{44}\mu_m^2},\ s_{\Sigma+2,nm}=ik_T\sqrt{C_{55}\lambda_n^2+C_{44}\mu_m^2}.$$

Thus, taking into account solutions (8) and (9), the Green functions of auxiliary problem (1), (2) have the form

$$G_{1k}(x_1,x_2,\xi,\tau)=\sum_{n=0}^{\infty}\sum_{m=1}^{\infty}G_{1knm}^s(\tau)\cos\lambda_n x_1\sin\mu_m x_2\sin\mu_m\xi,\ \lambda_n=\frac{\pi}{l_1}\left(n+\frac{1}{2}\right),$$

$$G_{2k}(x_1,x_2,\xi,\tau)=\sum_{n=0}^{\infty}\sum_{m=1}^{\infty}G_{1knm}^s(\tau)\sin\lambda_n x_1\cos\mu_m x_2\sin\mu_m\xi,\ \mu_m=\frac{\pi m}{l_2}, \tag{13}$$

$$G_{pk}(x_1,x_2,\xi,\tau)=\sum_{n=0}^{\infty}\sum_{m=1}^{\infty}G_{pknm}^s(\tau)\sin\lambda_n x_1\sin\mu_m x_2\sin\mu_m\xi,\quad p\geq 3,$$

where the functions $G_{lknm}^s(\tau)$ are found by Eqs. (11) and (12).

Assuming that $\alpha_i^{(q)}=0$ in Eqs. (10), we obtain Green's functions for the elastic Timoshenko plate.

Solution of the main problem

Next, we substitute the solution of problem (1), (3) into boundary conditions (2). As a result, we arrive at a system of integral equations relative to the functions $f_1(x_2,\tau)$ and $f_2(x_2,\tau)$, introduced into boundary conditions (3):

$$\int_0^\tau\int_0^{l_2}\sum_{k=1}^{2} G_{1k}\left(0,x_2,\xi,\tau-t\right) f_k\left(\xi,t\right)d\xi dt=-\int_0^\tau\int_0^{l_2} G_{13}\left(0,x_2,\xi,\tau-t\right) f_3\left(\xi,t\right)d\xi dt,$$

$$\begin{gathered}\int_0^\tau\int_0^{l_2}\sum_{k=1}^{2}\left[\frac{\partial G_{1k}\left(l_1,x_2,\xi,\tau-t\right)}{\partial x_1}+C_{12}\frac{\partial G_{2k}\left(l_1,x_2,\xi,\tau-t\right)}{\partial x_2}\right] f_k\left(\xi,t\right)d\xi dt+\\ +\int_0^\tau\int_0^{l_2}\sum_{k=1}^{2}\sum_{j=1}^{N}\alpha_1^{(j)}G_{j+3,k}\left(l_1,x_2,\xi,\tau-t\right) f_k\left(\xi,t\right)d\xi dt=\\ =-\int_0^\tau\int_0^{l_2}\left[\frac{\partial G_{13}\left(l_1,x_2,\xi,\tau-t\right)}{\partial x_1}+C_{12}\frac{\partial G_{23}\left(l_1,x_2,\xi,\tau-t\right)}{\partial x_2}\right] f_3\left(\xi,t\right)d\xi dt-\\ -\int_0^\tau\int_0^{l_2}\sum_{j=1}^{N}\alpha_1^{(j)}G_{j+3,3}\left(l_1,x_2,\xi,\tau-t\right) f_3\left(\xi,t\right)d\xi dt.\end{gathered}\tag{14}$$

Based on the form of Green's functions (13), the external load $f_3\left(x_2,\tau\right)$ is represented as a series

$$f_3\left(x_2,\tau\right)=\sum_{m=1}^{\infty} f_{3m}\left(\tau\right)\sin\mu_m x_2.\tag{15}$$

We search for functions $f_k\left(x_2,\tau\right)$ $\left(k=1,2\right)$ in similar form:

$$f_k\left(x_2,\tau\right)=\sum_{m=1}^{\infty} f_{km}\left(\tau\right)\sin\mu_m x_2.\tag{16}$$

If we substitute series (15) and functions (16) into system (14), then we arrive at a system of first-kind Volterra integral equations:

$$\sum_{j=1}^{2}\int_0^\tau a_{ijm}\left(\tau-t\right) f_{jm}\left(t\right)dt=\varphi_{im}\left(\tau\right),\tag{17}$$

where the following notations are used:

$$a_{11m}\left(\tau\right)=\sum_{n=0}^{\infty}G_{11mn}^{s}\left(\tau\right),\ a_{12m}\left(\tau\right)=\sum_{n=0}^{\infty}G_{12mn}^{s}\left(\tau\right),$$

$$\begin{gathered}a_{21m}\left(\tau\right)=\sum_{n=0}^{\infty}\left(-1\right)^n\left[-C_{12}\mu_m G_{21mn}^{s}\left(\tau\right)-\lambda_n G_{11mn}^{s}\left(\tau\right)+\sum_{j=1}^{N}\alpha_1^{(j)}G_{j+3,1mn}^{s}\left(\tau\right)\right],\\ a_{22m}\left(\tau\right)=\sum_{n=0}^{\infty}\left(-1\right)^n\left[-C_{12}\mu_m G_{22mn}^{s}\left(\tau\right)-\lambda_n G_{12mn}^{s}\left(\tau\right)+\sum_{j=1}^{N}\alpha_1^{(j)}G_{j+3,2mn}^{s}\left(\tau\right)\right],\end{gathered}\tag{18}$$

$$\begin{gathered}\varphi_{1m}\left(\tau\right)=-\int_0^\tau\sum_{n=0}^{\infty}G_{13mn}^{s}\left(\tau-t\right) f_{3m}\left(t\right)dt,\\ \varphi_{2m}\left(\tau\right)=\int_0^\tau\sum_{n=0}^{\infty}\left(-1\right)^n\left[C_{12}\mu_m G_{23mn}^{s}\left(\tau-t\right)+\lambda_n G_{13mn}^{s}\left(\tau-t\right)\right] f_{3m}\left(t\right)dt-\\ -\int_0^\tau\sum_{n=0}^{\infty}\left(-1\right)^n\sum_{j=1}^{N}\alpha_1^{(j)}G_{j+3,3mn}^{s}\left(\tau-t\right) f_{3m}\left(t\right)dt.\end{gathered}$$

Integration by parts reduces system (17) to

$$\sum_{j=1}^{2}\int_{0}^{\tau} A_{ijm}\left(\tau-t\right)\frac{\partial f_{jm}^{*}\left(t\right)}{\partial t}dt=\varphi_{im}\left(\tau\right),\quad A_{ijm}\left(\tau\right)=\int_{0}^{\tau} a_{ijm}\left(t\right)dt \tag{19}$$

so that it is subsequently solved numerically. Integrals in system (19) are approximated by the midpoint rectangle rule [21–23]:

$$\int_{0}^{t_k} A_{ijm}\left(t_k-t\right)\frac{\partial f_{jm}^{*}\left(t\right)}{\partial t}dt=h_t A_{ij}^{(1/2)} y_{jm}^{(k-1/2)}+h_t S_{ijm}^{(k-1/2)},$$

where $h_t = \tau/N_t$ is the partitioning step, N_t is the number of partition points on the segment $[0,\tau]$. The remaining quantities are determined as

$$\begin{gathered} t_k=kh_t,\ t_{k-1/2}=\left(k-\frac{1}{2}\right)h_t,\ S_{ijm}^{(k-1/2)}=\sum_{r=1}^{k-1} A_{ij}^{(k-r+1/2)} y_{jm}^{(r-1/2)}, \\ y_{jm}^{(k)}=\frac{\partial f_{jm}^{*}\left(t_k\right)}{\partial \tau},\ y_{jm}^{(k-1/2)}=\frac{\partial f_{jm}^{*}\left(t_k-t_{1/2}\right)}{\partial \tau},\ A_{ijm}^{(k)}=A_{ijm}\left(t_k\right)\quad \left(k=\overline{0,N_t}\right). \end{gathered} \tag{20}$$

Thus, system of integral equations (19) is reduced to a sequence of systems of linear algebraic equations

$$\mathbf{A}_m\mathbf{y}_m^{(k-1/2)}=\mathbf{b}_m^{(k-1/2)},\ \mathbf{A}_m=\begin{pmatrix} A_{11m}^{(1/2)} & A_{12m}^{(1/2)} \\ A_{21m}^{(1/2)} & A_{22m}^{(1/2)} \end{pmatrix},\ \mathbf{y}_m^{(k-1/2)}=\begin{pmatrix} y_{1m}^{(k-1/2)} \\ y_{2m}^{(k-1/2)} \end{pmatrix},$$

$$\mathbf{b}_m^{(k-1/2)}=\begin{pmatrix} b_{1m}^{(k-1/2)} \\ b_{2m}^{(k-1/2)} \end{pmatrix},\ b_{im}^{(k-1/2)}=\frac{1}{h_t}\left(\varphi_{im}\left(t_k\right)-h_t S_{i1m}^{(k-1/2)}-h_t S_{i2m}^{(k-1/2)}\right),$$

whose solutions are found by Cramer's rule:

$$y_{1m}^{(k-1/2)}=\frac{b_{1m}^{(k-1/2)}A_{22m}^{(1/2)}-b_{2m}^{(k-1/2)}A_{12m}^{(1/2)}}{A_{11m}^{(1/2)}A_{22m}^{(1/2)}-A_{12m}^{(1/2)}A_{21m}^{(1/2)}},\ y_{2m}^{(k-1/2)}=\frac{b_{2m}^{(k-1/2)}A_{11m}^{(1/2)}-b_{1m}^{(k-1/2)}A_{21m}^{(1/2)}}{A_{11m}^{(1/2)}A_{22m}^{(1/2)}-A_{12m}^{(1/2)}A_{21m}^{(1/2)}}. \tag{21}$$

Now, if we represent convolutions (4) as

$$\begin{gathered} \begin{Bmatrix} \chi_i\left(x_1,x_2,t_j\right) \\ w\left(x_1,x_2,t_j\right) \\ H_q\left(x_1,x_2,t_j\right) \end{Bmatrix}=\int_0^{t_j}\int_0^{l_2}\begin{Bmatrix} G_{i3}\left(x_1,x_2,\xi,t_j-t\right) \\ G_{33}\left(x_1,x_2,\xi,t_j-t\right) \\ G_{q+3,3}\left(x_1,x_2,\xi,t_j-t\right) \end{Bmatrix} f_3\left(\xi,t\right)d\xi dt+ \\ +h_t\int_0^{l_2}\sum_{m=1}^{\infty}\sum_{n=0}^{\infty}\sum_{k=1}^{2}\sum_{l=1}^{j}\begin{Bmatrix} \tilde{G}_{iknm}\left(t_{j-l+1/2}\right)\cos\lambda_n x_1\sin\mu_m x_2 \\ \tilde{G}_{3knm}\left(t_{j-l+1/2}\right)\sin\lambda_n x_1\cos\mu_m x_2 \\ \tilde{G}_{q+3,knm}\left(t_{j-l+1/2}\right)\sin\lambda_n x_1\sin\mu_m x_2 \end{Bmatrix} y_{km}^{(l-1/2)}\sin\mu_m\xi d\xi, \end{gathered} \tag{22}$$

$$\tilde{G}_{pknm}\left(\tau\right)=\int_0^{\tau} G_{pknm}^{s}\left(t\right)dt$$

and substitute equalities (21) there, we obtain a solution to the initial problem (1), (2) on bending of the Timoshenko cantilever plate.

Passage to the limit to the steady-state problem

If we impose for boundary conditions (3) that

$$f_k(\tau) = \tilde{f}_k H(\tau) \ (k = 1,2), \ f_3(\tau) = \tilde{f}_3 H(\tau)$$

($H(\tau)$ is the Heaviside function), and pass to the limit at $\tau \to \infty$, we obtain a solution to the problem of bending in the plate exposed to static load applied to the free edge.

The Green functions $G_{mk}^{(st)}(x_1, x_2, \xi)$ of the static problem are expressed in terms of the Green functions $G_{mk}(x_1, x_2, \xi, \tau)$ of the dynamic problem using the relations given in [22, 30]:

$$\begin{gathered} G_{mk}^{(st)}(x_1, x_2, \xi,) = \lim_{\tau\to\infty}\left[G_{mk}(x_1, x_2, \xi, \tau) * H(\tau)\right] = \\ = \lim_{s\to 0}\left[sG_{mk}^L(x_1, x_2, \xi, s)\frac{1}{s}\right] = \lim_{s\to 0} G_{mk}^L(x_1, x_2, \xi, s), \end{gathered} \tag{23}$$

where the asterisk indicates the time convolution.

By carrying out this passage to the limit in convolutions (4), we obtain a solution to the steady-state problem in the form

$$\begin{Bmatrix} \chi_i^{(st)}(x_1, x_2, \tau) \\ w^{(st)}(x_1, x_2, \tau) \\ H_q^{(st)}(x_1, x_2, \tau) \end{Bmatrix} = \int_0^{l_2} \sum_{k=1}^{3} \begin{Bmatrix} G_{ik}^{(st)}(x_1, x_2, \xi) \\ G_{3k}^{(st)}(x_1, x_2, \xi) \\ G_{q+3,k}^{(st)}(x_1, x_2, \xi) \end{Bmatrix} \tilde{f}_k(\xi) d\xi, \tag{24}$$

where

$$\begin{gathered} G_{1k}^{(st)}(x_1, x_2, \xi) = \sum_{n=0}^{\infty}\sum_{m=1}^{\infty} G_{1knm}^{Ls}(0)\cos\lambda_n x_1 \sin\mu_m x_2 \sin\mu_m \xi, \ \lambda_n = \frac{\pi}{l_1}\left(n + \frac{1}{2}\right), \\ G_{2k}^{(st)}(x_1, x_2, \xi) = \sum_{n=0}^{\infty}\sum_{m=1}^{\infty} G_{2knm}^{Ls}(0)\sin\lambda_n x_1 \cos\mu_m x_2 \sin\mu_m \xi, \ \mu_m = \frac{\pi m}{l_2}, \\ G_{pk}^{(st)}(x_1, x_2, \xi) = \sum_{n=0}^{\infty}\sum_{m=1}^{\infty} G_{pknm}^{Ls}(0)\sin\lambda_n x_1 \sin\mu_m x_2 \sin\mu_m \xi, \quad p \ge 3. \end{gathered} \tag{25}$$

Relation (8) and solution (9) are taken into account here.

The static analogue of system of equations (17) is written as

$$\sum_{j=1}^{2} \tilde{a}_{ijm} \tilde{f}_{jm} = \tilde{\varphi}_{im}. \tag{26}$$

Similar to notations in (18), the following notation is introduced in Eq. (26):

$$\begin{gathered} \tilde{a}_{11m} = \sum_{n=0}^{\infty} G_{11nm}^{Ls}(0), \ \tilde{a}_{12m} = \sum_{n=0}^{\infty} G_{12nm}^{Ls}(0), \\ \tilde{a}_{21m} = \sum_{n=0}^{\infty} (-1)^n \left[-C_{12}\mu_m G_{21nm}^{Ls}(0) - \lambda_n G_{11nm}^{Ls}(0) + \sum_{j=1}^{N} \alpha_1^{(j)} G_{q+3,1nm}^{Ls}(0)\right], \\ \tilde{a}_{22m} = \sum_{n=0}^{\infty} (-1)^n \left[-C_{12}\mu_m G_{22nm}^{Ls}(0) - \lambda_n G_{12nm}^{Ls}(0) + \sum_{j=1}^{N} \alpha_1^{(j)} G_{q+3,2nm}^{Ls}(0)\right], \end{gathered}$$

$$\tilde{\varphi}_{1m} = -\sum_{n=0}^{\infty} G_{13mn}^{Ls}(0) f_{3m}, \quad \tilde{f}_k(\xi) = \sum_{m=1}^{\infty} \tilde{f}_{km} \sin \mu_m \xi,$$

$$\tilde{\varphi}_{2m} = \sum_{n=0}^{\infty} (-1)^n \left[C_{12}\mu_m G_{23mn}^{Ls}(0) + \lambda_n G_{13mn}^{Ls}(0) - \sum_{j=1}^{N} \alpha_1^{(j)} G_{j+3,3mn}^{Ls}(0) \right] \tilde{f}_{3m}.$$

The solution of system (26) is found by Eq. (21). The following correspondences are used in this case:

$$y_{im}^{(k-1/2)} \leftrightarrow \tilde{f}_{jm},\ A_{ijm}^{(1/2)} \leftrightarrow \tilde{a}_{ijm},\ b_{im}^{(k-1/2)} \leftrightarrow \tilde{\varphi}_{im}.$$

Computational example

To simulate physical and mechanical processes, let us take a three-component plate ($N = 2$), consisting of an alloy of aluminum, zinc and copper (it is assumed that zinc and copper diffuse in duralumin). The characteristics of the plate and the required external conditions are given in Table.

Table

Computational parameters and their values [30]

Parameter	Notation	Unit	Value
Elastic constants	C_{1122}	N/m^2	$6.93\cdot10^{10}$
	$C_{1313} = C_{2323} = C_{1212}$		$2.56\cdot10^{10}$
Density of material	ρ	kg/m^3	2700
Characteristic length of problem	$l \times h^*$ $(l = h^*)$	m	$5.0\cdot10^{4}$
Initial concentration			
zinc	$n_0^{(1)}$	–	0.0084
copper	$n_0^{(2)}$		0.0450
Initial ambient temperature	T_0	K	700
Coefficients of diffusion	$D_{11}^{*(1)} = D_{22}^{*(1)}$	m^2/s	$2.62\cdot10^{-12}$
	$D_{11}^{*(2)} = D_{22}^{*(2)}$		$2.89\cdot10^{-15}$
Molar mass			
zinc	$m^{(1)}$	kg/mol	0.027
copper	$m^{(2)}$		0.064
Field coupling coefficients	$\alpha_{11}^{*(1)} = \alpha_{22}^{*(1)}$	J/kg	$1.55\cdot10^{7}$
	$\alpha_{11}^{*(2)} = \alpha_{22}^{*(2)}$		$6.14\cdot10^{7}$

We assume that the plate has the following dimensions: $l_1^* = 0.01$ m, $l_2^* = 0.01$ m, $h^* = 0.0005$ m. The load on the free edge $x_1 = l_1$ is set in the following form:

$$f_3(x_2, \tau) = -\varepsilon H(\tau) \sin x_2,\ \varepsilon = 10^{-3}. \tag{27}$$

Substituting data from (27) into equality (22), taking into account the found Green functions (13) and functions $\partial f_{km}(\tau)/\partial\tau$ from (21), we obtain plate deflections, rotations of normal fibers and concentration increments for zinc and copper. The results of the calculations are shown in Figs. 2–4.

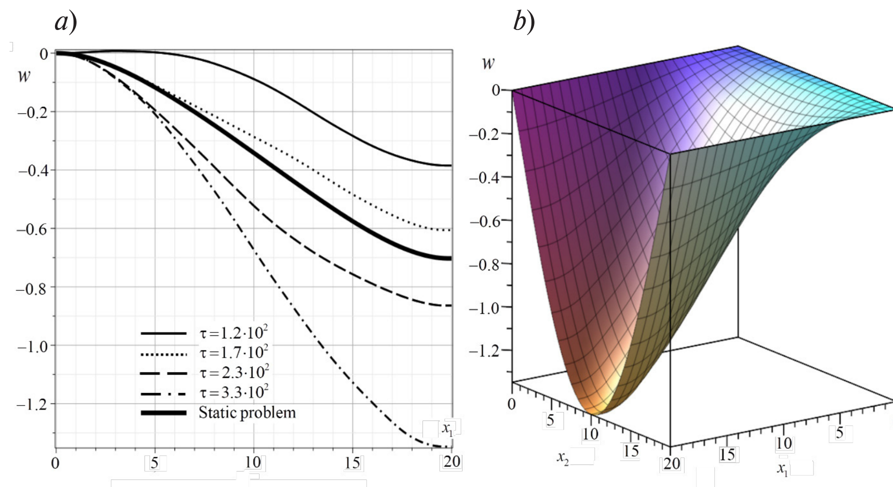

Fig. 2. Calculated distributions of plate deflections w on the plane (*a*) and in space (*b*): from the fixed end ($x_1 = 0$) to the free end ($x_1 = l_1$ is the load application point) at different time instants (*a*); at time $\tau = 3.3{\cdot}10^2$ ($2.66{\cdot}10^5$ s) (*b*)

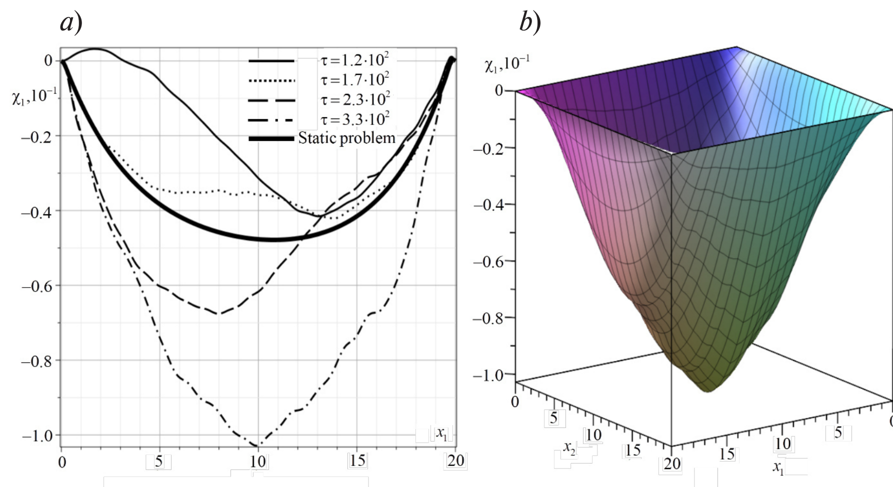

Fig. 3. Calculated distributions of rotations χ_1 in normal fiber on the plane (*a*) and in space (*b*): from the fixed end ($x_1 = 0$) to the free end ($x_1 = l_1$) at different time instants (*a*); at the time $\tau = 3.3{\cdot}10^2$ ($2.66{\cdot}10^5$ s) (*b*)

We used 40 terms of the Fourier series and 40 partition points for solving integral equation (19) to calculate unsteady mechanical fields. Numerical calculations show that an increase in these parameters does not lead to visible changes in the results obtained. For example, the difference between the 20th and 40th terms of the series is less than 1% for plate deflections, and about 3% for rotations of normal fibers. Steady diffusion fields were calculated using 100 terms of the Fourier series.

Comparing the results for the elastic diffusion model and the elastic model (for $\alpha_{ij}^{*(q)} = 0$) for the calculations of bending in the Timoshenko cantilever plate, we find that the effect of mass transfer on the mechanical field of the plate is negligible in the given time range. Thus, the graphs in Fig. 2 and 3 are equally applicable for both elastic and elastic diffusion problems. On the other hand, the deflections and rotations of normal fibers under unsteady loads are about twice as large as those under static loads (shown by bold lines in Figs. 2 and 3).

In particular, the considered passages to the limit for the elastic and static models serve to verify the algorithm proposed in the study for solving the unsteady problem for the Timoshenko cantilever plate. The solution of the steady-state problem is analytical, which is also very important for estimating the accuracy of the performed calculation.

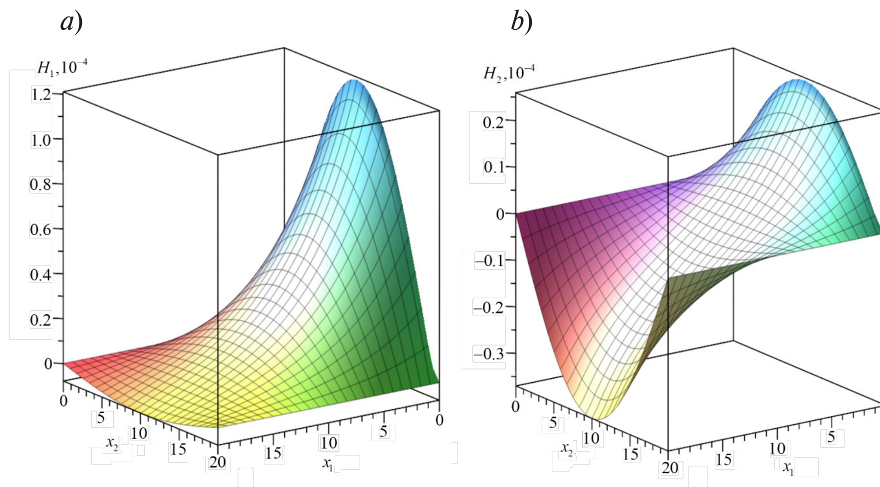

Fig. 4. Calculated steady-state diffusion fields reflecting spatial distributions of concentration increments for zinc (*a*) and copper (*b*)

Fig. 4 shows the steady-state diffusion fields of zinc and copper in the composition of the given alloy, initiated by bending deformations of the plate. At a given unsteady load (27), these are the limit values for the concentration increments of diffusing materials at $\tau \to \infty$.

The concentration increments found are very small, which is confirmed by experimental studies [31], according to which the effect of mechanical loads on the diffusion field becomes pronounced mainly during plastic deformations. Thus, elastic deformations have little effect on the kinetics of mass transfer.

Earlier numerical studies considered the case of hinge-supported beams [32], confirming that diffusion starts to affect the displacement field after a certain period of time, manifesting primarily as phase shifts of elastic and elastic diffusion vibrations relative to each other. However, these differences are observed over a time range significantly exceeding that shown in Figs. 2 and 3. In this case, calculations require a manifold increase in the number of partition points used to solve integral equation (19), which significantly increases the computational complexity of the algorithm and can be realistically achieved only in cases where the problem can be solved analytically, such as in [32].

Conclusion

We proposed a model of unsteady mechano-diffusion vibrations of a Timoshenko cantilever plate with hinged support on the sides adjacent to the cantilever. We developed a complex algorithm combining variable separation and equivalent boundary conditions, yielding a solution to the corresponding initial boundary value problem. The proposed algorithm was verified based on the limiting transition to the elastic problem for a bendable Timoshenko plate, along with the comparison with the solution of the steady-state elastic diffusion problem.

The calculation performed for the case of a three-component plate makes it possible to simulate the interaction of mechanical and diffusion fields in a bendable plate. It was found that unsteady bending of the console initiates diffusion fluxes in each of the components. The intensity of the resulting mass transfer is extremely low and essentially does not produce a reverse effect on the mechanical fields in the bendable plate, which is verified by comparing the obtained solution with the solution of the elastic problem for the Timoshenko plate.

REFERENCES

1. **Denisyuk E. Ya., Tereshatov V. V.,** A nonlinear theory of the process of elastomer swelling in low molecular-mass liquids, Polymer Sci. Ser. A. 42 (1) (2000) 56–67.

2. **Mikolajchuk M. A., Knyazeva A. G, Grabovetskaya G. P., Mishin I. P.,** Research of the stress influence on the diffusion in the coating plate, Bulletin of Perm National Research Polytechnic University. Mechanics. (3) (2012) 120–134 (in Russian).

3. **Flyachok V. M., Shvets R. N.,** Nekotoryye teoremy teorii mekhanodiffuzii anizotropnykh obolochek [Some theorems of the theory of mechanodiffusion of anisotropic shells], Math. Meth. & Phys. Mech. Fields. (21) (1985) 32–37 (in Russian).

4. **Shvets R. N., Flyachok V. M.,** Uravneniya mekhanodiffuzii anizotropnykh obolochek s uchetom poperechnykh deformatsiy [Mechanodiffusion equations of taking into account the transverse strains], Math.Meth.& Phys. Mech. Fields. (20) (1984) 54–61 (in Russian).

5. **Shvets R. N., Flyachok V. M.,** Variatsionnyy podkhod k resheniyu dinamicheskikh zadach mekhanotermodiffuzii anizotropnykh obolochek [A variational approach to solving dynamic problems of mechanothermal diffusion of anisotropic shells], Math. Phys.& Nonlinear Mech. (16) (1991) 54–6. 39–43 (in Russian).

6. **Ravrik M. S.,** Ob odnoy variatsionnoy formule smeshannogo tipa dlya kontaktnykh zadach termodiffuziynoy teorii deformatsii sloistykh obolochek [On one variational formula of mixed type for contact problems in the thermal diffusion theory of deformation of layered shells], Math. Meth. & Phys. Mech. Fields. (22) (1985) 40–44 (in Russian).

7. **Bhattacharya D., Kanoria M.,** The influence of two temperature generalized thermoelastic diffusion inside a spherical shell, Int. J. Eng. Tech. Res. 2 (5) (2014) 151–159.

8. **Ravrik M. S., Bichuya A. L.,** Osesimmetrichnoye napryazhennoye sostoyaniye nagretoy transversalno-izotropnoy sfericheskoy obolochki s krugovym otverstiyem pri diffuzionnom nasyshchenii [Axisymmetric stressed state of the heated transversally isotropic spherical shell with a circular hole under diffusion saturation], Math.Meth.& Phys. Mech. Fields. (17) (1983) 51–54 (in Russian).

9. **Aouadi M., Copetti M. I. M.,** A dynamic contact problem for a thermoelastic diffusion beam with the rotational inertia, Appl. Numer. Math. 126 (April) (2018) 113–137.

10. **Aouadi M., Copetti M. I. M.,** Exponential stability and numerical analysis of a thermoelastic diffusion beam with rotational inertia and second sound, Math. Comput. Simulat. 187 (Sept) (2021) 586–613.

11. **Aouadi M., Miranville A.,** Smooth attractor for a nonlinear thermoelastic diffusion thin plate based on Gurtin – Pipkin's model, Asymptot. Anal. 95 (1–2) (2015) 129–160.

12. **Shevchuk P. R., Shevchuk V. A.** Mekhanodiffuzionnyy effekt pri izgibe dvukhsloynogo brusa [Mechanodiffusion effect under bending of a double-layer beam], Phys. Chem. Mech. Mater. 23 (6) (1987) 75–79 (in Russian).

13. **Huang M., Wei P., Zhao L., Li Y.,** Multiple fields coupled elastic flexural waves in the thermoelastic semiconductor microbeam with consideration of small scale effects, Compos. Struct. 270 (15 Aug) (2021) 114104.

14. **Kumar R., Devi S., Sharma V.,** Resonance of nanoscale beam due to various sources in modified couple stress thermoelastic diffusion with phase lags, Mech. Eng. 23 (July) (2019) 36–49.

15. **Aouadi M.,** On thermoelastic diffusion thin plate theory, Appl. Math. Mech. (Eng. Ed.). 36 (5) (2015) 619–632.

16. **Aouadi M., Miranville A.,** Quasi-stability and global attractor in nonlinear thermoelastic diffusion plate with memory, Evol. Equ. Control Theory. 4 (3) (2015) 241–263.

17. **Zemskov A. V., Tarlakovskii D. V., Grigorevskiy N. V.,** Modeling an unsteady elastic diffusion processes in a Timoshenko plate, Proc. IX Int. Conf. on Comput. Meth. Coupl. Probl. Sci. Eng. (Coupled Problems 2021), Chia Laguna, Italy, 13–16 June 2021, DOI: 10.23967/coupled.2021.034.

18. **Vestyak V. A., Zemskov A. V., Tarlakovskii D. V.,** Modeling of unsteady elastic diffusion transverse vibrations of the isotropic simply supported Timoshenko plate, Mater. Phys. Mech. 50 (1) (2022) 141–157.

19. **Le K. C.,** Vibrations of shells and rods, Springer-Verlag, Berlin, 1999.

20. **Le K. C.,** An asymptotically exact theory of functionally graded piezoelectric shells, Int. J. Eng. Sci. 112 (March) (2017) 42–62.

21. **Zemskov A. V., Tarlakovskii D. V., Faykin G. M.,** Unsteady bending of a cantilevered Euler – Bernoully beam with diffusion, Comput. Continuum Mech. 14 (1) (2021) 40–50.

22. **Zemskov A. V., Tarlakovskii D. V., Faykin G. M.,** Unsteady bending of the orthotropic cantilever Bernoulli – Euler beam with the relaxation of diffusion fluxes, Z. Angew. Math. Mech. 102 (10) (2022) e202100107.

23. **Zemskov A. V., Tarlakovskii D. V.,** Unsteady bending of an orthotropic cantilever Timoshenko beam with allowance for diffusion flux relaxation, Comput. Math. Math. Phys. 62 (11) (2022) 1895–1911.

24. **Kim B. H., Mader O., Weimar U., et al.,** Detection of antibody peptide interaction using microcantilevers as surface stress sensors, J. Vac. Sci. Technol. B. 21 (4) (2003) 1472–1475.

25. **Alvarez M., Calle A., Tamayo J., et al.,** Development of nanomechanical biosensors for detection of the pesticide DDT, Biosens. Bioelectron. 18 (5–6) (2003) 649–653.

26. **Chen G. Y., Thundat T., Wachter E. A., Warmack R. J.,** Adsorption-induced surface stress and its effects on resonance frequency of microcantilevers, J. Appl. Phys. 77 (8) (1995) 3618–3622.

27. **Keller I. E., Dudin D. S.,** Mekhanika sploshnoy sredy. Zakony sokhraneniya [Continuum mechanics. Conservation laws], Perm National Research Polytechnic University Publishing, Perm, 2022 (in Russian).

28. **Mikhaylova E. Yu., Tarlakovskii D. V., Fedotenkov G. V.** Obshchaya teoriya uprugikh obolochek [General theory of elastic shells], MAI Publishing, Moscow, 2018 (in Russian).

29. **Ditkin V. A., Prudnikov A. P.,** Spravochnik po operatsionnomu ischisleniyu [Operational calculus handbook], Vysshaya Shkola Publishing, Moscow, 1965 (in Russian).

30. **Babichev A. P., Babushkina N. A., Bratkovskiy A. M., et al.,** Fizicheskiye velichiny: Spravochnik [Physical quantities: Handbook], Energoatomizdat Publishing, Moscow, 1991 (in Russian).

31. **Nirano K., Cohen M., Averbach V., Ujiiye N.,** Self-diffusion in alpha iron during compressive plastic flow, Trans. Metallurg. Soc. AIME. 227 (1963) 950.

32. **Zemskov A. V., Le V. H.,** Unsteady thermoelastic diffusion vibrations of the Bernoulli – Euler beam under the action of a distributed transverse load, Bulletin of Perm National Research Polytechnic University. Mechanics. (3) (2023) 75–85.

СПИСОК ЛИТЕРАТУРЫ

1. **Денисюк Е. Я., Терешатов В. В.** Нелинейная теория процессов набухания эластомеров в низкомолекулярных жидкостях // Высокомолекулярные соединения А. 2000. Т. 42. № 1. С. 71–83.

2. **Миколайчук М. А., Князева А. Г, Грабовецкая Г. П., Мишин И. П.** Изучение влияния механических напряжений на диффузию в пластине с покрытием // Вестник Пермского национального исследовательского политехнического университета (ПНИПУ). 2012. № 3. С. 120–134.

3. **Флячок В. М., Швец Р. Н.** Некоторые теоремы теории механодиффузии анизотропных оболочек // Математические методы и физико-механические поля. 1985. № 21. С. 32–37.

4. **Швец Р. Н., Флячок В. М.** Уравнения механодиффузии анизотропных оболочек с учетом поперечных деформаций // Математические методы и физико-механические поля. 1984. № 20. С. 54–61.

5. **Швец Р. Н., Флячок В. М.** Вариационный подход к решению динамических задач механотермодиффузии анизотропных оболочек // Математическая физика и нелинейная механика. 1991. № 16. С. 39–43.

6. **Раврик М. С.** Об одной вариационной формуле смешанного типа для контактных задач термодиффузийной теории деформации слоистых оболочек // Математические методы и физико-механические поля. 1985. № 22. С. 40–44.

7. **Bhattacharya D., Kanoria M.** The influence of two temperature generalized thermoelastic diffusion inside a spherical shell // International Journal of Engineering and Technical Research. 2014. Vol. 2. No. 5. Pp. 151–159.

8. **Раврик М. С., Бичуя А. Л.** Осесимметричное напряженное состояние нагретой трансверсально-изотропной сферической оболочки с круговым отверстием при диффузионном насыщении // Математические методы и физико-механические поля. 1983. № 17. С. 51–54.

9. **Aouadi M., Copetti M. I. M.** A dynamic contact problem for a thermoelastic diffusion beam with the rotational inertia // Applied Numerical Mathematics. 2018. Vol. 126. April. Pp. 113–137.

10. **Aouadi M., Copetti M. I. M.** Exponential stability and numerical analysis of a thermoelastic diffusion beam with rotational inertia and second sound // Mathematics and Computers in Simulation. 2021. Vol. 187. September. Pp. 586–613.

11. **Aouadi M., Miranville A.** Smooth attractor for a nonlinear thermoelastic diffusion thin plate based on Gurtin – Pipkin's model // Asymptotic Analysis. 2015. Vol. 95. No.1–2. Pp. 129–160.

12. **Шевчук П. Р., Шевчук В. А.** Механодиффузионный эффект при изгибе двухслойного бруса // Физико-химическая механика материалов. 1987. Т. 23. № 6. С. 75–79.

13. **Huang M., Wei P., Zhao L., Li Y.** Multiple fields coupled elastic flexural waves in the thermoelastic semiconductor microbeam with consideration of small scale effects // Composite Structures. 2021. Vol. 270. 15 August. P. 114104.

14. **Kumar R., Devi S., Sharma V.** Resonance of nanoscale beam due to various sources in modified couple stress thermoelastic diffusion with phase lags // Mechanical and Mechanics Engineering. 2019. Vol. 23. July. Pp. 36–49.

15. **Aouadi M.** On thermoelastic diffusion thin plate theory // Applied Mathematics and Mechanics (English Edition). 2015. Vol. 36. No. 5. Pp. 619–632.

16. **Aouadi M., Miranville A.** Quasi-stability and global attractor in nonlinear thermoelastic diffusion plate with memory // Evolution Equations and Control Theory. 2015. Vol. 4. No. 3. Pp. 241–263.

17. **Zemskov A. V., Tarlakovskii D. V., Grigorevskiy N. V.** Modeling an unsteady elastic diffusion processes in a Timoshenko plate // Proceedings of the IX International Conference on Computational Methods for Coupled Problems in Science and Engineering (Coupled Problems 2021).13–16 June 2021, Chia Laguna, Italy. DOI: 10.23967/coupled.2021.034.

18. **Vestyak V. A., Zemskov A. V., Tarlakovskii D. V.** Modeling of unsteady elastic diffusion transverse vibrations of the isotropic simply supported Timoshenko plate // Materials Physics and Mechanics. 2022. Vol. 50. No. 1. Pp. 141–157.

19. **Le K. C.** Vibrations of shells and rods. Berlin: Springer-Verlag, 1999. 425 p.

20. **Le K. C.** An asymptotically exact theory of functionally graded piezoelectric shells // International Journal of Engineering Science. 2017. Vol. 112. March. Pp. 42–62.

21. **Земсков А. В., Тарлаковский Д. В., Файкин Г. М.** Нестационарный изгиб консольно-закрепленной балки Бернулли – Эйлера с учетом диффузии // Вычислительная механика сплошных сред. 2021. Т. 14. № 1. С. 40–50.

22. **Zemskov A. V., Tarlakovskii D. V., Faykin G. M.** Unsteady bending of the orthotropic cantilever Bernoulli – Euler beam with the relaxation of diffusion fluxes // Zeitzschrift für Angewandte Mathematik und Mechanik. 2022. Vol. 102. No. 10. P. e202100107.

23. **Земсков А. В., Тарлаковский Д. В.** Нестационарный изгиб ортотропной консольно-закрепленной балки Тимошенко с учетом релаксации диффузионных потоков // Журнал вычислительной математики и математической физики. 2022. Т. 62. № 11. С. 1895–1911.

24. **Kim B. H., Mader O., Weimar U., Brock R., Kern D. P.** Detection of antibody peptide interaction using microcantilevers as surface stress sensors // Journal of Vacuum Science & Technology B. 2003. Vol. 21. No. 4. Pp. 1472–1475.

25. **Alvarez M., Calle A., Tamayo J., Lechuga L. M., Abad A., Montoya A.** Development of nanomechanical biosensors for detection of the pesticide DDT // Biosensors and Bioelectronics. 2003. Vol. 18. No. 5–6. Pp. 649–653.

26. **Chen G.Y., Thundat T., Wachter E. A., Warmack R. J.** Adsorption-induced surface stress and its effects on resonance frequency of microcantilevers // Journal of Applied Physics. 1995. Vol. 77. No. 8. Pp. 3618–3622.

27. **Келлер И. Э., Дудин Д. С.** Механика сплошной среды. Законы сохранения. Пермь: Изд-во Пермского национального исследовательского политехнического университета, 2022. 142 с.

28. **Михайлова Е. Ю., Тарлаковский Д. В., Федотенков Г. В.** Общая теория упругих оболочек. М.: Изд-во МАИ, 2018. 112 с.

29. **Диткин В. А., Прудников А. П.** Справочник по операционному исчислению. М.: Высшая школа, 1965. 568 с.

30. **Бабичев А. П., Бабушкина Н. А., Братковский А. М.** Физические величины: Справочник. М.: Энергоатомиздат, 1991. 1232 с.

31. **Nirano K., Cohen M., Averbach V., Ujiiye N.** Self-diffusion in alpha iron during compressive plastic flow // Transactions of the Metallurgical Society of AIME. 1963. Vol. 227. P. 950.

32. **Земсков А. В., Ле В. Х.** Нестационарные термоупругодиффузионные колебания балки Бернулли – Эйлера под действием распределенной поперечной нагрузки // Вестник Пермского национального исследовательского политехнического университета (ПНИПУ). Механика. 2023. № 3. С. 75–85.

THE AUTHORS

ZEMSKOV Andrei V.
Moscow Aviation Institute (National Research University)
Institute of Mechanics, Lomonosov Moscow State University
4 Volokolamskoe Ave., Moscow, 125993, Russia
azemskov1975@mail.ru
ORCID: 0000-0002-2653-6378

VESTYAK Anatoly V.
Moscow Aviation Institute (National Research University)
4 Volokolamskoe Ave., Moscow, 125993, Russia
kaf311@yandex.ru
ORCID: 0000-0002-1905-9438

TARLAKOVSKII Dmitry V.
Institute of Mechanics, Lomonosov Moscow State University
Moscow Aviation Institute (National Research University)
1 Leninskie Gory, Moscow, 119991, Russia
tdvhome@mail.ru
ORCID: 0000-0002-5694-9253

СВЕДЕНИЯ ОБ АВТОРАХ

ЗЕМСКОВ Андрей Владимирович – *доктор физико-математических наук, профессор, ведущий научный сотрудник научно-исследовательского отдела кафедры 311 Московского авиационного института (национальный исследовательский университет), ведущий научный сотрудник лаборатории динамических испытаний* Научно-исследовательского института *механики Московского государственного университета имени М. В. Ломоносова.*
125993, Россия, г. Москва, Волоколамское шоссе, 4
azemskov1975@mail.ru
ORCID: 0000-0002-2653-6378

ВЕСТЯК Анатолий Васильевич – *кандидат физико-математических наук, доцент кафедры 311 Московского авиационного института (национальный исследовательский университет).*
125993, Россия, г. Москва, Волоколамское шоссе, 4
kaf311@yandex.ru
ORCID: 0000-0002-1905-9438

ТАРЛАКОВСКИЙ Дмитрий Валентинович – *доктор физико-математических наук, заведующий лабораторией динамических испытаний Научно-исследовательского института механики Московского государственного университета имени М. В. Ломоносова, профессор кафедры 902 «Сопротивление материалов, динамика и прочность машин» Московского авиационного института (национальный исследовательский университет).*
119991, Россия, г. Москва, Ленинские Горы, 1
tdvhome@mail.ru
ORCID: 0000-0002-5694-9253

Received 27.03.2024. Approved after reviewing 21.05.2024. Accepted 21.05.2024.
Статья поступила в редакцию 27.03.2024. Одобрена после рецензирования 21.05.2024. Принята 21.05.2024.

© Peter the Great St. Petersburg Polytechnic University, 2024

PHYSICAL MATERIALS TECHNOLOGY

Original article
DOI: https://doi.org/10.18721/JPM.17307

ELECTRICAL AND OPTICAL PROPERTIES OF A NANOCOMPOSITE BASED ON POLYVINYL ALCOHOL AND FULLERENOL

E. A. Nikitina✉, *V. M. Kapralova, N. T. Sudar, V. M. Studzinskii, V. I. Gerasimov*

Peter the Great St. Petersburg Polytechnic University, St. Petersburg, Russia

✉ eanikitina26@icloud.com

Abstract. This work presents the results of comparison of optical properties at room temperature and electrical characteristics of films of polyvinyl alcohol (PVA) and nanocomposite based on PVA with small additives of fullerenol $C_{60}(OH)_{44}$ in a wide frequency range (25 Hz – 1 MHz) at temperatures from 294 to 398 K. The addition of 2 wt.% fullerenol leads to a significant absorption of light by such a film in the UV region of the spectrum (IR spectra of both film samples were identical), as well as to a decrease in dielectric permittivity ε'. The ε'' frequency dependences of both films showed peaks in the low-frequency region, which shifted towards higher frequencies when the films were heated. The values of the activation energy of conduction at direct current for PVA and polymer nanocomposite were found to be about 1.5 eV. An explanation of the observed effects is proposed.

Keywords: polyvinyl alcohol, fullerenol, nanocomposite, dielectric constant, dielectric loss

Funding: The reported study was carried out within the framework of the State Assignment for Fundamental Research (Subject Code FSEG-2023-0016).

Citation: Nikitina E. A., Kapralova V. M., Sudar N. T., Studzinskii V. M., Gerasimov V. I., Electrical and optical properties of a nanocomposite based on polyvinyl alcohol and fullerenol, St. Petersburg State Polytechnical University Journal. Physics and Mathematics. 17 (3) (2024) 76–86. DOI: https://doi.org/10.18721/JPM.17307

This is an open access article under the CC BY-NC 4.0 license (https://creativecommons.org/licenses/by-nc/4.0/)

Научная статья
УДК 564.163.2, 539.199
DOI: https://doi.org/10.18721/JPM.17307

ЭЛЕКТРИЧЕСКИЕ И ОПТИЧЕСКИЕ СВОЙСТВА НАНОКОМПОЗИТНОГО МАТЕРИАЛА НА ОСНОВЕ ПОЛИВИНИЛОВОГО СПИРТА И ФУЛЛЕРЕНОЛА

Е. А. Никитина✉, *В. М. Капралова, Н. Т. Сударь, В. М. Студзинский, В. И. Герасимов*

Санкт-Петербургский политехнический университет Петра Великого, Санкт-Петербург, Россия

✉ eanikitina26@icloud.com

Аннотация. В работе представлены результаты сравнения оптических свойств при комнатной температуре и электрических характеристик пленок поливинилового спирта (ПВС) и нанокомпозита на основе ПВС с малыми добавками фуллеренола $C_{60}(OH)_{44}$

© Nikitina E. A., Kapralova V. M., Sudar N. T., Studzinskii V. M., Gerasimov V. I., 2024. Published by Peter the Great St. Petersburg Polytechnic University.

в широком частотном диапазоне (25 Гц – 1 МГц) при температурах от 294 до 398 К. Установлено, что добавка 2 масс.% фуллеренола приводит к значительному поглощению такой пленкой света в УФ-области спектра (ИК-спектры обоих образцов пленок оказались идентичными), а также к снижению диэлектрической проницаемости ε′. На частотных зависимостях ε″ обеих пленок наблюдались пики в низкочастотной области, которые смещались в сторону высоких частот при нагреве пленок. Найденные значения энергии активации проводимости на постоянном токе для ПВС и полимерного нанокомпозита составили около 1,5 эВ. Предложено объяснение наблюдаемых эффектов.

Ключевые слова: поливиниловый спирт, фуллеренол, нанокомпозит, диэлектрическая проницаемость, диэлектрические потери

Финансирование: Работа выполнена в рамках Государственного задания на проведение фундаментальных исследований (код темы FSEG-2023-0016).

Ссылка для цитирования: Никитина Е. А., Капралова В. М., Сударь Н. Т., Студзинский В. М., Герасимов В. И. Электрические и оптические свойства нанокомпозитного материала на основе поливинилового спирта и фуллеренола // Научно-технические ведомости СПбГПУ. Физико-математические науки. 2024. Т. 17. № 3. С. 76–86. DOI: https://doi.org/10.18721/JPM.17307

Статья открытого доступа, распространяемая по лицензии CC BY-NC 4.0 (https://creativecommons.org/licenses/by-nc/4.0/)

Introduction

Inorganic metal oxides and semiconductors are most often used in organic field-effect transistors (OFETs) as gate dielectrics [1], which significantly complicates their manufacturing technology and limits the applicability of printing techniques used for production of these OFETs. Therefore, replacing inorganic dielectric films in these transistors with polymer dielectrics that can be obtained by solution-casting remains a major challenge [2].

It is suggested that polymer nanocomposite materials can meet such criteria [3–5]. The diverse range of water-soluble polymer nanocomposites are of particular interest. For instance, polyvinyl alcohol (PVA) and composites based on it show promise as materials for organic electronics [6–9].

PVA whose monomer unit has the formula $(CH(OH)-CH_2)_n-$ is a water-soluble thermoplastic polymer with good film-forming characteristics. The glass transition temperature of this polymer is $T_g \approx 358$ K, but it is also a crystallizing polymer (melting point in a nitrogen medium is 503 K). Due to the large number of hydrogen bonds, PVA molecules form dense crystallites randomly oriented inside amorphous regions [10].

The dielectric properties of PVA are fairly well-studied [11–15]. The dielectric permittivity shows significant dispersion in the low-frequency region of the spectrum under heating. The low-frequency dielectric permittivity ε in PVA reaches values of the order of 10^2 at $T \geq T_g$, while $\varepsilon \approx 6$ at a high frequency [11]. The frequency dependence of the dielectric loss tangent tgδ in PVA is characterized by the presence of a peak in the low-frequency region of the spectrum, whose location depends on temperature and shifts to higher frequencies under heating of the sample.

It is hypothesized that the cause for this behavior of the dielectric properties of PVA is the interphase polarization effect. It is suggested in [11] that it occurs due to blocking of charge carriers at the electrodes, leading to the formation of a double electric layer at the electrode–polymer interface. A more complex picture is considered in [12], supposing that the two structural phases with differing electrical characteristics in PVA are macromolecular globules and the boundaries between them. The study concludes that structures consisting of grains separated by barrier layers (Koops model [16]) can be produced in PVA. The combination of such identical structures acting as macro-relaxors determines the overall properties of the sample. However, the authors of the above studies do not provide any quantitative estimates.

Adding a small amount of carbon nanoparticles to polymer matrices (up to 1–3 wt%) can dramatically modify the properties of the matrix material (see, for example, [17, 18]). Such polymer nanocomposites have broad applications in organic electronics [19].

© Никитина Е. А., Капралова В. М., Сударь Н. Т., Студзинский В. М., Герасимов В. И., 2024. Издатель: Санкт-Петербургский политехнический университет Петра Великого.

This paper considers the properties of polymer nanocomposite films based on PVA and polyhydroxylated fullerene (fullerenol) $C_{60}(OH)_{44}$ as filler (PVA + $C_{60}(OH)_{44}$ composite) were studied. Like PVA, fullerenol $C_{60}(OH)_{44}$ is highly soluble in water, allowing to use this modification of fullerene as one of the components for water-soluble nanocomposite dielectrics. Its concentration in the PVA matrix can be used to purpose, it is possible to tailor the electrical characteristics of the resulting composite material.

There is no information in the literature on the electrophysical and dielectric properties of such composites. Dielectric spectroscopy is commonly used to study the dielectric characteristics in wide temperature and frequency ranges, providing data about the morphological structure of matter through its relaxation properties associated with molecular dynamics [20].

The goal of our study was to obtain the characteristics of conductivity and dielectric properties of the PVA + $C_{60}(OH)_{44}$ composite, analyzing their specifics to identify the types of interaction of the matrix with the filler in the given material.

Experimental procedure

The experimental samples were films prepared from PVA and PVA + $C_{60}(OH)_{44}$ nanocomposite with a thickness of 60–70 μm. Grade 16/1 PVA (GOST 10779-78) was used for to manufacture the films.

A 5 wt% PVA solution was poured onto the bottom of Petri dishes, dried at room temperature for four days, after which the films were separated from the substrate. To prepare PVA + $C_{60}(OH)_{44}$ nanocomposite films, an aqueous solution of fullerenol was gradually added to the PVA solution so that the concentration of $C_{60}(OH)_{44}$ in PVA + $C_{60}(OH)_{44}$ films was 2 wt%. Fullerenol was produced by the technique described in [21].

The optical properties of the films were studied at room temperature. An SF-56 spectrophotometer was used to measure the transmittance of the films. The IR spectra of the samples were recorded with a Shimadzu IRSpirit QATR-S FTIR spectrometer.

To carry out electrical measurements, graphite electrodes with a diameter of 37 mm were stencil-printed on both sides of the film using a conductive varnish spray based on colloidal graphite from SOLINS®GRAPHITE. The surface resistance of the carbon coating was approximately 1500 Ohms/square.

Next, the film samples were kept in a thermostat for 5 hours at a temperature of 398 K and a pressure of about 14 Pa. The heat treatment was intended for removing water and aerosol residues from the samples. Notably, according to the data in [22], the degree of crystallinity of PVA films obtained from aqueous solution reaches about 46% if they are annealed at a temperature of 393 K.

The frequency dependences of capacitance and dielectric loss tangent tgδ were measured with an E7-20 LCR meter in the frequency range from 25 Hz to 1 MHz at a temperature from 294 to 398 K. Since films were annealed at 398 K before the measurements, it was assumed that the measurement process at temperatures below 398 K should not affect the results and the degree of crystallinity of the film should not change.

The dielectric permittivity ε and the dielectric loss factor ε'' ($\varepsilon'' = \varepsilon \cdot \mathrm{tg}\delta$) were calculated using the formula for a parallel-plate capacitor based on the experimental values of capacitance and dielectric loss tangent tgδ measured at various temperatures and frequencies.

The resistance of films at DC voltage in the above temperature range was measured using a KEITHLEY 610 electrometer.

Experimental results and discussion

PVA films prepared by the above-described technique were transparent in the visible and near-IR and UV regions of the spectrum (Fig. 1). The transmittance of the PVA film was about 90% at a wavelength λ = 380 nm, subsequently remaining almost unchanged.

Adding fullerenol to PVA caused the films to change color to yellowish brown, with a significant level of light absorption by this component in the UV region of the spectrum. The PVA + $C_{60}(OH)_{44}$ composite film turned out to be almost opaque at wavelengths λ below 350 nm. The transmittance increased monotonously at higher wavelengths, reaching a value of about 80% only at the upper bound of the range, at a wavelength λ = 1100 nm.

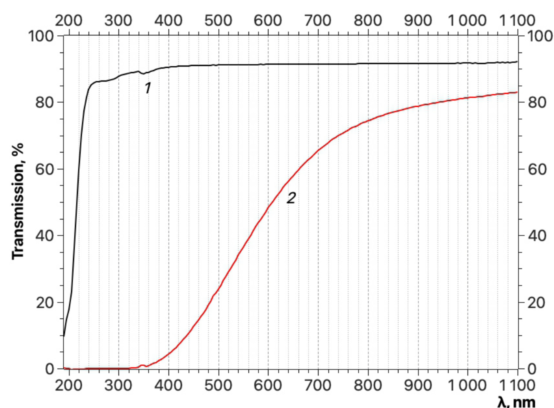

Fig. 1. Optical transmittance spectra of PVA (*1*) and PVA+$C_{60}(OH)_{44}$ (*2*) films at room temperature

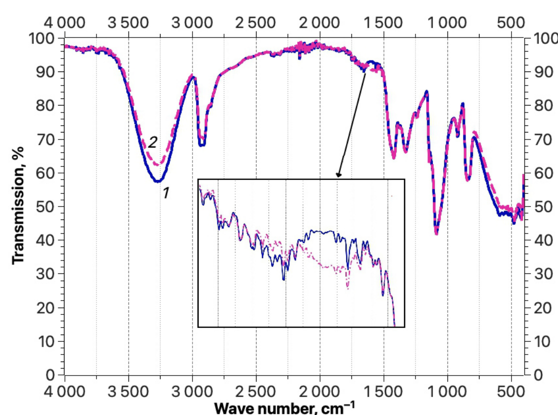

Fig. 2. IR spectra of PVA (*1*) and PVA+ $C_{60}(OH)_{44}$ (*2*) at room temperature (the inset shows the difference in the spectra in the region of 1600 cm^{-1} at high magnification)

The shape of IR spectra of the samples we obtained is in good agreement with the data known from the literature [23–25]. It can be seen from Fig. 2 that adding fullerenol does not produce any significant changes in the shape and position of the peaks. On the other hand, a notable decrease is observed in the intensity of the 3280 cm^{-1} band, corresponding to stretching of the covalent O–H bond, and the band at 2917 cm^{-1}, corresponding to asymmetric stretching of the $=CH_2$ group. The low–intensity absorption band at 1590 cm^{-1} (see the inset in Fig. 2), observed for the sample containing fullerenol $C_{60}(OH)_{44}$, can be attributed to the presence of C=C bonds in fullerenol [26–28].

Fig. 3 shows the frequency dependences of dielectric permittivity in PVA (curves *1–4*) and PVA + $C_{60}(OH)_{44}$ composite (curves *1′–4′*) films at different temperatures in the range of 294–384 K. Evidently, the values of ε for both the PVA film and the composite film are small and weakly depend on frequency at 294 K. Heating the films to a temperature close to the glass transition temperature of PVA leads to a significant increase in the low-frequency range of the spectrum at frequencies *f* below 10 kHz. The shapes of the ε(*f*) curves turn out to be similar for both film samples. The ε(*f*) dependences are characterized by a monotonic decrease in ε with an increase in frequency at all measurement temperatures. The value of ε in PVA is always slightly higher than that in the PVA + $C_{60}(OH)_{44}$ composite in the entire frequency range at temperatures not exceeding the glass transition temperature of PVA.

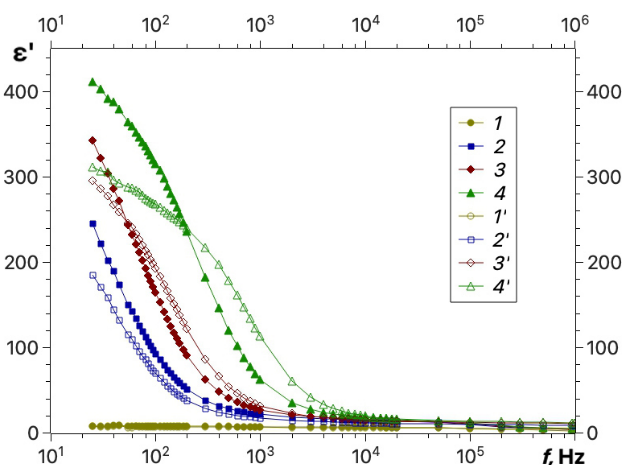

Fig. 3. Frequency dependences of dielectric permittivity in PVA film at 294 (*1*), 368 (*2*), 375 (*3*) and 384(*4*) K and PVA + $C_{60}(OH)_{44}$ composite film at 294 (*1′*), 363 (*2′*), 371 (*3′*) and 384 (*4′*) K

Fig. 4 shows the temperature dependences of the dielectric permittivity of the studied films at a frequency of 25 Hz. The values of ε in PVA films and the PVA + $C_{60}(OH)_{44}$ composite are approximately equal to 10 and nearly coincide at temperatures below 340 K. The increase in the dielectric permittivity observed in the temperature range of 340–375 K, i.e., in the T_g temperature range of PVA, is so rapid that at T = 375 K, ε ≈ 400 for the PVA film and ε ≈ 300 for the PVA + $C_{60}(OH)_{44}$ composite film. With a further increase in temperature, both film samples exhibit a significant decrease in the growth rate of ε (the curves reach saturation).

The frequency dependences of the dielectric loss factor are shown in Fig. 5. Analysis of these data shows that peaks (f_{max}) are observed on the curves at elevated temperatures, whose positions shift towards high frequencies with an increase in the measurement temperature.

Notably, according to the literature data (see, for example, [12]), such peaks are also observed at lower temperatures, but they are located in the region of infra-low frequencies. In particular, that study recorded a maximum of tgδ for PVA at 300 K at a frequency of several hertz.

Consequently, the explanation for the small values of ε″ that we observed at room temperature is that this quantity was measured on the right (high-frequency) slope of the curve with a maximum that was not reached during our measurements.

The dependence of lg[f_{max}(1/T)] in the given frequency range (Fig. 6) is close to linear for both PVA and the PVA + $C_{60}(OH)_{44}$ composite, i.e., it can be assumed that the position of the peak is described by the Arrhenius equation with the activation energy E_a. The activation energies are almost the same for PVA and the polymer nanocomposite, amounting to about

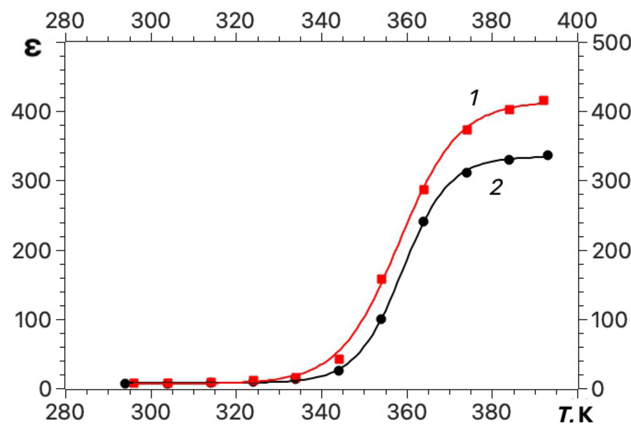

Fig. 4. Temperature dependences of dielectric permittivity in PVA (*1*) and PVA + $C_{60}(OH)_{44}$ composite (*2*) films at a frequency of 25 Hz

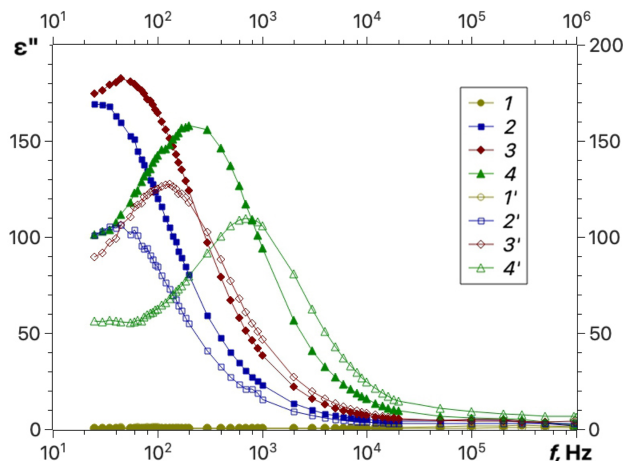

Fig. 5. Frequency dependences of dielectric loss factor for PVA film at 294 (*1*), 368 (*2*), 375 (*3*) and 384 (*4*) K and for PVA + $C_{60}(OH)_{44}$ film at (*1′*), 363 (*2′*), 371 (*3′*) and 384 (*4′*) K

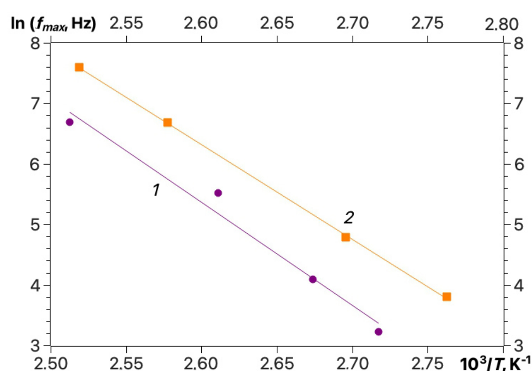

Fig. 6. Temperature dependences for logarithm of frequency at which the maximum ε″ is located in PVA (*1*) and in PVA+$C_{60}(OH)_{44}$ composite (*2*)

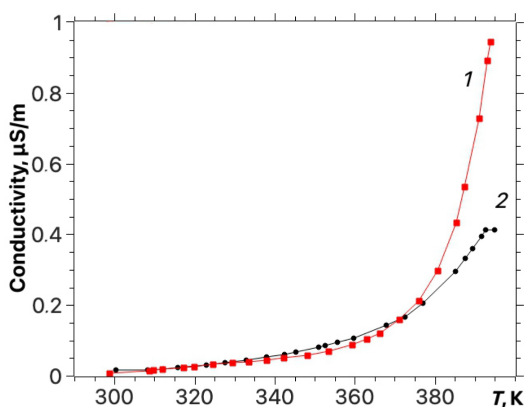

Fig. 7. Temperature dependences of DC conductivity of PVA (*1*) and PVA + $C_{60}(OH)_{44}$ (*2*) films

1.5 eV, however, the value of f_{max} for PVA turns out to be slightly lower. Furthermore, the quantity E_a is generally associated with large-scale motion, for example, with segmental mobility in macromolecular chains [29].

Fig. 7 shows the temperature dependences of DC conductivity of the films considered. The conductivity of both materials increases exponentially with increasing temperature. It can be seen that the conductivities of the nanocomposite film and the PVA film are approximately the same up to a temperature of about 370 K. At temperatures above 370 K, the conductivity of the PVA film begins to prevail over the conductivity of the nanocomposite film, and this difference increases with further heating.

Interestingly, the differences in the electrical characteristics of PVA and nanocomposite films become pronounced only at temperatures lying either in the region of glass transition temperature of PVA or above it. We believe that the differences are due to the following reasons. As noted above, PVA is a crystalline polymer, so that amorphous regions occupy about half of the volume of the studied PVA samples in the given conditions. It seems logical to assume that this is also typical for nanocomposite films. Since the sizes of fullerenol $C_{60}(OH)_{44}$ molecules are quite large (their diameter is estimated to be 1.5 ± 0.4 nm [11]), fullerenol molecules are accumulated mainly in the least ordered amorphous regions of the polymer. This may prevent the formation of a double electric layer at the interface, as well as the migration of charge carriers through the barrier layers. As a result, there is a decrease in both the capacitance of the material and its conductivity.

Conclusion

This paper reports on analysis of the optical and electrical properties of films prepared from polyvinyl alcohol (PVA) and nanocomposite material based on it with added fullerenol $C_{60}(OH)_{44}$ (PVA + $C_{60}(OH)_{44}$).

We found that even a small addition of fullerenol to PVA produces a modification in its coloration and significant absorption of light in the UV region of the spectrum.

A noticeable difference in the dielectric constant, dielectric loss factor and conductivity of the films was observed only at temperatures above the glass transition temperature of PVA. At elevated temperatures, the DC conductivity of the composite film and its dielectric permittivity at low frequencies turn out to be lower than the corresponding values for the PVA film. We believe that the reason for the observed difference is the accumulation of fullerenol molecules in amorphous barrier layers between PVA crystallites, preventing the formation of a double electric layer between the barriers and the crystallites as well as the migration of charge carriers through these barriers.

REFERENCES

1. **Caruso M. M., Davis D. A., Shen Q., et al.,** Mechanically-induced chemical changes in polymeric materials, Chem. Rev. 109 (11) (2009) 5755–5798.
2. **Tuyev V. I., Malyutin N. D., Loshchilov A. G., et al.,** Application of the additive printer (plotter) technology in electronics to form films from organic and inorganic materials, Proceedings of TUSUR University. (4 (38)) (2015) 52–63 (in Russian).
3. **Kozlov G. V.,** Structure and properties of particulate-filled polymer nanocomposites, Phys. Usp. 58 (1) (2015) 33–60.
4. **Pleshakov I. V., Prokof'ev A. V., Bibik E. E., et al.,** Spectral characteristics of composite obtained by embedding of magnetic nanoparticles into polymer matrix, Nanosyst.: Phys. Chem. Math. 12 (3) (2021) 279–282.
5. **Kolosova A. S., Sokolskaya M. K., Vitkalova I. A., et al.,** Modern polymer composite materials and their application, Mezhdunarodnyy zhurnal prikladnykh i fundamentalnykh issledovaniy [International Journal of Applied and Fundamental Research]. (5–1) (2018) 245–256 (in Russian).
6. **Van Etten E. A., Ximenes E. S., Tarasconi L. T., et al.,** Insulating characteristics of polyvinyl alcohol for integrated electronics, Thin Solid Films. 568 (1 Oct) (2014) 111–116.
7. **Aziz S. B.,** Modifying poly (vinyl alcohol) (PVA) from insulator to small-bandgap polymer: A novel approach for organic solar cells and optoelectronic devices, J. Electron. Mater. 45(1) (2016) 736–745.
8. **Nawaz A., Hümmelgen I. A.,** Poly (vinyl alcohol) gate dielectric in organic field-effect transistors, J. Mater. Sci. Mater. Electron. 30 (6) (2019) 5299–5326.
9. **Gematdinova V. M., Sidorov Yu. D., Polivanov M. A., Vasilenko S. V.,** Regulirovaniye rastvorimosti kompozitsionnykh materialov na osnove polivinilovogo spirta [Regulation of solubility of composites based on polyvinyl alcohol], Herald of Kazan Technological University. 19 (6) (2016) 96–99 (in Russian).
10. **Rosenberg M. E.,** Polymers based on vinyl acetate, Khimiya Publishing, Leningrad, 1983 (in Russian).
11. **Shekar B. C., Veeravazhuthi V., Sakthivel S., et al.,** Growth, structure, dielectric and AC conduction properties of solution grown PVA films, Thin Solid Films. 348(1–2) (1999) 122–129.
12. **Prosanov I. Yu., Uvarov N. F.,** Electrical properties of dehydrated polyvinyl alcohol, Phys. Solid State. 54 (2) (2012) 421–424.
13. **Benvenho A. R., Machado W. S., Cruz-Cruz I., Hümmelgen I. A.,** Study of poly (3-hexylthiophene)/cross-linked poly (vinyl alcohol) as semiconductor/insulator for application in low voltage organic field effect transistors, J. Appl. Phys. 113 (21) (2013) 214509.
14. **Muradov M. B., Eyvazova G. M., Hajimamedov R. H., Nuriyev M. A.,** Dielectrical relaxation in CdS/PVA nanocomposites, Prikladnaya fizika [Applied Physics]. (4) (2008) 135–138 (in Russian).
15. **Aziz S. B., Marif R. B., Brza M. A., et al.,** Employing of Trukhan model to estimate ion transport parameters in PVA based solid polymer electrolyte, Polymers. 11 (10) (2019) 1694.
16. **Koops C. G.,** On the dispersion of resistivity and dielectric constant of some semiconductors at audiofrequencies, Phys. Rev. 83 (1) (1951) 121–124.
17. **Valenkov A. M., Gofman I. V., Nosov K. S., et al.,** Polymeric composite systems modified with allotropic forms of carbon (review), Russ. J. Appl. Chem. 84 (5) (2011) 735–750.
18. **Muradyan V. E., Arbuzov A. A., Smirnov Yu. N., Lesnichaya V. A.,** Mechanochemical synthesis and properties of fullerene, Russ. J. Gen. Chem. 81 (8) (2011) 1671–1675.
19. **Penkova A. V., Acquah S. F. A., Piotrovskiy L. B., et al.,** Fullerene derivatives as nano-additives in polymer composites, Russ. Chem. Rev. 86 (6) (2017) 530–566.
20. **Shadrin E. B., Ilinskiy A. V., Kastro R. A., et al.,** The dielectric response modification of nanocrystalline vanadium dioxide films by doping with nickel and tungsten, St. Petersburg State Polytechnical University Journal. Physics and Mathematics. 15 (4) (2022) 7–31 (in Russian).
21. **Mazur A. C., Karpunin A. E., Proskurina O. V., et al.,** Nuclear magnetic resonance spectra of polyhydroxylated fullerene $C_{60}(OH)_n$, Phys. Solid State. 60 (7) (2018) 1468–1470.
22. **Tretinnikov O. N., Zagorskaya S. A.,** Determination of the degree of crystallinity of poly (vinyl alcohol) by FTIR spectroscopy, J. Appl. Spectrosc. 79 (4) (2012) 521–526.
23. **Jipa I. M., Stoica A., Stroescu M., et al.,** Potassium sorbate release from poly (vinyl alcohol)-bacterial cellulose films, Chem. Pap. 66 (2) (2012) 138–143.

24. **Soltani S., Asempour P. H., Jamshidi H.,** Investigation of reaction conditions for preparation of medium molecular weight poly (vinyl alcohol) as emulsifier, Iran. Polym. J. 16 (7) (2007) 439-447.

25. **Bhat N. V., Nate M. M., Kurup M. B., et al.,** Effect of γ-radiation on the structure and morphology of polyvinyl alcohol films, Nucl. Instrum. Meth. B. 237 (3–4) (2005) 585–592.

26. **Xing G., Zhang J., Zhao Y., et al.,** Influences of structural properties on stability of fullerenols, J. Phys. Chem. B. 108 (31) (2004) 11473–11479.

27. **Djordjevic A., Ignjatovic N., Seke M., et al.,** Synthesis and characterization of hydroxyapatite/fullerenol nanocomposites, J. Nanosci. Nanotechnol. 15 (2) (2015) 1538–1542.

28. **Kokubo K.,** Water soluble single-nano carbon particles: Fullerenol and its derivatives, In book: The delivery of nanoparticles. Ed. by A. A. Hashin, InTechOpen, London (2012) 317–332.

29. **Blythe A. R., Bloor D.,** Electrical properties of polymers, Cambridge University Press, Cambridge, UK, 2005.

СПИСОК ЛИТЕРАТУРЫ

1. **Caruso M. M., Davis D. A., Shen Q., Odom S. A., Sottos, N. R., White S. R., Moore J. S.** Mechanically-induced chemical changes in polymeric materials // Chemical Reviews. 2009. Vol. 109. No. 11. Pp. 5755–5798.

2. **Туев В. И., Малютин Н. Д., Лощилов А. Г., Артищев С. А., Здрок А. Е., Алланурoв А. М., Убайчин А. В.** Исследование возможностей применения аддитивной принтерной технологии формирования пленок органических и неорганических материалов электроники //Доклады ТУСУР (Томского государственного университета систем управления и радиоэлектроники). 2015. № 4 (38). С. 52–63.

3. **Козлов Г. В.** Структура и свойства дисперсно-наполненных полимерных нанокомпозитов // Успехи физических наук. 2015. Т. 185. № 1. С. 35–64.

4. **Pleshakov I. V., Prokof'ev A. V., Bibik E. E., Nepomnyashchaya E. K., Velichko E. N., Kostitsyna T. A., Seliutin D. M.** Spectral characteristics of composite obtained by embedding of magnetic nanoparticles into polymer matrix // Nanosystems: Physics, Chemistry, Mathematics. 2021. Vol. 12. No. 3. Pp. 279 – 282.

5. **Колосова А. С., Сокольская М. К., Виткалова И. А., Торлова А. С., Пикалов Е. С.** Современные полимерные композиционные материалы и их применение // Международный журнал прикладных и фундаментальных исследований. 2018. № 5. Часть 1. С. 245–256.

6. **Van Etten E. A., Ximenes E. S., Tarasconi L. T., Garcia I. T., Forte M. M., Boudinov H.** Insulating characteristics of polyvinyl alcohol for integrated electronics // Thin Solid Films. 2014. Vol. 568. 1 October. Pp. 111–116.

7. **Aziz S. B.** Modifying poly (vinyl alcohol) (PVA) from insulator to small-bandgap polymer: A novel approach for organic solar cells and optoelectronic devices // Journal of Electronic Materials. 2016. Vol. 45. No. 1. Pp. 736–745.

8. **Nawaz A., Hümmelgen I. A.** Poly (vinyl alcohol) gate dielectric in organic field-effect transistors // Journal of Materials Science: Materials in Electronics. 2019. Vol. 30. No. 6. Pp. 5299–5326.

9. **Гематдинова В. М., Сидоров Ю. Д., Поливанов М. А., Василенко С. В.** Регулирование растворимости композиционных материалов на основе поливинилового спирта // Вестник Казанского технологического университета. 2016. Т. 19. № 6. С. 96–99.

10. **Розенберг М. Э.** Полимеры на основе винилацетата. Ленинград: Химия, 1983. 176 с.

11. **Shekar B. C., Veeravazhuthi V., Sakthivel S., Mangalaraj D., Narayandass S. K.** Growth, structure, dielectric and AC conduction properties of solution grown PVA films // Thin Solid Films. 1999. Vol. 348. No. 1–2. Pp. 122–129.

12. **Просанов И. Ю., Уваров Н. Ф.** Электрические свойства дегидратированного поливинилового спирта // Физика твердого тела. 2012. Т. 54. № 2. С. 393–396.

13. **Benvenho A. R., Machado W. S., Cruz-Cruz I., Hümmelgen I. A.** Study of poly (3-hexylthiophene)/cross-linked poly (vinyl alcohol) as semiconductor/insulator for application in low voltage organic field effect transistors // Journal of Applied Physics. 2013. Vol. 113. No. 21. P. 214509.

14. **Мурадов М. Б., Эйвазова Г. М., Гаджимамедов Р. Г., Нуриев М. А.** Диэлектрическая релаксация в нанокомпозитах CdS/ПВС // Прикладная физика. 2008. № 4. С. 138–135.

15. **Aziz S. B., Marif R. B., Brza M. A., Hamsan M. H., Kadir M. F. Z.** Employing of Trukhan model to estimate ion transport parameters in PVA based solid polymer electrolyte // Polymers. 2019. Vol. 11. No. 10. P. 1694.

16. **Koops C. G.** On the dispersion of resistivity and dielectric constant of some semiconductors at audiofrequencies // Physical Review. 1951. Vol. 83. No. 1. Pp. 121–124.

17. **Валенков А. М., Гофман И. В., Носов К. С., Шаповалов В. М., Юдин В. Е.** Полимерные композиционные системы, модифицированные аллотропными соединениями углерода (Обзор) // Журнал прикладной химии. 2011. Т. 84. № 5. С. 705–720.

18. **Мурадян В. Е., Арбузов А. А., Смирнов Ю. Н., Лесничая В. А.** Механохимический синтез производных фуллерена и их свойства // Журнал общей химии. 2011. Т. 81. № 8. С. 1326–1330.

19. **Пенькова А. В., Пиотровский Л. Б., Маркелов Д. А., Семисалова А. С., Kroto H. W.** Производные фуллерена как нанодобавки для полимерных композитов // Успехи химии. 2017. Т. 86. № 6. С. 530–566.

20. **Шадрин Е. Б., Ильинский А. В., Кастро Р. А., Капралова В. М., Кононов А. А., Пашкевич М. Э.** Модификация диэлектрического отклика нанокристаллических пленок диоксида ванадия путем легирования никелем и вольфрамом // Научно-технические ведомости СПбГПУ. Физико-математические науки. 2022. Т. 15. № 4. С. 7–31.

21. **Мазур А. С., Карпунин А. Е., Проскурина О. В., Герасимов В. И., Плешаков И. В., Матвеев В. В., Кузьмин Ю. И.** Особенности спектров ядерного магнитного резонанса полигидроксилированного фуллерена $C_{60}(OH)_n$ // Физика твердого тела. 2018. Т. 60. № 7. С. 1451–1453.

22. **Третинников О. Н., Загорская С. А.** Определение степени кристалличности поливинилового спирта методом ИК-Фурье-спектроскопии // Журнал прикладной спектроскопии. 2012. Т. 79. № 4. С. 538–543.

23. **Jipa I. M., Stoica A., Stroescu M., Dobre L.-M., Dobre T., Jinga S., Tardei C.** Potassium sorbate release from poly (vinyl alcohol)-bacterial cellulose films // Chemical Papers. 2012. Vol. 66. No. 2. Pp. 138–143.

24. **Soltani S., Asempour P. H., Jamshidi H.** Investigation of reaction conditions for preparation of medium molecular weight poly (vinyl alcohol) as emulsifier // Iranian Polymer Journal. 2007. Vol. 16. No. 7. Pp. 439–447.

25. **Bhat N. V., Nate M. M., Kurup M. B., Bambole V. A., Sabharwal S.** Effect of γ-radiation on the structure and morphology of polyvinyl alcohol films // Nuclear Instruments and Methods in Physics Research B. 2005. Vol. 237. No. 3–4. Pp. 585–592.

26. **Xing G., Zhang J., Zhao Y., et al.** Influences of structural properties on stability of fullerenols // The Journal of Physical Chemistry B. 2004. Vol. 108. No. 31. Pp. 11473–11479.

27. **Djordjevic A., Ignjatovic N., Seke M., Jovic D., Uskokovic D., Rakocevic Z.** Synthesis and characterization of hydroxyapatite/fullerenol nanocomposites // Journal of Nanoscience and Nanotechnology. 2015. Vol. 15. No. 2. Pp. 1538 –1542.

28. **Kokubo K.** Water soluble single-nano carbon particles: Fullerenol and its derivatives // The delivery of nanoparticles. Edited by A. A. Hashin. London: InTechOpen, 2012. Pp. 317–332.

29. **Блайт Э. Р., Блур Д.** Электрические свойства полимеров. Пер. с англ. М.: Физматлит, 2008. 376 с.

THE AUTHORS

NIKITINA Elizaveta A.
Peter the Great St. Petersburg Polytechnic University
29 Politechnicheskaya St., St. Petersburg, 195251, Russia
eanikitina26@icloud.com
ORCID: 0000-0003-1394-2681

KAPRALOVA Viktoria M.
Peter the Great St. Petersburg Polytechnic University
29 Politechnicheskaya St., St. Petersburg, 195251, Russia
kapralova2006@yandex.ru
ORCID: 0000-0001-9050-4453

SUDAR Nicolay T.
Peter the Great St. Petersburg Polytechnic University
29 Politechnicheskaya St., St. Petersburg, 195251, Russia
sudar53@mail.ru
ORCID: 0000-0001-7380-7727

STUDZINSKII Vitalii M.
Peter the Great St. Petersburg Polytechnic University
29 Politechnicheskaya St., St. Petersburg, 195251, Russia
svm.fl@mail.ru
ORCID: 0000-0002-2149-2978

GERASIMOV Victor I.
Peter the Great St. Petersburg Polytechnic University
29 Politechnicheskaya St., St. Petersburg, 195251, Russia
viger53@rambler.ru
ORCID: 0009-0004-2167-0019

СВЕДЕНИЯ ОБ АВТОРАХ

НИКИТИНА Елизавета Александровна – *аспирантка, инженер Высшей школы электроники и микросистемной техники Санкт-Петербургского политехнического университета Петра Великого.*
195251, Россия, г. Санкт-Петербург, Политехническая ул., 29
eanikitina26@icloud.com
ORCID: 0000-0003-1394-2681

КАПРАЛОВА Виктория Маратовна – *кандидат физико-математических наук, доцент Высшей школы электроники и микросистемной техники Санкт-Петербургского политехнического университета Петра Великого.*
195251, Россия, г. Санкт-Петербург, Политехническая ул., 29
kapralova2006@yandex.ru
ORCID: 0000-0001-9050-4453

СУДАРЬ Николай Тобисович – *доктор физико-математических наук, профессор Высшей школы электроники и микросистемной техники Санкт-Петербургского политехнического университета Петра Великого.*
195251, Россия, г. Санкт-Петербург, Политехническая ул., 29
sudar53@mail.ru
ORCID: 0000-0001-7380-7727

СТУДЗИНСКИЙ Виталий Михайлович – *аспирант, инженер Высшей школы высоковольтной энергетики Санкт-Петербургского политехнического университета Петра Великого.*

195251, Россия, г. Санкт-Петербург, Политехническая ул., 29

svm.fl@mail.ru

ORCID: 0000-0002-2149-2978

ГЕРАСИМОВ Виктор Иванович – *кандидат технических наук, доцент Высшей школы механики и процессов управления Санкт-Петербургского политехнического университета Петра Великого.*

195251, Россия, г. Санкт-Петербург, Политехническая ул., 29

viger53@rambler.ru

ORCID: 0009-0004-2167-0019

Received 01.04.2024. Approved after reviewing 25.04.2024. Accepted 25.04.2024.

Статья поступила в редакцию 01.04.2024. Одобрена после рецензирования 25.04.2024. Принята 25.04.2024.

© Peter the Great St. Petersburg Polytechnic University, 2024

Original article
UDC 544.227
DOI: https://doi.org/10.18721/JPM.17308

EFFECT OF ARGON ION BOMBARDMENT ON THE COMPOSITION, ELECTRONIC STRUCTURE AND PHYSICAL PROPERTIES OF CADMIUM FLUORIDE

A. A. Abduvayitov [1], D. A. Tashmukhamedova [1], B. E. Umirzakov [1], J. B. Khujaniyozov [1], I. R. Bekpulatov [2] ✉, V. V. Loboda [3]

[1] Tashkent State Technical University Named after Islam Karimov, Tashkent, Uzbekistan;

[2] Karshi State University, Tashkent, Uzbekistan;

[3] Peter the Great St. Petersburg Polytechnic University, St. Petersburg, Russia

✉ bekpulatov85@rambler.ru

Abstract. In the paper, the effect of bombardment with Ar^+ ions on the composition, electronic and crystal structure of the surface layers of bulk single crystal samples and CdF_2(111) films has been studied using the methods of Auger electron and ultraviolet photoelectron spectroscopy, high-energy electron diffraction and recording the angular dependences of the reflectance factor of inelastically reflected electrons. The effect of this bombardment on the density of states of valence electrons and energy band parameters of CdF_2 was investigated for the first time. The degree of disorder of CdF_2 into components and evaporation of fluorine from the surface layers was established to depend on the energy and dose of Ar^+ ions. The complete evaporation of F in the form of a diatomic gas was shown for the first time to be observed in the energy range of 1 – 2 keV at a saturation dose.

Keywords: epitaxial layer, heterostructures, ion bombardment, Auger spectrum, photoelectron spectrum, disordered layer, electron density of state

Funding: The studies are being done within the Fundamental Scientific Project No. F-OT-2021-422 of The Republic of Uzbekistan and The Ministry of Science and Higher Education of the Russian Federation. The research is funded by the Ministry of Science and Higher Education of the Russian Federation within the framework of the program "The World-Class Research Centre: Advanced Digital Technologies" (Contract No. 075-15-2022-311 dated April 20, 2022).

For citation: Abduvayitov A. A., Tashmukhamedova D. A., Umirzakov B. E., Khujaniyozov J. B., Bekpulatov I. R., Loboda V. V., Effect of argon ion bombardment on the composition, electronic structure and physical properties of cadmium fluoride, St. Petersburg State Polytechnical University Journal. Physics and Mathematics. 17 (3) (2024) 87–96. DOI: https://doi.org/10.18721/JPM.17308

This is an open access article under the CC BY-NC 4.0 license (https://creativecommons.org/licenses/by-nc/4.0/)

Научная статья
УДК 544.227
DOI: https://doi.org/10.18721/JPM.17308

ВЛИЯНИЕ БОМБАРДИРОВКИ ИОНАМИ АРГОНА НА СОСТАВ, ЭЛЕКТРОННУЮ СТРУКТУРУ И ФИЗИЧЕСКИЕ СВОЙСТВА ФТОРИДА КАДМИЯ

А. А. Абдув йитов [1], Д. А. Т шмух медов [1], Б. Е. Умирз ков [1], Д. Б. Хуж ниёзов [1], И. Р. Бекпул тов [2] ✉, В. В. Лобод [3]

[1] Ташкентский государственный технический университет им. Ислама Каримова,

© Abduvayitov A. A., Tashmukhamedova D. A., Umirzakov B. E., Khujaniyozov J. B., Bekpulatov I. R., Loboda V. V., 2024. Published by Peter the Great St. Petersburg Polytechnic University.

г. Ташкент, Узбекистан;
[2] Каршинский государственный университет, г. Карши, Узбекистан;
[3] Санкт-Петербургский политехнический университет Петра Великого,
Санкт-Петербург, Россия
✉ bekpulatov85@rambler.ru

Аннотация. В работе изучено влияние бомбардировки ионами аргона Ar^+ на состав, электронную и кристаллическую структуру поверхностных слоев объемных монокристаллических образцов и пленок фторида кадмия CdF_2(111). Для этого использованы методы оже-электронной и ультрафиолетовой фотоэлектронной спектроскопии, дифракции быстрых электронов и регистрация угловой зависимости коэффициента отражения неупругоотраженных электронов. Впервые изучено влияние указанной бомбардировки на плотность состояния валентных электронов и энергетические зонные параметры CdF_2(111). Установлено, что степень разупорядочения CdF_2 на составляющие и испарение фтора с поверхностных слоев зависит от энергии и дозы ионов Ar^+. Впервые показано, что полное испарение фтора в виде двухатомного газа наблюдается в области энергий 1 – 2 кэВ при дозе насыщения.

Ключевые слова: эпитаксиальный слой, гетероструктуры, ионная бомбардировка, оже-спектр, фотоэлектронный спектр, неупорядоченный слой, плотность электронных состояний

Финансирование: Работа осуществляется в рамках Фундаментального научного проекта № Ф-ОТ-2021-422 Республики Узбекистан и Министерства науки и образования Российской Федерации. Исследование финансируется Министерством науки и образования Российской Федерации в рамках программы «Исследовательский класс мирового уровня: передовые цифровые технологии» (контракт № 075-15-2022-311 от 20 апреля 2022 года).

Для цитирования: Абдувайитов А. А., Ташмухамедова Д. А., Умирзаков Б. Е., Хужаниёзов Д. Б., Бекпулатов И. Р., Лобода В. В. Влияние бомбардировки ионами аргона на состав, электронную структуру и физические свойства фторида кадмия // Научно-технические ведомости СПбГПУ. Физико-математические науки. 2024. Т. 17. № 3. С. 87–96. DOI: https://doi.org/10.18721/ JPM.17308

Статья открытого доступа, распространяемая по лицензии CC BY-NC 4.0 (https:// creativecommons.org/licenses/by-nc/4.0/)

Introduction

The great interest in epitaxial fluoride layers is associated both with the unique properties of the latter and with the wide potential possibilities of their application in opto- and microelectronics [1 – 13]. In particular, metal fluorides are widely used in the creation of special semiconductor – dielectric – semiconductor (SDS) structures in the three-dimensional integrated circuits. Of particular interest are CdF_2/Si(111) heterostructures with a CaF_2 buffer layer [9, 14, 15]. The minimum thickness of the CaF_2 buffer layer was 0.9 nm [5]. In this case, CaF_2 plays the role of a barrier layer for the chemical reaction between CdF_2 and Si substrates [9]. At the same time, trivalent germanium turned out to be the most promising for doping CdF_2 [16].

Single-crystalline cadmium fluoride is a solid dielectric that can be converted into a semiconductor by doping with donor impurities and subsequent heating in a reducing atmosphere [16 – 18].

In Refs. [19, 20], the energy position of the levels of rare earth (RE) elements in the band diagram of BaF_2 and CdF_2 crystals was determined. The role of RE^{3+} and RE^{2+} ions in the carrier capture, luminescence, and the formation of radiation defects was assessed. It was shown that the significant difference in the luminescent properties of BaF_2:RE and CdF_2:RE was due to the position of excited energy levels in the band diagram of the crystals. In Ref. [21], Shubnikov – de Haas oscillations and a quantum staircase of the Hall resistance were discovered in a p-CdF_2 quantum well limited by $CdB_xF_{2-x}\delta$ barriers on the n-CdF_2 surface. Thanks to the low effective

© Абдувайитов А. А., Ташмухамедова Д. А., Умирзаков Б. Е., Хужаниёзов Д. Б., Бекпулатов И. Р., Лобода В. В., 2024. Издатель: Санкт-Петербургский политехнический университет Петра Великого.

mass of two-dimensional holes, the observation of the quantum Hall effect became possible at room temperature.

Studying the influence of various external influences, especially ion bombardment, on the composition, structure and physical properties of fluorides is of both fundamental and applied interest. In recent years, we have thoroughly studied the effect of ion bombardment on the composition, electronic and crystal structure, emission and optical properties of dielectric films and samples [12 – 27]. However, to date, the effect of low-energy ion bombardment on the composition and properties of CdF_2 films has been practically unstudied.

In this work, changes in the composition, electronic and crystal structure of CdF_2 (111) upon bombardment with Ar^+ ions were studied for the first time.

Experimental methods

The subject of research was a single-crystal sample of CdF_2 (111) with a thickness of about 0.5 mm and molecular beam epitaxial (MBE) films of CdF_2/Si(111) with a thickness of about 500 Å. Before ion bombardment, the samples under study were degassed at $T \approx 1000$ K for 3 hours in a vacuum (pressure $P \approx 10^{-7}$ Pa). The elemental and chemical compositions of the samples were determined by Auger electron spectroscopy (AES). The degree of amorphization of the CdF_2 film upon bombardment with Ar^+ ions and its crystallization during annealing, the type and parameters of the lattice were studied by high-energy electron diffraction (HEED) method and by measuring the angular dependences of the reflectance factor η of inelastically reflected electrons. To study the density of state of valence electrons and determine the parameters of energy bands, the method of ultraviolet photoelectron spectroscopy (UPS) was used. All measurements were carried out after the target was cooled to room temperature, in a vacuum with a pressure of at least 10^{-7} Pa. The choice of the (111) plane has been due to the fact that the CdF_2(111) surface has the lowest free energy ($E_{CdF2} \approx 5\cdot10^{-7}$ J·cm^{-2}, $E_{Si} \approx 1.35\cdot10^{-4}$ J·cm^{-2} and is atomically smooth.

Experimental results and their discussion

The Auger spectrum of a well-cleaned CdF_2(111) surface is shown in Fig. 1. It can be seen that the CdF_2 surface contains mainly an impurity of oxygen atoms with a concentration of no more than 1 at.%. The CdF_2 film surface has high crystalline perfection and an atomically smooth surface with a (1 × 1) structure reflection high-energy electron diffraction (RHEED) image (see inset in Fig. 1).

An analysis of the dependence of the intensity IF of the Auger peak from fluorine at an energy of 646 eV on the irradiation dose to the CdF_2(111) surface bombarded by Ar^+ ions with different energies E_0 (see Fig. 2) allows us to conclude the following. The intensive desorption of fluorine from the surface of CdF_2 occurs, starting from the irradiation dose $D = (1 - 5)\cdot10^{13}$ cm^{-2} and up to $D = 10^{16}$ cm^{-2}; the rate of decrease in the intensity I_F depending on the energy E_0. In particular, for $E_0 = 0.5$ keV at $D = 5\cdot10^{16}$ cm^{-2}, the intensity of the Auger peak corresponds to a minimum, but I_F is not equal to zero even at $D = 10^{17}$ cm^{-2}, and thus $D = (4 - 5)\cdot10^{16}$ cm^{-2} is the saturation dose D_s for $E_0 = 0.5$ keV. For $E_0 = 1.0$ keV, a decrease in I_F to zero is observed at $D = (6 - 8)\cdot10^{16}$ cm^{-2}. A decrease in I_F to zero occurred up to $E_0 = 2$ keV. At E_0 more than 2 – 3 keV, the I_F value, even at dose D more than 10^{17} cm^{-2}, was above zero. Apparently, at high energies of Ar^+ ions, the decomposition of CdF_2 predominantly occurs in the surface layer and complete evaporation of fluorine atoms from these layers does not occur. Or, the evaporation of Cd and CdF_2 as a whole may begin simultaneously with the evaporation of fluorine atoms.

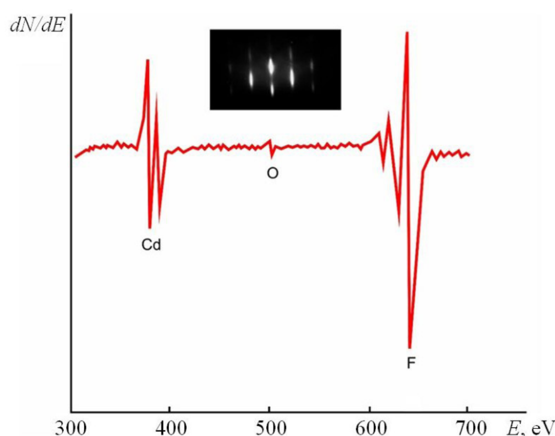

Fig. 1. The Auger spectrum and RHEED images (inset) of the pure CdF_2(111) surface

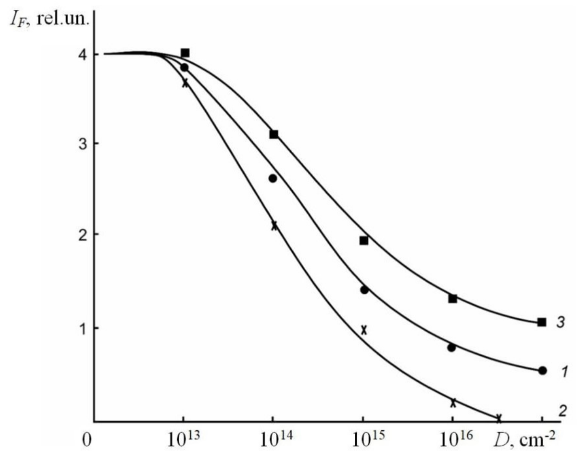

Fig. 2. Plots of the Auger F peak intensity (at E = 646 eV) versus the Ar^+ irradiation dose D for CdF_2 bombarded by Ar^+ ions with different energy values; E_0, keV: 0.5 (*1*), 1.0 (*2*), 2.5 (*3*)

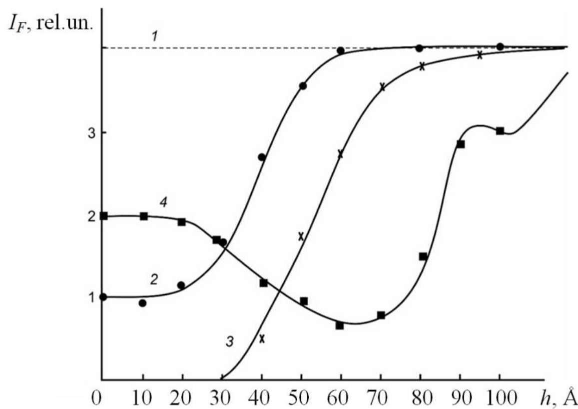

Fig. 3. The depth distribution profiles of F atoms from CdF_2 bombarded by Ar^+ ions at $D = D_s$ with different energy values; E_0, keV: 0.0 (*1*) 0.5 (*2*), 1.0 (*3*), 5.0 (*4*)

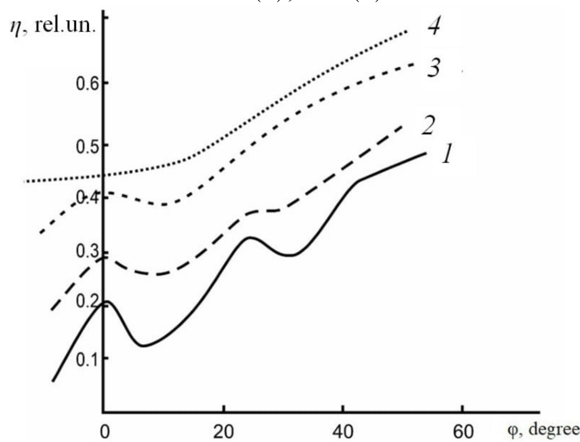

Fig. 4. The dependence of η on the angle φ (the angle of incidence of the primary beam) for amorphous CdF_2 films on Si(111) substrates; the film thickness values, Å: 10 (*1*), 20 (*2*), 40 (*3*), 50 (*4*). E_p = 0.8 keV

To answer this question, we studied the dependence of I_F on the depth h of a CdF_2 layer bombarded with Ar^+ ions with different energies at $D = D_s$ (Fig. 3). The plots in Fig.3 show that the intensity of the I_F peak decreases sharply (by ~ 4 times) at E_0 = 0.5 keV, and it practically does not change until the layer depth h = 20 – 80 Å, that corresponds to the projected range of Ar^+ ions.

Apparently, all F atoms in the form of diatomic gas F_2 evaporate from these layers. In the region $h \approx 25 - 50$ Å, the I_F concentration increases and, starting from $h \approx 50$ Å, the stoichiometric composition of CdF_2 is completely established. However, further studies showed that the CdF_2 layers were highly disordered to a depth of $h \approx 130 - 150$ Å. In the case of E_0 = 1.0 keV, the surface layers of the cadmium fluoride are completely decomposed into components to a depth of h = 30 – 40 Å, and almost all F atoms evaporate from these layers, and hence an amorphous cadmium film with a thickness of d = 30 – 40 Å is formed on the surface (see curve *3* in Fig. 3). When CdF_2 is bombarded by Ar^+ ions with E_0 = 5 keV, the greatest decomposition occurs at the depth of the projected range of Ar^+ ions ($h \approx 60 - 70$ Å). Apparently, most of the fluorine atoms go into vacuum, and the other part diffuses deep into the target. Therefore, the concentration of F increases significantly at a depth of h = 80 – 100 Å.

It is known that the thickness of disordered layers of a single crystal under ion bombardment is very difficult to determine experimentally. In this work, the depth of such layers was assessed by investigation of the angular dependences of the reflectance factor η of inelastically scattered electrons at the different primary electron energies E_p.

The dependences of η on the angle of incidence of the primary beam on the surface, for the Si(111) system with amorphous CdF_2 films of various thickness values are presented in Fig. 4. They were recorded at E_p = 0.8 keV. It can be seen that the main Si(111) peak is completely smoothed out at a film thickness of about 50 Å. A similar method was used to determine the thicknesses of the CdF_2 films at which the main Si peak was smoothed out in the range E_p = 1 – 10 keV. The results are given in Table.

Using the data from Table, the thickness of disordered layers d_p in the CdF_2(111) was estimated using the condition when bombarded with Ar^+ ions with different energies E_0 at doses $D = D_s$ (Fig. 5). This plot shows that

Table

The dependence of the thickness of the amorphous CdF_2/Si(111) films on the primary electron energies E_p

E_p, keV	0.8	1.0	3.0	5.0	10
d, Å	50	80	200	350	500

Footnote: d values were found under the condition when the main peak on the curve η(φ) was smoothed out at a given value of energy E_p.

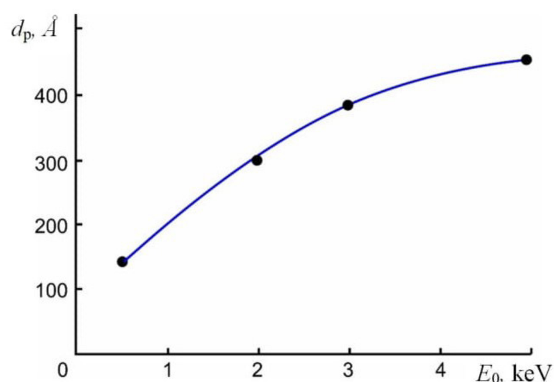

Fig. 5. A plot of the thickness of disordered layers versus the energy of Ar^+ ions

d_p increases exponentially from about 130 to 450 Å as E_0 increases from 0.5 to 5 keV.

The photoelectron spectra of a CdF_2/Si(111) epitaxial film before and after bombardment by Ar^+ ions at E_0 = 1 keV with different doses, taken at $h\nu$ = 21.2 eV (Fig. 6). These spectra provide information about the density of state of the valence band electrons, and the area under the energy distribution curve is proportional to the quantum yield Y of photoelectrons. The top of the valence band E_v of CdF_2 is taken as the reference point. In the spectrum of pure CdF_2, there are three clearly defined maxima (peaks) at energies E_{cv} = −1.6 eV, −3.8 eV, and −8.1 eV. It can be assumed that peak E_1 appears due to hybridization of the 5s level of Cd with the 2p level of F; the main contribution to the appearance of peak E_2 is made by 5s levels of Cd, and that to E_3 is made by 2p levels of F.

When CdF_2 film is bombarded by Ar^+ ions, a slight broadening of the curvilinear energy distribution of photoelectrons is observed at the dose $D = 10^{14}$ cm^{-2}, and a decrease in the intensity is observed at the peak of E_{cv} = −1.8 and 8.1 eV. Also, the shift of the peak in the initial state of the spectrum (E_{cv} = 0.6 − 1.0 eV) to the right leads to

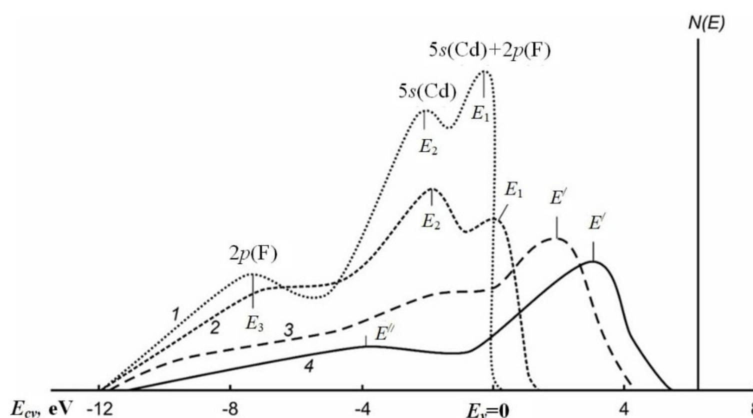

Fig. 6. The photoelectron spectra of the CdF_2 bombarded by Ar^+ ions with energy E_0 = 1 keV. Doses D, cm^{-2}: 0 (*1*), $1\cdot10^{14}$ (*2*); $5\cdot10^{15}$(*3*), $5\cdot10^{16}$(*4*)

a decrease in the gap width E_g of the CdF_2 film. At a dose of $5\cdot10^{15}$ cm^{-2}, a new peak E' characteristic of cadmium appears instead of E_1 and E_2 peaks, and the value of Y decreases by about 2 times in this case [19, 23].

Conclusion

In this work, the effect of bombardment with argon ions on the composition, electronic and crystal structure of the surface layers of single-crystal samples and CdF_2(111) films has been studied. The molecular beam epitaxial film of the CdF_2/Si(111) with a thickness of 500 Å was shown to have high stoichiometric and crystalline perfection with a surface structure of 1 × 1.

It was established that the intense desorption of fluorine atoms occurred, which continued up to dose $D = (5 - 10)\cdot 10^{16}$ cm^{-2}. The concentration of fluorine in the surface layers were found to go down to zero in the region $E_0 = 1 - 3$ keV, and not decrease to zero when E_0 being greater than 4 keV. The main mechanisms of these changes were clarified.

For the first time, the thickness of layers enriched with cadmium atoms and the thickness of highly disordered CdF_2/Si(111) layers were estimated. The change in the density of state of CdF_2 valence electrons upon bombardment by Ar^+ ions with $E_0 = 1$ keV was also studied for the first time using ultraviolet photoelectron spectroscopy (UPS) at different doses.

The results obtained in this work can undoubtedly be useful in the development of modern generation communications-electronics equipment.

REFERENCES

1. **Sugiyama M., Oshima M.,** MBE growth of fluorides, Microelectron. J. 27 (4–5) (1996) 361–382.
2. **Weng J., Gao Sh.-P.,** Layer-dependent band gaps and dielectric constants of ultrathin fluorite crystals, J. Phys. Chem. Solids. 148 (Jan) (2021) 109738.
3. **Illarionov Y. Y., Vexler M. I., Suturin S. M., et al.,** Electron tunneling in MIS capacitors with the MBE-grown fluoride layers on Si (111) and Ge (111): Role of transverse momentum conservation, Microelectron. Eng. 88 (7) (2011) 1291–1294.
4. **Banshchikov A. G., Illarionov Yu. Yu., Vexler M. I., et al.,** Trends in reverse-current change in tunnel MIS diodes with calcium fluoride on Si (111) upon the formation of an extra oxide layer, Semicond. 53 (6) (2019) 833–837.
5. **Izumi A., Kawabata K., Tsutsui K., et al.,** Growth of CdF_2CaF_2Si (111) heterostructure with abrupt interfaces by using thin CaF_2 buffer layer, Appl. Surf. Sci. 104–105 (2 Sept) (1996) 417–421.
6. **Sokolov N. S., Suturin S. M.,** MBE-growth peculiarities of fluoride (CdF_2–CaF_2) thin film structures, Thin Solid Films. 367 (1–2) (2000) 112–119.
7. **Mir A., Zaoui A., Bensaid D.,** The displacement effect of a fluorine atom in CaF_2 on the band structure, Appl. Surf. Sci. 439 (1 May) (2018) 1180–1185.
8. **Li Zh., Baskurt M., Sahin H., et al.,** Electronic properties of intrinsic vacancies in single-layer CaF_2 and its heterostructure with monolayer MoS_2, J. Appl. Phys. 130 (5) (2021) 055301.
9. **Kalugin A. I., Sobolev V. V.,** Optical properties of CdF_2 in a wide energy range, Tech. Phys. 49 (3) (2004) 338–341.
10. **Bekpulatov I. R., Imanova G. T., Kamilov T. S., et al.,** Formation of *n*-type CoSi monosilicide film which can be used in instrumentation, Int. J. Modern Phys. B. 37 (17) (2023) 22350164.
11. **Bekpulatov I. R., Shomukhammedova D. S., Shukurova D. M., Ibragimova B. V.,** Obtaining higher manganese silicide films with high thermoelectric properties, E3S Web Conf. 365 (30 Jan) (2023) 05015.
12. **Kamilov T. S., Rysbaev A. S., Klechkovskaya V. V., et al.,** The influence of structural defects in silicon on the formation of photosensitive Mn_4Si_7–Si(Mn)–Mn_4Si_7 and Mn_4Si_7–Si(Mn)–M heterostructures, Appl. Sol. Energy. 55 (6) (2019) 380–384.
13. **Rysbaev A. S., Khujaniyozov J. B., Bekpulatov I. R., et al.,** Effect of thermal and laser annealing on the atom distribution profiles in Si (111) implanted with P^+ and B^+ ions, J. Surf. Invest.: X-ray, Synchrotron Neutron Tech. 11 (2) (2017) 474–479.
14. **Shcheulin A. S., Kupchikov A. K., Angervaks A. E., et al.,** Radio-frequency response of semiconducting CdF_2:In crystals with Schottky barriers, Phys. Rev. B. 63 (20) (2001) 205207.
15. **Sorokin L. M., Kyutt R. N., Ratnikov V. V., Kalmykov A. E.,** Structural characterization of a short-period superlattice based on the CdF_2/CaF_2/ Si (111), Tech. Phys. Lett. 47 (12) (2021) 893–896.
16. **Ryskin A. I., Shcheulin A. S., Angervaks A. E.,** Semiconductor CdF_2: Ga and CdF_2 in crystals as media for real-time holography, Mater. 5 (5) (2012) 784–817.
17. **Kazansky S. A., Ryskin A. I.,** Clusters of group-III ions in activated fluorite-type crystals, Phys. Solid State. 44 (8) (2002) 1415–1425.
18. **Varlamov A. G., Ulanov V. A.,** Donornaya provodimost' cristalla CdF_2:V^{3+}, otozhonnogo v vakuume [Donor conductivity of the vacuum-annealed CdF_2:V^{3+} crystal], Izvestiya Vysshikh Uchebnykh Zavedenii Rossii. Problemy Energetiki [Energy Problems]. (9–10) (2006) 100–104 (in Russian).

19. **Rodnyĭ P. A., Khodyuk I. V., Stryganyuk G. B.,** Location of the energy levels of the rare-earth ions in BaF_2 and CdF_2, Phys. Solid State. 50 (9) (2008) 1639–1643.

20. **Dorenbos P.,** Systematic behaviour in trivalent lanthanide charge transfer energies, J. Phys. Cond. Matter. 15 (49) (2003) 8417–8434.

21. **Bagraev N. T., Gimbitskaya O. N., Klyachkin L. E., et al.,** Quantum Hall effect in (cadmium fluoride)-based nanostructures, Semicond. 43 (1) (2009) 75–77.

22. **Umirzakov B. E., Pugacheva T. S., Tashatov A. K., Tashmuchamedova D. A.,** Electronic structure and optical properties of CaF_2 films under low energy Ba^+ ion-implantation combined with annealing, Nucl. Instr. and Meth. B. 166–167 (2 May) (2000) 572–576.

23. **Umirzakov B. E., Tashmukhamedova D. A., Muradkabilov D. M., Boltaev Kh. Kh.,** Electron spectroscopy of the nanostructures created in Si, GaAs, and CaF_2 surface layers using low-energy ion implantation, Tech. Phys. 58 (6) (2013) 841–844.

24. **Umirzakov B. E., Tashatov A. K., Tashmukhamedova D. A., Normuradov M. T.,** Protsess formirovaniya nanoplyonok na poverkhnosti CaF_2 pri ionnoy implantatsii i posleduyushchem otzhige [Nanofilm formation process on the CaF_2 surface during ion implantation and subsequent annealing], Poverkhnost'. Rentgenovskie, Sinkhronnye i Nejtronnye Issledovaniya [Surface. X-ray, Synchrotron and Neutron Investigations]. (12) (2004) 90–94 (in Russian).

25. **Umirzakov B. E., Tashmukhamedova D. A., Ruzibaeva M. K., et al.,** Investigation of change of the composition and structure of the CdF_2/Si films surface at the low-energy bombardment, Nucl. Instr. and Meth. B. 326 (1 May) (2014) 322–325.

26. **Tashmukhamedova D. A., Yusupjanova M. B.,** Emission and optical properties of SiO_2/Si films, J. Surf. Invest.: X-ray, Synchrotron Neutron Tech. 10 (6) (2016) 1273–1275.

27. **Abduvayitov A. A., Boltaev Kh. Kh., Rozikov G. A.,** Study of the composition of uncontrolled impurities and the profiles of their distribution at the Ni–CdS interface, J. Surf. Invest.: X-ray, Synchrotron Neutron Tech. 16 (5) (2022) 860–863.

СПИСОК ЛИТЕРАТУРЫ

1. **Sugiyama M., Oshima M.** MBE growth of fluorides // Microelectronics Journal. 1996. Vol. 27. No. 4–5. Pp. 361–382.

2. **Weng J., Gao Sh.-P.** Layer-dependent band gaps and dielectric constants of ultrathin fluorite crystals // Journal of Physics and Chemistry of Solids. 2021. Vol. 148. January. P. 109738.

3. **Illarionov Y. Y., Vexler M. I., Suturin S. M., Fedorov V. V., Sokolov N. S., Tsutsui K., Takahashi K.** Electron tunneling in MIS capacitors with the MBE-grown fluoride layers on Si (111) and Ge (111): Role of transverse momentum conservation // Microelectronic Engineering. 2011. Vol. 88. No. 7. Pp. 1291–1294.

4. **Банщиков А. Г., Илларионов Ю. Ю., Векслер М. И., Wachter S., Соколов Н. С.** Характер изменения обратного тока в туннельных МДП-диодах с фторидом кальция на Si (111) при создании дополнительного оксидного слоя // Физика и техника полупроводников. 2019. Т. 53. № 6. С. 844–849.

5. **Izumi A., Kawabata K., Tsutsui K., Sokolov N. S., Novikov S. V., Khilko A. Yu.** Growth of $CdF_2CaF_2Si(111)$ heterostructure with abrupt interfaces by using thin CaF_2 buffer layer // Applied Surface Science. 1996. Vol. 104–105. 2 September. Pp. 417–421.

6. **Sokolov N. S., Suturin S. M.** MBE-growth peculiarities of fluoride (CdF_2–CaF_2) thin film structures // Thin Solid Films. 2000. Vol. 367. No. 1–2. Pp. 112–119.

7. **Mir A., Zaoui A., Bensaid D.** The displacement effect of a fluorine atom in CaF_2 on the band structure // Applied Surface Science. 2018. Vol. 439. 1 May. Pp. 1180–1185.

8. **Li Zh., Baskurt M., Sahin H., Gao S., Kang J.** Electronic properties of intrinsic vacancies in single-layer CaF_2 and its heterostructure with monolayer MoS_2 // Journal of Applied Physics. 2021. Vol. 130. No. 5. P. 055301.

9. **Калугин А. И., Соболев В. В.** Оптические свойства CdF_2 в широкой области энергии // Журнал технической физики. 2004. Т. 74. № 3. С. 58–61.

10. **Bekpulatov I. R., Imanova G. T., Kamilov T. S., Igamov B. D., Turapov I. Kh.** Formation of *n*-type CoSi monosilicide film which can be used in instrumentation // International Journal of Modern Physics B. 2023. Vol. 37. No. 17. P. 22350164.

11. **Bekpulatov I. R., Shomukhammedova D. S., Shukurova D. M., Ibragimova B. V.** Obtaining higher manganese silicide films with high thermoelectric properties // E3S Web of Conferences. 2023. Vol. 365. 30 January. Article No. 05015 (7 p).

12. **Kamilov T. S., Rysbaev A. S., Klechkovskaya V. V., Orekhov A. S., Igamov B. D., Bekpulatov I. R.** The influence of structural defects in silicon on the formation of photosensitive Mn_4Si_7–Si(Mn)–Mn_4Si_7 and Mn_4Si_7–Si(Mn) –M heterostructures // Applied Solar Energy. 2019. Vol. 55. No. 6. Pp. 380–384.

13. **Рысбаев А. С., Хужаниязов Ж. Б., Бекпулатов И. Р., Рахимов А. М., Пардаев О. Р.** Исследование влияния термического и лазерного отжига на профили распределения атомов в Si (111), имплантированного ионами P^+ и B^+ // Поверхность. Рентгеновские, синхротронные и нейтронные исследования. 2017. № 4. С. 98–103.

14. **Shcheulin A. S., Kupchikov A. K., Angervaks A. E., Onopko D. E., Ryskin A. I., Ritus A. I., Pronin A. V., Volkov A. A., Lunkenheimer P., Loidl A.** Radio-frequency response of semiconducting CdF_2: In crystals with Schottky barriers // Physical Review B. 2001. Vol. 63. No. 20. P. 205207.

15. **Сорокин Л. М., Кютт Р. Н., Ратников В. В., Калмыков А. Е.** Структурная характеризация короткопериодной сверхрешетки на основе гетероструктуры CdF_2/CaF_2/Si(111) методами просвечивающей электронной микроскопии и рентгеновской дифрактометрии // Письма в Журнал технической физики. 2021. Т. 47. № 15. С. 3–6.

16. **Ryskin A. I., Shcheulin A. S., Angervaks A. E.** Semiconductor CdF_2: Ga and CdF_2 in crystals as media for real-time holography // Materials (Basel). 2012. Vol. 5. No. 5. Pp. 784–817.

17. **Казанский С. А., Рыскин А. И.** Кластеры ионов III группы в активированных кристаллах типа флюорита // Физика твердого тела. 2002. Т. 44. № 8. С. 1356–1366.

18. **Варламов А. Г., Уланов В. А.** Донорная проводимость кристалла $CdF_2:V^{3+}$, отожженного в вакууме // Известия высших учебных заведений. Проблемы энергетики. 2006. № 9–10. С. 100–104.

19. **Родный П. А., Ходюк И. В., Стрыганюк Г. Б.** Энергетическое положение редкоземельных ионов в BaF_2 и CdF_2 // Физика твердого тела. 2008. Т. 50. № 9. С. 1578–1581.

20. **Dorenbos P.** Systematic behaviour in trivalent lanthanide charge transfer energies // Journal of Physics: Condensed Matter. 2003. Vol. 15. No. 49. Pp. 8417–8434.

21. **Баграев Н. Т., Гимбицкая О. Н., Клячкин Л. Е., Маляренко А. М., Шелых И. А., Рыскин А. И., Щеулин А. С.** Квантовый эффект Холла в наноструктурах на основе фторида кадмия // Физика и техника полупроводников. 2009. Т. 43. № 1. С. 844–849.

22. **Umirzakov B. E., Pugacheva T. S., Tashatov A. K., Tashmuchamedova D. A.** Electronic structure and optical properties of CaF_2 films under low energy Ba^+ ion-implantation combined with annealing // Nuclear Instruments and Methods in Physics Research B. 2000. Vol. 166–167. 2 May. Pp. 572–576.

23. **Умирзаков Б. Е., Ташмухамедова Д. А., Мурадкабилов Д. М., Болтаев Х. Х.** Электронная спектроскопия наноструктур, созданных в поверхностных слоях Si, GaAs и CaF_2 методом низкоэнергетической ионной имплантации // Журнал технической физики. 2013. Т. 83. № 6. С. 66–70.

24. **Умирзаков Б. Е., Ташатов А. К., Ташмухамедова Д. А., Нормурадов М. Т.** Процесс формирования нанопленок на поверхности CaF_2 при ионной имплантации и последующем отжиге // Поверхность. Рентгеновские, синхротронные и нейтронные исследования. 2004. № 12. С. 90–94.

25. **Umirzakov B. E., Tashmukhamedova D. A., Ruzibaeva M. K., Djurabekova F. G., Danaev S. B.** Investigation of change of the composition and structure of the CdF_2/Si films surface at the low-energy bombardment // Nuclear Instruments and Methods in Physics Research B. 2014. Vol. 326. 1 May. Pp. 322–325.

26. **Ташмухамедова Д. А., Юсупжанова М. Б.** Эмиссионные и оптические свойства тонких пленок SiO_2/Si // Поверхность. Рентгеновские, синхротронные и нейтронные исследования. 2016. № 12. С. 89–91.

27. **Abduvayitov A. A., Boltaev Kh. Kh., Rozikov G. A.** Study of the composition of uncontrolled impurities and the profiles of their distribution at the Ni–CdS interface // Journal of Surface Investigation: X-ray, Synchrotron and Neutron Techniques. 2022. Vol. 16. No. 5. Pp. 860–863.

THE AUTHORS

ABDUVAYITOV Akbarjon A.
Tashkent State Technical University Named after Islam Karimov
2 Universitet St., Tashkent, 100095, Uzbekistan
akbarjon.abduvayitov@gmail.com
ORCID: 0000-0001-6453-6523

TASHMUKHAMEDOVA Dilnoza A.
Tashkent State Technical University Named after Islam Karimov
2 Universitet St., Tashkent, 100095, Uzbekistan
d.ftmet@gmail.com
ORCID: 0000-0001-5813-7518

UMIRZAKOV Boltakhodja E.
Tashkent State Technical University Named after Islam Karimov
2 Universitet St., Tashkent, 100095, Uzbekistan
be.umirzakov@gmail.com
ORCID: 0000-0002-9815-2111

KHUJANIYOZOV Jumanazar B.
Tashkent State Technical University Named after Islam Karimov
2 Universitet St., Tashkent, 100095, Uzbekistan
KhujaniyozovJB@mail.ru
ORCID: 0000-0001-6067-8196

BEKPULATOV Ilkhom R.
Karshi State University
17 Kuchabog St., Karshi,180119, Uzbekistan
bekpulatov85@rambler.ru
ORCID: 0000-0001-7955-3932

LOBODA Vera V.
Peter the Great St. Petersburg Polytechnic University
29 Politechnicheskaya St., St. Petersburg, 195251, Russia
vera_loboda@mail.ru
ORCID: 0000-0003-3103-7060

СВЕДЕНИЯ ОБ АВТОРАХ

АБДУВАЙИТОВ Акбаржон Абдумаджитович – *кандидат физико-математических наук, доцент кафедры общей физики Ташкентского государственного технического университета, г. Ташкент, Узбекистан.*
100095, Узбекистан, г. Ташкент, Университетская ул., 2.
akbarjon.abduvayitov@gmail.com
ORCID: 0000-0001-6453-6523

ТАШМУХАМЕДОВА Дилноза Артикбаевна – *доктор физико-математических наук, профессор кафедры общей физики Ташкентского государственного технического университета имени Ислама Каримова, г. Ташкент, Узбекистан.*
100095, Узбекистан, г. Ташкент, Университетская ул., 2
d.ftmet@gmail.com
ORCID: 0000-0001-5813-7518

УМИРЗАКОВ Балтоходжа Ерматович – *доктор физико-математических наук, профессор кафедры общей физики Ташкентского государственного технического университета имени Ислама Каримова, г. Ташкент, Узбекистан.*
100095, Узбекистан, г. Ташкент, Университетская ул., 2
be.umirzakov@gmail.com
ORCID: 0000-0002-9815-2111

ХУЖАНИЁЗОВ Джуманазар Бобокулович – *кандидат физико-математических наук, доцент кафедры общей физики Ташкентского государственного технического университета, г. Ташкент, Узбекистан.*
100095, Узбекистан, г. Ташкент, Университетская ул., 2.
KhujaniyozovJB@mail.ru
ORCID: 0000-0001-6067-8196

БЕКПУЛАТОВ Ильхом Рустамович – *доктор физико-математических наук, проректор по научной работе и инновациям Каршинского государственного университета, г. Карши, Узбекистан.*
180119, Узбекистан, г. Карши, ул. Кучабог, 17
bekpulatov85@rambler.ru
ORCID: 0000-0001-7955-3932

ЛОБОДА Вера Владимировна – *кандидат физико-математических наук, директор Высшей школы электроники и микросистемной техники Санкт-Петербургского политехнического университета Петра Великого, Санкт-Петербург, Россия.*
195251, Россия, г. Санкт-Петербург, Политехническая ул., 29
vera_loboda@mail.ru
ORCID: 0000-0003-3103-7060

Received 09.12.2023. Approved after reviewing 19.04.2024. Accepted 19.04.2024.
Статья поступила в редакцию 09.12.2023. Одобрена после рецензирования 19.04.2024. Принята 19.04.2024.

© Санкт-Петербургский политехнический университет Петра Великого, 2024

Original article
DOI: https://doi.org/10.18721/JPM.17309

INFLUENCE OF LOW-ENERGY ELECTRON BOMBARDMENT ON THE COMPOSITION AND STRUCTURE OF THE GALLIUM PHOSPHIDE SURFACE

S. B. Donaev[1,2]✉, *G. M. ugli Shirinov*[1], *B. Y. Umirzakov*[1], *V. V. Loboda*[3]

[1] Tashkent state technical university named after Islam Karimov, Tashkent, Uzbekistan;

[2] Karshi State University, Karshi, Uzbekistan;

[3] Peter the Great St. Petersburg Polytechnic University, St. Petersburg, Russia

✉ sardor.donaev@gmail.com

Abstract. In the paper, the patterns of changes in the composition and structure of the surface layers of GaP(111) in bombardment by electrons with energies from 3 to 10 keV and doses in the range 10^{17}–10^{20} cm^{-2} have been studied using the method of Auger electron spectroscopy and recording the angular dependence of the electron inelastic reflection coefficient. It was established that the surface layers of GaP were enriched with P atoms at E = 3 keV, and with Ga atoms at E = 10 keV. In both cases, the Ga atoms distribution profiles over the depth the sample were non-monotonic. The electron energy value at which an inversion of the surface composition took place was estimated. An analysis of the results obtained was given.

Keywords: Auger electron spectroscopy, nanosized phase, electron bombardment, surface concentration of atoms

Citation: Donaev S. B., Shirinov G. M. ugli, Umirzakov B. Y., Loboda V. V., Influence of low-energy electron bombardment on the composition and structure of the gallium phosphide surface, St. Petersburg State Polytechnical University Journal. Physics and Mathematics. 17 (3) (2024) 97–104. DOI: https://doi.org/10.18721/JPM.17309

This is an open access article under the CC BY-NC 4.0 license (https://creativecommons.org/licenses/by-nc/4.0/)

Научная статья
УДК 544.227
DOI: https://doi.org/10.18721/JPM.17309

ВЛИЯНИЕ НИЗКОЭНЕРГЕТИЧЕСКОЙ ЭЛЕКТРОННОЙ БОМБАРДИРОВКИ НА СОСТАВ И СТРУКТУРУ ПОВЕРХНОСТИ ФОСФИДА ГАЛЛИЯ

С. Б. Донаев[1,2]✉, *Г. М. Ширинов*[1], *Б. Е. Умирзаков*[1], *В. В. Лобода*[3]

[1] Ташкентский государственный технический университет им. Ислама Каримова, г. Ташкент, Узбекистан;

[2] Каршинский государственный университет, г. Карши, Узбекистан;

[3] Санкт-Петербургский политехнический университет Петра Великого, Санкт-Петербург, Россия

✉ sardor.donaev@gmail.com

Аннотация. В работе изучены закономерности изменения состава и структуры поверхностных слоев GaP (111) при бомбардировке электронами с энергиями E_e = 3 – 10 кэВ и дозами D = 10^{17} – 10^{20} см$^{-2}$. Для этого использован метод оже-электронной спектроскопии и регистрация угловой зависимости коэффициента неупругого отражения электронов. Установлено, что при E_e = 3 кэВ поверхностные слои GaP обогащаются атомами P, а случае E_0 = 10 кэВ – атомами Ga. В обоих случаях

© Donaev S. B., Shirinov G. M. ugli, Umirzakov B. Y., Loboda V. V., 2024. Published by Peter the Great St. Petersburg Polytechnic University.

профили распределения атомов Ga по глубине образца имеют немонотонный характер. Оценено значение энергии электронов, при котором происходит инверсия состава поверхности. Дан анализ полученных результатов.

Ключевые слова: оже-электронная спектроскопия, наноразмерная фаза, электронная бомбардировка, поверхностная концентрация атомов

Ссылка для цитирования: Донаев С. Б., Ширинов Г. М., Умирзаков Б. Е., Лобода В. В. Влияние низкоэнергетической электронной бомбардировки на состав и структуру поверхности фосфида галлия // Научно-технические ведомости СПбГПУ. Физико-математические науки. 2024. Т. 17. № 3. С. 97–104. DOI: https://doi.org/10.18721/JPM.17309

Статья открытого доступа, распространяемая по лицензии CC BY-NC 4.0 (https://creativecommons.org/licenses/by-nc/4.0/)

Introduction

Nanoscale heterostructures based on binary semiconductors, including gallium phosphide (GaP), are widely used and show potential for creating monolithic optoelectronic integrated circuits, photovoltaic cells, optical and electronic pumping lasers, as well as microwave electronics devices [1–6]. It is therefore important to accumulate data on the electronic, optical, emission and electrophysical properties of these structures and analyze various factors influencing their properties [7–10].

Diverse methods are used to modify the physical properties of binary compounds, including thermal heating, etching, laser irradiation as well as ion bombardment and implantation. Monolithic integrated circuits on substrate surface (silicon is commonly used) are typically fabricated by growing epitaxial films with a direct bandgap transition [1, 11].

GaAlP and GaAlAs nanophases and nanofilms were obtained in [12–14] by implantation of Al^{3+} ions into gallium phosphide and arsenide (GaP (111) and GaAs (111)). It was found that quantum-size effects appear for GaAlP nanophases with surface dimensions less than 35–40 nm and thicknesses of 3.5–4.0 nm. Due to the large bandgap in GaAsP (2.26 eV) and favorable displacements of the valence band and the conduction band [15, 16], the efficiency of GaAsP/Si-based solar cells can theoretically reach 41.9% [17].

Experimental studies and computer simulation were carried out in recent years on the effect of ion bombardment of inert gases on the composition and surface structure of GaP and InGaP films [18, 19].

For example, the effect of surface defects on the trajectory of dechanneled ions and its dependence on the energy and scattering angle of these ions was studied in [19]. It was established experimentally that metallization of $CoSi_2$ and GaP surfaces occurs upon bombardment with Ar^+ ions [18].

Thus, the effects of ion bombardment, heating, and laser irradiation on the composition and physical properties of A^3B^5 single crystals are well-understood. However, the effect of electron bombardment on the composition and structure of single-crystal gallium phosphide samples remains virtually unexplored.

The goal of this paper is to analyze the effect of electron bombardment on the composition and structure of the surface layer of single-crystal gallium phosphide GaP (111).

Experimental procedure

Single crystal GaP (111) samples with a diameter of about 10 mm and a thickness of 1 mm were selected as the object of study. The samples were studied by Auger electron spectroscopy (AES) and ultraviolet photoelectron spectroscopy to record the angular dependences of inelastic electron backscattering coefficients. The depth distribution profiles of embedded atoms were obtained by Auger analysis performed by sputtering 1 keV Ar^+ ions over the sample surface; the ion incidence angle was approximately 80–85° relative to normal, the etch rate of the surface was about 5 ± 1 E/min.

© Донаев С. Б., Ширинов Г. М., Умирзаков Б. Е., Лобода В. В., 2024. Издатель: Санкт-Петербургский политехнический университет Петра Великого.

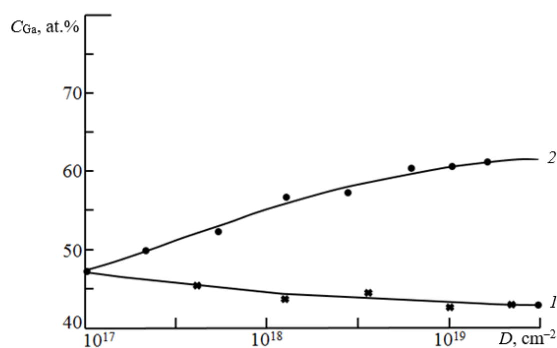

Fig. 1. Surface concentration of Ga atoms as function of electron irradiation dose for GaP surface bombarded by electrons with energies E_e = 3 keV (*1*) and 10 keV (*2*)

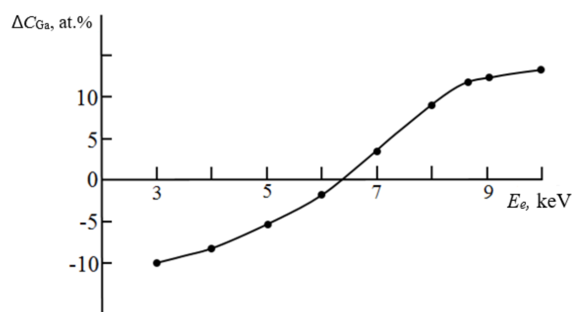

Fig. 2. Relative surface concentration of Ga atoms as function of electron bombardment energy E_e = 3–10 keV at $D = D_s$

Results and discussion

GaP surface was bombarded by electrons with energies E_e in the range of 3–10 keV at doses D ranging from 10^{17} to 10^{20} cm^{-2} and current density j of the order of $5\cdot10^{16}$ electrons/cm^2. No noticeable changes were observed in the composition and structure of GaP surface of gallium phosphide with an increase in the dose to the level $D \approx 10^{18}$ cm^{-2}. Fig. 1 shows the dependences of surface concentration C_{Ga} of gallium atoms on the radiation dose D for GaP bombarded with electrons with energies of 3 and 10 keV. It can be seen for the energy E_e = 3 keV that the surface concentration C_{Ga} decreases monotonically 8–10 at.% in the dose range $D = 10^{17}$–10^{19} cm^{-2}, i.e., the surface is enriched with phosphorus atoms. At E_e = 10 keV, C_{Ga} increases by 12–15 at.% with an increase in dose from 10^{17} to $5\cdot10^{19}$ cm^{-2}. In both cases, a further increase in dose does not lead to a change in the magnitude of C_{Ga}, i.e., the corresponding dependence curve reaches saturation. At E_e = 3 keV, the saturation dose D_s is 10^{19} cm^{-2}, while $D_s \approx 5\cdot10^{19}$ cm^{-2} at E_e = 10 keV. Thus, the surface concentration C_{Ga} at dose $D = D_s$ may decrease or increase depending on the energy E_e.

Fig. 2 shows the dependence of relative surface concentration ΔC_{Ga} on the energy E_e in the range E_e = 3–10 keV at $D = D_s$. It can be seen that the curve of this dependence passes through zero in the range E_e = 6–7 keV. The variation rate of ΔC_{Ga} decreases starting from $E_e \approx 9$ keV. GaP decomposes into its constituent atoms in the process of electron bombardment, and surface disordering occurs in the near-surface region of GaP.

The degree of surface disordering was estimated from the angular dependences of the inelastic electron backscattering coefficient η at E_{dis} = 800 eV; this coefficient is denoted as η_{800} in Fig. 3. The escape depth of inelastically backscattered electrons was about 100–120 E. As evident from Fig. 3, the curve η(φ) of unirradiated GaP (111) shows pronounced peaks due to inelastic backscattering of electrons from different crystal planes. A significant decrease in the absorption intensity and the shift in the main peaks were observed after irradiation with electrons with E_e = 3 keV. Complete disordering of the layers likely did not occur. At E_e = 10 keV, the peaks on the η(φ) curves were completely smoothed out, which is typical for amorphized films.

The changes in GaP composition in the near-surface layer during electron bombardment were estimated by recording the distribution profiles of Ga atoms at $D = D_s$ over the depth h of the sample (Fig. 4). Evidently, at E_e = 3 keV, the relative concentration ΔC_{Ga} did not change considerably up to a depth of 15–20 E (see curve *1* in Fig. 4). The concentration increases monotonically from about –10 to +9 at.% in the range of depths $h \approx 20$–110 E; then, as the depth increases, it decreases approximately exponentially, approaching zero at $h \approx 160$–165 E. At E_e = 10 keV, the $\Delta C_{Ga}(h)$ curve decreases as it passes through zero, then through a minimum at $h \approx 200$ E, grows exponentially and finally approaches zero starting from $h \approx 250$ E.

Analysis of results obtained. The main changes in the composition and structure of surface and near-surface layers observed during electron bombardment occur at doses D not less than 10^{17} cm^{-2}. A noticeable decomposition of GaP into constituent atoms and disordering of surface layers occurs at $E_e \approx 3$ keV starting with a dose $D \approx 4\cdot10^{17}$ cm^{-2}, and at $E_e \approx 10$ keV starting with a dose $D \approx 10^{17}$ cm^{-2}. With an increase in the electron irradiation dose, the degree of disordering in surface layers of GaP increases both in the case of E_e = 3 keV and at E_e = 10 keV.

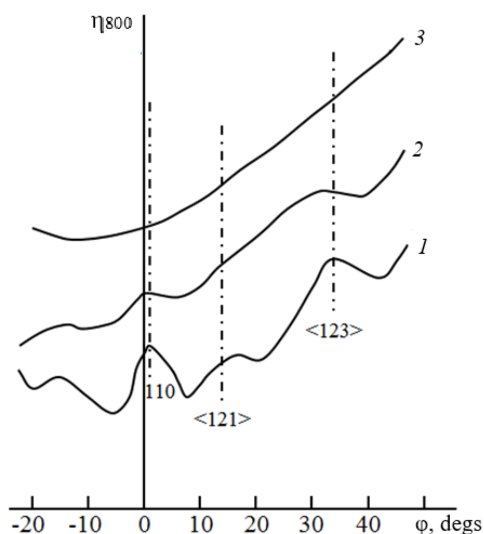

Fig. 3. Angular distribution of inelastic electron backscattering by GaP surface before bombardment (curve *1*); for GaP bombarded with 3 keV (curve *2*) and 10 keV (curve *3*) electrons

Vertical dash-dotted lines show the positions of the peaks on the curves associated with inelastic backscattering of electrons from various crystal planes of GaP. E_{dis} = 800 eV

Phosphorus atoms diffuse towards the surface in the process of electron bombardment due to the difference in the atomic masses of phosphorus and gallium (the atomic mass of P is smaller than the atomic mass of Ga). Apparently, only a small part of GaP molecules decomposes at an electron energy E_e = 3 keV, and there is no noticeable evaporation of atoms from the surface.

Thus, the surface layers are enriched with P atoms and depleted in Ga atoms at depths of no more than 50 E. As P atoms escape from the near-surface layer at $h \approx 50-90$ E, the concentration of Ga atoms in this layer increases (see Curve *1* in Fig. 4). This follows from the fact that the areas under the curves $-\Delta C_{\text{Ga}}(h)$ and $+\Delta C_{\text{Ga}}(h)$ are virtually identical. In the case of electron energy E_e = 10 keV, the main change in the composition occurs to depths $h \approx 250-300$ E. The majority of P atoms diffusing to the surface evaporate; this means that the surface layers are enriched with Ga atoms to a depth of 120–150 E. A small fraction of P atoms cannot diffuse up to the surface, and these atoms increase the concentration of phosphorus at depths of 160–240 E (see Curve *2* in Fig. 4).

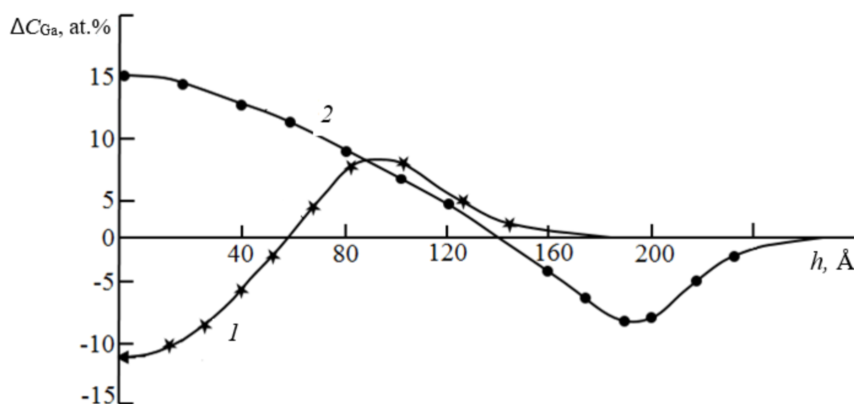

Fig. 4. Distribution profiles of Ga atoms over depth *h* of GaP sample bombarded by electrons with energies E_e = 3 keV (*1*) and 10 keV (*2*), at $D = D_s$

Conclusion

The study provides a first glimpse into the effect of electron bombardment on the composition and crystal structure of GaP (111) surface serving as a target in the electron energy range E_e = 3–10 keV. We detected the variations in the surface concentrations of gallium and phosphorus atoms and their depth distribution profiles depending on the energy and electron dose. It is established that at the surface region of GaP is enriched with phosphorus atoms at $E_e \leq 6$ keV, and with gallium atoms at $E_e \geq 6$ keV. According to the estimates obtained, the electron energy at which inversion of the composition of the surface layer occurs was approximately 6.4 keV.

Our findings can be useful for developing monolithic integrated circuits based on $A^{III}B^{V}$ compounds.

REFERENCES

1. **Lazarenko A. A., Nikitina E. V., Pirogov E. V., et al.,** Molecular beam epitaxy of GaPN, GaPAsN, and InGaPN nitride solid solutions, Semicond. 48 (3) (2014) 392–396.

2. **Yonezu H., Furukawa Y., Wakahara A.,** III–V epitaxy on Si for photonics applications, J. Cryst. Growth. 310 (23) (2008) 4757–4762.

3. **Egorov A. Yu., Kryzhanovskaya N. V., Sobolev M. S.,** Optical properties of quantum-confined heterostructures based on $GaP_xN_yAs_{1-x-y}$ alloys, Semicond. 45 (9) (2011) 1164–1168.

4. **Yonezu H.,** Control of structural defects in-group III–V–N alloys grown on Si, Semicond. Sci. Technol. 17 (8) (2002) 762–768.

5. **Ladugin M. A., Andreev A. Yu., Yarotskaya I. V., et al.,** Comparative study of GaAs/GaInP and GaAs/AlGaAs quantum wells grown by metalorganic vapor phase epitaxy, Inorg. Mater. 55 (4) (2019) 315–319.

6. **Razeghi M.,** Technology of quantum devices, Springer, New York, 2016.

7. **Plankina S. M., Vikhrova O. V., Zvonkov B. N., et al.,** On the combined application of Raman spectroscopy and photoluminescence spectroscopy for the diagnostics of multilayer heterostructures, Semicond. 53 (9) (2019) 1207–1210.

8. **Limmer W., Glunk M., Mascheck S., et al.,** Coupled plasmon-LO-phonon modes in $Ga_{1-x}Mn_xAs$, Phys. Rev. B. 66 (20) (2002) 205209.

9. **Bonera E., Fanciulli M., Batchelder D. N.,** Raman spectroscopy for a micrometric and tensorial analysis of stress in silicon, Appl. Phys. Lett. 81 (18) (2002) 3377–3379.

10. **Sobolev M. S., Lazarenko A. A., Nikitina E. V., et al.,** MBE growth of GaP on a Si substrate, Semicond. 49 (4) (2015) 559–562.

11. **Furykawa Y., Yoneza H., Wakahara A.,** Monolithic integration of light-emitting devices and silicon transistors, SPIE Newsroom. 19 Nov. 2007. https://spie.org/news/0914-monolithic-integration-of-light-emitting-devices-and-silicon-transistors#_=_.

12. **Donaev S. B., Umirzakov B. E., Tashmukhamedova D. A.,** Electronic structure of $Ga_{1-x}Al_xAs$ nanostructures grown on the GaAs surface by ion implantation, Tech. Phys. 60 (10) (2015) 1563–1566.

13. **Umirzakov B. E., Tashmukhamedova D. A., Muradkabilov D. M., Boltaev Kh. Kh.,** Electron spectroscopy of the nanostructures created in Si, GaAs, and CaF_2 surface layers using low-energy ion implantation, Tech. Phys. 58 (6) (2013) 841–844.

14. **Shirinov G. M., Donaev S. B., Umirzakov B. Y., Loboda V. V.,** Emission, optical and electrical properties of GaInP/GaP nanofilms, St. Petersburg State Polytechnical University Journal. Physics and Mathematics. 16 (2) (2023) 89–93.

15. **Feifel M., Ohlmann J., Benick J., et al.,** MOVPE grown gallium phosphide-silicon heterojunction solar cells, IEEE J. Photovolt. 7 (2) (2017) 502–507.

16. **Garcia-Tabares E., Martin D., Garcia I., et al.,** Optimization of the silicon subcell for III–V on silicon multijunction solar cells: Key differences with conventional silicon technology, AIP Conf. Proc. 1477 (2012) 5–9.

17. **Connolly J. P., Mencaraglia D., Renard C., Bouchier D.,** Designing III–V multijunction solar cells on silicon, Prog. Photovolt. Res. Appl. 22 (7) (2014) 810–820.

18. **Boltaev X. X., Tashmuhamedova D. A., Donaev S. B., Umirzakov B. E.,** Influence of bombardment of ions Ar^+ on property and structure of surface nanofilms $CoSi_2$/Si(111), Proc. of SIMS-2014, Munster, Germany; Sept. 7–9 (2014) 125.

19. **Kutliev U. O., Otabaev M. U., Karimov M. K., et al.,** Scattering of low-energy Ne^+ ions from the stepped surface of InGaP(001)<110> at the small angles of incidence, Phys. Chem. Solid State. 24 (3) (2023) 542–548.

СПИСОК ЛИТЕРАТУРЫ

1. **Лазаренко А. А., Никитина Е. В., Пирогов Е. В., Соболев М. С., Егоров А. Ю.** Молекулярно-пучковая эпитаксия азотсодержащих твердых растворов GaPN, GaPAsN и InGaPN // Физика и техника полупроводников. 2014. Т. 48. № 3. С. 407–411.

2. **Yonezu H., Furukawa Y., Wakahara A.** III–V epitaxy on Si for photonics applications // Journal of Crystal Growth. 2008. Vol. 310. No. 23. Pp. 4757–4762.

3. **Егоров А. Ю., Крыжановская Н. В., Соболев М. С.** Оптические свойства квантово-размерных гетероструктур на основе твердых растворов $GaP_xN_yAs_{1-x-y}$ // Физика и техника полупроводников. 2011. № 9. С. 1209–1213.

4. **Yonezu H.** Control of structural defects in-group III–V–N alloys grown on Si // Semiconductor Science and Technology. 2002. Vol. 17. No. 8. Pp. 762–768.

5. **Ладугин М. А., Андреев А. Ю., Яроцкая И. В., Рябоштан Ю. Л., Багаев Т. А., Падалица А. А., Мармалюк А. А., Васильев М. Г.** Сравнительный анализ квантовых ям GaAs/GaInP и GaAs/AlGaAs, полученных в условиях МОС-гидридной эпитаксии// Неорганические материалы. 2019. Т. 55. № 4. С. 345–349.

6. **Razeghi M.** Technology of quantum devices. New York: Springer, 2016. 560 p.

7. **Планкина С. М., Вихрова О. В., Звонков Б. Н., Зубков С. Ю., Крюков Р. Н., Нежданов А. В., Павлов Д. А., Пашенькин И. Ю., Сушков А. А.** Комплексное применение спектроскопии комбинационного рассеяния света и фотолюминесценции для диагностики многослойных гетероструктур // Физика и техника полупроводников. 2019. Т. 53. № 9. С. 1233–1236.

8. **Limmer W., Glunk M., Mascheck S., Koeder A., Klarer D., Schoch W., Thonke K., Sauer R., Waag A.** Coupled plasmon-LO-phonon modes in $Ga_{1-x}Mn_xAs$ // Physical Review B. 2002. Vol. 66. No. 20. P. 205209.

9. **Bonera E., Fanciulli M., Batchelder D. N.** Raman spectroscopy for a micrometric and tensorial analysis of stress in silicon // Applied Physics Letters. 2002. Vol. 81. No. 18. Pp. 3377–3379.

10. **Соболев М. С., Лазаренко А. А., Никитина Е. В., Пирогов Е. В., Гудовских А. С., Егоров А. Ю.** Молекулярно-пучковая эпитаксия GaP на подложке Si // Физика и техника полупроводников. 2015. Т. 49. № 4. С. 569–572.

11. **Furykawa Y., Yoneza H., Wakahara A.** Monolithic integration of light-emitting devices and silicon transistors // SPIE Newsroom. 2007. 19 November. https://spie.org/news/0914-monolithic-integration-of-light-emitting-devices-and-silicon-transistors#_=_.

12. **Данаев С. Б., Умирзаков Б. Е., Ташмухамедова Д. А.** Электронная структура наноразмерных структур $Ga_{1-x}Al_xAs$, созданных на поверхности GaAs методом ионной имплантации // Журнал технической физики. 2015. Т. 85. № 10. С. 148–151.

13. **Умирзаков Б. Е., Ташмухамедова Д. А., Мурадкабилов Д. М., Болтаев Х. Х.** Электронная спектроскопия наноструктур, созданных в поверхностных слоях Si, GaAs и CaF_2 методом низкоэнергетической ионной имплантации // Журнал технической физики. 2013. Т. 83. № 6. С. 66–70.

14. **Shirinov G. M., Donaev S. B., Umirzakov B. Y., Loboda V. V.** Emission, optical and electrical properties of GaInP/GaP nanofilms // St. Petersburg State Polytechnical University Journal. Physics and Mathematics. 2023. Vol. 16. No. 2. Pp. 89–93.

15. **Feifel M., Ohlmann J., Benick J., et al.** MOVPE grown gallium phosphide-silicon heterojunction solar cells // IEEE Journal of Photovoltaics. 2017. Vol. 7. No. 2. Pp. 502–507.

16. **Garcia-Tabares E., Martin D., Garcia I., Lelievre J. F., Rey-Stolle I.** Optimization of the silicon subcell for III-V on silicon multijunction solar cells: Key differences with conventional silicon technology // AIP Conference. Proceedings. 2012. Vol. 1477. Pp. 5–9.

17. **Connolly J. P., Mencaraglia D., Renard C., Bouchier D.** Designing III-V multijunction solar cells on silicon // Progress in Photovoltaics: Research and Application. 2014. Vol. 22. No. 7. Pp. 810–820.

18. **Boltaev X. X., Tashmuhamedova D. A., Donaev S. B., Umirzakov B. E.** Influence of bombardment of ions Ar^+ on property and structure of surface nanofilms $CoSi_2$/Si(111) // Proceedings of the Conference on Secondary Ion Mass Spectrometry (SIMS-2014). Munster, Germany, September 7–9, 2014. P. 125.

19. **Kutliev U. O., Otabaev M. U., Karimov M. K., Masharipov F. K., Woiciechowski I.** Scattering of low-energy Ne^+ ions from the stepped surface of InGaP(001)<110> at the small angles of incidence // Physics and Chemistry of Solid State. 2023. Vol. 24. No. 3. Pp. 542–548.

THE AUTHORS

DONAEV Sardor B.
Tashkent State Technical University Named after Islam Karimov,
Karshi State University
2, Universitetskaya St., Tashkent,100095, Uzbekistan
sardor.donaev@gmail.com
ORCID: 0000-0001-5656-126X

SHIRINOV Ganjimurod M. ugli
Tashkent State Technical University Named after Islam Karimov
2, Universitetskaya St., Tashkent,100095, Uzbekistan
ganjimurod777@gmail.com
ORCID: 0000-0002-7188-2560

UMIRZAKOV Baltokhodja Y.
Tashkent State Technical University Named after Islam Karimov
2, Universitetskaya St., Tashkent,100095, Uzbekistan
be.umirzakov@gmail.com
ORCID: 0000-0002-9815-2111

LOBODA Vera V.
Peter the Great St. Petersburg Polytechnic University
29 Politechnicheskaya St., St. Petersburg, 195251, Russia
vera_loboda@mail.ru
ORCID: 0000-0003-3103-7060

СВЕДЕНИЯ ОБ АВТОРАХ

ДОНАЕВ Сардор Бурханович – *доктор физико-математических наук, проректор по науке и инновациям* Ташкентского государственного технического университета имени Ислама Каримова.
100095, Узбекистан, г. Ташкент, Университетская ул., 2
sardor.donaev@gmail.com
ORCID: 0000-0001-5656-126X

ШИРИНОВ Ганжимурад Мамир угли – *докторант кафедры общей физики Ташкентского государственного технического университета имени Ислама Каримова*.
100095, Узбекистан, г. Ташкент, Университетская ул., 2
ganjimurod777@gmail.com
ORCID: 0000-0002-7188-2560

УМИРЗАКОВ Балтоходжа Ерматович – *доктор физико-математических наук, профессор кафедры общей физики Ташкентского государственного технического университета* имени Ислама Каримова.
100095, Узбекистан, г. Ташкент, Университетская ул., 2
be.umirzakov@gmail.com
ORCID: 0000-0002-9815-2111

ЛОБОДА Вера Владимировна – *кандидат физико-математических наук, директор Высшей школы электроники и микросистемной техники Санкт-Петербургского политехнического университета Петра Великого.*
195251, Россия, г. Санкт-Петербург, Политехническая ул., 29
vera_loboda@mail.ru
ORCID: 0000-0003-3103-7060

Received 19.02.2024. Approved after reviewing 09.04.2024. Accepted 09.04.2024.
Статья поступила в редакцию 19.02.2024. Одобрена после рецензирования 09.04.2024. Принята 09.04.2024.

© Peter the Great St. Petersburg Polytechnic University, 2024

MECHANICS

Original article
DOI: https://doi.org/10.18721/JPM.17310

AN ANALYSIS OF THE ACCURACY OF SHORT-WAVE AND LONG-WAVE ASYMPTOTICS FOR STATIONARY LAMB WAVES IN THE ISOTROPIC LAYER

Ya. K. Astapov, A. V. Lukin✉, *I. A. Popov*

Peter the Great St. Petersburg Polytechnic University, St. Petersburg, Russia

✉ lukin_av@spbstu.ru

Abstract. In the paper, the exact and asymptotic approximate solutions for symmetric and antisymmetric Lamb waves in the homogeneous isotropic elastic film have been analyzed. Using the numerical methods of the theory of continuation of solutions of nonlinear equations, the dispersion curves were calculated for waves with different variability across the layer thickness. Based on the results obtained, the nature of the displacement field and the variability of oscillation forms depending on the wave number were studied. The asymptotic correctness of the Timoshenko and Euler – Bernoulli beam models as long-wave asymptotics of Lamb waves was analyzed.

Keywords: Lamb waves, Euler–Bernoulli beam model, Timoshenko beam model, bifurcation theory

Funding: The research was supported by the Council on Grants of the President of the Russian Federation for state support of young scientists (Grant No. MK-4577.2022.1.1).

Citation: Astapov Ya. K., Lukin A. V., Popov I. A., An analysis of the accuracy of short-wave and long-wave asymptotics for stationary Lamb waves in the isotropic layer, St. Petersburg State Polytechnical University Journal. Physics and Mathematics. 17 (3) (2024) 105–117. DOI: https://doi.org/10.18721/JPM.17310

This is an open access article under the CC BY-NC 4.0 license (https://creativecommons.org/licenses/by-nc/4.0/)

Научная статья
УДК 534-16
DOI: https://doi.org/10.18721/JPM.17310

АНАЛИЗ ТОЧНОСТИ КОРОТКОВОЛНОВЫХ И ДЛИННОВОЛНОВЫХ АСИМПТОТИК ДЛЯ СТАЦИОНАРНЫХ ВОЛН ЛЭМБА В ИЗОТРОПНОМ СЛОЕ

Я. К. Астапов, А. В. Лукин✉, *И. А. Попов*

Санкт-Петербургский политехнический университет Петра Великого, Санкт-Петербург, Россия

✉ lukin_av@spbstu.ru

Аннотация. В работе анализируются точные и асимптотические приближенные решения для симметричных и антисимметричных волн Лэмба в однородном изотропном упругом слое. При помощи численного аппарата теории продолжения решений нелинейных уравнений вычислены дисперсионные кривые для волн с различной изменяемостью по толщине слоя. На основе полученных результатов исследован характер поля перемещений и изменчивость форм колебаний в зависимости от величины волнового числа. Проведен анализ асимптотической корректности балочных моделей Тимошенко, Бернулли – Эйлера как длинноволновых асимптотик волн Лэмба.

© Astapov Ya. K., Lukin A. V., Popov I. A., 2024. Published by Peter the Great St. Petersburg Polytechnic University.

Ключевые слова: волны Лэмба, модель балки Бернулли – Эйлера, модель балки Тимошенко, теория бифуркации

Финансирование: Работа выполнена при поддержке Совета по грантам Президента Российской Федерации для государственной поддержки молодых российских ученых (грант № МК4577.2022.1.1-).

Ссылка для цитирования: Астапов Я. К., Лукин А. В., Попов И. А. Анализ точности коротковолновых и длинноволновых асимптотик для стационарных волн Лэмба в изотропном слое // Научно-технические ведомости СПбГПУ. Физико-математические науки. 2024. Т. 17. № 3. С. 105–117. DOI: https://doi.org/10.18721/JPM.17310

Статья открытого доступа, распространяемая по лицензии CC BY-NC 4.0 (https://creativecommons.org/licenses/by-nc/4.0/)

Introduction

Modern requirements for new generation 5G TV and radio communication devices necessitate expanding the frequency range used to receive and transmit the signal. The ultrahigh frequency (UHF) range (over 6 GHz) is considered for this purpose. However, modern models of resonators used to generate and filter signals cannot operate at such high frequencies. Therefore, new models that ensure uninterrupted communication in a given range must be designed. While there are many types of elastic waves in solids, Lamb waves generated in thin layers show promise for solving this problem [1]. It was established that certain wave modes of this type are capable of transmitting microwave signal with minimal losses [2–4]. Numerous studies have considered this subject [5]. The design of electroacoustic transducers in a given frequency range under the constraints of microsystem technology relies on multiparametric calculations to select the optimal resonator configuration: layer thickness, electrode gap in interdigital transducers, orientation of a single crystal, etc. [6–9]. Furthermore, it is necessary to determine the specific operating modes of resonator vibrations (their variability across the layer thickness), providing the required values of the electromechanical coupling factor, additionally allowing for effective excitation by an electric field. The solutions for such problems can be obtained by combining qualitative analytical estimations based on simplified models with detailed numerical calculations based on verified procedures.

This paper reports on the qualitative study of stationary elastic Lamb waves in a homogeneous isotropic elastic layer. We performed a rigorous analytical study of the dispersion curves of symmetric and antisymmetric Lamb waves, their asymptotic analysis, direct numerical solution of the problem and comparison with known models of structural mechanics.

Mathematical model used

A homogeneous isotropic elastic layer oriented along the x_1 axis in length and along the x_3 axis in thickness is considered. The layer is assumed to be infinitely long with a thickness of $2h$ ($-h \le x_3 \le h$). The problem is considered in a plane strain statement. The schematic of the model is shown in Fig. 1.

A system of elastodynamics equations is considered:

$$\mu \nabla^2 \boldsymbol{u} + (\lambda + \mu)\,\mathrm{grad}(\mathrm{div}(\boldsymbol{u})) = \rho \ddot{\boldsymbol{u}}, \tag{1}$$

where λ, μ are the Lamé parameters, ρ is the density of the material, **u** is the vector of the displacement field.

It is known [10] that representing system of equations (1) as

$$\boldsymbol{u} = \mathrm{grad}\,\Phi + \mathrm{rot}\,\psi \tag{2}$$

reduces it to the system of wave equations:

© Астапов Я. К., Лукин А. В., Попов И. А., 2024. Издатель: Санкт-Петербургский политехнический университет Петра Великого.

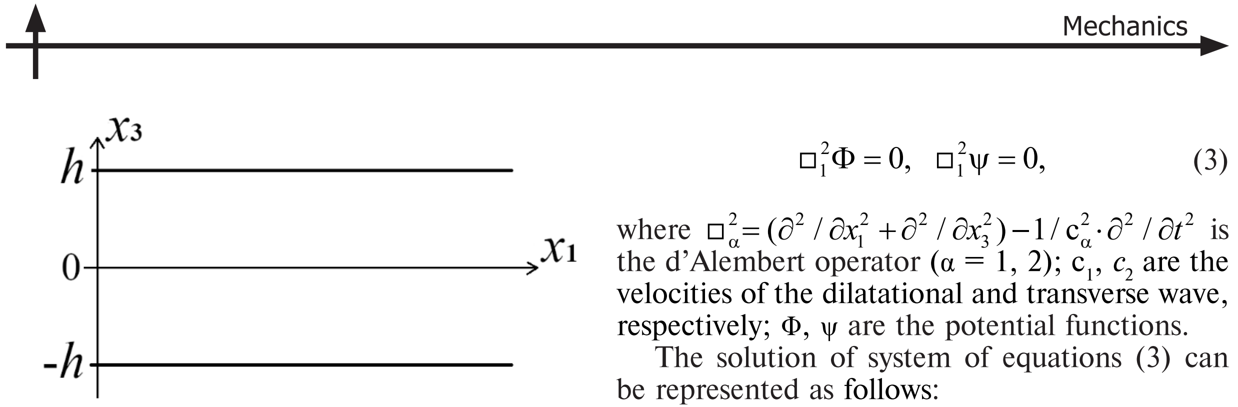

Fig. 1. Schematic of homogeneous isotropic thin layer; $2h$ is its thickness

$$\square_1^2\Phi = 0, \quad \square_1^2\psi = 0, \tag{3}$$

where $\square_\alpha^2 = (\partial^2/\partial x_1^2 + \partial^2/\partial x_3^2) - 1/c_\alpha^2 \cdot \partial^2/\partial t^2$ is the d'Alembert operator (α = 1, 2); c_1, c_2 are the velocities of the dilatational and transverse wave, respectively; Φ, ψ are the potential functions.

The solution of system of equations (3) can be represented as follows:

$$\begin{aligned} \Phi &= (A\sinh(\nu_1 x_3) + B\cosh(\nu_1 x_3))e^{ik(x_1 - ct)}, \\ \psi &= (C\sinh(\nu_2 x_3) + D\cosh(\nu_2 x_3))e^{ik(x_1 - ct)}, \end{aligned} \tag{4}$$

where k is the wavenumber, $\nu_\alpha = \sqrt{k^2 - k_\alpha^2}$ ($k_\alpha = \omega/c_\alpha$, α = 1, 2), ω is the frequency, c is the phase velocity.

The boundary conditions are dictated by the absence of stresses on the faces of the plate:

$$\sigma_{13}(x_1, \pm h, t) = 0, \quad \sigma_{33}(x_1, \pm h, t) = 0. \tag{5}$$

Applying boundary conditions (5) to solution (4), we obtain:

$$\begin{cases} 2i\beta_1(\cosh(\nu_1 h)A + \sinh(\nu_1 h)B) - (1+\beta_2^2)(\sinh(\nu_2 h)C + \cosh(\nu_2 h)D) = 0, \\ 2i\beta_1(\cosh(\nu_1 h)A - \sinh(\nu_1 h)B) + (1+\beta_2^2)(\sinh(\nu_2 h)C - \cosh(\nu_2 h)D) = 0, \\ [(\lambda+2\mu)\beta_1^2 - \lambda](\sinh(\nu_1 h)A + \cosh(\nu_1 h)B) + 2i\mu\beta_2(\cosh(\nu_2 h)C + \sinh(\nu_2 h)D) = 0, \\ [(\lambda+2\mu)\beta_1^2 - \lambda](-\sinh(\nu_1 h)A + \cosh(\nu_1 h)B) + 2i\mu\beta_2(\cosh(\nu_2 h)C - \sinh(\nu_2 h)D) = 0, \end{cases} \tag{6}$$

The notation $\beta_\alpha = \nu_\alpha/k$, ($\alpha$ = 2 ,1) is introduced here.

The solution of this system of algebraic equations is a family of dispersion curves for Lamb waves.

Symmetric waves

Consider a particular case of a symmetric wave. A wave is called symmetric when the particles of the medium make symmetrical horizontal and antisymmetric vertical movements relative to the cross-section midline. Thus, the vertical movements in the upper and lower half-spaces are oppositely directed and the cross-section midline (x_1 = 0) remains undeformed. Symmetric waves are generally denoted as S_0, S_1, S_2, ...

Then solution (4) takes the form

$$\begin{aligned} \Phi &= B\cosh(\nu_1 x_3)e^{ik(x_1 - ct)}, \\ \psi &= C\sinh(\nu_2 x_3)e^{ik(x_1 - ct)}. \end{aligned} \tag{7}$$

System (6) is simplified, taking the form

$$\begin{cases} 2i\beta_1\sinh(\nu_1 h)B) - (1+\beta_2^2)\sinh(\nu_2 h)C = 0, \\ [(\lambda+2\mu)\beta_1^2 - \lambda]\cosh(\nu_1 h)B) + 2i\mu\beta_2\cosh(\nu_2 h)C = 0. \end{cases} \tag{8}$$

Using the condition for the existence of a nontrivial solution of system (8), we obtain a transcendental equation of the form

$$\frac{\tanh(\nu_1 h)}{\tanh(\nu_2 h)} = \frac{(1+\beta_2^2)^2}{4\beta_1\beta_2}. \tag{9}$$

This equation takes a dimensionless form

$$\frac{\tanh(\tilde{k}\sqrt{1-\delta^2\tilde{c}^2})}{\tanh(\tilde{k}\sqrt{1-\tilde{c}^2})} = \frac{(2-\tilde{c}^2)^2}{4\sqrt{1-\delta^2\tilde{c}^2}\sqrt{1-\tilde{c}^2}}, \tag{10}$$

if we introduce the following notations:

$$\tilde{k} = kh,\ \tilde{c} = \frac{c}{c_2},\ \tilde{\omega} = \tilde{k}\cdot\tilde{c} = \frac{khc}{c_2},\ \delta = \frac{c_2}{c_1}. \tag{11}$$

Eq. (10) is transcendental with respect to the dimensionless phase velocity of the wave and the wavenumber. Limiting cases are known for Eq. (10) [11].

Consider the first limiting case when the traveling wave length is significantly greater than the plate thickness, i.e., $\lambda = 2\pi/k \gg 2h$. Then the hyperbolic tangents of Eq. (10) are replaced by their arguments. Transforming Eq. (10), we obtain:

$$4(1-\delta^2\tilde{c}^2) = (2-\tilde{c}^2),$$

$$\tilde{c} = 2\sqrt{1-\delta^2}.$$

Let $\mu = \lambda$ (i.e., Poisson's ratio $\nu = 1/4$). Then we can establish that $\delta^2 = 1/3$. As a result, we obtain the threshold value of the dimensionless phase velocity:

$$\tilde{c} = \tilde{c}_p = 2\sqrt{2/3} \approx 1.633\ldots. \tag{12}$$

Consider the second limiting case, when the wavelength is much smaller than the thickness, i.e., $\lambda = 2\pi/k \ll 2h$; then the tangent ratio can be assumed to equal unity. Transformation of Eq. (10) takes the following form:

$$(2-\tilde{c}^2)^2 = 4\sqrt{1-\delta^2\tilde{c}^2}\sqrt{1-\tilde{c}^2}. \tag{13}$$

This equality is the characteristic equation of Rayleigh surface waves [10]. The value of the phase velocity for $\delta^2 = 1/3$ is

$$\tilde{c} = \tilde{c}_R \approx 0.9194\ldots. \tag{14}$$

The solution of transcendental equation (10) was obtained by the numerical framework from the theory of continuation of solutions of nonlinear equations [11]. Fig. 2 shows the dispersion curves and the dependence of the phase velocity on the wavenumber for the first three branches of the wave solution at different values of Poisson's ratio.

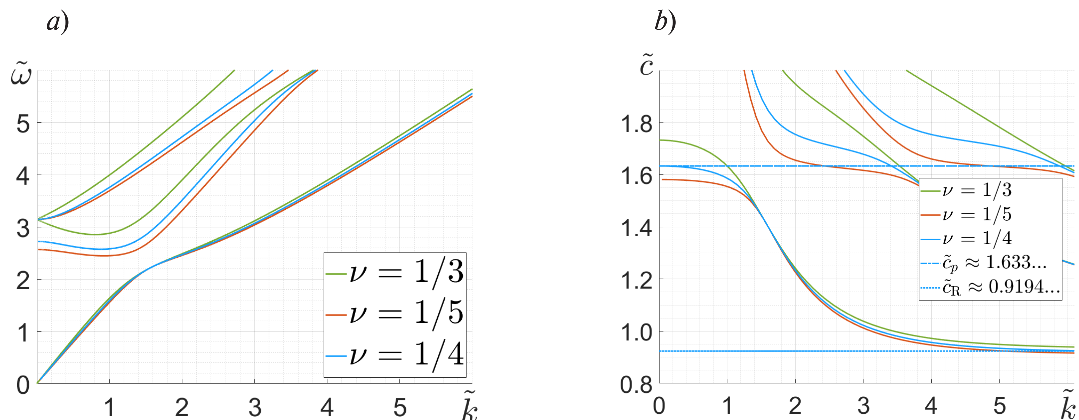

Fig. 2. Graphs for solution of Eq. (10): dispersion curves of symmetric Lamb waves (*a*); dependences of phase velocity (*b*) on wavenumber

Fig. 2,*b* confirms the correctness of both asymptotic estimates (long-wave and short-wave).

The fields of displacement in the layer were constructed for the results obtained. Their form was obtained by substituting solution (7) into Eq. (2). Fig. 3 shows the displacement fields of the first three wave modes at different values of the wavenumber: near the long-wave approximation ($\tilde{k}$ = 1) (*a*); for an arbitrary value ($\tilde{k}$ = 2) (*b*); near the short-wave approximation ($\tilde{k}$ = 6) (*c*). The displacement fields are constructed for a segment of an infinitely long plate (see Fig. 1); its segment = 2 pi/k corresponds to one period of wave oscillation. This value is plotted along the abscissa, the thickness of the plate is plotted along the ordinate.

The colored curves visualize the vertical displacements u_3, the grid visualizes the horizontal displacements u_1.

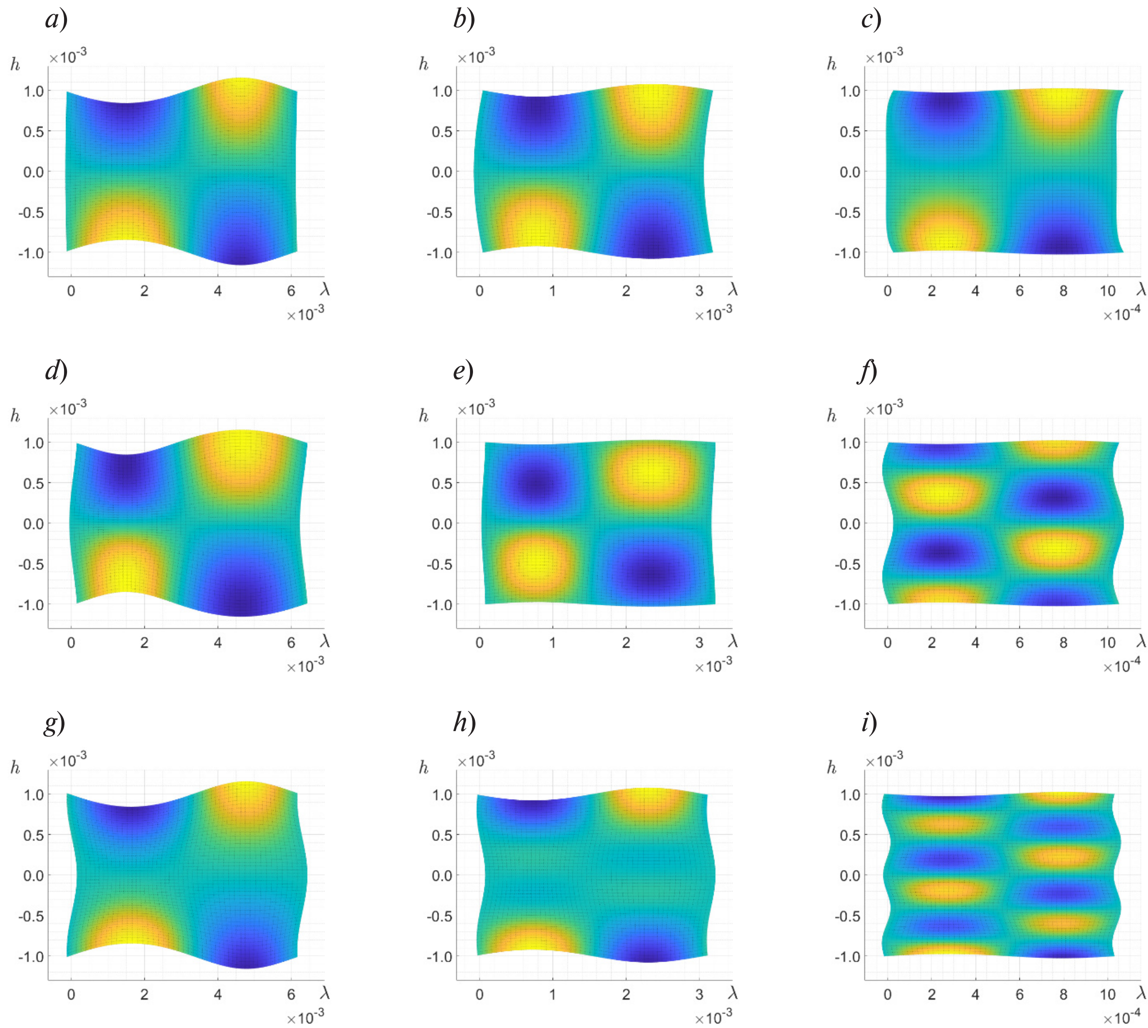

Fig. 3. Displacement fields for first three modes (*S*0, *S*1, *S*2) of symmetric waves at different wavenumbers $\tilde{k}$: mode *S*0 (*a*, *b*, *c*); mode *S*1 (*d*, *e*, *f*); mode *S*2 (*g*, *h*, *i*)

Analyzing the graphs, we can conclude that the number of fixed nodes increases with an increase in the value of the wavenumber in the layer. Notably, the point mass describes an elliptic trajectory during the oscillation period [12], while the behavior of the plate's eigenmode with increasing wavenumber is somewhat unexpected. This generates the additional problem of analyzing the variability of the wave mode with varying wavenumber. The results for the first three modes of symmetric waves are shown in Fig. 4.

As evident from Fig. 4,*b*, the behavior of the displacement field u_3 remains almost unchanged with varying wavenumber: a midline with no displacements is observed, while upper and lower half-spaces of the plate make antiphase oscillations along the x_3 axis. On the other hand, the

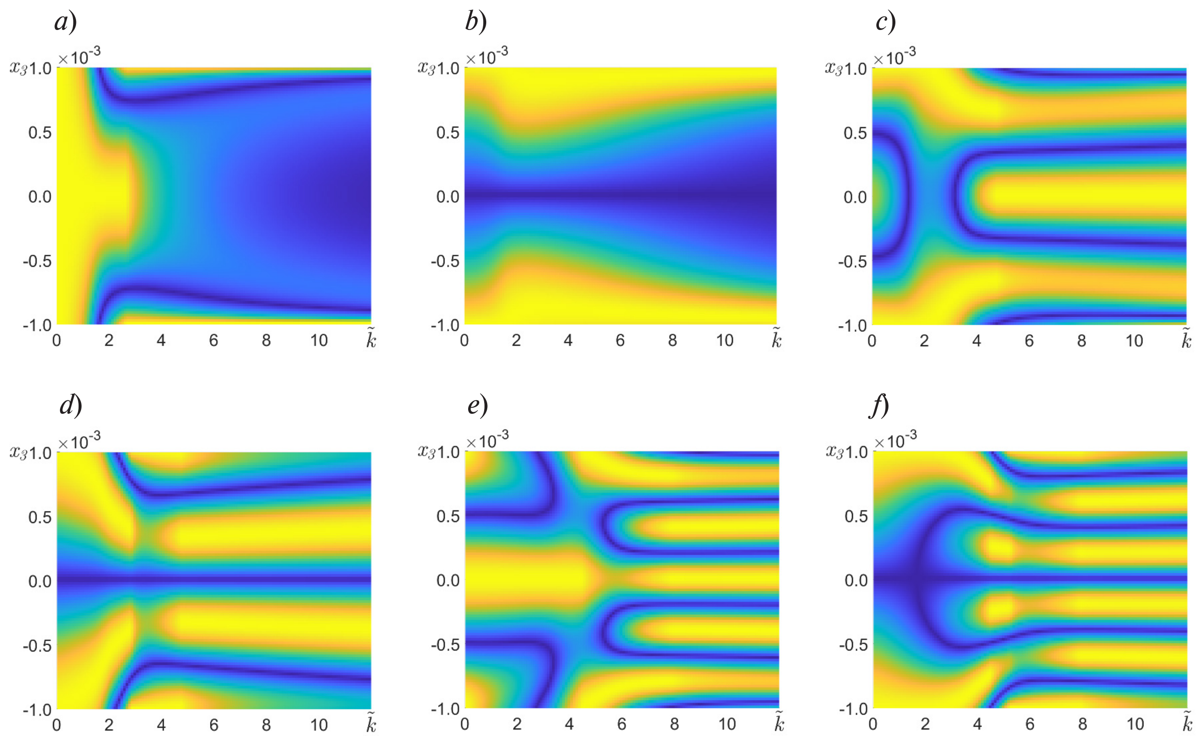

Fig. 4. Dependences of displacement fields u_1 (*a*, *c*, *e*) and u_3 (*b, d, f*) for three branches of solutions (*S*0, *S*1, *S*2) of symmetric wave versus wavenumber; branch *S*0 (*a*, *b*); branch *S*1 (*c*, *d*); branch *S*2 (*e*, *f*)

behavior of displacements u_1 changes: initially, strictly longitudinal oscillations in the horizontal direction are observed, but as the wavenumber $\tilde{k}$ approaches 1.75, a new node appears, so that antiphase oscillations in the horizontal direction are observed in the cross-section. It is also clear that the condition of the short-wave approximation is satisfied, namely, strong damping of oscillations in the bulk of the layer is observed with an increase in the wavenumber. The behavior of the second (see Fig. 4, *c*, *d*) and third (Fig. 4, *e*, *f*) wave modes changes dramatically in the long-wave approximation. On the other hand, this behavior is preserved for the wavenumber $\tilde{k} > 6$.

Antisymmetric waves

Consider the case of antisymmetric waves. A wave is called antisymmetric when the particles of the medium make antisymmetric horizontal and symmetric vertical movements relative to the cross-section midline. The vertical oscillations of the half-spaces occur in one direction, and the midline is deformed. Solution (4) takes the following form:

$$\begin{gathered}\Phi = A\sinh(\nu_1 x_3)e^{ik(x_1-ct)},\\ \psi = D\cosh(\nu_2 x_3)e^{ik(x_1-ct)}.\end{gathered} \tag{15}$$

System of equations (8) is written as follows for the obtained solutions (15):

$$\begin{cases} 2i\beta_1\cosh(\nu_1 h)A - (1+\beta_2^2)\cosh(\nu_2 h)D = 0,\\ [(\lambda+2\mu)\beta_1^2 - \lambda]\sinh(\nu_1 h)A + 2i\mu\beta_2\sinh(\nu_2 h)D = 0.\end{cases} \tag{16}$$

If we take the determinant of system (16) and perform non-dimensionalization (11), we obtain the following transcendental equation:

$$\frac{\tanh(\nu_1 h)}{\tanh(\nu_2 h)} = \frac{4\beta_1\beta_2}{(1+\beta_2^2)^2}. \tag{17}$$

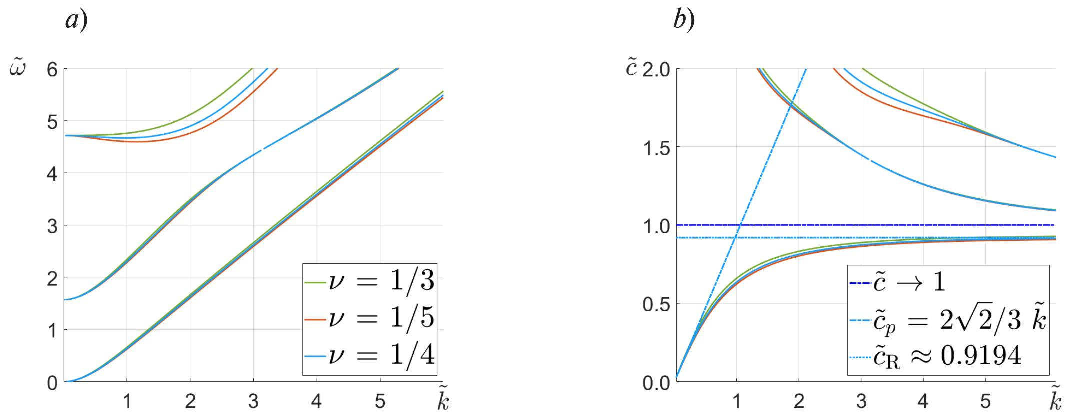

Fig. 5. Graphs for solution of Eq. (17): dispersion curves of antisymmetric Lamb waves (*a*); dependences of phase velocity on wavenumber (*b*)

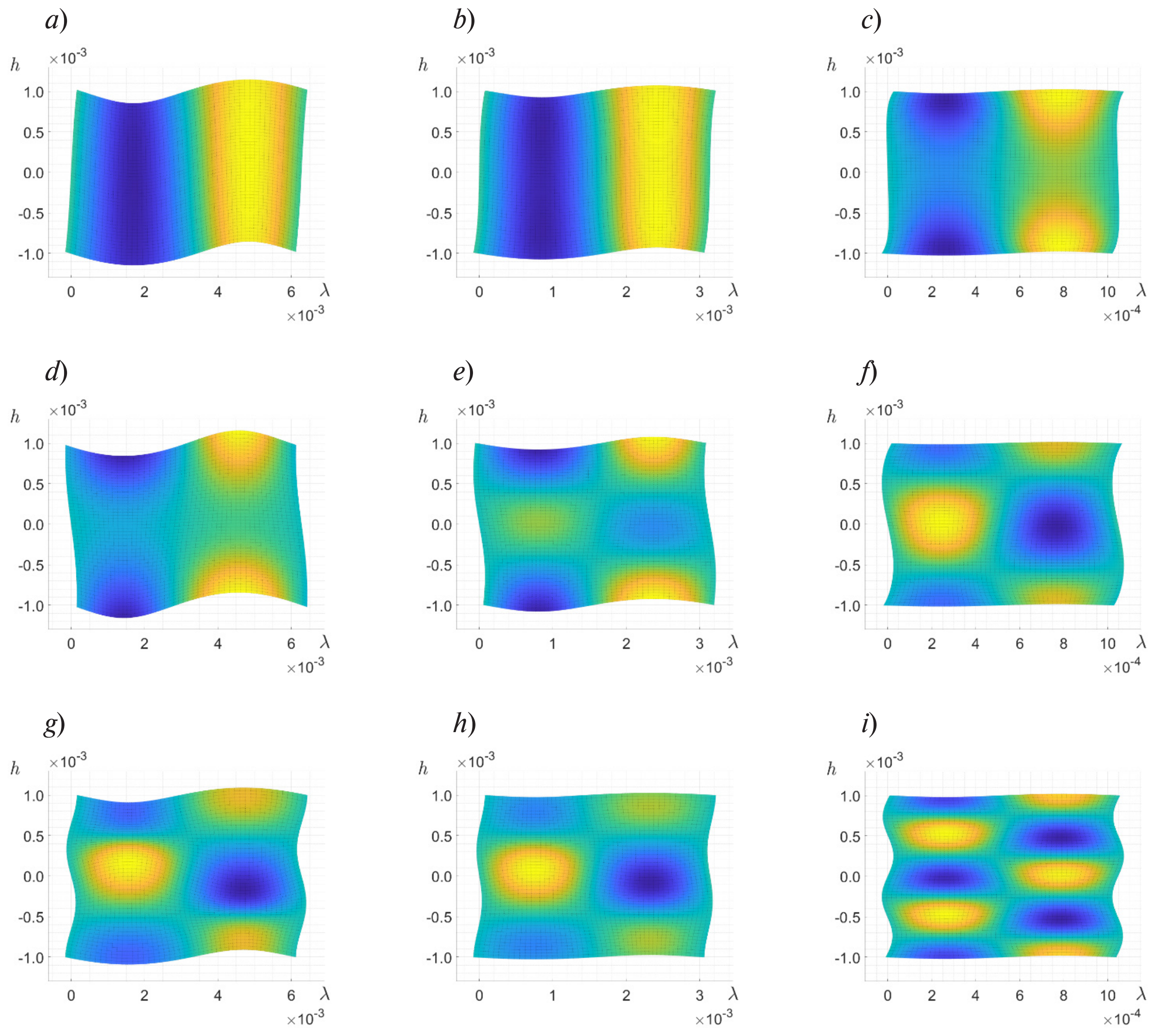

Fig. 6. Displacement fields of first three modes (*A*0, *A*1, *A*2) of antisymmetric waves at different wavenumbers $\tilde{k}$: mode *A*0 (a, *b*, *c*); mode *A*1 (*d*, *e*, *f*); mode *A*2 (*g*, *h*, *i*)

Consider the limiting cases for Eq. (17). If the wavelength significantly exceeds the thickness of the layer, the inequality $\tilde{c} < 1 < 1/\delta$ holds true. After all the transformations (in accordance with the data presented in [10]), the transcendental equation takes the following form:

$$\tilde{c}^2 = \frac{4}{3}\tilde{k}^2(1-\delta^2). \tag{18}$$

Let $\mu = \lambda$ (i.e., $\nu = 1/4$); then $\delta^2 = 1/3$, which implies that

$$\tilde{c}_p = \frac{2\sqrt{2}}{3}\tilde{k}. \tag{19}$$

Thus, we obtain a linear asymptote for the long-wave approximation from Eq. (19).

Consider another limiting case where the wavelength is much smaller than the plate thickness and the inequality $\tilde{c} < 1 < 1/\delta$ holds true. Transforming Eq. (17), we arrive again at the characteristic equation for Rayleigh surface waves (13), (14). The phase velocity for case $\tilde{c} > 1$ tends to 1.

Fig. 5 shows the dispersion curves of antisymmetric oscillations and the dependence of phase velocity on wavenumber. Evidently (see Fig. 5,*b*), the results obtained for the first branch of antisymmetric waves satisfy both approximations. It is assumed [10] that the phase velocity for the remaining modes tends to unity in the case of the short-wave approximation.

The same as for symmetric oscillations, displacement fields of antisymmetric oscillations were constructed (Fig. 6).

As seen from Fig. 6,*a*, the first mode of antisymmetric oscillations resembles bending vibrations of a beam. Also, similar to the symmetric case, a change in the wave mode is observed with an increasing wavenumber. Based on this, we analyzed the variability of the wave mode with varying wavenumber (Fig. 7).

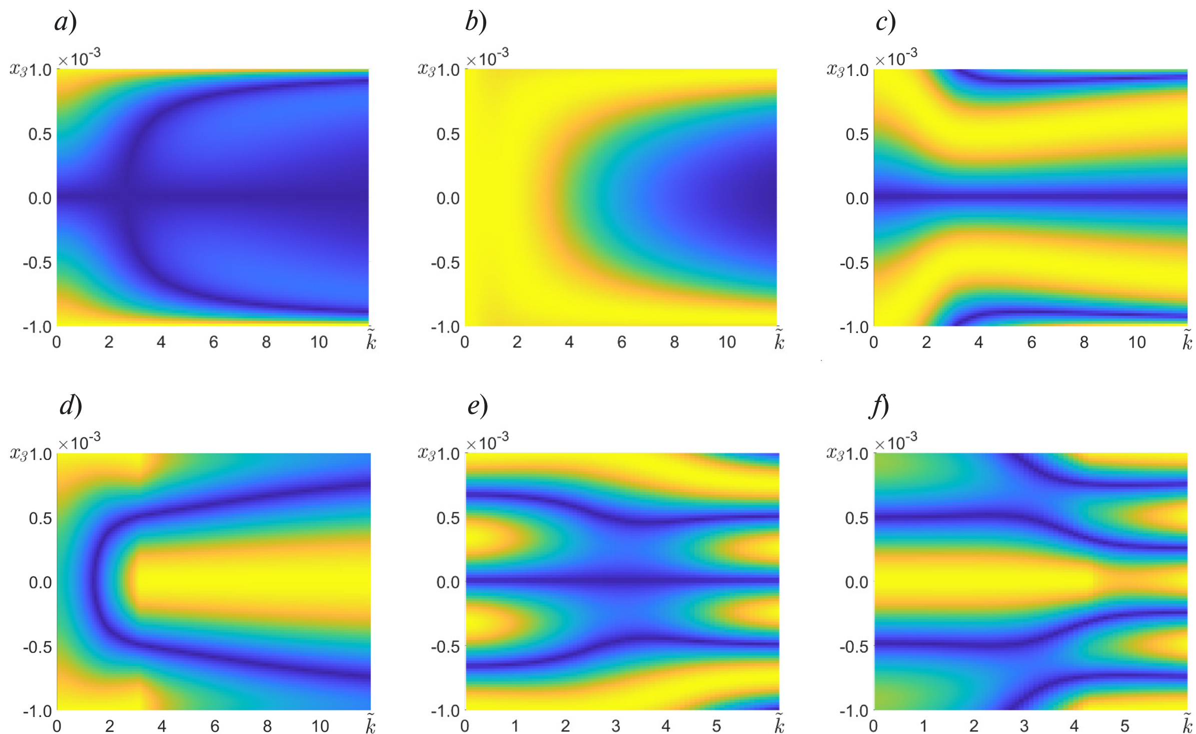

Fig. 7. Dependences of displacement fields u_1 (*a*, *c*, *e*) and u_3 (*b*, *d*, *f*) for three branches of solutions (*A*0, *A*1, *A*2) of antisymmetric wave versus wavenumber; branch *A*0 (a, *b*); branch *A*1 (*c*, *d*); branch *A*2 (*e*, *f*)

It is clear from Fig. 7,*b* that the amplitude of oscillations dampens rapidly in the bulk of the layer with increasing wavenumber, which corresponds to the short-wave approximation. Additionally, at low values of the parameter $\tilde{k}$, oscillations are performed by the entire cross-section, whereas in the short-wave case, oscillations occur in the upper and lower half-spaces of the plate, without actually interacting with each other [13]. This effect is explained by the type of wave, since at high values of the wavenumber (as mentioned above), the wave becomes similar in nature to a Rayleigh surface wave, characterized by rapid damping in the half-space [10]. In addition, an interesting branching effect of the nodal curve is observed in Fig. 7,*a*. Apparently, the branching occurs at the same wavenumbers at which the aforementioned antisymmetric wave is divided into two components formed in the upper and lower half-spaces of the plate. Based on these considerations, it can be expected that similar branchings will no longer be observed with a further increase in the wavenumber: on the contrary, complete damping of oscillations should happen in the bulk of the material.

Analysis of asymptotic correctness of beam models

As noted above, the long-wave approximation of the first mode of the antisymmetric wave resembles in form the transverse vibrations of a beam. Two models of bending vibrations of a beam are common and well-studied in engineering practice: the Euler–Bernoulli beam and the Timoshenko beam. In view of this observation, it is advisable to compare the results obtained with the dispersion relations for these models.

It is known [12] that the problem for the Euler–Bernoulli beam model in the case of a hinged support is determined by the system:

$$\begin{cases} EI\dfrac{\partial^4 w}{\partial x^4}+\dfrac{\rho}{A}\dfrac{\partial^2 w}{\partial t^2}=0, \quad (0<x<l) \\ w(x,t)=0, \quad \dfrac{\partial^2 w}{\partial x^2}=0, \quad (x=0,l) \\ w(x,0)=W(x), \end{cases} \tag{20}$$

where w is the vertical displacement, E is Young's modulus, I is the moment of inertia of the cross-section, A is the cross-sectional area, $W(x)$ are the initial displacement distributions, p is the surface density, l *is* the length of the beam.

The solution of system (20) can be represented as an infinite sum of traveling waves:

$$w(x,t)=\frac{1}{2}\sum_{n=0}^{\infty}A_n\left[\sin\left(\frac{n\pi}{l}x-\omega_n t\right)+\sin\left(\frac{n\pi}{l}x+\omega_n t\right)\right], \tag{21}$$

where the frequency ω_n is determined by the expression

$$\omega_n=(n\pi/l)^2\sqrt{EIA/\rho}.$$

The wavelength in this case is $\lambda_n=2l/n$. Therefore, the phase velocity is expressed as

$$c_n=\frac{\omega_n\lambda_n}{2\pi}=n\pi\sqrt{\frac{EIA}{\rho l^2}}. \tag{22}$$

For the Timoshenko beam model, the system takes the form:

$$\begin{cases} EI\dfrac{\partial^2\psi}{\partial x^2}+k'AG\left(\dfrac{\partial w}{\partial x}-\psi\right)-\dfrac{\rho I}{A^2}\dfrac{\partial^2\psi}{\partial t^2}=0, \\ k'AG\left(\dfrac{\partial^2 w}{\partial x^2}-\dfrac{\partial\psi}{\partial x}\right)-\dfrac{\rho}{A}\dfrac{\partial^2 w}{\partial t^2}=0, \\ w(x,t)=\dfrac{\partial}{\partial x}\psi(x,t)=0\ (x=0,l), \end{cases} \tag{23}$$

where ψ is the bending rotation, $k'=5/6$ is the correction factor for the rectangular cross-section, G is the shear modulus.

The expression for the eigenfrequency spectrum follows from system (23):

$$\tilde{\omega}_n^2=\frac{\left(\eta^2+\alpha^2\right)n^2\pi^2+1\pm\sqrt{\left(\left(\eta^2+\alpha^2\right)n^2\pi^2+1\right)^2-2\eta^2\alpha^2n^4\pi^4}}{2\eta^2\alpha^2}, \tag{24}$$

where $\tilde{\omega}_n$ is the dimensionless frequency, $\tilde{\omega}_n^2=\omega^2(\rho l^4)/(EIA)$; η is a dimensionless parameter expressing the ratio between bending and shear stiffness, $\eta^2=(EI)/(k'AGl^2)$; α is a dimensionless parameter expressing the ratio between the forces of inertia of the cross-section with respect to rotation and transverse displacement, $\alpha^2=I/(Al^2)$.

Eq. (24) gives two branches of solutions for bending $(\tilde{\omega}_{n,1})$ and shear $(\tilde{\omega}_{n,2})$ vibrations.

It was of interest to build finite element (FE) models of Euler–Bernoulli and Timoshenko beams. The models were constructed in the COMSOL Multiphysics package. For comparison, Fig. 8 shows the results of analytical and FE modeling of the Euler–Bernoulli beam and the Timoshenko beam, as well as the previously presented calculation results using the Lamb elastic wave model in a thin layer.

Analysis of the data in Fig. 8 shows that the lower branch of the solution for the Timoshenko beam model coincides with the first branch of the wave solution of antisymmetric Lamb waves. We should note that this is not a consistent pattern. As noted above, the phase velocity of the lower branch of the Lamb wave solution in the short-wave approximation tends to the phase velocity of Rayleigh surface waves c_R, which, in turn, depends on the value of Poisson's ratio (14). At the same time, the phase velocity of the wave for the Timoshenko beam model tends to the velocity of transverse oscillations $c_T=\sqrt{k'G/\rho}$ with an increase in the wavenumber. In dimensionless form, these asymptotics are the result of taking the square root of the correction factor k'.

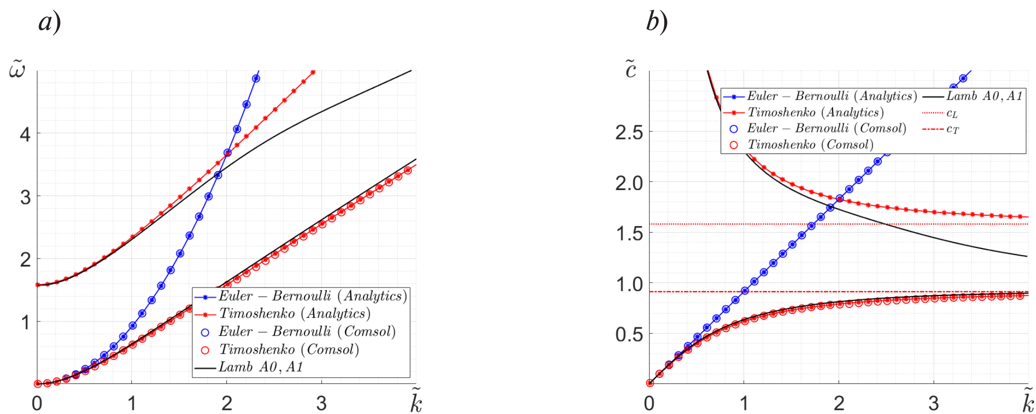

Fig. 8. Comparison of calculated results for three models:
Euler–Bernoulli beams, Timoshenko beams and elastic Lamb waves;
dispersion curves (*a*), dependences of phase velocity on wavenumber (*b*)

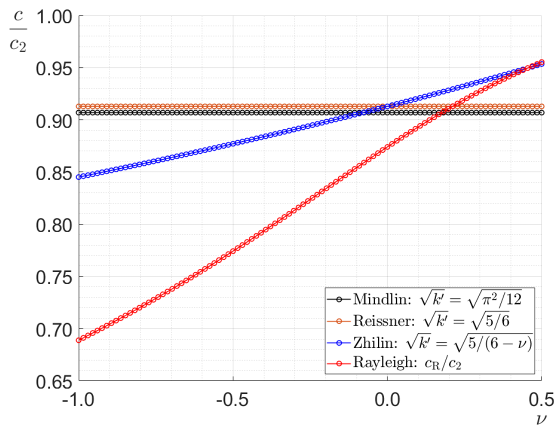

Fig. 9. Comparison of dependences of threshold phase velocities on Poisson's ratio

As discussed above, the value of the correction factor is taken as $k' = 5/6$, which was proposed by Reissner. Another frequently used value of the correction factor was proposed by Mindlin: $k' = \pi^2/12$. The following definition was proposed by Zhilin [14]:

$$k' = \frac{5}{6-\nu}, \quad (25)$$

obtained by finding the solution for the frequency equation of plate vibration with an accuracy up to the second correction term.

Fig. 9 shows a comparison of the dimensionless threshold values of the phase velocities of Rayleigh surface waves c_R and transverse oscillations c_T at different values of Poisson's ratio ν and correction factor k'. These proposals do not coincide with the investigated Rayleigh surface wave model. There are, however, certain values of Poisson's ratio at which the asymptotics coincide.

Based on this, we can conclude that coincidence of the characteristics of elastic Lamb waves and waves in the Timoshenko beam is observed only for a long-wave approximation, while the results diverge if the dimensionless wavenumber $\tilde{k} = k \cdot h \approx 1$.

Conclusion

We performed a qualitative analytical study of stationary Lamb waves in a homogeneous isotropic thin layer. Dispersion curves and phase velocity dependences on the wavenumber were constructed for symmetric and antisymmetric waves in accordance with the obtained solutions. The displacement and variability fields were calculated for the wave mode of the first branch of the wave solution with variable value of the wavenumber. The characteristics of antisymmetric Lamb waves were compared with the wave characteristics of Euler—Bernoulli and Timoshenko beams. The data help determine the accuracy of long-wave and short-wave asymptotic approximations for symmetric and antisymmetric Lamb waves, including approximations based on the application of beam models of structural mechanics.

Our findings can serve as a basis for verification of numerical methods of wave mechanics used in modeling wave processes in electroacoustic devices.

REFERENCES

1. **Lu R., Gong S.,** RF acoustic microsystems based on suspended lithium niobate thin films: Advances and outlook, J. Micromech. Microeng. 31 (11) (2021) 114001.

2. **Yang Y., Lu R., Gao L., Gong S.,** 10—60-GHz Electromechanical resonators using thin-film lithium niobate, IEEE Trans. Microw. Theory Techn. 68 (12) (2020) 5211—5220.

3. **Yang Y., Lu R., Gong S.,** Scaling acoustic filters towards 5G, Proc. 2018 IEEE International Electron Devices Meeting (IEDM), 01—05 Dec., San Francisco, CA, USA (2018) 39.6.1—39.6.4.

4. **Yang Y., Gao L., Gong S.,** X-band miniature filters using lithium niobate acoustic resonators and bandwidth widening technique, IEEE Trans. Microw. Theory Techn. 69 (3) (2021) 1602—1610.

5. **Wu J., Zhang Sh., Zhang L., et al.,** Exploring low-loss surface acoustic wave devices on heterogeneous substrates, IEEE Trans. Ultrason. Ferroelectr. Freq. Control. 69 (8) (2022) 2579—2584.

6. **Naumenko N. F.,** Optimal orientations of $LiTaO_3$ for application in plate mode resonators, J. Appl. Phys. 118 (3) (2015) 034505.

7. **Naumenko N. F.,** Laterally excited bulk acoustic resonators (XBARs): Optimization method and application to resonators on $LiTaO_3$, Proc. 2022 IEEE MTT-S Int. Conf. Microwave Acoustics and Mechanics (IC-MAM). 18—20 July 2022, Munich, Germany (2022) 70—73.

8. **Naumenko N. F.,** Advanced numerical technique for analysis of surface and bulk acoustic waves in resonators using periodic metal gratings, J. Appl. Phys. 116 (10) (2014) 104503.

9. **Naumenko N. F.,** Temperature behavior of SAW resonators based on $LiNbO_3$/Quartz and $LiTaO_3$/Quartz substrates, IEEE Trans. Ultrason. Ferroelectr. Freq. Control. 68 (11) (2021) 3430–3437.

10. **Novatski V.,** Teoriya uprugosty [Elasticity theory], Mir Publishing, Moscow, 1975 (in Russian).

11. **Govaerts W., Kuznetsov Yu. A., Meijer H.G.E., et al.,** MATCONT: Continuation toolbox for ODEs in Matlab, Utrecht University, Utrecht (The Netherlands), 2019.

12. **Géradin, M., Rixen D. J.,** Mechanical vibrations: Theory and application to structural dynamics. 3-rd Ed., John Willey and Sons, Chichester (West Sussex, UK), 2015.

13. **Biryukov S. V., Gulyaev Yu. V., Krylov V. V., Plessky V. P.,** Surface acoustic waves in inhomogeneous media (Springer Series on Wave Phenomena, Vol. 20), Springer-Verlag, Berlin Heidelberg, 1995.

14. **Zhilin P. A.,** Prikladnaya Mehanika: Osnovy teorii obolochek [Applied Mechanics: Basics of shell theory], Polytechnic University Publishing, Saint-Petersburg, 2006 (in Russian).

СПИСОК ЛИТЕРАТУРЫ

1. **Lu R., Gong S.** RF acoustic microsystems based on suspended lithium niobate thin films: Advances and outlook // Journal of Micromechanics and Microengineering. 2021. Vol. 31. No. 11. P. 114001.

2. **Yang Y., Lu R., Gao L., Gong S.** 10–60-GHz Electromechanical resonators using thin-film lithium niobate // IEEE Transaction on Microwave Theory and Techniques. 2020. Vol. 68. No. 12. Pp. 5211–5220.

3. **Yang Y., Lu R., Gong S.** Scaling acoustic filters towards 5G // Proceedings of the 2018 IEEE International Electron Devices Meeting (IEDM). San Francisco, CA, USA. 01–05 December, 2018. Pp. 39.6.1–39.6.4.

4. **Yang Y., Gao L., Gong S.** X-band miniature filters using lithium niobate acoustic resonators and bandwidth widening technique // IEEE Transaction on Microwave Theory and Techniques. 2021. Vol. 69. No. 3. Pp. 1602–1610.

5. **Wu J., Zhang Sh., Zhang L., Zhou H., Zheng P., Yao H., Li Zh., Huang K., Wu T., Ou X.** Exploring low-loss surface acoustic wave devices on heterogeneous substrates // IEEE Transactions on Ultrasonics, Ferroelectrics, and Frequency Control. 2022. Vol. 69. No. 8. Pp. 2579–2584.

6. **Naumenko N. F.** Optimal orientations of $LiTaO_3$ for application in plate mode resonators // Journal of Applied Physics. 2015. Vol. 118. No. 3. P. 034505.

7. **Naumenko N. F.** Laterally excited bulk acoustic resonators (XBARs): Optimization method and application to resonators on $LiTaO_3$ // Proceedings of the 2022 IEEE MTT-S International Conference on Microwave Acoustics and Mechanics (IC-MAM). 18 – 20 July 2022, Munich, Germany. 2022. Pp. 70–73.

8. **Naumenko N. F.** Advanced numerical technique for analysis of surface and bulk acoustic waves in resonators using periodic metal gratings // Journal of Applied Physics. 2014. Vol. 116. No. 10. P. 104503.

9. **Naumenko N. F.** (2021). Temperature behavior of SAW resonators based on $LiNbO_3$/Quartz and $LiTaO_3$/Quartz substrates // IEEE Transactions on Ultrasonics, Ferroelectrics, and Frequency Control. 2021. Vol. 68. No. 11. Pp. 3430–3437.

10. **Новацкий В.** Теория упругости. Пер. с польского. М.: Мир, 1975. 872 с.

11. **Govaerts W., Kuznetsov Yu. A., Meijer H.G.E., Al-Hdaibat B., de Witte V., Dhooge A., Mestrom W., Neirynck N., Riet A. M., Sautios B.** MATCONT: Continuation toolbox for ODEs in Matlab. Utrecht (The Netherlands): Utrecht University, 2019. 124 p.

12. **Géradin, M., Rixen D. J.** Mechanical vibrations: theory and application to structural dynamics. 3-rd edition. Chichester (West Sussex, UK): John Willey and Sons, 2015. 598 p.

13. **Бирюков С. В., Гуляев Ю. В., Крылов В. В., Плесский В. П.** Поверхностные акустические волны в неоднородных средах. М.: Наука. Гл. редакция физ.-мат. лит-ры, 1991. 416 с.

14. **Жилин П. А.** Прикладная механика: Основы теории оболочек. СПб.: Издательство Политехнического университета, 2006.

THE AUTHORS

ASTAPOV Yaroslav K.
Peter the Great St. Petersburg Polytechnic University
29 Politechnicheskaya St., St. Petersburg, 195251, Russia
astapov.yaroslav.00@mail.ru
ORCID: 0009-0008-0216-462X

LUKIN Aleksey V.
Peter the Great St. Petersburg Polytechnic University
29 Politechnicheskaya St., St. Petersburg, 195251, Russia
lukin_av@spbstu.ru
ORCID: 0000-0003-2016-8612

POPOV Ivan A.
Peter the Great St. Petersburg Polytechnic University
29 Politechnicheskaya St., St. Petersburg, 195251, Russia
popov_ia@spbstu.ru
ORCID: 0000-0003-4425-9172

СВЕДЕНИЯ ОБ АВТОРАХ

АСТАПОВ Ярослав Константинович – *студент Физико-механического института Санкт-Петербургского политехнического университета Петра Великого.*
195251, Россия, г. Санкт-Петербург, Политехническая ул., 29
astapov.yaroslav.00@mail.ru
ORCID: 0009-0008-0216-462X

ЛУКИН Алексей Вячеславович – *кандидат физико-математических наук, доцент Высшей школы механики и процессов управления Санкт-Петербургского политехнического университета Петра Великого.*
195251, Россия, г. Санкт-Петербург, Политехническая ул., 29
lukin_av@spbstu.ru
ORCID: 0000-0003-2016-8612

ПОПОВ Иван Алексеевич – *ведущий инженер Высшей школы механики и процессов управления Санкт-Петербургского политехнического университета Петра Великого.*
195251, Россия, г. Санкт-Петербург, Политехническая ул., 29
popov_ia@spbstu.ru
ORCID: 0000-0003-4425-9172

Received 31.01.2024. Approved after reviewing 22.04.2024. Accepted 22.04.2024.
Статья поступила в редакцию 31.01.2024. Одобрена после рецензирования 22.04.2024. Принята 22.04.2024.

© Peter the Great St. Petersburg Polytechnic University, 2024

Original article
DOI: https://doi.org/10.18721/JPM.17311

ASYMPTOTIC METHODS FOR SOLVING THE STOKES PROBLEM FOR A FLAT CONTOUR

E. N. Afanasov[1]✉, *S. G. Kadyrov*[2], *V. N. Sorokin*[2]

[1] LLC "Evolution Marine Digital", St. Petersburg, Russia;

[2] State Marine Technical University, St. Petersburg, Russia

✉ zhenya.afanasov@yandex.ru

Abstract. The paper presents asymptotic methods for solving the problem of small harmonic oscillations of a flat contour immersed in an incompressible viscous liquid. In the case of large values of the dimensionless viscosity parameter, asymptotic approximations up to the third order have been obtained. In the case of small values of this viscosity parameter, the main term of the asymptotic of the hydrodynamic force on an arbitrary smooth contour was constructed and its form was proved not to depend on the shape of the contour. The results obtained were confirmed by an example of the problem of oscillations of an elliptical cylinder.

Keywords: Stokes problem, viscous incompressible fluid, solid body vibrations, elliptical cylinder

Citation: Afanasov E. N., Kadyrov S. G., Sorokin V. N., Asymptotic methods for solving the Stokes problem for a flat contour, St. Petersburg State Polytechnical University Journal. Physics and Mathematics. 17 (3) (2024) 118–133. DOI: https://doi.org/10.18721/JPM.17311

This is an open access article under the CC BY-NC 4.0 license (https://creativecommons.org/licenses/by-nc/4.0/)

Научная статья
УДК 532.5.032
DOI: https://doi.org/10.18721/JPM.17311

АСИМПТОТИЧЕСКИЕ МЕТОДЫ РЕШЕНИЯ ЗАДАЧИ СТОКСА ДЛЯ ПЛОСКОГО КОНТУРА

Е. Н. Афанасов[1]✉, *С. Г. Кадыров*[2], *В. Н. Сорокин*[2]

[1] ООО «Эволюция морских цифровых технологий», Санкт-Петербург, Россия;

[2] Санкт-Петербургский государственный морской технический университет, Санкт-Петербург, Россия

✉ zhenya.afanasov@yandex.ru

Аннотация. В работе излагаются асимптотические методы решения задачи о малых гармонических колебаниях плоского контура, погруженного в несжимаемую вязкую жидкость. В случае больших значений безразмерного параметра вязкости получены асимптотические формулы вплоть до третьего порядка. В случае малых значений этого параметра вязкости построен главный член асимптотики гидродинамической силы на произвольном гладком контуре и доказано, что его вид не зависит от формы контура. Полученные результаты подтверждены примером задачи о колебаниях эллиптического цилиндра.

Ключевые слова: задача Стокса, вязкая несжимаемая жидкость, колебания твердого тела, эллиптический цилиндр

Ссылка для цитирования: Афанасов Е. Н., Кадыров С. Г., Сорокин В. Н. Асимптотические методы решения задачи Стокса для плоского контура // Научно-технические ведомости СПбГПУ. Физико-математические науки. 2024. Т. 17. № 3. С. 118–133. DOI: https://doi.org/10.18721/JPM.17311

© Afanasov E. N., Kadyrov S. G., Sorokin V. N., 2024. Published by Peter the Great St. Petersburg Polytechnic University.

Статья открытого доступа, распространяемая по лицензии CC BY-NC 4.0 (https://creativecommons.org/licenses/by-nc/4.0/)

Introduction

The theoretical model of a cantilever beam of arbitrary cross-section (Fig. 1), which is excited by an arbitrary driving force and immersed in viscous liquid, is the main one used to develop devices in nanotechnology and in viscosity measurements. The liquid is typically assumed to be incompressible, the length of the beam significantly exceeds its other dimensions. The formulation for a cross-section of the general form leads to the concept of the hydrodynamic function [1–3], describing the hydrodynamic load and taking into account the geometry of the cross-section of the beam. Depending on the cross-section of the beam, this hydrodynamic function must be calculated numerically or (preferably) analytically.

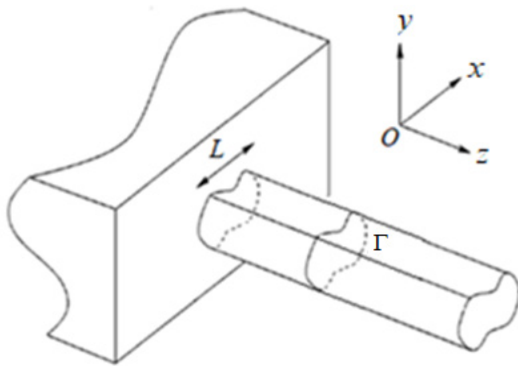

Fig. 1. Schematic representation of cantilever beam of arbitrary cross-section: Γ is the contour, L is its characteristic size

The problem on determining the hydrodynamic load on an infinite cylinder making small-amplitude oscillations in viscous liquid has been the subject of numerous theoretical and experimental studies (see, for example, [4–8]).

Problem statement

Let a rigid (non-deformable) contour Γ immersed in incompressible viscous liquid with kinematic viscosity ν and density ρ make small harmonic oscillations with a given frequency ω and velocity amplitude u_0. The oscillation amplitude is assumed to be much smaller than the size of the contour. The motion of the contour is assumed to be plane-parallel.

To write the equations of motion in dimensionless form, we introduce the characteristic contour size L, the characteristic velocity ωL and the characteristic pressure $\rho\omega^2 L^2$. Adopting the above assumptions, the linearized hydrodynamic equations of viscous incompressible liquid take the following form [9]:

$$\begin{cases} \Delta \mathbf{v} - \beta \nabla p + i\beta \mathbf{v} = 0, \\ div\ \mathbf{v} = 0, \end{cases} \tag{1}$$

where $\mathbf{v} = (v_x, v_y)$ is the velocity vector of the liquid; p is the pressure; β is a dimensionless parameter, $\beta = \omega^2 L^2/\nu$.

In applications, the β parameter can vary in an extremely wide range: from 10^{-3} [1, 10, 11] to 10^5 [12]. From now on, the dimensionless amplitude of the velocity u_0 is assumed to be equal to 1 for convenience.

Let us formulate the boundary conditions of the problem.

No-slip conditions of the following form are imposed on the contour line:

$$v_n\big|_\Gamma = u_n,\ \ v_\tau\big|_\Gamma = u_\tau, \tag{2}$$

where (v_n, v_τ) are the normal and tangential components of the velocity vector of the liquid, (u_n, u_τ) are the (given) velocity vector components of the contour points.

In addition, perturbations of the velocity field induced by oscillations are dampened with distance from Γ:

© Афанасов Е. Н., Кадыров С. Г., Сорокин В. Н., 2024. Издатель: Санкт-Петербургский политехнический университет Петра Великого.

$$\mathbf{v} \to 0,\ \sqrt{x^2 + y^2} \to \infty. \tag{3}$$

If we use the representation of the velocity vector components in terms of two scalar functions (referred to as potentials for brevity [13]), namely,

$$v_x = \frac{\partial \varphi}{\partial x} + \frac{\partial \psi}{\partial y},\ v_y = \frac{\partial \varphi}{\partial y} - \frac{\partial \psi}{\partial x},$$

then system of equations (1) and boundary conditions (2), (3) can be written as

$$\begin{cases} \Delta\varphi = 0, \\ \Delta\psi + i\beta\psi = 0, \end{cases} \tag{4}$$

$$p = i\varphi.$$

$$\begin{cases} \dfrac{\partial \varphi}{\partial n} + \dfrac{\partial \psi}{\partial \tau} = u_n, \\ \dfrac{\partial \varphi}{\partial \tau} - \dfrac{\partial \psi}{\partial n} = u_\tau, \\ \varphi, \psi \to 0, \sqrt{x^2 + y^2} \to \infty. \end{cases} \tag{5}$$

As established in [14], the hydrodynamic force $\mathbf{R}$ acting on a plane contour with a normal $\mathbf{n} = \left(n_x, n_y\right)$, making small harmonic oscillations, is determined in terms of the potentials by the formula

$$\mathbf{R} = i\rho\omega \int_\Gamma \left(-\varphi\mathbf{n} - \psi\left(\mathbf{n} \times \mathbf{k}\right)\right) dl, \tag{6}$$

where l is the length of the contour Γ; $\mathbf{k}$ is the unit vector, $\mathbf{k}$ = (0, 0, 1).

The problem described by system of equations (4) and boundary conditions (5) is called the Stokes problem. Relations (4), (5) describe any kind of plane motion of the contour. The oscillations in the examples discussed later in this paper occur in a direction parallel to the Ox axis.

For each equation of system (4), taking into account boundary conditions (5), we can formulate the corresponding boundary integral equation and thus construct a system of two boundary integral equations [14]:

$$\begin{cases} \dfrac{1}{2}\varphi(M_0) - \displaystyle\int_\Gamma \varphi(M)\varphi_n^*(M, M_0)\,dl = \int_\Gamma \left(\dfrac{\partial \psi(M)}{\partial \tau} - u_n(M)\right)\varphi^*(M, M_0)\,dl, \\ \dfrac{1}{2}\psi(M_0) - \displaystyle\int_\Gamma \psi(M)\psi_n^*(M, M_0)\,dl = \int_\Gamma \left(u_\tau(M) - \dfrac{\partial \varphi(M)}{\partial \tau}\right)\psi^*(M, M_0)\,dl, \end{cases} \tag{7}$$

where $\varphi^*(M,M_0)$, $\psi^*(M,M_0)$ are Green's functions for the equations of system (4); $\varphi_n^*(M,M_0)$, $\psi_n^*(M,M_0)$ are their derivatives in the direction of the external normal $\mathbf{n}$ at the integration point; $H_0^{(1)}$ is the zero-order Hankel function of the first kind; $r(M,M_0)$ is the distance between the integration point M and observation point M_0 lying on the contour;

$$\varphi^*(M, M_0) = \frac{1}{2\pi}\ln\frac{1}{r(M, M_0)},\ \psi^*(M, M_0) = \frac{i}{4}H_0^{(1)}\left(r(M, M_0)\sqrt{i\beta}\right),$$

$$\varphi_n^*(M, M_0) = \frac{\partial \varphi^*(M, M_0)}{\partial n},\ \psi_n^*(M, M_0) = \frac{\partial \psi^*(M, M_0)}{\partial n}.$$

Asymptotics of the Stokes problem for a circular contour

The exact solution to the problem of oscillations in a circular cylinder in incompressible viscous liquid at rest along the *Ox* axis as well as the formula for calculating the hydrodynamic drag of the cylinder were obtained by Stokes [4].

Let us give the asymptotic formulas obtained by the potential method in [15]. In polar coordinates r, θ at $\beta \to \infty$, they have the form

$$\begin{cases} \varphi(1,\theta) \underset{\beta\to\infty}{\sim} \varphi_\infty(1,\theta) + O\left(\dfrac{1}{\beta^2}\right),\ \varphi_\infty(1,\theta) = \left(-1 + \dfrac{2}{i\sqrt{i\beta}} + \dfrac{1}{i\beta} - \dfrac{1}{4\beta\sqrt{i\beta}}\right)\cos\theta, \\ \psi(1,\theta) \underset{\beta\to\infty}{\sim} \psi_\infty(1,\theta) + O\left(\dfrac{1}{\beta^2}\right),\ \psi_\infty(1,\theta) = \left(\dfrac{2}{i\sqrt{i\beta}} + \dfrac{1}{i\beta} - \dfrac{1}{4\beta\sqrt{i\beta}}\right)\sin\theta, \end{cases} \tag{8}$$

for $\beta \to 0$ and finite r,

$$\begin{cases} \varphi(r,\theta) \underset{\beta\to 0}{\sim} \dfrac{1}{\left(i\sqrt{i\beta}\right)^2\left(\ln\left(\left(i\sqrt{i\beta}\right)^2\right) + 2\gamma - 2\ln 2\right)}\tilde{\varphi}(r,\theta) + O(\beta), \\ \psi(r,\theta) \underset{\beta\to 0}{\sim} \dfrac{1}{\left(i\sqrt{i\beta}\right)^2\left(\ln\left(\left(i\sqrt{i\beta}\right)^2\right) + 2\gamma - 2\ln 2\right)}\tilde{\psi}(r,\theta) + r\sin\theta + O(\beta), \\ \tilde{\varphi}(r,\theta) = \dfrac{4}{r}\cos\theta,\ \tilde{\psi}(r,\theta) = \dfrac{4}{r}\sin\theta. \end{cases} \tag{9}$$

and, according to Eq. (6), we obtain the following expressions for $R(\beta)$:

$$\begin{cases} R(\beta) \underset{\beta\to\infty}{\sim} R_\infty(\beta),\ R_\infty(\beta) = i\pi\left(1 - \dfrac{4}{i\sqrt{i\beta}} - \dfrac{2}{i\beta} + \dfrac{1}{2\beta\sqrt{i\beta}}\right), \\ R(\beta) \underset{\beta\to 0}{\sim} R_0(\beta),\ R_0(\beta) = -\dfrac{8i\pi}{\left(i\sqrt{i\beta}\right)^2\left(\ln\left(\left(i\sqrt{i\beta}\right)^2\right) + 2\gamma - 2\ln 2\right)}. \end{cases} \tag{10}$$

The exact expression for $R(\beta)$ is given in [4, 5, 8].

Fig. 2 shows the results of calculating the modulo relative error

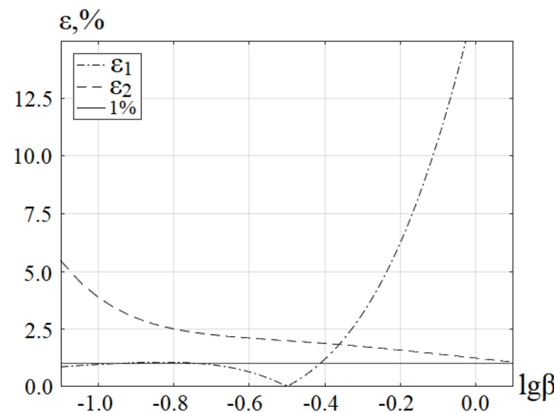

Fig. 2. Calculation of modulo relative error by Eqs. (8), (9)
The solid line shows the error level equal to 1% (for comparison)

$$\varepsilon_1 = \left|\frac{|R_0(\beta)| - |R(\beta)|}{|R(\beta)|}\right|,\ \varepsilon_2 = \left|\frac{|R_\infty(\beta)| - |R(\beta)|}{|R(\beta)|}\right|$$

(as percentages) by Eqs. (8), (9).

For clarity, Fig. 2 shows the error level of 1% (solid line). Evidently, outside the range $\lg\beta \in (-0.8,0)$, i.e., at $\beta \notin (0.16,1)$, the calculation error for the hydrodynamic force on the cylinder contour does not exceed 1% if the appropriate asymptotics are used.

Asymptotic solution of the Stokes problem for large β values

The classical formulas obtained by Stokes suggest that asymptotic expansion of the required potentials should be carried out as an asymptotic series in powers of the small parameter $\frac{1}{\lambda} = \frac{1}{i\sqrt{i\beta}}$:

$$\varphi(M_0) \underset{|\lambda|\to\infty}{\sim} \sum_{k=0} \frac{1}{\lambda^k}\varphi^{(k)}(M_0),\ \psi(M_0) \underset{|\lambda|\to\infty}{\sim} \sum_{k=1} \frac{1}{\lambda^k}\psi^{(k)}(M_0). \tag{11}$$

We introduce a local Cartesian coordinate system $(x,\tilde{y})$ with the origin at the observation point M_0 and the axis $M_0\tilde{x}$ directed tangentially toward the contour Γ.

The equation of the curve in the local coordinate system has the form $\tilde{y} = \tilde{y}(\tilde{x})$, while $\tilde{y}(0) = \left.\frac{d\tilde{y}}{d\tilde{x}}\right|_{\tilde{x}=0} = 0$.

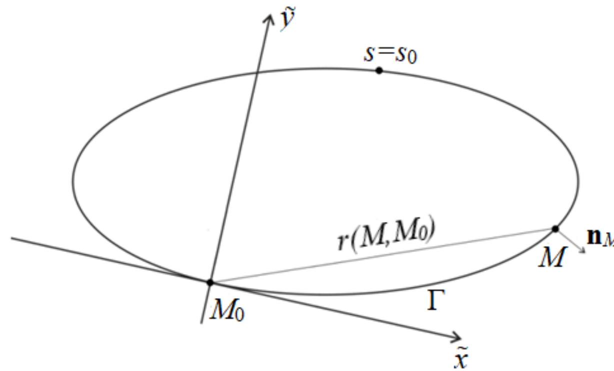

Fig. 3. Local Cartesian coordinate system introduced:
Γ is the contour; M_0 is the observation point; s is the arc length measured counterclockwise from the observation point M_0; s_0 is an arbitrary point

We define the contour Γ by natural parameterization $\tilde{x} = \tilde{x}(s)$, $\tilde{y} = \tilde{y}(s)$, where $s \in [0, L]$ is the arc length measured counterclockwise from the observation point M_0.

To represent the integrals containing the function ψ^* and its derivatives in system of equations (7) in a form convenient for obtaining asymptotics, we use integral representations of Hankel functions [16]:

$$\frac{i}{4}H_0^{(1)}\left(\sqrt{i\beta}r\right) = \frac{1}{2\pi}\int_0^\infty e^{\lambda r ch t}dt,\ \frac{i}{4}H_1^{(1)}\left(\sqrt{i\beta}r\right) = \frac{i\lambda r}{2\pi}\int_0^\infty e^{\lambda r ch t} sh^2 t dt. \tag{12}$$

Let us write the integrals in Eqs. (12) in the following form:

$$I(\lambda)=\int_0^L f(s)e^{\lambda S(s)}ds=I_1(\lambda)+I_2(\lambda)=\int_0^{s_0} f(s)e^{\lambda S(s)}ds+\int_{s_0}^L f(s)e^{\lambda S(s)}ds,$$

where s_0 is an arbitrary fixed internal point of the variation range of the parameter s: $s_0\in[0,L]$.

According to the information from monograph [17], the following expressions are hold true:

$$I_1(\lambda)\underset{|\lambda|\to\infty}{\sim}\left(\frac{c_0}{\lambda}+\frac{c_1}{\lambda^2}+\frac{c_2}{\lambda^3}+\ldots\right)e^{\lambda S(s)}\Big|_{s=0+0},c_k=\left(-D^k\frac{f(s)}{S'(s)}\right)\Bigg|_{s=0+0},$$

$$I_2(\lambda)\underset{|\lambda|\to\infty}{\sim}-\left(\frac{c_0}{\lambda}+\frac{c_1}{\lambda^2}+\frac{c_2}{\lambda^3}+\ldots\right)e^{\lambda S(s)}\Big|_{s=L-0},c_k=\left(-D^k\frac{f(s)}{S'(s)}\right)\Bigg|_{s=L-0},\tag{13}$$

$$D=-\frac{1}{S'(s)}\frac{d}{ds}.$$

To calculate the coefficients c_k, one-sided Taylor series expansions known from differential geometry can be used [18]:

$$\tilde{x}(s)=\pm s\mp\frac{\kappa^2 s^3}{6}+\ldots,\ \tilde{y}(s)=\frac{\kappa s^2}{2}\pm\kappa'(s)\frac{s^3}{6}+\ldots,\ r=\pm s\mp\frac{\kappa^2 s^3}{24}+\ldots.\tag{14}$$

In these formulas, κ is the curvature of the curve at point M_0, $\kappa=-|\mathbf{r}''(s)|$; the combination of plus and minus signs corresponds to the Taylor expansions on the right at point $s = 0$ and on the left at point $s = L$.

Using the above formulas and performing simple (but laborious) calculations, we can prove that the following relations hold true for any function $f(s)$ given on the contour:

$$\int_\Gamma f(s)\frac{i}{4}H_0^{(1)}\left(\sqrt{i\beta}r\right)ds\underset{|\lambda|\to\infty}{\sim}-\frac{1}{2\lambda}f(s)-\frac{1}{4\lambda^3}\left(\frac{\partial^2 f(s)}{\partial s^2}+\frac{1}{4}f(s)\kappa^2\right),\tag{15}$$

$$\int_\Gamma f(s)\frac{i}{4}\frac{\partial}{\partial n}H_0^{(1)}\left(\sqrt{i\beta}r\right)ds\underset{|\lambda|\to\infty}{\sim}\frac{\kappa}{4\lambda}f(s).\tag{16}$$

The remaining step is to use these relations and substitute the asymptotic series (11) into the right-hand and left-hand sides of Eqs. (7), to equate the coefficients at the same powers $1/\lambda$, ultimately obtaining the following groups of equations and relations:

boundary integral equations for $\varphi^{(k)}$ ($k = 0, 1, 2, 3$), which are approximations of the potential φ,

$$\frac{1}{2}\varphi^{(0)}(M_0)-\int_\Gamma\varphi^{(0)}(M)\varphi_n^*(M,M_0)dl=-\int_\Gamma u_n(M)\varphi^*(M,M_0)dl,\tag{17}$$

$$\frac{1}{2}\varphi^{(k)}(M_0)-\int_\Gamma\varphi^{(k)}(M)\varphi_n^*(M,M_0)dl=\int_\Gamma\frac{\partial\psi^{(k)}(M)}{\partial s}\varphi^*(M,M_0)dl,\ k=1,2,3;\tag{18}$$

relations at contour points for $\psi^{(k)}$ ($k = 1, 2, 3$), which are approximations of the potential ψ (the point M_0 is not referenced below for simplicity),

$$\psi^{(1)}=-u_\tau+\frac{\partial\varphi^{(0)}}{\partial s},\tag{19}$$

$$\psi^{(2)} = \frac{\kappa\psi^{(1)}}{2} + \frac{\partial\varphi^{(1)}}{\partial s}, \tag{20}$$

$$\psi^{(3)} = \frac{\kappa\psi^{(2)}}{2} + \frac{1}{2}\frac{\partial^2\psi^{(1)}}{\partial s^2} + \frac{\kappa^2}{8}\psi^{(1)} + \frac{\partial\varphi^{(2)}}{\partial s}. \tag{21}$$

The relations for $k = 0, 1$ correspond to the well-known (linear) Morison equation [19, 20]; for $k = 2$, they were obtained and proved in [21]; as for the relations for $k = 3$, they were obtained for the first time.

Importantly, the boundary integral equations (17), (18) are absolutely equivalent to the Neumann boundary-value problems for the Laplace equation:

$$\Delta\varphi^{(0)} = 0, \left.\frac{\partial\varphi^{(0)}}{\partial n}\right|_\Gamma = u_n; \tag{22}$$

$$\Delta\varphi^{(k)} = 0, \left.\frac{\partial\varphi^{(k)}}{\partial n}\right|_\Gamma = -\left.\frac{\partial\psi^{(k)}}{\partial s}\right|_\Gamma, \ k = 1,2,3. \tag{23}$$

Asymptotics of the Stokes problem for a circular contour (example). Sequentially performing calculations by Eqs. (22), (23) for potential φ and (19)–(21) for potential ψ, we obtain:

$$\begin{cases} \Delta\varphi^{(0)} = 0, \left.\frac{\partial\varphi^{(0)}}{\partial r}\right|_{r=1} = \cos\theta, \ \varphi^{(0)}(r,\theta) = -\frac{1}{r}\cos\theta, \\ \psi^{(1)}(1,\theta) = 2\sin\theta; \end{cases}$$

$$\begin{cases} \Delta\varphi^{(1)} = 0, \left.\frac{\partial\varphi^{(1)}}{\partial r}\right|_{r=1} = -2\cos\theta, \ \varphi^{(1)}(r,\theta) = \frac{2}{r}\cos\theta, \\ \psi^{(2)}(1,\theta) = -\sin\theta; \end{cases}$$

$$\begin{cases} \Delta\varphi^{(2)} = 0, \left.\frac{\partial\varphi^{(2)}}{\partial r}\right|_{r=1} = \cos\theta, \ \varphi^{(2)}(r,\theta) = -\frac{1}{r}\cos\theta, \\ \psi^{(3)}(1,\theta) = -\frac{1}{4}\sin\theta; \end{cases}$$

$$\Delta\varphi^{(3)} = 0, \left.\frac{\partial\varphi^{(3)}}{\partial r}\right|_{r=1} = -\frac{1}{4}\cos\theta, \ \varphi^{(3)}(r,\theta) = -\frac{1}{4r}\cos\theta.$$

The results obtained at $r = 1$ coincide with Eqs. (8).

Neumann problem for potentials $\varphi^{(k)}$ ($k = 1, 2, 3$). In some cases, it is possible to find solutions of Eqs. (22), (23) by the Fourier method [21], but numerical methods can also be used. However, such solutions can be obtained via conformal mapping.

The only solution to the Neumann problem, i.e.,

$$\Delta\varphi^{(k)} = 0, \left.\frac{\partial\varphi^{(k)}}{\partial r}\right|_{r=R} = \Phi(\eta), \tag{24}$$

for the exterior of the circle $r = R$ is given by the Dini formula [22]:

$$\varphi^{(k)}(\eta) = \frac{R}{\pi}\int_0^{2\pi} \Phi(t)\ln\left|\sin\frac{\eta - t}{2}\right| dt, \tag{25}$$

where η, t are the angular coordinates of the observation point and the integration points.

Let us introduce the conformal mapping $z = z(\zeta)$ that is the exterior of a circle of radius R to the exterior of the contour Γ.

Let the contour Γ be defined parametrically, specifically,

$$z(\eta) = x(\eta) + iy(\eta),$$

corresponds to the circle $\zeta = Re^{i\eta}$.

There is a single conformal mapping for which the point $\zeta = R$ on the circle corresponds to the point $z = 1$ on the contour Γ and the ray $\operatorname{Re}\zeta \geq R$, $\operatorname{Im}\zeta = 0$ on the plane ζ turns into a ray $\operatorname{Re} z \geq 1$, $\operatorname{Im} z = 0$ on the plane z. Then the solution of the Neumann problem at the points of this contour can be found using the following formula [22]:

$$\varphi^{(k)}(\eta)\Big|_{\Gamma} = -\frac{1}{\pi}\int_0^{2\pi} \frac{\partial\psi^{(k)}}{\partial t}\bigg|_{\zeta = \mathrm{R}\,e^{it}} \left|z'(\zeta)\right|\Big|_{\zeta = \mathrm{R}\,e^{it}} \ln\left|\sin\frac{\eta - t}{2}\right| dt. \tag{26}$$

However, since

$$\frac{\partial\psi^{(k)}}{\partial t}\bigg|_{\zeta = \mathrm{R}\,e^{it}} = \frac{\partial\psi^{(k)}}{\partial t}\bigg|_{\Gamma} \frac{1}{\left|z'(\zeta)\right|\Big|_{\zeta = \mathrm{R}\,e^{it}}},$$

we ultimately obtain:

$$\varphi^{(k)}(\eta)\Big|_{\text{Ã}} = -\frac{1}{\pi}\int_0^{2\pi} \frac{\partial\psi^{(k)}}{\partial t}\bigg|_{\text{Ã}} \ln\left|\sin\frac{\eta - t}{2}\right| dt. \tag{27}$$

This is the formula reconstructing the values of $\varphi^{(k)}$ (k = 1, 2, 3) on the contour Γ from the known values of $\psi^{(k)}\big|_{\Gamma}$.

It is known that conformal mapping preserves the angles between curves, so the cosines of the angles between the normals to the contour Γ and the coordinate axes (on the z plane) and the cosines of the angles between the normals to the circle and the coordinate axes (on the plane ζ) coincide at the corresponding points.

Let us prove that

$$\int_0^{2\pi} \varphi^{(k)}(\eta)\begin{Bmatrix}\cos m\eta \\ \sin m\eta\end{Bmatrix} d\eta = \pm\int_0^{2\pi} \psi^{(k)}(\eta)\begin{Bmatrix}\sin m\eta \\ \cos m\eta\end{Bmatrix} d\eta,\ \ m = 1, 2, \ldots. \tag{28}$$

Indeed, it follows from Eqs. (27) that

$$\int_0^{2\pi} \varphi^{(k)}(\eta)\begin{Bmatrix}\cos m\eta \\ \sin m\eta\end{Bmatrix} d\eta = -\int_0^{2\pi} \frac{\partial\psi^{(k)}}{\partial t} dt \frac{1}{\pi}\int_0^{2\pi} \begin{Bmatrix}\cos m\eta \\ \sin m\eta\end{Bmatrix} \ln\left|\sin\frac{\eta - t}{2}\right| dt,\ \ m = 1, 2, \ldots. \tag{29}$$

On the other hand, since the following equality holds true (see the formulas in book [23]):

$$\frac{1}{\pi}\int_0^{2\pi} \begin{Bmatrix}\cos m\eta \\ \sin m\eta\end{Bmatrix} \int_0^{2\pi} \ln\left|\sin\frac{\eta - t}{2}\right| dt = -\frac{1}{m}\begin{Bmatrix}\cos m\eta \\ \sin m\eta\end{Bmatrix},\ \ m = 1, 2, \ldots, \tag{30}$$

then, integrating Eq. (29) by parts, we obtain the required equality (28). The proof is obtained.

Thus, the Fourier series for the functions $\varphi^{(k)}$, $\psi^{(k)}$ are harmonic conjugates to each other outside the contour [24].

In particular, for $m = 1$, $\cos\eta = n_x$, $\sin\eta = n_y$, equality (28) implies the property of potentials $\varphi^{(k)}$, $\psi^{(k)}$, useful in calculating the force:

$$\int_\Gamma \varphi^{(k)} n_x dl = \int_\Gamma \psi^{(k)} n_y dl. \quad (31)$$

As a consequence of this formula, it is sufficient to find the functions $\varphi^{(k)}$ to calculate the force, and then obtain information about the function $\psi^{(k)}$ at the contour points using local formulas (19)–(21).

Asymptotic solution of the Stokes problem for "small" values of β

Eqs. (9) for solving the problem of cylinder oscillations at small values of β suggest the structure of the asymptotics of such solutions for an arbitrary contour.

It follows from the equations that potentials φ, ψ for $\beta \to 0$ are the sum of harmonic functions in the exterior of the circle, proportional to $(\lambda^2 \ln\lambda^2)^{-1}$ and terms of the form 0, $y = r\sin\theta$, which describe homogeneous flow of an oscillating liquid.

Let the functions $\Phi(x,y)$, $\Psi(x,y)$ represent the potential and the function of a current homogeneous in the entire plane of oscillatory flow of an ideal incompressible fluid. The complex potential of such flow follows the expression [25]:

$$W(x,y) = \Phi(x,y) - i\Psi(x,y).$$

Let us introduce the potentials

$$\varphi = \varphi' + \Phi, \ \psi = \psi' + \Psi$$

(the primes are omitted below).

Now the system of differential equations (4) takes the form

$$\begin{cases} \Delta\varphi = 0, \\ \Delta\psi + i\beta\psi = -i\beta\Psi. \end{cases} \quad (32)$$

The equation for the function ψ is not homogeneous, although the boundary conditions for system (32) are expressed as

$$\begin{cases} \left.\dfrac{\partial\varphi}{\partial n}\right|_\Gamma = -\left.\dfrac{\partial\psi}{\partial\tau}\right|_\Gamma, \\ \left.\dfrac{\partial\psi}{\partial n}\right|_\Gamma = \left.\dfrac{\partial\varphi}{\partial\tau}\right|_\Gamma; \end{cases} \quad (33)$$

are homogeneous, the damping conditions at infinity are as follows:

$$\varphi + \Phi \to 0, \ \psi + \Psi \to 0, \ \sqrt{x^2 + y^2} \to \infty.$$

Let Ω_R be a part of the plane $z = x + iy$ with an inner boundary Γ and an arbitrary outer boundary γ_R with the diameter $2R$. Applying Green's second formula [22] to a pair of functions ψ, ψ^* in a bounded domain Ω_R and placing the observation point on the contour Γ, we construct an integral equation for the potential ψ:

$$\frac{1}{2}\psi - \int_\Gamma \psi\psi_n^* dl = -\int_\Gamma \psi^* \frac{\partial\varphi}{\partial\tau} dl + \int_{\gamma_R} \left(\psi\psi_n^* - \psi^* \frac{\partial\psi}{\partial n}\right) dl + i\beta \iint_{\Omega_R} \psi^* (\psi + \Psi) dxdy. \quad (34)$$

We used the second of the boundary conditions (33) to derive this equation, the arguments of all functions were omitted for brevity.

We search for an asymptotic representation of the potentials $\varphi(x,y)$, $\psi(x,y)$ for $\beta \to 0$ in the form

$$\varphi = \frac{1}{\lambda^2 \ln \lambda^2} \tilde{\varphi}(x,y), \psi = \frac{1}{\lambda^2 \ln \lambda^2} \tilde{\psi}(x,y), \tag{35}$$

where $\tilde{\varphi}(x,y)$, $\tilde{\psi}(x,y)$ are unknown real smooth functions bounded in the domain of Ω_R, which are to be determined.

Notably,

$$\begin{gathered} \psi^*(M_0,M) \underset{\beta\to 0}{\sim} -\frac{1}{4\pi}\ln\lambda^2 + \frac{1}{2\pi}\ln\frac{1}{r(M_0,M)} = -\frac{1}{4\pi}\ln\lambda^2 + \varphi^*(M_0,M), \\ \psi_n^*(M_0,M) \underset{\beta\to 0}{\sim} \varphi_n^*(M_0,M). \end{gathered} \tag{36}$$

for finite $r(M,M_0)$.

We substitute relations (35), (36) into integral equation (34), multiply it by $\lambda^2 \ln \lambda^2$ and pass to the limit at $\beta \to 0$. Then, for finite R, we obtain:

$$\int_\Gamma \tilde{\psi}\psi_n^* dl \underset{\beta\to 0}{\sim} \int_\Gamma \tilde{\psi}\varphi_n^* dl,$$

$$\int_\Gamma \psi^* \frac{\partial\tilde{\varphi}}{\partial\tau} dl = \int_\Gamma \left(-\frac{1}{4\pi}\ln\lambda^2 + \varphi^*\right)\frac{\partial\tilde{\varphi}}{\partial\tau} dl = -\frac{1}{4\pi}\ln\lambda^2 \int_\Gamma \frac{\partial\tilde{\varphi}}{\partial\tau} dl + \int_\Gamma \varphi^* \frac{\partial\tilde{\varphi}}{\partial\tau} dl = \int_\Gamma \varphi^* \frac{\partial\tilde{\varphi}}{\partial\tau} dl,$$

$$i\beta \iint_{\Omega_R} \psi^*(\psi + \Psi) dxdy \underset{\beta\to 0}{\to} 0.$$

As for the term

$$\int_{\gamma_R} \left(\tilde{\psi}\varphi_n^* - \left(-\frac{1}{4\pi}\ln\lambda^2 + \varphi^*\right)\frac{\partial\tilde{\psi}}{\partial n} \right) dl,$$

then, for an arbitrary fixed value of β and $R \to \infty$, it can be considered arbitrarily small.

We treat the potential φ similarly. As a result, we obtain the following system:

$$\begin{cases} \frac{1}{2}\tilde{\varphi} - \int_\Gamma \tilde{\varphi}\varphi_n^* dl = \int_\Gamma \varphi^* \frac{\partial\tilde{\psi}}{\partial\tau} dl, \\ \frac{1}{2}\tilde{\psi} - \int_\Gamma \tilde{\psi}\varphi_n^* dl = -\int_\Gamma \varphi^* \frac{\partial\tilde{\varphi}}{\partial\tau} dl. \end{cases} \tag{37}$$

The boundary integral equations (37) indicate that the functions $\tilde{\varphi}(x,y)$, $\tilde{\psi}(x,y)$ are harmonic conjugate functions in the exterior of the contour Γ, and the function

$$F(z) = \frac{1}{\lambda^2 \ln \lambda^2}\left(\tilde{\varphi}(x,y) - i\tilde{\psi}(x,y)\right)$$

is analytical in this region.

Thus, the problem was reduced to finding the complex potential of some fictitious flow of ideal incompressible fluid occurring in the exterior of the contour Γ of the plane $z = x + iy$, placed in homogeneous flow with a complex potential W. The solution to this classical problem is easy to obtain if we use a conformal mapping of such a region to the exterior of a unit circle [25].

Let $z = z(\zeta)$, $\zeta = \zeta(z)$ be known analytical functions implementing this mapping.
The complex velocity at infinity, on the plane ζ, is determined by the formula

$$\begin{cases} \left(\dfrac{dW}{d\zeta}\right)_\infty = k\left(\dfrac{dW}{dz}\right)_\infty, \\ k = \left(\dfrac{dz}{d\zeta}\right)_\infty . \end{cases} \quad (38)$$

The hydrodynamic force can also be found from the known function $F(z)$. Let us confine ourselves to the case of contour movement along the Ox axis. Then, according to Eq. (6),

$$R \underset{\beta\to 0}{\sim} -i\frac{1}{\lambda^2 \ln\lambda^2}\oint_\Gamma\left(\tilde{\varphi}dy - \tilde{\psi}dx\right). \quad (39)$$

On the other hand (see [24]),

$$\oint_\Gamma F(z)dz = \frac{1}{\lambda^2 \ln\lambda^2}\oint_\Gamma\left(\tilde{\varphi} - i\tilde{\psi}\right)\left(dx + idy\right) =$$

$$= \frac{1}{\lambda^2 \ln\lambda^2}\oint_\Gamma\left(\tilde{\varphi}dx + \tilde{\psi}dy\right) + i\frac{1}{\lambda^2 \ln\lambda^2}\oint_\Gamma\left(\tilde{\varphi}dy - \tilde{\psi}dx\right).$$

Consequently, we obtain the relation

$$R \underset{\beta\to 0}{\sim} -i\,\mathrm{Im}\oint_\Gamma F(z)\,dz = 2\pi i\,\mathrm{Res}\,F(z)\Big|_{z=\infty}. \quad (40)$$

In the case of a circular contour of unit radius on the plane of the complex variable $\zeta = \xi + i\eta$, it follows from the asymptotic formulas (9) that

$$\begin{cases} \tilde{\varphi}(\zeta,\eta) = 4\dfrac{\xi}{|\zeta|^2}, \tilde{\psi}(\zeta,\eta) = 4\dfrac{\eta}{|\zeta|^2}, \\ F(\zeta) = \dfrac{4}{\lambda^2 \ln\lambda^2}\dfrac{1}{\zeta}, \end{cases}$$

and

$$R(\beta) \underset{\beta\to 0}{\sim} \frac{8\pi i}{\lambda^2 \ln\lambda^2}\,\mathrm{Res}\,\frac{1}{\zeta}\bigg|_{\zeta=\infty}.$$

However, $\mathrm{Res}\,\dfrac{1}{\zeta}\bigg|_{\zeta=\infty} = -1$, so ultimately we obtain:

$$R_0(\beta) = -\frac{8i\pi}{\lambda^2 \ln\lambda^2}. \quad (41)$$

Eq. (41) is a solution to the problem of the asymptotics of hydrodynamic force for $\beta \to 0$. In accordance with this formula, the main term of the asymptotics of the hydrodynamic force at small values of β takes this form and does not depend on the shape of the smooth contour. This effect is mentioned in [1] for contours shaped as a circle and a plate. However, it turns out that it occurs in all cases. This can be verified only for the Stokes problem for an elliptic contour, which has an analytical solution [15].

Asymptotics of the Stokes problem for elliptic contour

Let us illustrate the application of the constructed asymptotics with the example of the Stokes problem for an elliptic contour.

Asymptotic solution for "large" values of β. The asymptotic solution to this problem in the first approximation was obtained in [21]. To construct the following approximations, we turn to Eqs. (19)–(21) and (27). Their application requires numerical calculation of integrals containing functions and their derivatives, as well as numerical determination of integrals with a kernel containing a logarithmic singularity. The quadrature formula proposed in [26] was used for this procedure. Omitting the technical details, let us present only some of the calculation results.

Fig. 4 compares the calculation results of the force magnitude $R_x(\beta)$, obtained in [21] by the numerical solution of the Stokes problem on oscillations of an elliptical contour along a larger axis (parameter $\varepsilon = 0.2$) with the calculation results $R_x^{(k)}(\beta)$ ($k = 1, 2, 3$), obtained taking into account one, two and three terms of the asymptotic dependences (19)–(21) and (27), respectively. Note that the half-sum of the ellipse's semi-axes was chosen as the characteristic length L.

Fig. 4 shows that the second and third approximations significantly improve the result in the range of "moderate" β values. A good agreement with the numerical solution for large values of the parameter β is already achieved by the first approximation [21].

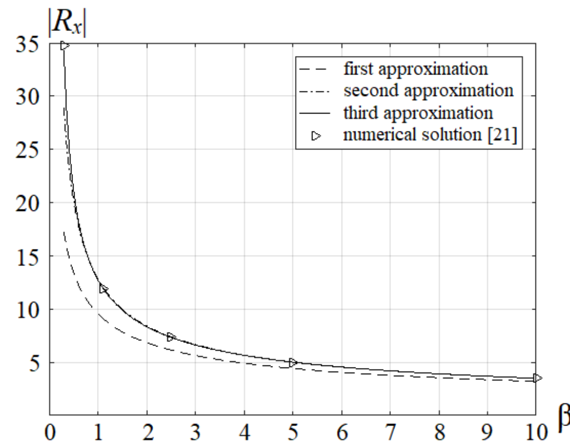

Fig. 4. Comparison of caculation results for magnitude of $R_x(\beta)$ obtained in [21] with calculation results for magnitude of $R_x^{(k)}(\beta)$ ($k = 1, 2, 3$)

Asymptotic solution for "small" values of β. Two terms of asymptotic expansions of potentials at $\beta \to 0$ and finite values of ξ take the following form (the first terms were given in [15]):

$$\begin{cases} \varphi(\xi,\eta) \underset{\beta\to 0}{\sim} \dfrac{8e^{-\xi-\xi_0}}{(1-\varepsilon)\lambda^2 \ln\lambda^2}\cos\eta - \dfrac{1}{2}e^{-\xi-\xi_0}\left(1+\varepsilon-e^{2\xi_0}+\varepsilon e^{2\xi_0}\right)\cos\eta, \\ \psi(\xi,\eta) \underset{\beta\to 0}{\sim} \dfrac{8e^{-\xi-\xi_0}}{(1-\varepsilon)\lambda^2 \ln\lambda^2}\sin\eta + \dfrac{1}{2}e^{-\xi-\xi_0}\left(e^{2\xi}-1\right)(1+\varepsilon)\sin\eta, \end{cases} \tag{42}$$

where ε is the ratio of the ellipse's semi-axes, $\varepsilon \in [0,1]$; ξ, η are elliptical coordinates, $\xi \in [\xi_0,+\infty]$, $\eta \in [0,2\pi]$; $x = h\,\mathrm{ch}\xi\cos\eta$, $y = h\,\mathrm{sh}\xi\sin\eta$, $h = \sqrt{1-\varepsilon^2}$, $z = x+iy = h\,ch(\xi+i\eta)$.

The contour of the ellipse corresponds to the value $\xi_0 = \mathrm{arth}\varepsilon$.

It is easy to prove that

$$1+\varepsilon-e^{2\xi_0}+\varepsilon e^{2\xi_0}=0, \quad \frac{e^{-\xi-\xi_0}\left(e^{2\xi}-1\right)(1+\varepsilon)}{2}\sin\eta = y.$$

Then it follows from Eqs. (42) that

$$\begin{cases} \varphi(\xi,\eta) \underset{\beta\to 0}{\sim} \dfrac{8e^{-\xi-\xi_0}}{(1-\varepsilon)\lambda^2 \ln\lambda^2}\cos\eta, \\ \psi(\xi,\eta) \underset{\beta\to 0}{\sim} \dfrac{8e^{-\xi-\xi_0}}{(1-\varepsilon)\lambda^2 \ln\lambda^2}\sin\eta + y; \end{cases}$$

$$F(\xi,\eta) = \frac{8e^{-\xi-\xi_0}}{(1-\varepsilon)\lambda^2 \ln\lambda^2}(\cos\eta - i\sin\eta) = \frac{8}{\lambda^2 \ln\lambda^2}\frac{1}{he^{\xi+i\eta}}.$$

Furthermore,

$$he^{\xi+i\eta} = he^{arch\frac{z}{h}} = z + \sqrt{z^2 - h^2}.$$

Therefore,

$$F(z) = \frac{8}{\lambda^2 \ln\lambda^2}\frac{1}{\zeta(z)}. \quad (43)$$

A well-known conformal mapping [24] of the form

$$z = \frac{1}{2}\left((1+\varepsilon)\zeta + \frac{(1-\varepsilon)}{\zeta}\right) \quad (44)$$

maps the exterior of the circle $|\zeta| = 1$ to the exterior of the ellipse with semi-axes 1 and ε.

It follows from expression (44) that

$$\zeta(z) = \frac{z + \sqrt{z^2 - h^2}}{1+\varepsilon}.$$

By mapping (43) to the exterior of a unit circle

$$F(\zeta) = \frac{8k}{\lambda^2 \ln\lambda^2}\frac{1}{(1+\varepsilon)\zeta}.$$

and in accordance with Eq. (40), we obtain (as expected) that

$$R_0(\beta) = -\frac{8i\pi}{\lambda^2 \ln\lambda^2}. \quad (45)$$

Conclusion

We constructed asymptotic formulas for the problem of small harmonic oscillations of a plane contour immersed in incompressible viscous liquid. It was established that the main term of the asymptotic hydrodynamic force does not depend on the shape of a smooth contour for small values of the parameter β. The second and third asymptotic approximations obtained for large values of β (see Fig. 4) allow to significantly improve the results of calculating the hydrodynamic force in the range of moderate numbers β.

Thus, calculations of the hydrodynamic force in an arbitrary smooth contour in a wide range of β values can be performed using the appropriate asymptotics.

REFERENCES

1. **Sader J. E.,** Frequency response of cantilever beams immersed in viscous fluids with applications to the atomic force microscope, J. Appl. Phys. 84 (1) (1998) 64–76.

2. **Maali A., Hurth C., Boisgard R., et al.,** Hydrodynamics of oscillating atomic force microscopy cantilevers in viscous fluids, J. Appl. Phys. 97 (7) (2005) 074907.

3. **Quicones M., Camargo H., Baquero H.,** Frequency response of a microcantilever immersed in fluid, Proc. 4th World Congress on New Technologies (NewTech'18), Madrid, Spain, August 19–21, 2018. (2018) 122.

4. **Stokes G. G.,** On the effect of internal friction of fluids on the motion of pendulums, Trans. Camb. Phil. Soc. 9 (2) (1851) 8–106.

5. **Rosenhead L.** (Ed.), Laminar boundary layers, Oxford University Press, Oxford (UK), 1963.

6. **Ray M.,** Vibration of an infinite elliptic cylinder in a viscous liquid, Z. Angew. Math. Mech. 16 (2) (1936) 99–108.

7. **Kanwal R. P.,** Vibrations of an elliptic cylinder and a flat plate in a viscous fluid, Z. Angew. Math. Mech. 35 (1–2) (1955) 17–22.

8. **Tanahashi T.,** Force acting on an oscillating cylinder in incompressible viscous fluid, Keio Eng. Rep. 25 (11) (1972) 129–140.

9. **Landau L. D., Lifshitz E. M.,** Course of theoretical physics, in 10 Vols. Vol. 6. Fluid Mechanics, Pergamon Press, Oxford, UK, 1959.

10. **Ricci A., Giuri E.,** Fluid Structure Interaction (FSI) analysis of microcantilevers vibrating in fluid environment, Proc. Europ. COMSOL Conf., March 30, 2009. Milan, Italy (2009) 1–11.

11. **Kirstein S., Mertesdorf M., Schoenhoff M.,** The influence of a viscous fluid on the vibration dynamics of scanning near-field optical microscopy fiber probes and atomic force microscopy cantilevers, J. Appl. Phys. 84 (4) (1998) 1782–1790.

12. **Chaplin J. R., Subbiah K.,** Hydrodynamic damping of a cylinder in still water and a transverse current, Appl. Ocean Res. 20 (4) (1998) 251–259.

13. **Guz A. N.,** Dinamika szhimayemoy vyazkoy zhidkosti [Dynamics of compressible viscous fluid], A.S.K. Publishing, Kiev, 1998 (in Russian).

14. **Kadyrov S. G.,** The method of boundary integral equations in the issue of small oscillations of bodies in a viscous compressible fluid, Morskoy Vestnik. (S1 (10)) (2013) 85–87 (in Russian).

15. **Afanasov E. N., Kadyrov S. G., Pevzner V. V.,** The Stokes problem for an elliptic contour, St. Petersburg State Polytechnical University Journal. Physics and Mathematics. 16 (3) (2023) 177–188 (in Russian).

16. **Gradshteyn I. S., Ryzhik I. M.,** Table of integrals, series, and products; Edited by D. Zwillinger and V. Moll, Academic Press, Elsevier Inc., New York, 2014.

17. **Fedoryuk M. V.,** Asimptotika: integraly i ryady [Asymptotics: Integrals and series]. Moscow, Nauka Publishing., 1987 (in Russian).

18. **Pogorelov A. V.,** Differential geometry, P. Noordhoff N. V., Groningen, Netherlands, 1954.

19. **Troesch A. W., Kim S. K.,** Hydrodynamic forces acting on cylinders oscillating at small amplitudes, J. Fluids Struct. 5 (1) (1991) 113–126.

20. **Bearman P. W., Downie M. J., Graham J. M. R., Obasaju E. D.,** Forces on cylinders in viscous oscillatory flow at low Keulegan–Carpenter numbers, J. Fluid Mech. 154 (May) (1985) 337–356.

21. **Afanasov E. N., Kadyrov S. G.,** Boundary integral equations and asymptotic solutions of the plane problem of small oscillations of body in a viscous incompressible fluid; Simulation, Computer and Full-Scale Experiment in Natural Sciences. (4) (2016) 4–18 (in Russian).

22. **Mikhlin S. G.,** Mathematical physics: An advanced course, North-Holland Pub. Co., Amsterdam, 1970.

23. **Lifanov I. K.,** Osobyye integralnyye uravneniya i metody ikh chislennogo resheniya [Special integral equations and methods for their numerical solution], MAKS Press, Moscow, 2006 (in Russian).

24. **Lavrent'ev M. A., Shabat B. V.,** Metody teorii funkcij kompleksnogo peremennogo [Methods of the theory of functions of complex variable], Nauka Publishing, Moscow, 1973 (in Russian).

25. **Kochin N. E., Kibel' I. A., Roze N. V.,** Theoretical hydromechanics, Vol. 1, Interscience Publ., New York, 1964.

26. **Meleshko I. N., Lasyi P. G., Dovga Yu. A.** Approximate calculation method for integrals with logarithmic peculiarity of special type, Science & Technique. (3) (2012) 47–50 (in Russian).

СПИСОК ЛИТЕРАТУРЫ

1. **Sader J. E.** Frequency response of cantilever beams immersed in viscous fluids with applications to the atomic force microscope // Journal of Applied Physics. 1998. Vol. 84. No. 1. Pp. 64–76.

2. **Maali A., Hurth C., Boisgard R., Jai C., Cohen-Bouhacina T., Aimé J.-P.** Hydrodynamics of oscillating atomic force microscopy cantilevers in viscous fluids // Journal of Applied Physics. 2005. Vol. 97. No. 7. P. 074907.

3. **Quicones M., Camargo H., Baquero H.** Frequency response of a microcantilever immersed in fluid // Proceedings of the 4th World Congress on New Technologies (NewTech'-18). Madrid, Spain. August 19–21, 2018. P. 122.

4. **Stokes G. G.** On the effect of internal friction of fluids on the motion of pendulums // Transactions of the Cambridge Philosophical Society. 1851. Vol. 9. Part 2. Pp. 8–106.

5. **Rosenhead L.** (Editor). Laminar boundary layers. Oxford (UK): Oxford University Press, 1963. 688 p.

6. **Ray M.** Vibration of an infinite elliptic cylinder in a viscous liquid // Zeitschrift für Angewandte Mathematik und Mechanik. 1936. Vol. 16. No. 2. Pp. 99–108.

7. **Kanwal R. P.** Vibrations of an elliptic cylinder and a flat plate in a viscous fluid // Zeitschrift für Angewandte Mathematik und Mechanik. 1955. Vol. 35. No. 1–2. Pp. 17–22.

8. **Tanahashi T.** Force acting on an oscillating cylinder in incompressible viscous fluid // Keio Engineering Reports. 1972. Vol. 25. No. 11. Pp. 129–140.

9. **Ландау Л. Д., Лифшиц Е. М.** Теоретическая физика. В 10 тт. Т. 6. Гидродинамика. М.: Наука, 1986. 736 с.

10. **Ricci A., Giuri E.** Fluid Structure Interaction (FSI) analysis of microcantilevers vibrating in fluid environment // Proceedings of the European COMSOL Conference. March 30, 2009. Milan, Italy. 2009. Pp. 1–11.

11. **Kirstein S., Mertesdorf M., Schoenhoff M.** The influence of a viscous fluid on the vibration dynamics of scanning near-field optical microscopy fiber probes and atomic force microscopy cantilevers // Journal of Applied Physics.1998. Vol. 84. No. 4. Pp.1782–1790.

12. **Chaplin J. R., Subbiah K.** Hydrodynamic damping of a cylinder in still water and a transverse current // Applied Ocean Research. 1998. Vol. 20. No. 4. Pp. 251–259.

13. **Гузь А. Н.** Динамика сжимаемой вязкой жидкости. Киев: А.С.К., 1998. 350 с.

14. **Кадыров С. Г.** Метод граничных интегральных уравнений в задаче о малых колебаниях тел в сжимаемой вязкой жидкости // Морской вестник. 2013. Апрель. Спецвыпуск. № 1 (10). С. 85–87.

15. **Афанасов Е. Н., Кадыров С. Г., Певзнер В. В.** Задача Стокса для эллиптического контура // Научно-технические ведомости СПбГПУ. Физико-математические науки. 2023. Т. 16. № 3. С. 177–188.

16. **Градштейн И. С., Рыжик И. М.** Таблицы интегралов, сумм, рядов и произведений. Изд. 4-е. М.: Физматгиз, 1963. 1100 с.

17. **Федорюк М. В.** Асимптотика: интегралы и ряды. М.: Наука. Гл. ред. физ-мат. лит-ры, 1987. 544 с.

18. **Погорелов А. В.** Дифференциальная геометрия. Изд. 6-е. М.: Наука. Гл. ред. физ-мат. лит-ры, 1974. 176 с.

19. **Troesch A. W., Kim S. K.** Hydrodynamic forces acting on cylinders oscillating at small amplitudes // Journal of Fluids and Structures. 1991. Vol. 5. No. 1. Pp. 113–126.

20. **Bearman P. W., Downie M. J., Graham J. M. R., Obasaju E. D.** Forces on cylinders in viscous oscillatory flow at low Keulegan–Carpenter numbers //Journal of Fluid Mechanics. 1985. Vol. 154. May. Pp. 337–356.

21. **Афанасов Е. Н., Кадыров С. Г.** Граничные интегральные уравнения и асимптотика решения плоской задачи о малых колебаниях тела в вязкой несжимаемой жидкости // Математическое моделирование, компьютерный и натурный эксперимент в естественных науках. 2016. № 4. С. 4–18.

22. **Михлин С. Г.** Курс математической физики. М.: Наука. Гл. ред. физ-мат. лит-ры, 1968. 576 с.

23. **Лифанов И. К.** Особые интегральные уравнения и методы их численного решения. М: МАКС Пресс, 2006. 70 с.

24. **Лаврентьев М. А., Шабат Б. В.** Методы теории функций комплексного переменного. Изд. 4-е. М.: Наука. Гл. ред. физ-мат. лит-ры, 1973. 736 с.

25. **Кочин Н. Е., Кибель И. А., Розе Н. В.** Теоретическая гидромеханика. Часть 1. Изд. 6-е. М.: Физматгиз, 1963. 584 с.

26. **Мелешко И. Н., Ласый П. Г., Довга Ю. А.** Приближенный метод вычисления интегралов с логарифмической особенностью специального вида // Наука и техника. 2012. № 3. С. 47–50.

THE AUTHORS

AFANASOV Evgeny N.
LLC «Evolution Marine Digital»
4-3 Alexandrovsky Park, St. Petersburg, 197198, Russia
zhenya.afanasov@yandex.ru
ORCID: 0009-0001-6193-5083

KADYROV Sergey G.
State Marine Technical University
3 Lotsmanskaya St., St. Petersburg, 190008, Russia
skadyrov@gmail.com
ORCID: 0009-0004-3383-7613

SOROKIN Vadim N.
State Marine Technical University
3 Lotsmanskaya St., St. Petersburg, 190008, Russia
sorokin_v_n@mail.ru
ORCID: 0009-0000-2883-2763

СВЕДЕНИЯ ОБ АВТОРАХ

АФАНАСОВ Евгений Николаевич – *инженер-гидродинамик ООО «Эволюция морских цифровых технологий».*
197198, Россия, г. Санкт-Петербург, Александровский парк, 4, к. 3
zhenya.afanasov@yandex.ru
ORCID: 0009-0001-6193-5083

КАДЫРОВ Сергей Газимурович – *кандидат технических наук, доцент кафедры математики Санкт-Петербургского государственного морского технического университета.*
190008, Россия, г. Санкт-Петербург, Лоцманская ул., 3
skadyrov@gmail.com
ORCID: 0009-0004-3383-7613

СОРОКИН Вадим Николаевич – *старший преподаватель кафедры математики Санкт-Петербургского государственного морского технического университета.*
190008, Россия, г. Санкт-Петербург, Лоцманская ул., 3
sorokin_v_n@mail.ru
ORCID: 0009-0000-2883-2763

Received 09.04.2024. Approved after reviewing 17.04.2024. Accepted 17.04.2024.

Статья поступила в редакцию 09.04.2024. Одобрена после рецензирования 17.04.2024. Принята 17.04.2024.

© Peter the Great St. Petersburg Polytechnic University, 2024

Original article
DOI: https://doi.org/10.18721/JPM.17312

A TOPOLOGY OPTIMIZATION ALGORITHM FOR ELECTROELASTICITY COUPLED PROBLEMS

A. D. Novokshenov✉, *I. Abdulin, D. V. Vershinin*

Peter the Great St. Petersburg Polytechnic University, St. Petersburg, Russia

✉ novoksh_ad@spbstu.ru

Abstract. A problem of applying topology optimization to elastic deformable bodies exposed to coupled electric and mechanical fields has been studied. The main goal was to find the optimal distribution of electric and mechanical properties in the given area, taking into account restrictions on the final volume of the structure. A topology optimization algorithm was formulated and implemented (as program code in Python) for bodies under the action of the coupled electric and mechanical fields. The algorithm included solving the coupled electroelasticity problem using the finite element method, analyzing derivatives of the objective function, and optimizing by the dual procedure within the method of moving asymptotes. The algorithm was tested in numerical experiments on the optimization problem of a piezoelectric actuator exposed to uniform or linearly distributed electric fields. As a result, the distributions of mechanical and electrical properties were obtained for various values of the stiffness coefficient.

Keywords: topology optimization, finite element method, method of moving asymptotes, piezoelectric actuator

Funding: The reported study was funded by Russian Science Foundation (Grant No. 22-71-00108), https://rscf.ru/project/22-71-00108/

Citation: Novokshenov A. D., Abdulin I., Vershinin D. V., A topology optimization algorithm for electroelasticity coupled problems, St. Petersburg State Polytechnical University Journal. Physics and Mathematics. 17 (3) (2024) 134–147. DOI: https://doi.org/10.18721/JPM.17312

This is an open access article under the CC BY-NC 4.0 license (https://creativecommons.org/licenses/by-nc/4.0/)

Научная статья
УДК 539.3
DOI: https://doi.org/10.18721/JPM.17312

АЛГОРИТМ ТОПОЛОГИЧЕСКОЙ ОПТИМИЗАЦИИ ДЛЯ СВЯЗАННЫХ ЗАДАЧ ЭЛЕКТРОУПРУГОСТИ

А. Д. Новокшенов✉, *И. Абдулин, Д. В. Вершинин*

Санкт-Петербургский политехнический университет Петра Великого, Санкт-Петербург, Россия

✉ novoksh_ad@spbstu.ru

Аннотация. Исследована проблема применения топологической оптимизации к упругим деформируемым телам, находящимся в условиях воздействия связанных электрических и механических полей. Основная задача состояла в оптимизации распределения электрических и механических свойств материала в заданной области с учетом ограничения на итоговый объем конструкции. Сформулирован и реализован алгоритм топологической оптимизации (в виде программного кода на языке Python) для тел, находящихся под действием связанных электрических и механических полей. Алгоритм включал в себя решение связанной задачи электроупругости с помощью метода конечных элементов, анализ производных целевой функции и оптимизацию двойственным методом в рамках метода скользящих асимптот. Алгоритм был опробован

© Novokshenov A. D., Abdulin I., Vershinin D. V., 2024. Published by Peter the Great St. Petersburg Polytechnic University.

в численных экспериментах на задаче оптимизации пьезоэлектрического актуатора, помещенного в однородное либо в линейно-распределенное электрические поля. В итоге получены распределения механических и электрических свойств для различных значений коэффициента жесткости.

Ключевые слова: топологическая оптимизация, метод конечных элементов, метод скользящих асимптот, пьезоэлектрический актуатор

Финансирование: Исследование выполнено за счет гранта Российского научного фонда № 00108-71-22, https://rscf.ru/project/22-71-00108/.

Ссылка для цитирования: Новокшенов А. Д., Абдулин И., Вершинин Д. В. Алгоритм топологической оптимизации для связанных задач электроупругости // Научно-технические ведомости СПбГПУ. Физико-математические науки. 2024. Т. 17. № 3. С. 134–147. DOI: https://doi.org/10.18721/JPM.17312

Статья открытого доступа, распространяемая по лицензии CC BY-NC 4.0 (https://creativecommons.org/licenses/by-nc/4.0/)

Introduction

Structural and topological optimization (TO) is a field with long, rich history. For instance, the problem on the optimal weight of a column whose simply-supported end is subjected to a compressive force was first solved by Lagrange [1]. One of the earliest studies on structural optimization was written by Michell in 1904 [2]. As numerical methods, in particular, the finite element method (FEM), emerged in the 1960s, great strides were made in structural (including topological) optimization [3]. Complete theories were consequently developed in the 1980s, described in detail by Bendsше et al. [4, 5].

Numerous methods have been formulated for analyzing and improving the performance of piezoelectric structures in terms of size and geometry [6–9], structure and number of layers [10], optimization with respect to sub-parameters [11–13]. TO methods were commonly used in various fields of physics [14, 15], including piezoelectricity. Algorithms for optimization of piezoelectric actuators [16, 17], sensors [18] and energy storage devices [19–21] were constructed by introducing suitable objective functions and new parameters. There are also various modifications of these methods, for example, taking into account the constraints on mechanical stresses [22].

The homogenization method was used to solve the problem in earlier studies [23, 24]. Alternative approaches were presented in the subsequent years: method for solid isotropic material with penalization (SIMP) [25], bi-directional evolutionary structural optimization (BESO) [26] and level-set method (LSM) [27].

Analysis of the literature indicates that the existing algorithms for topological optimization can be divided into three classes:

based on optimality criteria (heuristic);

based on derivative analysis (mathematical programming methods);

genetic algorithms for topological optimization.

We selected the method of moving asymptotes (MMA) [28] as the main optimization algorithm, as it is one of the most universal and stable methods used for optimizing structures.

An algorithm for solving the topological optimization problem for the coupled electroelasticity problem is formulated and presented in this paper based on analysis of existing publications.

The algorithm relies on the method of moving asymptotes, a finite element solution of the coupled electroelasticity problem and parameterization of material properties using a modified SIMP method. The algorithm is implemented in Python and tested for the optimization problem of a piezoelectric actuator for the case of a DC electric field.

Topological optimization

Topological optimization is a mathematical method allowing to obtain the optimal distribution of material within a given space under given configurations of external loads, boundary conditions and constraints to achieve the best performance of the system.

© Новокшенов А. Д., Абдулин И., Вершинин Д. В., 2024. Издатель: Санкт-Петербургский политехнический университет Петра Великого.

The most typical problem of topological optimization is minimization of the structure's compliance. Mathematically, it is equivalent to minimizing the work of external forces [5], i.e.,

$$\min_{\mathbf{u}\in\mathbf{U}} A^{ex}(\mathbf{u}) \tag{1}$$

under the given constraints:

$$\begin{gathered} A^{ex}(\delta\mathbf{u}) = \delta(\rho_b\psi(\varepsilon(\mathbf{u}))), \forall\delta\mathbf{u}\in\mathbf{U}, \\ V \le \alpha V_0, 0<\alpha<1, \end{gathered} \tag{2}$$

where $A^{ex}(\delta\mathbf{u})$ is the work of external forces on the obtained displacements; $\psi(\varepsilon(\mathbf{u}))$ is the free-energy density; $\delta\mathbf{u}$ is the possible displacement; $\mathbf{U}$ is the allowable displacement; ρ_b is the density of the body; V, V_0 are the final and initial volumes of the structure; α is the proportion of the final material.

The first constraint in Eqs. (2) is the equilibrium condition in variational form.

This problem is usually solved by discretization of the domain and using FEM. Therefore, it is necessary to reformulate the problem for the appropriate finite element formulation, namely,

$$\min_{\mathbf{u}\in\mathbf{U}} \mathbf{f}^T\mathbf{u}, \tag{3}$$

under the following constraints:

$$\begin{gathered} \mathbf{K}(E_e)\mathbf{u} = \mathbf{f}, E_e \in E_{per}, \\ \mathbf{K}(E_e) = \sum_{e=1}^{N} \mathbf{K_e}(E_e), \\ \sum_{e=1}^{N} \rho_e v_e = V = \alpha V_0, 0<\alpha<1, \end{gathered} \tag{4}$$

where $\mathbf{f}$ is the column of forces; $\mathbf{u}$ is the column of displacements; $\mathbf{K}$ is the stiffness matrix of the system; v_e is the volume of the finite element numbered e; ρ_e, E_e are the density and Young's modulus of the finite element numbered e; E_{per} are the allowable values of Young's modulus.

The method of moving asymptotes (MMA) is used as a tool for solving this problem.

Algorithm for solving the coupled electroelasticity problem (CEEP)

Governing equations for the CEEP. The relations for the linear CEEP for a piezoelectric material, without taking into account the temperature effect, can be written as follows [29]:

$$\begin{gathered} \mathbf{T} = \mathbf{c}^E\mathbf{S} - \mathbf{e}^T\mathbf{E}, \\ \mathbf{D} = \mathbf{eS} + \boldsymbol{\varepsilon}^S\mathbf{E}, \end{gathered} \tag{5}$$

where $\mathbf{T}$ is the vector of mechanical stresses; $\mathbf{S}$ is the vector of mechanical strains; $\mathbf{E}$ is the electric field strength; $\mathbf{D}$ is the vector of electric displacement; $\mathbf{c}^E$ is the stiffness matrix at constant electric field $\mathbf{E}$; $\boldsymbol{\varepsilon}^S$ is the permittivity matrix at constant strain $\mathbf{S}$; $\mathbf{e}$ is the matrix of piezoelectric coupling coefficients; the superscript T indicates transposition.

The electric field strength $\mathbf{E}$ is determined by the relation

$$\mathbf{E} = -\text{grad}\varphi, \tag{6}$$

where φ is the electric potential.

For the model presented in this paper, a piezoelectric material of tetragonal crystal class [30] with orthotropic anisotropy is considered. This class includes most piezoelectric materials, in particular well-known materials such as lead zirconate titanate $PbZr_{1-x}Ti_xO_3$ (PZT).

In view of the above, the mechanical stiffness tensor $\mathbf{c}^E$, the piezoelectric matrix $\mathbf{e}^T$ and the dielectric constant $\boldsymbol{\varepsilon}^S$ for the complete three-dimensional case have the following form:

$$\mathbf{c}^{\mathbf{E}} = \begin{pmatrix} c_{11}^{\ E} & c_{12}^{\ E} & c_{13}^{\ E} & 0 & 0 & 0 \\ c_{12}^{\ E} & c_{11}^{\ E} & c_{13}^{\ E} & 0 & 0 & 0 \\ c_{13}^{\ E} & c_{13}^{\ E} & c_{33}^{\ E} & 0 & 0 & 0 \\ 0 & 0 & 0 & c_{44}^{\ E} & 0 & 0 \\ 0 & 0 & 0 & 0 & c_{44}^{\ E} & 0 \\ 0 & 0 & 0 & 0 & 0 & c_{66}^{\ E} \end{pmatrix}, \ \mathbf{e}^{T} = \begin{pmatrix} 0 & 0 & 0 & 0 & e_{15} & 0 \\ 0 & 0 & 0 & e_{15} & 0 & 0 \\ e_{31} & e_{31} & e_{33} & 0 & 0 & 0 \end{pmatrix}, \tag{7}$$

$$\boldsymbol{\varepsilon}^{S} = \begin{pmatrix} \varepsilon^{S}_{\ 11} & 0 & 0 \\ 0 & \varepsilon^{S}_{\ 11} & 0 \\ 0 & 0 & \varepsilon^{S}_{\ 33} \end{pmatrix}.$$

Next, consider a plate consisting of a piezoelectric material distributed between two electrodes (Fig. 1).

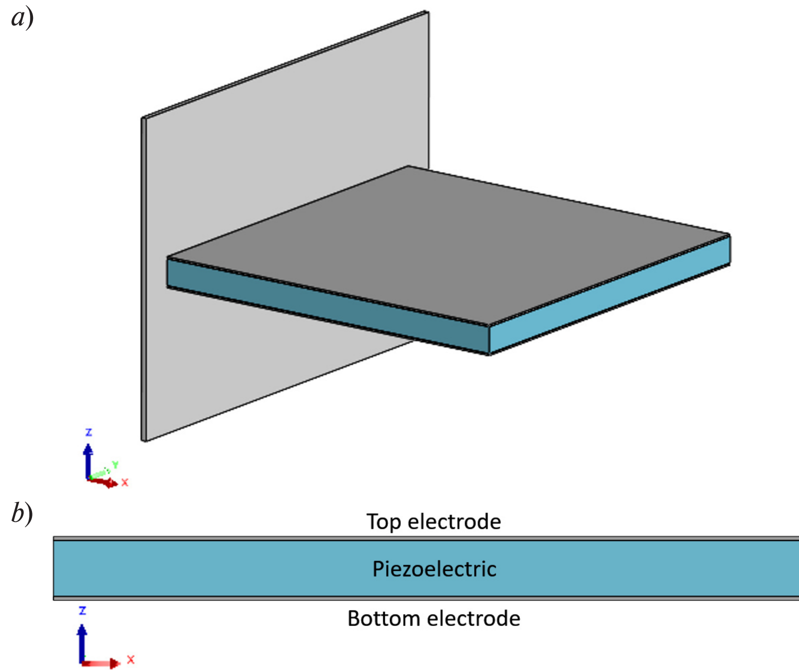

Fig. 1. Isometric view (*a*) and side view (*b*) of plate made of piezoelectric material with top and bottom electrodes

We can make the following assumptions based on the configuration of the system considered [31]:
the ratio of the length or width of the plate to its thickness should be less than 0.1;
displacements and loads in the system can occur only in the plane of the plate;
the thickness of the electrodes is negligible compared to the thickness of the plate;
the mechanical part of the problem is linear;
the electrodes are perfectly conducting;
The piezoelectric polarization vector is directed perpendicular to the plate plane (along the *OZ* axis);
the value of the potential φ at the bottom electrode of the plate is assumed to be zero;
the electric field **E** is uniform along the thickness of the plate (in the direction of the *OZ* axis);
the electric potential φ follows a linear law along the thickness of the plate (in the direction of the *OZ* axis).

The first two assumptions allow to use the formulation for the plane stress problem of elasticity theory. The assumption that the thickness of the electrodes is small allows to neglect their effect on the stiffness of the system. In addition, when the polarization axis of the piezoelectric material is oriented along the *OZ* direction, its behavior in the plane turns out to be isotropic. Moreover, in this case, the only influence exerted on the material is from the electric field in the *OZ* direction.

Thus, the compressed (2D) form of the piezoelectric governing equation can be written as [7]:

$$\begin{bmatrix} T_1 \\ T_2 \\ T_3 \\ D_3 \end{bmatrix} = \begin{bmatrix} c^*_{11} & c^*_{12} & 0 & -e^*_{31} \\ c^*_{12} & c^*_{12} & 0 & -e^*_{31} \\ 0 & 0 & c^*_{33} & 0 \\ c^*_{31} & c^*_{31} & 0 & \varepsilon^*_{33} \end{bmatrix} \begin{bmatrix} S_1 \\ S_2 \\ S_3 \\ E_3 \end{bmatrix}, \tag{8}$$

where the components of the matrix can be expressed in terms of the components introduced earlier:

$$\begin{gathered} c^*_{11} = c_{11}{}^E - \frac{(c_{13}{}^E)^2}{c_{33}{}^E},\; c^*_{12} = c_{12}{}^E - \frac{(c_{13}{}^E)^2}{c_{33}{}^E},\; c^*_{33} = c_{66}{}^E, \\ e^*_{31} = e_{31} - e_{33}\frac{c_{13}{}^E}{c_{33}{}^E},\; \varepsilon^*_{33} = \varepsilon^S{}_{33} + \frac{(e_{33})^2}{c_{33}{}^E}. \end{gathered} \tag{9}$$

Governing equation (8) is used for subsequent finite element modeling of the system.

Finite element model of the system. For finite element modeling of the piezoelectric plate, the region was partitioned into flat rectangular linear elements with two Gaussian integration points.

The strain vector of an element can be represented as

$$\mathbf{S} = \mathbf{B}_u \mathbf{u}, \tag{10}$$

where $\mathbf{B}_u$ is the matrix of partial derivatives for calculating the strain vector.

The electric field strength is generally a vector quantity calculated as the gradient of the electric potential by Eq. (6). However, the last two assumptions about the nature of the electric field and the orientation of the piezoelectric material (see above) make it possible to reduce the consideration of the field strength to a scalar quantity, i.e., its projection on the *OZ* axis. Then the magnitude of the electric field strength is calculated as

$$E = -B_\varphi \varphi,\; B_\varphi = \frac{1}{h}, \tag{11}$$

where h is the thickness of the plate.

Next, we use the Hamilton variational principle without taking into account the dissipative forces in the system; we can write a linear differential equation for one element in matrix form [29]:

$$\begin{pmatrix} \mathbf{m} & 0 \\ 0 & 0 \end{pmatrix} \begin{pmatrix} \ddot{\mathbf{u}} \\ \ddot{\boldsymbol{\varphi}} \end{pmatrix} + \begin{pmatrix} \mathbf{k}_{uu} & \mathbf{k}_{u\phi} \\ \mathbf{k}_{\phi u} & -\mathbf{k}_{\phi\phi} \end{pmatrix} \begin{pmatrix} \mathbf{u} \\ \boldsymbol{\varphi} \end{pmatrix} = \begin{pmatrix} \mathbf{f} \\ \mathbf{q} \end{pmatrix}, \tag{12}$$

where $\mathbf{m}$ is the matrix of inertial coefficients; $\mathbf{k}_{uu}$ is the local stiffness matrix; $\mathbf{f}$ is the vector of external mechanical force; $\boldsymbol{q}$ is the electric charge; $\mathbf{k}_{u\varphi}$ is the piezoelectric coupling matrix.

The matrix $\mathbf{k}_{u\varphi}$ is calculated by the formula

$$\mathbf{k}_{u\phi} = h\int_\Omega \mathbf{B}_u^T \mathbf{e}^T \mathbf{B}_\phi \,|\,J\,|\, d\xi d\eta, \tag{13}$$

where ξ, η are the local coordinates of the element; J is the Jacobian of the element.

In accordance with the FEM algorithm, local matrices and load vectors should be assembled into global ones, after which we can write the equation for the entire region under consideration:

$$\begin{pmatrix} \mathbf{M} & \mathbf{0} \\ \mathbf{0} & \mathbf{0} \end{pmatrix} \begin{pmatrix} \ddot{\mathbf{U}} \\ \ddot{\mathbf{\Phi}} \end{pmatrix} + \begin{pmatrix} \mathbf{K}_{uu} & \mathbf{K}_{u\phi} \\ \mathbf{K}_{\phi u} & -\mathbf{K}_{\phi\phi} \end{pmatrix} \begin{pmatrix} \mathbf{U} \\ \mathbf{\Phi} \end{pmatrix} = \begin{pmatrix} \mathbf{F} \\ \mathbf{Q} \end{pmatrix}. \tag{14}$$

We consider the quasi-static problem of a spring mechanism under the action of an external electric field. This formulation gives zero derivatives of the quantities with respect to time. In addition, it is assumed that there is no external electric charge in the system ($\mathbf{Q} = 0$). This formulation of the problem leads us to the following system of equations for FEM:

$$\mathbf{K}_{uu}\mathbf{U} + \mathbf{K}_{u\phi}\mathbf{\Phi} = \mathbf{F}. \tag{15}$$

This system is used to calculate the displacement field under the influence of an external electric field. Then, after deriving the equation of the coupled problem for FEM, we can use it for parameterizing this problem for topological optimization.

Interpolation scheme of piezoelectric material. In this paper, an extension of the SIMP scheme is used to interpolate the given material, which requires the following dependences of local matrices on fictitious density and polarization [31]:

$$\begin{gathered} \mathbf{k}_{uu}(\rho) = (E_{min} + \rho^{p_{uu}}(E_0 - E_{min}))\mathbf{k}^0{}_{uu}, \\ \mathbf{k}_{u\phi}(\rho, P) = (e_{min} + \rho^{p_{u\phi}}(e_0 - e_{min}))(2P-1)^{p_P}\mathbf{k}^0{}_{u\phi}, \end{gathered} \tag{16}$$

where E_0, e_0 are the numbers used to determine the initial characteristics of the element material, $E_0 = e_0 = 1$; ρ is the fictitious density of the element material (taking values from 0 to 1); P is the polarization variable determining the polarization direction of the piezoelectric material (taking values from 0 to 1); p_{uu}, $p_{u\varphi}$, p_P are the penalization factors for stiffness, piezoelectric coupling and polarization, respectively; $E_{\min}$ and $e_{\min}$ are small numbers for determining the minimum possible values for stiffness and piezoelectric coupling coefficient.

The presence of small numbers $E_{\min}$ and $e_{\min}$ is necessary to eliminate numerical uncertainties that arise during the iterative optimization process.

The interpolation scheme given by Eq. (16) is known as PEMAP-P (piezoelectric material with penalization and polarization) and was introduced by Kцgl and Silva in 2005 [25] for optimization of adaptive materials and, in particular, piezoelectric plates.

The polarization variables P reflect the behavior of the material in the presence of an electrostatic field: for P from 0 to 0.5, the material is compressed under the action of the field, and for P from 0.5 to 1.0, it expands.

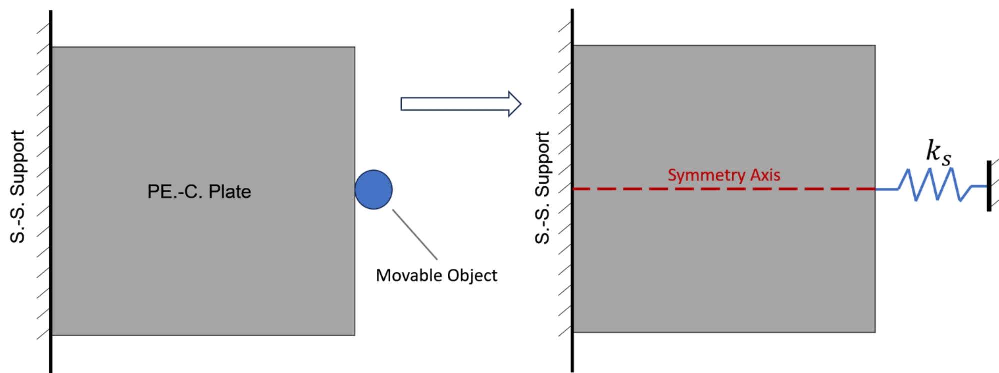

Fig. 2. Scheme of spring mechanism for problem statement:
S.-S. Support are single-sided supports; PE.-C. Plate is the piezoelectric plate;
Movable Object; Symmetry Axis; k_s is the spring stiffness

Problem statement for the piezoelectric actuator. Consider the problem of topological optimization of an electric actuator (Fig. 2). The initial scheme is a square piezoelectric plate (PE.-C. Plate) (Fig. 2, see also the subsection "Finite element model of the system"), whose left end is constrained in all degrees of freedom. The material expands or contracts under the action of an electric field, depending on its polarization.

The goal of the optimization is to ensure maximum displacement or pressure load generated by the midpoint on the right side of the plate with a constraint on the volume: $V = 0.4\ V_0$. The gray area (see Fig. 2 on the left) shows the initial region for subsequent optimization.

An additional spring with the stiffness k_s is attached to the midpoint on the right side to model the interaction of the spring mechanism with a movable object:

$$k_s = K_s k_0, \tag{17}$$

where K_s is a parameter characterizing the force of interaction with the movable object; k_0 is the largest value in the stiffness matrix of the system, i.e., $k_0 = \max K_{ij}$.

By varying the parameter K_s, we can make prioritize either greater displacement of the point considered or the pressure load generated. For example, at $K_s = 1.0$, $k_s = k_0$ (see Eq. (17)), and thus the maximum pressure load for the optimized topology is achieved. Conversely, by setting small values for this parameter, for example, $K_s = 0.01$, the plate is optimized accordingly to ensure the maximum possible displacement.

Following the classical approach to solving optimization problems for compliant mechanisms, described in monograph [5], we can write the statement for this problem as minimization of the following objective function:

$$J = -\mathbf{L}^T\mathbf{U}, \tag{18}$$

with the constraints of the form

$$\begin{gathered}\sum_{e=1}^{N_e} \rho_e v_e = V = \alpha V_0, 0 < \alpha < 1,\\ 0 < \rho_e \le 1,\\ 0 < P_e \le 1,\end{gathered} \tag{19}$$

where $\mathbf{L}$ is a vector (equal to 1 for the component that corresponds to the degree of freedom of the displacements that we are interested in, and equal to 0 for all other components); $\mathbf{U}$ is the displacement vector; ρ_e, v_e, P_e are the density, volume and polarization of the element numbered e.

Calculation of derivatives of the objective function. Using methods based on gradient descent, which include the method of moving asymptotes (selected in this paper) requires to calculate the derivatives of the objective function with respect to optimization variables at each iteration of the process:

$$\begin{aligned}\frac{\partial J}{\partial \rho_e} &= \frac{\partial}{\partial \rho_e}(-\mathbf{L}^T\mathbf{U} + \mathbf{\Lambda}^T(\mathbf{K}_{uu}\mathbf{U} + \mathbf{K}_{u\varphi}\mathbf{\Phi} - \mathbf{F})) =\\ &= \frac{\partial}{\partial \rho_e}((-\mathbf{L}^T + \mathbf{\Lambda}^T\mathbf{K}_{uu})\mathbf{U} + \mathbf{\Lambda}^T\mathbf{K}_{u\varphi}\mathbf{\Phi} - \mathbf{\Lambda}^T\mathbf{F}).\end{aligned} \tag{20}$$

To avoid calculating the derivatives of the objective function with respect to displacements, the adjoint method is used, where an additional adjoint problem must be solved to find the values of the derivatives

$$-\mathbf{L}^T + \mathbf{\Lambda}^T\mathbf{K}_{uu} = \mathbf{0}, \tag{21}$$

where $\mathbf{\Lambda}^T$ is a global adjoint vector, $\mathbf{\Lambda}^T = [\lambda_1, \lambda_2, ..., \lambda_{ndorf}]^T$.

$\boldsymbol{\Lambda}^T$ is used to find the derivatives of the objective function:

$$\frac{\partial J}{\partial \rho_e} = \boldsymbol{\lambda}_e^T \frac{\partial \mathbf{k}_{uu}}{\partial \rho_e} \mathbf{u}_e + \boldsymbol{\lambda}_e^T \frac{\partial \mathbf{k}_{u\varphi}}{\partial \rho_e} \varphi_e, \tag{22}$$

where $\boldsymbol{\lambda}_e^T$ is an adjoint element vector (consists of components λ_i of the conjugate vector $\boldsymbol{\Lambda}^T$ belonging to the element numbered e); $\mathbf{u}_e$ is the displacement vector, which consists of displacements of nodes of the element numbered e.

We use a similar procedure and write the derivatives of the objective function with respect to the polarizations P_e:

$$\frac{\partial J}{\partial P_e} = \boldsymbol{\lambda}_e^T \frac{\partial \mathbf{k}_{u\varphi}}{\partial P_e} \varphi_e. \tag{23}$$

The derivatives of the element matrices of stiffness and piezoelectric coupling are calculated by direct differentiation of expressions (16):

$$\begin{aligned} \frac{\partial \mathbf{k}_{uu}}{\partial \rho_e} &= p_{uu}(E_0 - E_{min})\rho_e^{(p_{uu}-1)}\mathbf{k}^0{}_{uu}, \\ \frac{\partial \mathbf{k}_{u\varphi}}{\partial \rho_e} &= p_{u\varphi}(e_0 - e_{min})\rho_e^{(p_{u\varphi}-1)}(2P_e-1)^{p_P}\mathbf{k}^0{}_{u\varphi}, \\ \frac{\partial \mathbf{k}_{u\varphi}}{\partial P_e} &= 2p_P(e_0 - e_{min})(2P_e-1)^{(p_P-1)}\rho_e^{p_{u\varphi}}\mathbf{k}^0{}_{u\varphi}. \end{aligned} \tag{24}$$

After finding expressions for calculating the derivatives, we can use them to solve the optimization problem by the method of moving asymptotes.

Software implementation of the algorithm. The constructed algorithm of topological optimization for the coupled electroelasticity problem, taking into account the density distribution of the piezoelectric material as well as its polarization, consists of the following steps.

Step 1. Change all design variables (fictitious densities) to satisfy the constraint on the volume fraction.

Step 2. Perform finite element calculation of the stress-strain state of the plate under the action of an electric field.

Step 3. Solve the coupled problem.

Step 4. Calculate the derivatives of the objective function based on design variables (densities and polarization).

Step 5. Construct a convex approximation of the function, find the minimum in terms of the dual function (the inner loop in MMA).

Step 6. Recalculate the vector of design variables (the solution found is the next step of the approximation point).

Step 7. Perform a convergence test. If convergence is not achieved, return to Step 2.

The algorithm was implemented in Python. A finite element solver was written for the coupled electroelasticity problem, along with a module for calculating derivatives. The developed modules were integrated with the MMA algorithm, which is publicly available.

Testing of the developed algorithm

To test the algorithm, two cases with different electric field distributions were considered: uniform or linear along the *OX* axis.

Case of uniform electric field. A uniform field distribution is obtained by setting the same potential values on the right and left edges of the plate.

Fig. 3 shows the obtained results of the density distribution in the material and its polarization for different values of the parameter K_S both in the case of a uniform electric field and in the case of a field linearly distributed along the *OX* axis (see the next subsection).

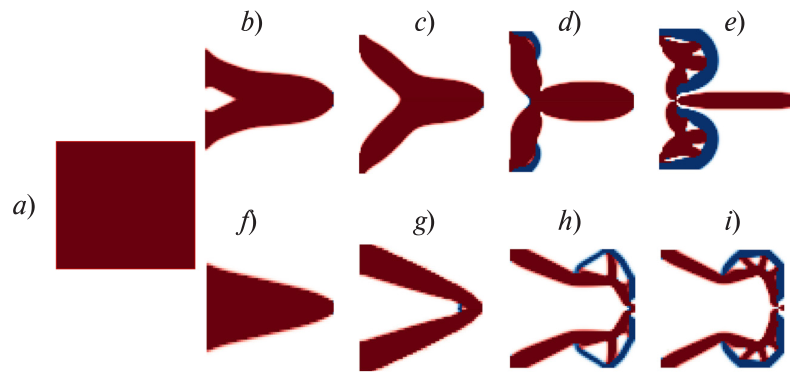

Fig. 3. Optimized distributions of material density
and polarization at different values of the parameter K_S
The material is placed in a uniform electric field (*b*–*e*) or in a field
linearly distributed along the *OX* axis (*f*–*i*); *a* is the initial topology;
values of K_S: 1.0000 (*b*, *f*), 0.1000 (*c*, *g*), 0.0125 (*d*), 0.0150 (*h*), 0.0050 (*e*, *i*)
Extension of the material is colored brown, compression is colored blue

Table

Optimization results for spring mechanism in piezoelectric plate placed in two types of electric fields (see Fig. 3)

Parameter K_S	Displacement gain η	
	Homogeneous field	Linear field along *OX* axis
1.0000	0.84	0.78
0.1000	1.04	0.93
0.0125	1.51	–
0.0150	–	1.84
0.0050	2.70	3.08

Note. K_S is the parameter characterizing the force of interaction with the movable object.

In addition, the table shows the displacement gains η compared with the initial system. Evidently, the gain coefficient η increases with a decrease in the spring stiffness, but, on the other hand, the pressure load decreases as well. The optimal distribution of the material for high values of the parameter K_S has a relatively straightforward simply connected structure with single polarization (Fig. 3, *b*–*c*). If this parameter is reduced, more complex material distributions with different tensile and compressive regions become optimal (Fig. 3, *d*–*e*), making the structure more flexible and compliant.

The results obtained are in good agreement with the results presented in [31]; this allows us to conclude that the developed algorithm is correct.

Case of electric field linearly distributed along the *OX* axis. To solve the problem for the condition of a nonuniform electric field, a zero potential value was set on the left edge of the plate, and a non-zero value was set on the right. The calculation yielded an electric field linearly distributed along the *OX* axis.

Fig. 3, *f*–*i* shows the obtained results of the density and polarization distribution for different values of the parameter K_S for the case of a field linear along the *OX* axis.

Furthermore, Table summarizes the displacement gains η for comparison (also compared to the initial system).

The above comparison suggests that the optimization results for this problem statement turn out to be very similar to the corresponding results for a uniform electric field. More uniform structures are observed at higher K_S (Fig. 3, *f*–*g*), which is provided by an increase in the pressure load. Small values of the parameter K_S lead to more complex distributions of the material with tensile and compressive regions (Fig. 3, *h*–*i*), which provides an increase in the displacement gain η.

Conclusion

In this paper, we explored the applications of topological optimization to bodies exposed to coupled fields. Based on review of the literature, we constructed and implemented an algorithm in Python code to find the optimal distribution of mechanical and electrical properties of a material, maximizing the compliance of the structure or the pressure load in a given direction with constraints on volume. The developed algorithm consists of solving the coupled electroelasticity problem by the finite element method, parameterizing the electrical and mechanical properties of the material by the modified SIMP method, finding derivatives of the objective function with respect to the design parameters, constructing a convex approximation and solving the dual optimization procedure within the framework of the moving asymptote method. The algorithm was tested by solving the optimization problem for a piezoelectric plate with a uniform electric field. Additional results were obtained for the case of a linearly distributed electric field. High values of the spring coefficient were observed for more homogeneous structures, ensuring an increase in the pressure force.

Our findings are consistent with the literature data. The results for a linearly distributed electric field were obtained for the first time.

Our results can be useful for designing various micro-electromechanical systems, but the algorithm should be further refined to account for technological constraints. One of the possible options in this case is to add a derivative filter to the algorithm, as well as a design variable filter.

A further direction of research is to introduce machine learning methods accelerating the convergence process for the solution by the method of moving asymptotes (MMA) as well as for the non-iterative solution of the problem.

REFERENCES

1. **Egorov Yu. V.,** On the Lagrange problem about the optimal form for circular hollow columns, Comptes Rendus Mécanique. 331 (10) (2003) 699–704.

2. **Michell A. G. M.,** The limits of economy of material in frame structures, Phil. Mag. Ser. 6. 8 (47) (1904) 589–597.

3. **Prager W., Taylor J. E.** Problems of optimal structural design, J. Appl. Mech. 35 (1) (1968) 102–106.

4. **Bendsше M. P., Dнaz A. R., Kikuchi N.,** Topology and generalized layout optimization of elastic structures, Chapter in book: Bendsше M. P., Soares C. A. M. (Eds.), Topology design of structures, NATO ASI Book Ser. Vol. 227, Springer, Dordrecht (1993) 159–205.

5. **Bendsше M. P., Sigmund O.,** Topology optimization: Theory, methods, and applications, Springer-Verlag, Berlin, Heidelberg, 2003.

6. **Schlinquer T., Mohand-Ousaid A., Rakotondrabe M.,** Optimal design of a unimorph piezoelectric cantilever devoted to energy harvesting to supply animal tracking devices, IFAC-PapersOnLine. 50 (1) (2017) 14600–14605.

7. **Bafumba Liseli J., Agnus J., Lutz P., Rakotondrabe M.,** Optimal design of piezoelectric cantilevered actuators for charge-based self-sensing application, Sensors. 19 (11) (2019) 2582.

8. **Homayouni-Amlashi A., Mohand-Ousaid A., Rakotondrabe M.,** Analytical modelling and optimization of a piezoelectric cantilever energy harvester with in-span attachment, Micromachines. 11 (6) (2020) 591.

9. **Muthalif A. G. A., Nordin N. H. D.,** Optimal piezoelectric beam shape for single and broadband vibration energy harvesting: Modeling, simulation and experimental results, Mech. Syst. Signal Process. 54–55 (March) (2015) 417–426.

10. **Rabenorosoa K., Rakotondrabe M.,** Performances analysis of piezoelectric cantilever based energy harvester devoted to mesoscale intra-body robot, Proc. SPIE. Vol. 9494: Next-Generation Robotics II; and Machine Intelligence and Bio-inspired Computation: Theory and Applications. Baltimore, US, 2016 (95–107).

11. **Rakotondrabe M.,** Combining self-sensing with an unknown input-observer to estimate the displacement, the force and the state in piezoelectric cantilevered actuator, American Control Conference. 17–19 June, 2013, Washington, DC, USA. (2013) 4523–4530.

12. **Khadraoui S., Rakotondrabe M., Lutz P.,** Optimal design of piezoelectric cantilevered actuators with guaranteed performances by using interval techniques, IEEE/ASME Trans. Mechatron. 19 (5) (2014) 1660–1668.

13. **Rakotondrabe M.,** Performances inclusion for stable interval systems, American Control Conference. 29 June – 1 July 2011, San Francisco, California, USA (2011) 4367–4372.

14. **Alexandersen J., Andreasen C. S.,** A review of topology optimization for fluid-based problems, Fluids. 5 (1) (2020) 29.

15. **Deaton J. D., Grandhi R. V.,** A survey of structural and multidisciplinary continuum topology optimization: post 2000, Struct. Multidiscip. Optim, 49 (1) (2014) 1–38.

16. **Moretti M., Silva E. C.,** Topology optimization of piezoelectric bimaterial actuators with velocity feedback control, Front. Mech. Eng. 14 (2) (2019) 190–200.

17. **Goncalves J. F., De Leon D. M., Perondi E. A.,** Simultaneous optimization of piezoelectric actuator topology and polarization, Struct. Multidiscip. Optim. 58 (3) (2018) 1139–1154.

18. **Menuzzi O., Fonseca J.S., Perondi E.A., et al.,** Piezoelectric sensor location by the observability gramian maximization using topology optimization. Comput. Appl. Math. 37 (1) (2018) 237–252.

19. **Homayouni-Amlashi A., Mohand-Ousaid A., Rakotondrabe M.,** Topology optimization of 2DOF piezoelectric plate energy harvester under external in-plane force, J. Micro-Bio Robot. 16 (16 March) (2020) 1–13.

20. **Homayouni-Amlashi A. Mohand-Ousaid A., Rakotondrabe M.,** Multidirectional piezoelectric plate energy harvesters designed by topology optimization algorithm, IEEE Robotics and Automation Letters. 5 (2) (2019) 462–469.

21. **Townsend S., Grigg S., Picelli R., et al.,** Topology optimization of vibrational piezoelectric energy harvesters for structural health monitoring applications, J. Intell. Mater. Syst. Struct. 30 (18–19) (2019) 2894–2907.

22. **Wein F., Kaltenbacher M., Stingl M.,** Topology optimization of a cantilevered piezoelectric energy harvester using stress norm constraints, Struct. Multidiscipl. Optim. 48 (1) (2013) 173–185.

23. **Suzuki K., Kikuchi N.,** A homogenization method for shape and topology optimization, Comp. Meth. Appl. Mech. Eng. 93 (3) (1991) 291–318.

24. **Bendsше M. P., Sigmund O.,** Optimization of structural topology, shape, and material, Springer-Verlag, Berlin, Heidelberg, New York, 1995.

25. **Кцgl M., Silva E. C. N.,** Topology optimization of smart structures: Design of piezoelectric plate and shell actuators, Smart Mater. Struct. 14 (2) (2005) 387–399.

26. **De Almeida B. V.,** Topology optimization of bimorph piezo-electric energy harvesters considering variable electrode location, Smart. Mater. Struct. 28 (8) (2019) 085030.

27. **Chen S., Gonella S., Chen W., Liu W. K.,** A level set approach for optimal design of smart energy harvesters, Comput. Meth. Appl. Mech. Eng. 199 (37–40) (2010) 2532–2543.

28. **Svanberg K.,** The method of moving asymptotes – A new method for structural optimization, Int. J. Numer. Meth. Eng. 24 (2) (1987) 359– 373.

29. **Lerch R.,** Simulation of piezoelectric devices by two-and three-dimensional finite elements, IEEE Trans. Ultrason. Ferroelectr. Freq. Control. 37 (3) (1990) 233–247.

30. **Piefort V.,** Finite element modelling of piezoelectric active structures: PhD thesis, Bruxelles, Belgium: Universite Libre de Bruxelles, 2001, 125 p.

31. **Homayouni-Amlashi A., Schlinquer T., Mohand-Ousaid A., Rakotondrabe M.,** 2D topology optimization MATLAB codes for piezoelectric actuators and energy harvesters, Struct. Multidiscipl. Optim. 63 (2) (2020) 983–1014.

СПИСОК ЛИТЕРАТУРЫ

1. **Егоров Ю. В.** О задаче Лагранжа об оптимальной форме колонны // Доклады Академии наук. 2003. Т. 392. № 5. С. 598—602.

2. **Michell A. G. M.** The limits of economy of material in frame structures // Philosophical Magazine. 1904. Series 6. Vol. 8. No. 47. November. Pp. 589—597.

3. **Prager W., Taylor J. E.** Problems of optimal structural design // Journal of Applied Mechanics. 1968. Vol. 35. No. 1. Pp. 102—106.

4. **Bendsше M. P., Dнaz A. R., Kikuchi N.** Topology and generalized layout optimization of elastic structures (Chapter) // Bendsше M. P., Soares C. A. M. (Eds.) Topology design of structures, NATO ASI Book Series. Vol. 227. Dordrecht (Netherlands): Springer, 1993. Pp. 159—205.

5. **Bendsше M. P., Sigmund O.** Topology optimization: Theory, methods, and applications. Berlin, Heidelberg: Springer-Verlag, 2003. 370 p.

6. **Schlinquer T., Mohand-Ousaid A., Rakotondrabe M.** Optimal design of a unimorph piezoelectric cantilever devoted to energy harvesting to supply animal tracking devices // IFAC-PapersOnLine. 2017. Vol. 50. No. 1. Pp. 14600—14605.

7. **Bafumba Liseli J., Agnus J., Lutz P., Rakotondrabe M.** Optimal design of piezoelectric cantilevered actuators for charge-based self-sensing application // Sensors. 2019. Vol. 19. No. 11. P. 2582.

8. **Homayouni-Amlashi A., Mohand-Ousaid A., Rakotondrabe M.** Analytical modelling and optimization of a piezoelectric cantilever energy harvester with in-span attachment // Micromachines. 2020. Vol. 11. No. 6. P. 591.

9. **Muthalif A. G. A., Nordin N. H. D.** Optimal piezoelectric beam shape for single and broadband vibration energy harvesting: Modeling, simulation and experimental results // Mechanical Systems and Signal Processing. 2015. Vol. 54—55. March. Pp. 417—426.

10. **Rabenorosoa K., Rakotondrabe M.** Performances analysis of piezoelectric cantilever based energy harvester devoted to mesoscale intra-body robot // Proceedings of SPIE. Vol. 9494: Next-Generation Robotics II; and Machine Intelligence and Bio-inspired Computation: Theory and Applications. Baltimore, US, 2016.

11. **Rakotondrabe M.** Combining self-sensing with an unknown input-observer to estimate the displacement, the force and the state in piezoelectric cantilevered actuator // American Control Conference. 17—19 June, 2013.Washington, DC, USA. Pp. 4523—4530.

12. **Khadraoui S., Rakotondrabe M., Lutz P.** Optimal design of piezoelectric cantilevered actuators with guaranteed performances by using interval techniques // IEEE/ASME Transactions on Mechatronics. 2014. Vol. 19. No. 5. Pp. 1660—1668.

13. **Rakotondrabe M.** Performances inclusion for stable interval systems // American Control Conference. 29 June — 1 July 2011, San Francisco, California, USA. Pp. 4367—4372.

14. **Alexandersen J., Andreasen C. S.** A review of topology optimization for fluid-based problems // Fluids. 2020. Vol. 5. No. 1. P. 29.

15. **Deaton J. D., Grandhi R. V.** A survey of structural and multidisciplinary continuum topology optimization: post 2000 // Structural and Multidisciplinary Optimization. 2014. Vol. 49. No. 1. Pp. 1—38.

16. **Moretti M., Silva E. C.** Topology optimization of piezoelectric bimaterial actuators with velocity feedback control // Frontiers in Mechanical Engineering. 2019. Vol. 14. No. 2. Pp. 190—200.

17. **Goncalves J. F., De Leon D. M., Perondi E. A.** Simultaneous optimization of piezoelectric actuator topology and polarization // Structural and Multidisciplinary Optimization. 2018. Vol. 58. No. 3. Pp. 1139—1154.

18. **Menuzzi O., Fonseca J. S., Perondi E. A., Goncalves J. F., Padoin E., Silveira O. A.** Piezoelectric sensor location by the observability Gramian maximization using topology optimization // Computational Applied Mathematics. 2018. Vol. 37. No. 1. Pp. 237—252.

19. **Homayouni-Amlashi A., Mohand-Ousaid A., Rakotondrabe M.** Topology optimization of 2DOF piezoelectric plate energy harvester under external in-plane force // Journal of Micro-Bio Robotics. 2020. Vol. 16. 16 March. Pp. 1—13.

20. **Homayouni-Amlashi A. Mohand-Ousaid A., Rakotondrabe M.** Multidirectional piezoelectric plate energy harvesters designed by topology optimization algorithm // IEEE Robotics and Automation Letters. 2019. Vol. 5. No. 2. Pp. 462—469.

21. **Townsend S., Grigg S., Picelli R., Featherston C., Kim H. A.** Topology optimization of vibrational piezoelectric energy harvesters for structural health monitoring applications // Journal of Intellectual Material Systems and Structures. 2019. Vol. 30. No. 18–19. Pp. 2894–2907.

22. **Wein F., Kaltenbacher M., Stingl M.** Topology optimization of a cantilevered piezoelectric energy harvester using stress norm constraints // Structural and Multidisciplinary Optimization. 2013. Vol. 48. No. 1. Pp. 173–185.

23. **Suzuki K., Kikuchi N.** A homogenization method for shape and topology optimization // Computer Methods in Applied Mechanics and Engineering. 1991. Vol. 93. No. 3. Pp. 291–318.

24. **Bendsшe M. P., Sigmund O.** Optimization of structural topology, shape, and material. Berlin, Heidelberg, New York: Springer-Verlag, 1995. 370 p.

25. **Kцgl M., Silva E. C. N.** Topology optimization of smart structures: Design of piezoelectric plate and shell actuators // Smart Materials and Structures. 2005. Vol. 14. No. 2. Pp. 387–399.

26. **De Almeida B. V.** Topology optimization of bimorph piezo-electric energy harvesters considering variable electrode location // Smart Materials and Structures. 2019. Vol. 28. No. 8. P. 085030.

27. **Chen S., Gonella S., Chen W., Liu W. K.** A level set approach for optimal design of smart energy harvesters // Computer Methods in Applied Mechanics and Engineering. 2010. Vol. 199. No. 37–40). Pp. 2532–2543.

28. **Svanberg K.** The method of moving asymptotes – A new method for structural optimization // International Journal for Numerical Methods in Engineering. 1987. Vol. 24. No. 2. Pp. 359– 373.

29. **Lerch R.** Simulation of piezoelectric devices by two-and three-dimensional finite elements // IEEE Transactions on Ultrasonics, Ferroelectrics, and Frequency Control. 1990. Vol. 37. No. 3. Pp. 233–247.

30. **Piefort V.** Finite element modelling of piezoelectric active structures: PhD thesis, Bruxelles, Belgium: Universite Libre de Bruxelles, 2001. 125 p.

31. **Homayouni-Amlashi A., Schlinquer T., Mohand-Ousaid A., Rakotondrabe M.** 2D topology optimization MATLAB codes for piezoelectric actuators and energy harvesters // Structural and Multidisciplinary Optimization. 2020. Vol. 63. No. 2. Pp. 983–1014.

THE AUTHORS

NOVOKSHENOV Aleksei D.
Peter the Great St. Petersburg Polytechnic University
29 Politechnicheskaya St., St. Petersburg, 195251, Russia
novoksh_ad@spbstu.ru
ORCID: 0000-0001-5874-5994

ABDULIN Ilya
Peter the Great St. Petersburg Polytechnic University
29 Politechnicheskaya St., St. Petersburg, 195251, Russia
abdulin.i.2001@gmail.com
ORCID: 0009-0008-6553-4077

VERSHININ Denis V.
Peter the Great St. Petersburg Polytechnic University
29 Politechnicheskaya St., St. Petersburg, 195251, Russia
vershinindv42@gmail.com
ORCID: 0009-0004-9552-3433

СВЕДЕНИЯ ОБ АВТОРАХ

НОВОКШЕНОВ Алексей Дмитриевич – *кандидат технических наук, доцент Высшей школы механики и процессов управления, старший научный сотрудник Центра компьютерного инжиниринга Санкт-Петербургского политехнического университета Петра Великого.*
195251, Россия, г. Санкт-Петербург, Политехническая ул., 29
novoksh_ad@spbstu.ru
ORCID: 0000-0001-5874-5994

АБДУЛИН Илья – *инженер отдела кросс-отраслевых технологий Санкт-Петербургского политехнического университета Петра Великого.*
195251, Россия, г. Санкт-Петербург, Политехническая ул., 29
abdulin.i.2001@gmail.com
ORCID: 0009-0008-6553-4077

ВЕРШИНИН Денис Вячеславович – *инженер отдела кросс-отраслевых технологий Санкт-Петербургского политехнического университета Петра Великого.*
195251, Россия, г. Санкт-Петербург, Политехническая ул., 29
vershinindv42@gmail.com
ORCID: 0009-0004-9552-3433

Received 08.04.2024. Approved after reviewing 23.04.2024. Accepted 23.04.2024.
Статья поступила в редакцию 08.04.2024. Одобрена после рецензирования 23.04.2024. Принята 23.04.2024.

© Peter the Great St. Petersburg Polytechnic University, 2024

Astrophysics

Original article
UDC 524.6.
DOI: https://doi.org/10.18721/JPM.17313

INDIVIDUAL BEHAVIOR OF GAS HYDRODYNAMICS FROM PAIRS OF ISOLATED GALAXIES IN INTERACTION

E. Teófilo-Salvador ✉

National Autonomous University of Mexico, Mexico

✉ mca.ts.eduardo2015@gmail.com

Abstract. The hydrodynamic behavior of the gas of a selected pair of interacting galaxies has been reviewed based on numerical simulation using Illustris and IllustrisTNG. 210 halos were identified visually, using the Explorer; but their number was reduced due to selection taking into account found distances, masses and particle emission conditions, then the halos were refined and received specific cuts using Python. Among them, 34% did not interact at all, due to asymmetries ranging from 18 to 74%. The pair with ID 473420-473421 turned out to be the best interacting pair, and it was most marked at $z = 1$ and 5. This sample provided more information about the behavior of the gas present, such as the formation of tidal tails, with a relative velocity of 9 to 213 km/s. The density fields were affected by distribution velocities and radial motion in galaxy interaction processes, the gas flow created transitions between the two disks in the radial velocity field, with longer jets in regions of cold gas compared to those of hot one.

Keywords: ID 473420-473421, pair of isolated galaxies, numerical simulation

Funding: The author thanks the National Council of Humanities, Sciences and Technologies of Mexico, for the financial support for the postdoctoral stay 2021–2022 with numbers 930457 and 2420881 for 2022–2023, and to the ESTL-UAEH.

For citation: Teófilo-Salvador E., Individual behavior of gas hydrodynamics from pairs of isolated galaxies in interaction, St. Petersburg State Polytechnical University Journal. Physics and Mathematics. 17 (3) (2024) 148–160. DOI: https://doi.org/10.18721/JPM.17313

This is an open access article under the CC BY-NC 4.0 license (https://creativecommons.org/licenses/by-nc/4.0/)

Научная статья
УДК 524.6
DOI: https://doi.org/10.18721/JPM.17313

ИЗУЧЕНИЕ ПАР ИЗОЛИРОВАННЫХ ВЗАИМОДЕЙСТВУЮЩИХ ГАЛАКТИК В АСПЕКТЕ ГИДРОДИНАМИЧЕСКОГО ПОВЕДЕНИЯ ГАЗА

Э. Теофило-С льв дор ✉

Национальный автономный университет Мексики, г. Мехико, Мексика

✉ mca.ts.eduardo2015@gmail.com

Аннотация. В работе рассмотрено гидродинамическое поведение газа в выбранной паре изолированных галактик, основанное на численном моделировании Illustris и IllustrisTNG. Визуально в браузере Explorer было идентифицировано 210 ореолов, но их количество было уменьшено за счет выбора, учитывающего найденные расстояния, массы и условия выброса частиц; затем с помощью Python ореолы были доработаны и получили специфические разрезы. Среди них 34 % вообще не совершали взаимодействия ввиду наличия асимметрии (18 – 74%). Наилучшей взаимодействующей парой оказалась пара с идентификатором 473420-473421, причем она была лучше всего выражена при

© Teófilo-Salvador E., 2024. Published by Peter the Great St. Petersburg Polytechnic University.

значениях красного космологического смещения $z = 1$ и 5. Выбранная пара позволила получить больше информации о поведении присутствующего газа, например он проявляется в образовании приливных хвостов после взаимодействия с относительной скоростью от 9 до 213 км/с. На поля плотности влияют скорости распределения газов и их радиальное движение в процессах взаимодействия галактик; поток газа создает переходы между двумя дисками в поле радиальных скоростей, причем с более длинными струями в областях холодного газа, по сравнению с таковыми в горячих областях.

Ключевые слова: ID 473420-473421, пара изолированных галактик, численное моделирование

Финансирование. Автор благодарит Национальный совет Мексики по гуманитарным наукам, естественным наукам и технологиям за финансовую поддержку пребывания в докторантуре в 2021–2022 гг. (№№ 930457 и 2420881 от 2022–2023).

Для цитирования: Теофило-Сальвадор Э. Изучение пар изолированных взаимодействующих галактик в аспекте гидродинамического поведения газа // Научно-технические ведомости СПбГПУ. Физико-математические науки. 2024. Т. 17. № 3. С. 148–160. DOI: https://doi.org/10.18721/ JPM.17313

Статья открытого доступа, распространяемая по лицензии CC BY-NC 4.0 (https://creativecommons.org/licenses/by-nc/4.0/)

Introduction

The interaction of galaxies can occur as harassment, interaction, collision, fusion or cannibalism. Simulations have made it possible to describe these phenomena. The morphology and distribution of galaxy radial velocities are signs of recent interaction [1]. Gas-rich systems show star formation due to debris generated [2]. The presence of gas clouds and the density varies due to different coupling mechanisms such as intra clouds [3]. It was shown in Ref. [4] that cold gas inputted tend to smear the central metallicity of the galaxy, and M. Spavone et al. described in Ref. [5] that tidal encounters considerably removed the amount of mass from galaxies, and interaction and accretion mechanisms showed regions still being assembled. It was reported in Ref. [6] that gas mass flow altered the azimuth angle and became longer in directions aligned with the major and minor axes of the galaxies. Quantifying gas temperature, density, entropy, and cooling times is difficult, because entropy is sensitive to feedback energy injection, and is an indicator of gas cooling time [7].

Pairs of galaxies have been studied by many scientists. M. H. Hani et al. [8] analyzed 27,691 post-merger samples with $0 < z < 1$ (z is the cosmological redshift) uniformly distributed, obtaining star formation effects with redshift evolution. K. A. Blumenthal et al. [9] reported 446 pairs with $z = 0$, including star formation rate, galactic winds, metal enrichment, gas heating and cooling, black hole growth, and feedback. I. Wang et al. [10] applied CNN algorithms to report 6114 unique *R*-band galaxies with different orientations by classification into galaxy merger fractions.

R. Davé et al. [11] compared gas properties from the Simba, Eagle, and IllustrisTNG databases, based on cold interstellar gas modeling, with luminosity functions and gas mass ratios. These databases have been supported by codes for numerical simulations such as Enzo, Gadget, Flash, Athena, Ramses, Octo-Tiger, Gizmo or Arepo [12]. The Arepo code is more precise in the interactions between fast moving fluids and shocks such as gas, it ensures a better description due to mixing, of vorticity in curved shocks and a more efficient and realistic extraction of gas from the created substructures [13].

The simulations involve evolution over time and other elements; for example, the gas with dust is released more efficiently [14]. The condensation of metals in the gas phase forms dust grains that can reduce and induce a change in the cooling rate of the outer parts of the galaxy, this implies a change in active galactic nuclei, due to the change in the accretion rate [15]. J. S. Millard et al. [16] established that the evolution of the dust mass can generate a bias depending on the type of galaxies to be studied (satellite or central), leading to alterations in the surrounding gas.

© Теофило-Сальвадор Э., 2024. Издатель: Санкт-Петербургский политехнический университет Петра Великого.

The study of galaxy interaction has not been significant in statistical samples for large cosmological simulations [8], as even multiple physical processes can generate the same process asymmetry [17]. The behavior of the gas in the galactic interaction process is multicomponent, heterogeneous, irregular and discontinuous, due to morphology, propagation speed, travel speed, mass, density and distance, among other factors.

The goal of this research was to develop a simulation-based method for treating pairs of isolated galaxies interacting in the hydrodynamic gas behavior.

Methodology

Fig. 1 shows the methodological procedure designed to conduct the research.

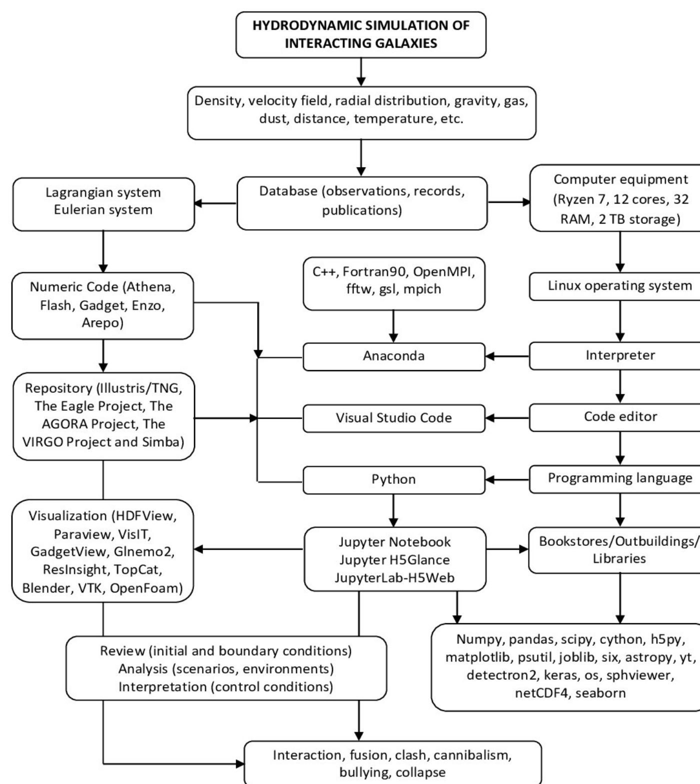

Fig. 1. Diagram of the methodology used (own elaboration)

Selection of galaxy pairs, processing and reduction. It started with the review of numerical codes [18]; an isolated galaxy was created with Enzo, Gadget-2 simulated a pair of interacting galaxies without the presence of gas and dust. To include the Arepo code approach, the IllustrisTNG database was used with 250 TB of data, including interactions ranging from 1 Gyr to less than 500 Myr [10]. Based on the Sublink merge tree methodology used in Ref. [8], in combination with the methodology used in Ref. [19], haloes were associated with their hosts and descendants, and at Jupyter-lab, haloes were identified with pairs of galaxies of similar masses, including interaction distance maxima.

For the visualization and interactive exploration of large data sets, such as those generated by simulations [20], the IllustrisTNG explore 2D and 3D interface was used, layers of different types of particles (gas, stars, dark matter and black holes) were superimposed. Free galaxies and satellite galaxies were taken into account, with massive haloes of 10^{12} $M_{\odot}$ and the case of not containing dark matter were considered purely stellar clusters [21]. At 400 kpc/h, through visual identification, 210 haloes with uniform interaction were recognized, at $z = 0$, under criteria of morphology, gas displacement, formation of bridges and tidal tails.

Identifying pairs in filaments was avoided due to the dense areas of gas and dust. Galaxies with the presence of gas and halos with low star formation were selected to obtain average

temperatures of the order of 104 K [7]. Similar to classification made in Ref. [9], each image was visually classified as interacting or not, based on the presence of a near neighbor, perturbed disks, and/or tidal features. Subsequently, the mass was reduced from 10^{12} to 10^{10} $M_{\odot}$.

Primary and secondary orbital motion was identified; with orbital decay, the pairs could interact or had interacted, so it was necessary to reduce the peripheral distance to 150 kpc. When considering the complete trajectories, samples that would not interact or that had had distant contact in the past were eliminated. To increase the reduction, it was inspected again and again, as some were in multiple subhaloes or were in the same group.

The sizes, distances, masses and their evolution over time were refined using Python. For the dataset of interest and the rendered images, 512 snapshots were generated and downloaded per galaxy, on average 19 GB per simulation review. The samples were no longer cut when central galaxies with satellites were detected, because they are not separated in the recorded observations [21].

The slices of interest were analyzed in Jupyter-lab and the snaps in Glnemo2 to identify interactive dynamic behavior, subsequently in VisIt and Paraview to detect variations or perceive attributes that were not observed in Glnemo2. The datasets and snapshots were also analyzed in HDFView.

Mechanics of pairs galaxies. The interaction speeds of $100 < V_{int} < 400$ km/s were discretized, with a similarity of masses and gas fraction greater than 20 %, in a high-velocity environment of almost frontal collision, and trajectories with traces of bridges or tails tidal [22].

In revising the interactions from $z = 0$ to $z = 10$, several pairs deconfigured the structures, causing a stretching of the field lines, and the vortex lines formed post-shock flows. These vortices were associated with tides, shear, and turbulence because they showed depletion and gas emissions [3, 23]. A normal, stationary alignment and a Mach number of 2 – 4 were needed for smooth interactions, which further reduced the initial samples. The post-shock wind was revised in prolonged interaction, generating a water hammer, the winds and jets aligned to generate a slowing of the flow patterns, this depended on the properties of the host galaxy.

Of the host galaxy, the circumgalactic neighborhood and the cosmic network were reviewed, the presence of disturbed or distorted filaments was tracked, to recognize the interaction force, such as the balance of forces of the tail or tidal bridges, defined as Q_{int} (with all masses as total mass [9]):

$$Q_{int} = \frac{F_{tidal} = \dfrac{M_n D_c}{R_{nc}^3}}{F_{bind} = \dfrac{M_c}{D_c^2}}, \tag{1}$$

where M_n is the mass of the neighboring galaxy; R_{nc} is the distance from the center of the galaxy to the neighboring one; M_c is the mass of the central galaxy; D_c is the diameter of the plant.

Under these criteria, the best pair that represented the interaction process was selected.

Hydrodynamics of the interacting gas. The equations of state and gravity were recognized, along with Poisson's equation, relaxation time, time to reach thermal equilibrium, and rate of energy change. The data sets were associated with the variables of the equations: conservation of mass, momentum and conservation of energy, which were of the following form:

$$\frac{\partial \rho}{\partial t} + \nabla \cdot (\rho \mathbf{u}) = 0, \tag{2a}$$

$$\left(\frac{\partial}{\partial t} + \mathbf{u} \cdot \nabla\right) u^i + \frac{1}{\rho} \partial_j P^{ij} = g^i, \tag{2b}$$

$$\frac{3}{2}\left(\frac{\partial}{\partial t} + \mathbf{u} \cdot \nabla\right)\frac{T}{m} + \frac{1}{\rho} P^{ij} \partial_i u_j + \frac{1}{\rho} \nabla \cdot \mathbf{q} = \frac{\dot{\varepsilon}}{m}, \tag{2c}$$

where $\mathbf{u}$ is the velocity of dark matter; P^{ij} is the pressure tensor; T is the temperature; $\mathbf{q}$ is the heat flux; ε is the local warming rate.

Moreover, the velocity dispersion was taken to be 1D (for simplicity) [24].

The exclusion of current interactions was imposed in advance, and in those cases where

the distribution of gas in and around a satellite galaxy was confused or perturbated [13]. When analyzing gas, IllustrisTNG was considered to overproduce cold gas in massive galaxies and molecular gas in small ones [11].

Results and discussion

Samples of galaxy pairs. As in Ref. [25], the selection of pairs was sensitive to the criteria and methods used. For data analysis, even training with CNN has shown 72 % accuracy between interactions and noninteractions [10], resulting in 28 % uncertainty. As in Ref. [9], in 34% of cases, there were errors in visual identification, due to vision, interpretation and visualization, the errors had the following sources:

i) finite resolution of the simulations;

ii) the stellar material was not the best indicator of a tail tidal force;

iii) the simulations instead of the observations;

iv) in very large impacts, the tidal forces were not strong enough to generate visible bridges or tails;

v) in cases of 1 Gyr the tide was partially noticeable, due to the evolution of the bridge or tail material that was deposited on the discs and could mix with the surrounding material.

The gas fraction ranged from 0.25 to 0.35, less than 10% of the paired samples contained no gas. The selected pairs had an asymmetry ranging from 18 to 74%, and only 26% reflected a symmetry being agree with that in Ref. [17]. A. B. Watts et al. described an asymmetry of more

Table 1

Positions and sizes of the pair of galaxes at different values of the redshift z

<table>
<tr><th rowspan="2">z</th><th colspan="3">Position, ckpc/h</th><th colspan="4">Size (particles)</th></tr>
<tr><th>x</th><th>y</th><th>z</th><th>Gas</th><th>Dark matter</th><th>Stars</th><th>Black holes</th></tr>
<tr><td rowspan="2">0.0</td><td>9796.38</td><td>31580.00</td><td>61031.80</td><td>111249</td><td>156742</td><td>32402</td><td rowspan="2">1</td></tr>
<tr><td>9810.80</td><td>31577.40</td><td>61048.00</td><td>791</td><td>1724</td><td>12280</td></tr>
<tr><td rowspan="2">0.5</td><td>51075.10</td><td>56805.90</td><td>41085.70</td><td rowspan="4">0</td><td>33</td><td rowspan="4">0</td><td rowspan="18">0</td></tr>
<tr><td>51108.10</td><td>56944.60</td><td>40970.80</td><td>29</td></tr>
<tr><td rowspan="2">1.0</td><td>63984.00</td><td>636.11</td><td>58526.30</td><td>30</td></tr>
<tr><td>64012.50</td><td>659.74</td><td>58565.70</td><td>29</td></tr>
<tr><td rowspan="2">2.0</td><td>37898.40</td><td>42362.70</td><td>38639.50</td><td></td><td>23</td><td></td></tr>
<tr><td>22008.60</td><td>69636.30</td><td>14789.10</td><td>1932</td><td>7060</td><td>70</td></tr>
<tr><td rowspan="2">3.0</td><td>24914.00</td><td>28079.20</td><td>36573.80</td><td>0</td><td>29</td><td>0</td></tr>
<tr><td>40989.50</td><td>34735.90</td><td>39956.60</td><td>992</td><td>1864</td><td>5</td></tr>
<tr><td rowspan="2">4.0</td><td>3037.73</td><td>59471.70</td><td>64579.70</td><td>470</td><td>1388</td><td>8</td></tr>
<tr><td>3140.84</td><td>48911.40</td><td>63645.70</td><td>738</td><td>1089</td><td>5</td></tr>
<tr><td rowspan="2">5.0</td><td>17824.60</td><td>47431.50</td><td>56736.60</td><td>15</td><td>21</td><td rowspan="2">0</td></tr>
<tr><td>17823.10</td><td>47399.80</td><td>56704.20</td><td>13</td><td>10</td></tr>
<tr><td rowspan="2">6.0</td><td>40417.40</td><td>67385.70</td><td>35386.40</td><td>97</td><td>131</td><td rowspan="2">1</td></tr>
<tr><td>40401.40</td><td>67403.60</td><td>35880.20</td><td>44</td><td>112</td></tr>
<tr><td rowspan="2">10</td><td>27507.70</td><td>54003.90</td><td>67587.70</td><td>38</td><td>44</td><td>0</td></tr>
<tr><td>28187.10</td><td>16769.50</td><td>53251.80</td><td>35</td><td>48</td><td>1</td></tr>
</table>

Footnotes. 1. Here and in the other tables the data is presented for a pair of isolated interacting galaxes ID 473420-473421 (snapshots 99, 67, 50, 33, 25, 21, 17, 13 and 4). 2. For each value of z the numbers in the 1st and 2nd rows refer to galaxes ID 473420 and ID 473421, respectively.

Notation: *c*kpc/h is the comoving coordinate accepted in cosmology; where letter *c* means “comoving”, kpc is kiloparsec, h is hour(s) in a cell, which is a spatial location within the periodic simulation domain of BoxSize.

Table 2

Masses, metallicity and star formation rates of the pair of galaxes at the redshift z

<table>
<tr><th rowspan="2">z</th><th colspan="5">Mass, 10^{10} $M_{\odot}/h$</th><th rowspan="2">Gas metallicity M_z/M_{total}</th><th rowspan="2">Star formation rate, $M_{\odot}$/yr</th></tr>
<tr><th>Gas</th><th>Dark matter</th><th>Stars</th><th>Black holes</th><th>Wind</th></tr>
<tr><td rowspan="2">0.0</td><td>11.374700</td><td>79.244700</td><td>2.254370</td><td>0.003639</td><td>0.001651</td><td>0.017736</td><td>24.549200</td></tr>
<tr><td>0.087954</td><td>0.871610</td><td>0.806995</td><td>0.004752</td><td rowspan="17">0</td><td>0.011294</td><td>0.338937</td></tr>
<tr><td rowspan="2">0.5</td><td rowspan="2">0</td><td>0.016684</td><td rowspan="2">0</td><td rowspan="2">0</td><td rowspan="5">0</td><td rowspan="5">0</td></tr>
<tr><td>0.014662</td></tr>
<tr><td rowspan="2">1.0</td><td rowspan="2">0</td><td>0.015167</td><td rowspan="2">0</td><td rowspan="2">0</td></tr>
<tr><td>0.014662</td></tr>
<tr><td rowspan="2">2.0</td><td>0</td><td>0.011628</td><td>0</td><td rowspan="2">0</td></tr>
<tr><td>0.209526</td><td>3.569360</td><td>0.006044</td><td>0.001747</td><td>0.089967</td></tr>
<tr><td rowspan="2">3.0</td><td>0</td><td>0.014662</td><td>0</td><td rowspan="2">0</td><td>0</td><td>0</td></tr>
<tr><td>0.111012</td><td>0.942391</td><td>0.000412</td><td>0.000568</td><td>0.009249</td></tr>
<tr><td rowspan="2">4.0</td><td>0.051526</td><td>0.701737</td><td>0.000869</td><td rowspan="2">0</td><td>0.001407</td><td>0.018829</td></tr>
<tr><td>0.079690</td><td>0.550570</td><td>0.000429</td><td>0.000660</td><td>0.018412</td></tr>
<tr><td rowspan="2">5.0</td><td>0.001488</td><td>0.010617</td><td rowspan="2">0</td><td rowspan="2">0</td><td rowspan="6">0</td><td rowspan="2">0</td></tr>
<tr><td>0.001333</td><td>0.005056</td></tr>
<tr><td rowspan="2">6.0</td><td>0.010942</td><td>0.066230</td><td>0.000097</td><td rowspan="2">0</td><td>0.003665</td></tr>
<tr><td>0.004793</td><td>0.056624</td><td>0.000117</td><td>0.001090</td></tr>
<tr><td rowspan="2">10</td><td>0.003587</td><td>0.022245</td><td>0</td><td rowspan="2">0</td><td>0.001684</td></tr>
<tr><td>0.003486</td><td>0.024268</td><td>0.000128</td><td>0.001959</td></tr>
</table>

Notations: $M_{\odot}$/yr, $M_{\odot}/h$ are the solar mass by year and by hour in the cell (see notation to Table 1); M_z / M_{total} is the ratio of the mass of all metals M_z to total mass.

than 40% within a virial radius, with morphologies reminiscent the hydrodynamic interaction of gases.

Dynamics of interaction simulation. The gas flow generated a transition strip in the radial velocity field, with a velocity distribution dispersing between the two disks and towards the center of the galaxies. In regions with cold gas, defined trails and filaments, longer, larger and redder tidal tails, were identified that differed in past interactions compared to recent ones.

In perpendicular encounters, an irregular distribution of masses was obtained, with the rotational movement of the most massive galaxy predominating. By removing the gas from the parallel interaction simulations, slightly inclined orbits were identified, with compensation for energy, density and velocity of the particles. Velocity followed curved or parabolic orbits, higher masses generated lower velocities and vice versa. This allowed us to differentiate a local maximum in its relative velocity (pericenter) and a minimum in each apocenter [9].

Mechanics in the specific sample simulation. The pair ID 473420-473421 was the one that best represented the interaction; its parameters are listed in Tables 1 – 4.

According to the tables data, there is interaction of the galaxy pair at z = 0.0, 0.5 and 1.0 (current era, 5.216 Gyr, 7.925 Gyr). At z = 2.0, 3.0 and 4.0 they move away (10.519, 11.658 and 12.263 Gyr). At z = 5.0 and 6.0 there is interaction (12.626 and 12.871 Gyr ago), and they separate at z = 10 (13.071 Gyr ago), see Fig. 2.

Table 3

Speed of the pair of galaxes at the redshift z

z	Speed, km/s					
	x	*y*	*z*	Maximum	Dispersal	Max radial
0.0	–9.9233	325.0820	–81.7149	213.7140	124.4350	30.3153
	69.5782	325.0830	–76.3504	126.2480	73.1109	3.1939
0.5	18.1919	236.0840	113.0530	9.3480	5.3219	9.9155
	–20.1042	370.8730	106.8270	11.4675	5.9947	6.2147
1.0	113.9510	–154.9760	–156.2260	13.3961	6.5835	5.3254
	64.8812	–89.2324	–235.2910	10.7468	5.3715	7.8986
2.0	–91.6826	–58.4907	75.3331	14.1931	7.9692	2.9171
	–324.7330	213.6400	–16.7254	79.9984	49.7336	57.7372
3.0	–81.3137	162.9840	305.3210	12.3979	6.9828	10.2084
	–100.1590	44.0363	–91.9193	54.9958	40.0558	39.2967
4.0	6.9603	–108.6070	–45.8049	61.7656	36.9068	28.9783
	18.3043	85.7583	–151.3030	51.4435	29.4478	33.5619
5.0	49.0199	–46.2195	–157.8860	12.4697	7.5701	8.5875
	62.9138	–41.1166	–153.0230	13.8873	7.7348	7.8690
6.0	–88.5341	–11.9263	188.1560	28.0516	17.0778	10.5887
	–98.9697	–37.7205	127.6330	31.9846	18.8272	13.9484
10	–186.4820	57.2344	–18.4205	27.9581	16.0782	12.6381
	19.9795	28.3001	–2.7225	27.7100	15.6528	12.4080

Table 4

The stellar photometry and spin of the pair of galaxes at the redshift z

z	Spin projection, (kpc/h)·(km/s)			Stellar photometry, mag		
	x	*y*	*z*	U	B	R
0.0	–291.0730	2942.2300	1143.6600	–22.6033	–22.1590	–22.4746
	–4.2051	83.4657	51.8481	–19.2736	–19.2736	–20.1710
0.5	0.4490	0.1847	–4.5583	0	0	0
	0.0693	5.6761	2.3837			
1.0	–0.6634	–2.3124	–1.3589	0	0	0
	5.6909	–6.5446	–0.5885			
2.0	–0.6987	0.8323	4.3076	0	0	0
	–147.6000	43.1684	–8.8838	–17.2910	–16.7648	–16.9979
3.0	–0.5921	–2.9726	–3.0945	0	0	0
	–84.5564	13.7292	–37.6379	–14.0718	–13.8110	–13.9165
4.0	–18.8156	–4.8045	66.8842	–15.3748	–15.0411	–15.1354
	34.2060	–0.4913	22.9933	–13.6737	–13.5620	–13.7512
5.0	0.4352	0.5800	–4.4037	0	0	0
	–2.4665	–0.7813	0.8567			
6.0	–1.7047	24.5405	–2.1670	–13.4396	–12.9881	–12.9330
	–1.0106	–2.3014	–2.7356	–12.6724	–12.4701	–12.5300
10	–0.1994	–1.6702	–0.8099	0	0	0
	0.3973	–2.3438	–0.0715	–15.0174	–13.6546	–13.5246

Footnotes. 1. Spin projections on the axes were computed for each as the weighted by mass sum of relative coordinates, multiplied by the relative velocity of all particles participating in the cell. 2. Mag units are taken as eight bands according to IllustrisTNG.
Notations: U, B, R are ultraviolet, blue and red magnitudes.

The velocity pattern at z = 0.0, 1.0 and 5.0 was similar for both galaxies in the y and z directions, this reflected a more stable and balanced interaction. The maximum dispersion velocity was 124.35 and 73.11 km/s, respectively, for galaxies 473420 and 473421 at z = 0. The interaction resistance was very low of $\ln Q_{int}$ = 1.5 for masses close to 10^{12} and 2.5 for 10^{10}, so only the most distant ones contributed to a small tidal field. For the hydrodynamic analysis, greater precision was confirmed when analyzing the interaction part of the particles and subsequently analyzing the hydrodynamic part [11].

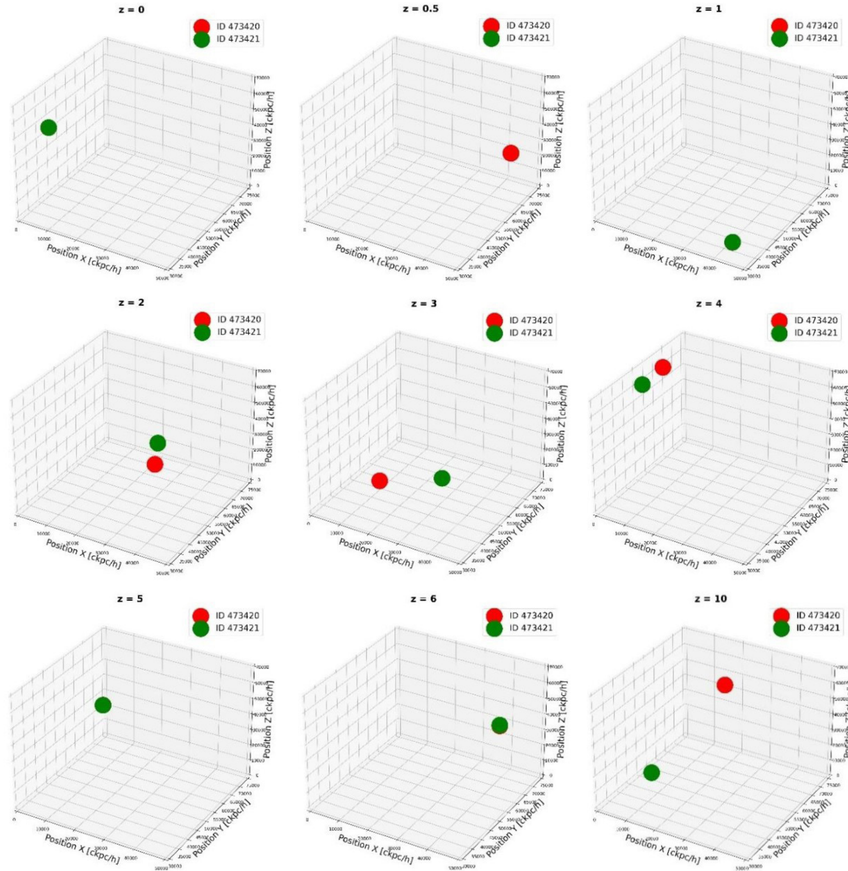

Fig. 2. Trajectory of snapshots 99, 67, 50, 33, 25, 21, 17, 13, 4 (own creation)

Gas hydrodynamics and the specific sample. Not all pairs contained gas, the halo finder did not associate gas particles despite the significant stellar masses. This represented 12 %, within the range of 7 % for Ref. [21]. Thus, gas averages were not appropriate for the interacting distributions [21]. Of the 300 snapshots examined, more than 60 % of the external gas had no effect on the internal one, the rebound caused changes in the relative speed, with small variations in angle and direction.

For the pair ID 473420-473421, the formation of tidal tails depended on the properties and geometry of the galaxies. The dominant metallicities produced massive star formation in the tidal tails, with strong interaction at z = 1 and 5. The specific relative velocity was from 9.34 to 213.71 km/s from 0 to 13.071 Gyr. High speeds separated the dark matter from the hot gas and compressed it by rebound, for the formation of star-like bodies, according to Ref. [22]. The interaction decreased towards low mass regions, due to distorted morphologies.

Galaxy 473421, with fewer particles and a smaller disk, was dominated by dark matter, generating similar rotation curves at z = 5. Heterogeneous, discontinuous and dispersed interactions were part of the evolution [13]. In Fig. 3, dramatic morphological transformations are observed, with deformation and distribution of gas in the galaxies, framed with rounded edges in each image.

Gas content showed no correlation with morphology. The gas fractions were very high and depended on the speed, mass and size of the galaxies.

In Fig. 3, the material was initially uncoupled and recoupled hydrodynamically and the winds removed the metal content of the mass, to keep it in equilibrium during the interaction. According to Ref. [9], the gas masses were ejected from the star-forming regions in the interactions, and the wind speed was proportional to the dispersion speed of the dark matter.

In the density fields, radial motion generated dense sweep, drag, and tidal tails, so gas coupling was strong. This led to the transfer of the thermal and ionization state of the evolved gas. Density increased with size, with dispersion speed not so great; in brighter regions the effect of gravity was greater, compared to the external pressure of the system. According to Ref. [8], this could lead to a substantial improvement in the density of the interacting gas. The interactions resulted in gas flows, created turbulence and could compress the gas. This process may be involved in the formation of new bodies. Like the possible formation of stars in areas with excess gas or denser gas, 2/3 of the central part of the galaxies is formed in this pair.

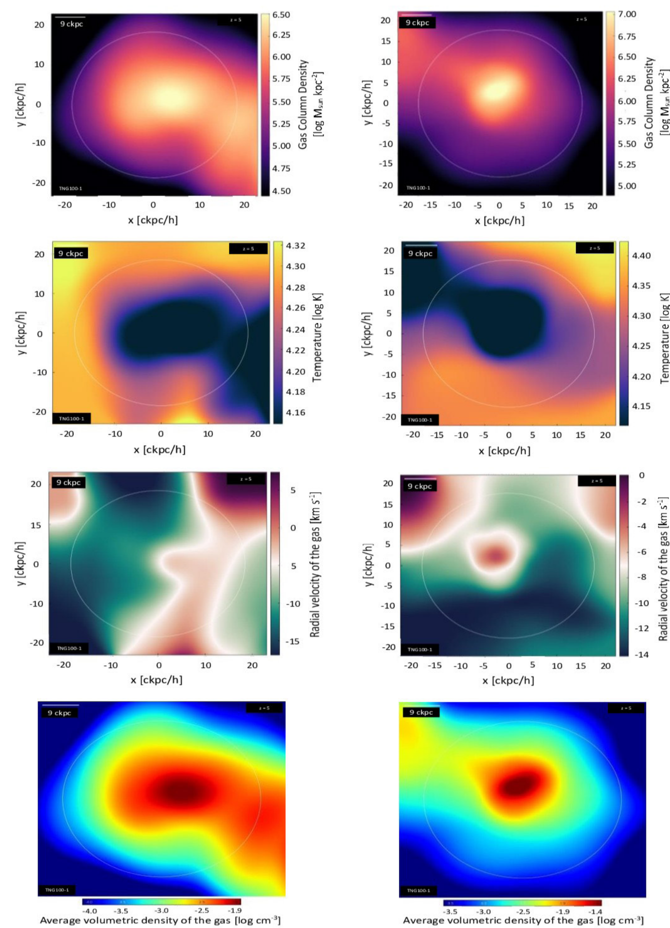

Fig. 3. Images of gas hydrodynamic parameters for a pair of interacting galaxies ID 473421 (left) and ID 473420 (right) based on simulation of TNG100-1 at $z = 5$. Parameters: cold gas density (1st row), gas temperature (2nd row), radial velocity (3rd row), volumetric density (4th row)

The gas entropy served as a good tool for diagnosing feedback (closed-loop) injection, because the gas was ejected by the shock which led to the emergence of wind with colossal kinetic energy not only due to the extinction of the masses, but also to the change in the thermodynamic properties of the gas elements itself, both inside galaxies and on their periphery. This affected ongoing star formation, with gas accreting up to several hundred kiloparsecs [7]. In terms of

massiveness, galaxy 473420 had a greater mass in the interaction process at $z = 1$ and 5, with little new gas which affected the kinetic feedback due to head-on collisions, with injection by sweeping and dragging of particles.

The gas metallicity was correlated with the radial velocity and flow direction along to the trajectories, as an indicator of the properties of the medium, the position and speed of the particles [6]. In interactions, the amount of gas participating in them exceeded the stellar mass, trajectory, density and temperature.

The hydrodynamic survey made it possible to trace the evolution before or after interaction, merger, contact or harassment, and the temporal influence of properties on galaxies, although the observations cannot trace the evolution due to the timing scheme. As in Ref. [19], the variety of tools and information provided by IllustrisTNG, made it possible to evaluate interactions, gas evolution and properties of galaxies (metallicity, morphology and star formation, orbital tracking).

Conclusions

Astrophysical and cosmological simulations require updated information, high-performance supercomputers and rigorous numerical codes for the analysis and interpretation of large data sets (gas, stars, black holes and dark matter), that, at different scales, shape the structure and evolution of the galaxies.

Of 210 samples of galaxy pairs, the visualization method presented disadvantages due to errors such as vision and interpretation of 34 %, less than 10 % did not present gas, and only 26 % reflected an interaction symmetry.

Of 300 snapshots, in more than 60 % the external gas did not influence the internal one, the interaction decreased towards low mass regions, due to distorted morphologies. The gas fractions depended on the speed, mass and size of the galaxies.

The pair that best represented the interaction evolution was ID 473420-473421 at $z = 0$, 1 and 5, where the distance between pairs of galaxies influenced the tidal tails, only at long distances was a relative degree of resistance to the interaction of 1.5 observed. The gas flow generated transitions in the radial velocity field between the two disks, with longer filaments in regions of cold gas compared to those of hot one.

The speed of the gases depended on their temperature and density, as well as on the rates of chemical reactions, which in turn depended on the rates of heating and cooling. These rates affected the interaction depending on the amount of added mass. In light interactions, bursts, weak flashes and short-lived asymmetries were observed, in interactions with a large amount of gas they were more prominent and lasting, until the system stabilized and the gas regrouped again, as shown in the pair ID 473420-473421.

Data availability

Related data is available at www.tng-project.org/, www.illustris-project.org/, https://www.youtube.com/@ingenieriacienciasbasicasy2477/videos

REFERENCES

1. **Fuentes-Carrera I., Amram P., Balkowski C., et al.,** Disentangling interacting galaxy pairs and entangling them back, ASP Conf. Ser. 390 (2008) 186–187.

2. **Paudel S., Duc P. A., Ree C. H.,** A case study for a tidal interaction between dwarf galaxies in UGC 6741, Astron. J. 149 (3) (2015) 114.

3. **Renaud F., Bournaud F., Agertz O., et al.,** A diversity of starburst-triggering mechanisms in interacting galaxies and their signatures in CO emission, Astron. Astrophys. 625 (13 May) (2019) A65.

4. **Zhang B-q., Cao Ch., Xu C. K., et al.,** The multi-object spectroscopy observation of seven interacting galaxy pairs: metallicity gradients and star formation distributions, Publ. Astron. Soc. Pac. 132 (1009) (2020) 034101.

5. **Spavone M., Iodice E., Capaccioli M., et al.,** VEGAS: A VST early-type galaxy survey. III. Mapping the galaxy structure, interactions, and intragroup light in the NGC 5018 group, Astrophys. J. 864 (2) (2018) 149.

6. **Péroux C., Nelson D., de Voort F., et al.,** Predictions for the angular dependence of the gas mass flow rate and metallicity in the circumgalactic medium, MNRAS. 2020. Vol. 499 (2, 21 Oct) (2020) 2462–2473.

7. **Zinger E., Pillepich A., Nelson D., et al.,** Ejective and preventative: The IllustrisTNG black hole feedback and its effects on the thermodynamics of the gas within and around galaxies, MNRAS. 499 (1, 10 Oct) (2020) 768–792.

8. **Hani M. H., Gosain H., Ellison S. L., et al.,** Interacting galaxies in the IllustrisTNG simulations – II: Star formation in the post-merge stage, MNRAS. 493 (3, 1 Apr) (2020) 3716–3731.

9. **Blumenthal K. A., Moreno J., Barnes J. E., et al.,** Galaxy interactions in IllustrisTNG-100, I: The power and limitations of visual identification, MNRAS. Monthly Notices of the Royal Astronomical Society. 492 (2, 1 Febr) (2020) 2075–2094.

10. **Wang I., Pearson W. J., Rodriguez-Gomez V.,** Towards a consistent framework of comparing galaxy merge in observations and simulations, Astron. Astrophys. 644 (03 Dec) (2020) A87.

11. **Davé R., Crain R. A., Stevens A. R. H., et al.,** Galaxy cold gas content in modern cosmological hydrodynamic simulations, MNRAS. 497 (1, 1 Sept) (2020) 146–166.

12. **Teófilo-Salvador E., Ambrocio-Cruz P., Rosado-Solis M.,** Methodological characterization and computational codes in the simulation of interacting galaxies, Artif. Intell. Appl. 2 (1) (2024) 45–58.

13. **Yun K., Pillepich A., Zinger E., et al.,** Jellyfish galaxies with the IllustrisTNG simulations: I. Gas-stripping phenomena in the full cosmological context, MNRAS. 483 (1, 11 Febr) (2019) 1042–1066.

14. **Armijos-Abendaco J., Lypez E., Llerena M., et al.,** Dust deficiency in the interacting galaxy NGC 3077, Galaxies. 5 (3) (2017) 53.

15. **Vogelsberger M., McKinnon R., O´Neil S., et al.,** Dust in and around galaxies: Dust in cluster environments and its impact on gas cooling, MNRAS. 487 (4, 21 Aug) (2019) 4870–4883.

16. **Millard J. S., B. Diemer D., Eales S. A., et al.,** IllustrisTNG and S2COSMOS: possible conflicts in the evolution of neutral gas and dust, MNRAS. Monthly Notices of the Royal Astronomical Society. 500 (1, 1 Jan) (2021) 871–888.

17. **Watts A.B., Power C., Catinella B., et al.,** Global HI asymmetries in IllustrisTNG: A diversity of physical processes disturb the cold gas in galaxies, MNRAS. 499 (4, 15 Oct) (2020) 5205–5219.

18. **Teófilo-Salvador E., Ambrocio-Cruz P., Rosado-Solis M.,** Introduction to Enzo for hydrodynamic simulations in astrophysics, Electron. J. Comput. Inform. Biomed. Electronic. (ReCIBE). 11 (2) (2022) C3-17.

19. **Patton D. R., Wilson K. D., Metrow C. J., et al.,** Interacting galaxies in the IllustrisTNG simulations – I: Triggered star formation in a cosmological context // arXiv: 2003.00289v2 [Astropphysics of Galaxies] Preprint 30 March 2020. Pp. 1–19. https://doi.org/10.48550/arXiv.2003.00289.

20. **Nelson D., Springel V., Pillepich A., et al.,** The IllustrisTNG simulations: Public data release, arXiv: 1812.05609v3[Astropphysics of Galaxies] for this version. 2021. (29 Jan) (2021) 1–30; https://doi.org/10.48550/arXiv.1812.05609.

21. **Diemer B., Stevens A. R. H., Lagos C. P., et al.,** Atomic and molecular gas in IllustrisTNG galaxies at low redshift, MNRAS. 2019. Vol. 487 (2, 1 Aug) 1529–1550.

22. **Shin E-J., Yung M., Kwon G., et al.,** Dark matter deficient galaxies produced via high-velocity galaxy collision in high-resolution numerical simulations, Astrophys. J. 899 (2) (2020) 25.

23. **Nolting C., Jones T. W., O´Neill B. J., Mendygral P. J.,** Interactions between radio galaxies and cluster shocks. I. Jet axes aligned with shock normal, Astrophys. J. 876 (2) (2019) 154.

24. **Famaey B., Khoury J., Penco R., A. Sharma A.,** Baryon-interacting dark matter: Heating dark matter and the emergence of galaxy scaling relations, J. Cosmolog. Astropart. Phys. 2020 (6) (2020) 025.

25. **Grylls P., Shankar F., Conselice C.,** The significant effects of stellar mass estimation on galaxy pair fractions, MNRAS. 99 (2, 1 Dec) (2020) 2265–2275.

СПИСОК ЛИТЕРАТУРЫ

1. **Fuentes-Carrera I., Amram P., Balkowski C., Flores H., Puech M., Yang Y., Rosado M., Hernбndez-Toledo H.** Disentangling interacting galaxy pairs and entangling them back // ASP Conference Series. 2008. Vol. 390. Pathways through an Eclectic Universe. Pp. 186–187.

2. **Paudel S., Duc P. A., Ree C. H.** A case study for a tidal interaction between dwarf galaxies in UGC 6741 // The Astronomical Journal. 2015. Vol. 149. No. 3. P. 114.

3. **Renaud F., Bournaud F., Agertz O., Kraljic K., Schinnerer E., Bolatto A., Daddi E., Hughes A.** A diversity of starburst-triggering mechanisms in interacting galaxies and their signatures in CO emission // Astronomy & Astrophysics. 2019. Vol. 625. 13 May. P. A65.

4. **Zhang B-q., Cao Ch., Xu C. K., Zhou Z-m., Wu Y.** The multi-object spectroscopy observation of seven interacting galaxy pairs: Metallicity gradients and star formation distributions // Publications of the Astronomical Society of the Pacific. 2020. Vol. 132. No. 1009. P. 034101.

5. **Spavone M., Iodice E., Capaccioli M., et al.** VEGAS: A VST early-type galaxy survey. III. Mapping the galaxy structure, interactions, and intragroup light in the NGC 5018 group // The Astrophysical Journal. 2018. Vol. 864. No. 2. P. 149.

6. **Péroux C., Nelson D., de Voort F., Pilleich A., Marinacci F., Vogelsberger M., Hernquist L.** Predictions for the angular dependence of the gas mass flow rate and metallicity in the circumgalactic medium // Monthly Notices of the Royal Astronomical Society. 2020. Vol. 499. No. 2. 21 October. Pp. 2462–2473.

7. **Zinger E., Pillepich A., Nelson D., Weinberger R., Pakmor R., Springel V., Hernquist L., Marinacci F., Vogelsberger M.** Ejective and preventative: The IllustrisTNG black hole feedback and its effects on the thermodynamics of the gas within and around galaxies // Monthly Notices of the Royal Astronomical Society. 2020. Vol. 499. No. 1. 10 October. Pp. 768–792.

8. **Hani M. H., Gosain H., Ellison S. L., Patton D. R., Torrey P.** Interacting galaxies in the IllustrisTNG simulations – II: Star formation in the post-merge stage // Monthly Notices of the Royal Astronomical Society. 2020. Vol. 493. No. 3. 1 April. Pp. 3716–3731.

9. **Blumenthal K. A., Moreno J., Barnes J. E., Hernquist L., Torrey P., Claytor Z., Rodriguez-Gomez V., Marinacci F., Vogelsberger M.** Galaxy interactions in IllustrisTNG-100, I: the power and limitations of visual identification // Monthly Notices of the Royal Astronomical Society. 2020. Vol. 492. No. 2. 1 February. Pp. 2075–2094.

10. **Wang I., Pearson W. J., Rodriguez-Gomez V.** Towards a consistent framework of comparing galaxy merge in observations and simulations // Astronomy & Astrophysics. 2020. Vol. 644. 03 December. P. A87.

11. **Davé R., Crain R. A., Stevens A. R. H., Narayanan D., Saintonge A., Catinella B., Cortese L.** Galaxy cold gas content in modern cosmological hydrodynamic simulations // Monthly Notices of the Royal Astronomical Society. 2020. Vol. 497. No. 1. 1 September. Pp. 146–166.

12. **Teófilo-Salvador E., Ambrocio-Cruz P., Rosado-Solis M.** Methodological characterization and computational codes in the simulation of interacting galaxies // Artificial Intelligence and Applications. 2024. Vol. 2. No. 1. Pp. 45 – 58.

13. **Yun K., Pillepich A., Zinger E., et al.** Jellyfish galaxies with the IllustrisTNG simulations: I. Gas-stripping phenomena in the full cosmological context // Monthly Notices of the Royal Astronomical Society. 2019. Vol. 483. No.1. 11 February. Pp. 1042–1066.

14. **Armijos-Abendaco J., Lypez E., Llerena M., Aldás F., Logan C.** Dust deficiency in the interacting galaxy NGC 3077 // Galaxies. 2017. Vol. 5. No. 3. P. 53.

15. **Vogelsberger M., McKinnon R., O´Neil S., Marinacci F., Torrey P., Kannan R.** Dust in and around galaxies: Dust in cluster environments and its impact on gas cooling// Monthly Notices of the Royal Astronomical Society. 2019. Vol. 487. No. 4. 21 August. Pp. 4870–4883.

16. **Millard J. S., B. Diemer D., Eales S. A., Gomez H. L., Beeston R., Smith M. W. L.** IllustrisTNG and S2COSMOS: possible conflicts in the evolution of neutral gas and dust// Monthly Notices of the Royal Astronomical Society. 2021. Vol. 500. No. 1. 1 January. Pp. 871–888.

17. **Watts A.B., Power C., Catinella B., Cortese L., Stevens A. R. H.** Global HI asymmetries in IllustrisTNG: a diversity of physical processes disturb the cold gas in galaxies // Monthly Notices of the Royal Astronomical Society. 2020. Vol. 499. No. 4. 15 October. Pp. 5205–5219.

18. **Teófilo-Salvador E., Ambrocio-Cruz P., Rosado-Solis M.** Introduction to enzo for hydrodynamic simulations in astrophysics // Computaciyn e Informбtica [Computer Science & Informatics]. 2022. Vol. 11. No. 2. P. C3-17.

19. **Patton D. R., Wilson K. D., Metrow C. J., Ellison S. L., Torrey P., Brown W., Hani M. H., McAlpine S., Moreno J., Woo J.** Interacting galaxies in the IllustrisTNG simulations – I: Triggered star formation in a cosmological context // arXiv: 2003.00289v2 [Astropphysics of Galaxies] Preprint 30 March 2020. Pp. 1–19. https://doi.org/10.48550/arXiv.2003.00289.

20. **Nelson D., Springel V., Pillepich A. et al.** The IllustrisTNG simulations: Public data release // arXiv: 1812.05609v3[Astropphysics of Galaxies] for this version. 2021. 29 January. Pp. 1–30. https://doi.org/10.48550/arXiv.1812.05609.

21. **Diemer B., Stevens A. R. H., Lagos C. P., et al.** Atomic and molecular gas in IllustrisTNG galaxies at low redshift // Monthly Notices of the Royal Astronomical Society. 2019. Vol. 487. No. 2. 1 August. Pp. 1529–1550.

22. **Shin E-J., Yung M., Kwon G., Kim J-H., Lee J., Jo Y., Kiat O. B.** Dark matter deficient galaxies produced via high-velocity galaxy collision in high-resolution numerical simulations // The Astrophysical Journal. 2020. Vol. 899. No. 2. P. 25.

23. **Nolting C., Jones T. W., O´Neill B. J., Mendygral P. J.** Interactions between radio galaxies and cluster shocks. I. Jet axes aligned with shock normal // The Astrophysical Journal. 2019. Vol. 876. No. 2. P. 154.

24. **Famaey B., Khoury J., Penco R., A. Sharma A.** Baryon-interacting dark matter: Heating dark matter and the emergence of galaxy scaling relations // Journal of Cosmology and Astroparticle Physics. 2020. Vol. 2020. No. 6. P. 025.

25. **Grylls P., Shankar F., Conselice C.** The significant effects of stellar mass estimation on galaxy pair fractions // Monthly Notices of the Royal Astronomical Society. 2020. Vol. 499. No. 2. 1 December. Pp. 2265–2275.2001.06017.

THE AUTHOR

TEÓFILO-SALVADOR Eduardo
National Autonomous University of Mexico (UNAM)
National School of Earth Sciences-UNAM
Scientific Research S/N, C. U., 04510, México
mca.ts.eduardo2015@gmail.com
ORCID: 0000-0001-8794-2938

СВЕДЕНИЯ ОБ АВТОРЕ

ТЕОФИЛО-САЛЬВАДОР Эдуардо – *PhD (науки о Земле), профессор Национального автономного университета Мексики (UNAM), профессор Национальной школы наук о Земле, UNAM; г. Мехико, Мексика.*
Scientific Research S/N, C. U., 04510, México
mca.ts.eduardo2015@gmail.com
ORCID: 0000-0001-8794-2938

Received 04.01.2024. Approved after reviewing 17.04.2024. Accepted 17.04.2024.
Статья поступила в редакцию 04.01.2024. Одобрена после рецензирования 17.04.2024. Принята 17.04.2024.

© Санкт-Петербургский политехнический университет Петра Великого, 2024

Научное издание

НАУЧНО-ТЕХНИЧЕСКИЕ ВЕДОМОСТИ САНКТ-ПЕТЕРБУРГСКОГО ГОСУДАРСТВЕННОГО ПОЛИТЕХНИЧЕСКОГО УНИВЕРСИТЕТА. ФИЗИКО-МАТЕМАТИЧЕСКИЕ НАУКИ

«ST. PETERSBURG STATE POLYTECHNICAL UNIVERSITY JOURNAL. PHYSICS AND MATHEMATICS»
ТОМ 17, № 3, 2024

Учредитель и издатель – Федеральное государственное автономное образовательное учреждение высшего образования «Санкт-Петербургский политехнический университет Петра Великого»

Журнал зарегистрирован Федеральной службой по надзору в сфере информационных технологий и массовых коммуникаций (Роскомнадзор).
Свидетельство о регистрации ПИ № ФС77-51457 от 19.10.2012 г.

Редакция

д-р физ.-мат. наук, профессор *В. К. Иванов* – председатель ред. коллегии
д-р физ.-мат. наук, профессор *А. Э. Фотиади* – зам. председателя ред. коллегии
д-р физ.-мат. наук, профессор *В. В. Дубов*
д-р физ.-мат. наук, профессор *П. А. Карасёв*
канд. физ.-мат. наук, доцент *В. М. Капралова*
канд. физ.-мат. наук *О. А. Ящуржинская* – научный редактор, корректор
А. С. Колгатина – переводчик
Н. А. Бушманова – ответственный секретарь

Телефон редакции 8 (812) 552-62-16

Сайт https://physmath.spbstu.ru/

E-mail: physics@spbstu.ru

Компьютерная верстка *Н. А. Бушмановой*

Подписано в печать 30.09.2024. Формат 60х84/8. Печать цифровая.
Усл. печ. л. Тираж 1000. Заказ .

Отпечатано с готового оригинал-макета, предоставленного ИЦ "ИКИ",
в Издательско-полиграфическом центре
Санкт-Петербургского политехнического университета.
195251, Санкт-Петербург, Политехническая ул., 29.
Тел.: (812) 552-77-17; 550-40-14.

УСЛОВИЯ ПУБЛИКАЦИИ СТАТЕЙ

в журнале «Научно-технические ведомости
Санкт-Петербургского государственного политехнического университета.
Физико-математические науки»

1.ОБЩИЕ ПОЛОЖЕНИЯ

Журнал «Научно-технические ведомости Санкт-Петербургского государственного политехнического университета. Физико-математические науки» является периодическим печатным научным рецензируемым изданием. Зарегистрирован в Федеральной службе по надзору в сфере информационных технологий и массовых коммуникаций (Свидетельство ПИ №ФС77-52144 от 11 декабря 2012 г.) и распространяется по подписке агентства «Роспечать» (индекс издания 71823).

С 2008 года журнал издавался в составе сериального издания "Научно-технические ведомости СПбГПУ". **Сохраняя преемственность и продолжая научные и публикационные традиции сериального издания «Научно-технические ведомости СПбГПУ», журнал издавали под сдвоенными международными стандартными сериальными номерами ISSN 1994-2354 (сериальный) 2304-9782.** В 2012 году он зарегистрирован как самостоятельное периодическое издание **ISSN 2304-9782** (Свидетельство о регистрации ПИ № ФС77-52144 от 11 декабря 2012 г.). С 2012 г. начат выпуск журнала в двуязычном оформлении.

Издание входит в Перечень ведущих научных рецензируемых журналов и изданий (перечень ВАК) и принимает для печати материалы научных исследований, а также статьи для опубликования основных результатов диссертаций на соискание ученой степени доктора наук и кандидата наук по следующим основным научным направлениям: **Физика, Математика, Механика**, включая следующие шифры научных специальностей: 1.1.8., 1.1.9., 1.3.2., 1.3.3., 1.3.4., 1.3.5., 1.3.6., 1.3.7., 1.3.8., 1.3.11., 1.3.19.

Журнал представлен в Реферативном журнале ВИНИТИ РАН и включен в фонд научно-технической литературы (НТЛ) ВИНИТИ РАН, а также в международной системе по периодическим изданиям «Ulrich's Periodicals Directory». Индексирован в базах данных «Российский индекс научного цитирования» (РИНЦ), Web of Science (Emerging Sources Citation Index).

Периодичность выхода журнала – 4 номера в год.

Редакция журнала соблюдает права интеллектуальной собственности и со всеми авторами научных статей заключает издательский лицензионный договор.

2. ТРЕБОВАНИЯ К ПРЕДСТАВЛЯЕМЫМ МАТЕРИАЛАМ

2.1. Оформление материалов

1. Рекомендуемый объем статей – 12-20 страниц формата А-4 с учетом графических вложений. Количество графических вложений (диаграмм, графиков, рисунков, фотографий и т.п.) не должно превышать шести.

2. Число авторов статьи, как правило, не должно превышать пяти человек.

3. Авторы должны придерживаться следующей обобщенной структуры статьи: вводная часть (актуальность, существующие проблемы – объем 0,5 – 1 стр.); основная часть (постановка и описание задачи, методика исследования, изложение и обсуждение основных результатов); заключительная часть (предложения, выводы – объем 0,5 – 1 стр.); список литературы (оформление по ГОСТ 7.0.5-2008).

В списки литературы **рекомендуется** включать ссылки на научные статьи, монографии, сборники статей, сборники конференций, электронные ресурсы с указанием даты обращения, патенты.

Как правило, **нежелательны** ссылки на диссертации и авторефераты диссертаций (такие ссылки допускаются, если результаты исследований еще не опубликованы, или не представлены достаточно подробно).

В списки литературы **не рекомендуется** включать ссылки на учебники, учебно-методические пособия, конспекты лекций, ГОСТы и др. нормативные документы, на законы и постановления, а также на архивные документы (если все же необходимо указать такие источники, то они оформляются в виде сносок).

Рекомендуемый объем списка литературы для обзорных статей – не менее 50 источников, для остальных статей – не менее 10.

Доля источников давностью менее 5 лет должна составлять не менее половины. Допустимый процент самоцитирования – не выше 10 – 20. Объем ссылок на зарубежные источники должен быть не менее 20%.

4. УДК (UDC) оформляется и формируется в соответствии с ГОСТ 7.90-2007.

5. Набор **текста** осуществляется в редакторе **MS Word.**

6. **Формулы** набираются в редакторе MathType (не во встроенном редакторе Word) (мелкие формулы, символы и обозначения набираются без использования редактора формул). **Таблицы** набираются в том же формате, что и основной текст. В тексте буква «ё» заменяется на букву «е» и оставляется только в фамилиях.

7. **Рисунки** (в формате .tiff, .bmp, .jpeg) и **таблицы** оформляются в виде отдельных файлов. Шрифт – **Times New Roman**, размер шрифта основного текста – 14, интервал – 1,5. Таблицы большого размера могут быть набраны кеглем 12. Параметры страницы: поля слева – 3 см, сверху и снизу – 2 см, справа – 1,5 см. Текст размещается без знаков переноса. Абзацный отступ – 1 см.

2.2. Представление материалов

1. Представление всех материалов осуществляется в электронном виде через электронную редакцию (http://journals.spbstu.ru). После регистрации в системе электронной редакции автоматически формируется персональный профиль автора, позволяющий взаимодействовать как с редакцией, так и с рецензентом.

2. Вместе с материалами статьи должно быть представлено экспертное заключение о возможности опубликования материалов в открытой печати.

3. Файл статьи, подаваемый через электронную редакцию, должен содержать только сам текст без названия, списка литературы, аннотации и ключевых слов, фамилий и сведений об авторах. Все эти поля заполняются отдельно через электронную редакцию.

2.3. Рассмотрение материалов

Предоставленные материалы (п. 2.2) первоначально рассматриваются редакционной коллегией и передаются для рецензирования. После одобрения материалов, согласования различных вопросов с автором (при необходимости) редакционная коллегия сообщает автору решение об опубликовании статьи. В случае отказа в публикации статьи редакция направляет автору мотивированный отказ.

При отклонении материалов из-за нарушения сроков подачи, требований по оформлению или как не отвечающих тематике журнала материалы не публикуются и не возвращаются.

Редакционная коллегия не вступает в дискуссию с авторами отклоненных материалов.

При поступлении в редакцию значительного количества статей их прием в очередной номер может закончится **ДОСРОЧНО**.

E-mail: physics@spbstu.ru,
Тел. редакции 8 (812) 552-62-16.
Сайт журнала: https://physmath.spbstu.ru/